NORTHWESTERN UNIVERSITY

Searches for New Physics Using High Mass Dimuons at the CDF II Experiment

A DISSERTATION

SUBMITTED TO THE GRADUATE SCHOOL

IN PARTIAL FULFILLMENT OF THE REQUIREMENTS

for the degree

DOCTOR OF PHILOSOPHY

Field of Physics and Astronomy

By

Müge Karagöz Ünel

EVANSTON, ILLINOIS

December 2004

VOLUME I and II

ABSTRACT

Searches for New Physics Using High Mass Dimuons at the CDF II Experiment

Müge Karagöz Ünel

The Collider Detector at Fermilab collected approximately 200 pb^{-1} of Tevatron $p\bar{p}$ collision data at $\sqrt{s} = 1.96$ TeV between spring 2002 and fall 2003. We present results for searches for new physics in the dimuon final state using these data. The searches include heavy neutral particles predicted within extended gauge groups (various Z′s), Technicolor (vector mesons), R-parity violating Supersymmetry (scalar neutrino), and warped extra dimensions (Randall-Sundrum gravitons). We present 95% Confidence Level (C.L.) upper limits on the production cross section times the branching ratio of new particles as a function of the dimuon invariant mass and place 95% C.L. lower mass bounds on the particles. Current limits exceed published limits of previous direct searches in the dimuon channel. We also pioneered search strategies and exploration of some models. Limit results from the electron and muon combined channels are also presented.

To my late eldest brother, Turgay Karagöz,

who unexpectedly passed away

as I was finishing my thesis....

Acknowledgments

"So let us then try to climb the mountain, not by stepping on what is below us, but to pull us up at what is above us, for my part, at the stars."

M.C. Escher

"The roads by which men arrive at their insights into celestial matters seem to me almost as worthy of wonder as those matters in themselves.", said Kepler in his famous book [1]. My journey in high energy physics has been something like that. I have most probably not yet reached many insights, but I sure traveled a very winding and interesting road during my years as a student. Northwestern University and CDF experiment at Fermilab have been the last stations on the road. My thanks are due to my adviser Prof. Michael Schmitt, for giving me the opportunity to perform my research and for letting me become an independent scientist. My analysis supervisor

[1] Johannes Kepler, Astronomia Nova, summary of Cap. 45.

at Fermilab, Kaori Maeshima ("Kaori-san") has welcomed me to work with her. This allowed me to perform my thesis analysis with muons, the particles whose detection system I worked two years on during its commissioning. Kaori deserves a big gratitude, not for only the opportunity, but also for her continuing support, friendliness and kindness. Many appreciations also go to the other members of the high mass dilepton search group I worked with: Koji Ikado and Tim Nelson. I also thank the CDF spokespersons for their efforts in running the CDF experiment.

Sometimes we make decisions and we end up either regretting them or telling how lucky we have been. The latter is true with the beam halo monitoring project I worked on under the supervision of Rick Tesarek. I am indebted to his encouraging and enthusiastic personality and to his knowledge, without which the project may not have been as fun and fruitful. Rick was also helpful to my work in many ways. He also was an important member of the gang of people who introduced the USA to me: the nature, the culture, the history. None will be forgotten. *"Kopernigk's* "The Book of the Revolutions of the Heavenly Spheres" *was an all-time worst-seller. The main reason for this is the book's supreme unreadability*[2] ", comments Koestler. This thesis may not be the best piece of work, let alone a readable one. One thing I know, it would be an order of magnitude worse, if Rick has not taken his time to read through it and came back with many red scribbled pages. I do appreciate his

[2] A. Koestler, The Sleepwalkers, Part 3, Section 1.

help a lot.

The cool guy of the muon folks, Phil Schlabach! How can I not be grateful to him! With his vast knowledge form Run I, he almost made one feel useless, since he has "been there, done that". Phil, you have been one of the greatest personalities I met at CDF. CDF was fun with you, especially with your wonderful stories, after a couple of beers.

Stephan Lammel has been the exotic group convener for the duration of my analysis. I feel a deep gratitude for his input, support on my presentations, analysis, for useful discussion on physics and for his encouragement. Input from a person who has gained so much experience on exotics was very valuable. I also thank Steve Worm and and his replacement, Beate Heinemann, for the last year as the other conveners. Chris Hays and Rocio Vilar has been two VEGy group leaders who I also feel thankful. Rocio especially deserves for her kind friendship and support. Other many exotic group members' input and help are also appreciated, especially, John Conway's help with the statistical analysis issues.

The CDF muon group was very nice to be a part of. Jonathan Lewis is another great Fermilab physicist. He was the person who thought me how to interpret the sizes of nuts and bolts! Ken Bloom was the muon software guru. I enjoyed working with him on the muon software development. Abraham Gallas deserves his share of lines here. I will not forget him, since, at one point in my life, he was the person i

saw more than anybody else: Going down the collision hall on a Sunday at 8am was no extraordinary event during the commissioning quest. I know he is as proud as I am that I came up with results using the CMX. Hey Abraham, if you are in any other collision hall these days, just be careful, since you never know who may "leave their cryogenic pipes unattended".

Life has its tricks, and the life of a graduate student is no exception to this. My USA graduate school journey started in Texas A&M. There, I had the opportunity to work with Prof. Teruki Kamon. I had a vast amount of support from him in the short time I was at TAMU and I will always appreciate this. Another TAMU person who deserves my gratitude is James Done, for helping me during my US adaptation time and for his never-ending confidence in my abilities.

Many phenomenologists/theorists were also great help to us about various physics models. I especially acknowledge Heather Logan and Steve Mrenna, for useful discussions and their friendly and prompt approaches. Steve is definitely in my top 10 "wizards of phys" list.

Being in the lab environment was an experience. The Fermilab scientists, staff and technicians; they were all very helpful and nice. The Fermilab technicians were there whenever I needed help or supplies. George W. and the others: thank you for being great help! Carol P. and Barb P., I thank you, too. In the first couple of years at CDF II, it was not easy to perform analysis. Software and hardware shaped

up while trying to get results in a frenzy environment. We managed to do better and better, eventually! It is true that the next generation of graduate students may neither live nor appreciate the times of frustration that we went through in those first years. But, it was worth it!

Stephan Lammel deserves thanks also for his enjoyable coffee breaks and for his kind friendship. It has been an honor being a member of the "coffee club" whose members included many nice and friendly faces of the CDF community. Farrukh, thank you for the leg of lamb grill at my graduation party! Ingyin Zaw witnessed only the last part of my graduate studentship (which is assumed to be the most miserable part!) and she has become one of my best folks in a short time with her kind and fun friendship. I will definitely miss our chats. Other uncountable friends and colleagues also deserve thanks for one reason or another.

The Northwestern group... Victoria, I will always remember you as "the weather girl" and your detailed forecasts have been greatly appreciated. Dale, you deserve big thanks for your kind rides to NWU on mondays and your enjoyable company. Also, thank you for helping with the CMX responsibilities, for which you have done a good job! Steve Eichblatt, thanks to you for being the "other" for a long time in the NWU HEP office, thus, being my first, and one of my very best friends. Thank you for many intriguing physics and "philosophy of life" discussions, your help on daily life, your encouragement to me and your always very fun and relaxing company

to me and to Gokhan. Are you in for one more Turkey trip? Bob Tilden! What can I say about the coolest guy in the whole NWU-HEP community! Thank you for your continuing help with many things and your company, which will be missed a lot. I hope I see more of your wonderful photographs. Northwestern folks, especially Atakan Gürkan for being there for many many things and for many many cherry wines he brought from Turkey. Teresa for being a friend before even meeting me in person and for her "Super Muge"'s. Thanks to Paolo, for his many tips and input for thesis and graduation issues. Northwestern HEP faculty has valued members. I greatly appreciate the support from Dave Buchholz, in many ways. Heidi Schellman is one of the coolest, rare-to-find women scientists and she always gave me confidence by appreciating my work. I also thank the NWU office staff, for their help and friendliness. And to all the other friends at NWU, they know who they are.

During my last year at Fermilab (how late, it was), I joined the most fun group at CDF: the DSD band! I will never forget the practices at Dee (a very huge hug to her!) and Steve Hahn's always welcoming home and the gigs we performed. Steve, Greg Feild, Larry Nodulman, and the other members deserve big thanks for putting up with a novice like me. They not only welcomed me to a band, but to the coolest group of people at CDF. Thank you, DSD, for bringing joy to my life at its toughest. (Todd, are we performing Cranberries in Barcelona?)

The Turkish community at Fermilab was not big, but consisted of a nice group

of scientists. I especially acknowledge Selcuk Cihangir and Muzaffer Atac for their kind and supportive approach. The wonderful dishes Taylan and Kenan cooked in the Fermilab village house are also appreciated.

My best pals from Boğaziçi Univ. HEP group have always been there for me, too. I will not forget the continuing support and confidence in me, from Ömer, Bahadır and Ahmet, all throughout these years when all of us were all scattered in one place of the US and miraculously came together every now and then.

Whatever I was able to accomplish in my life and in my graduate years, I owe it to my family and my dear husband, my NGU, Gökhan Ünel. My family's never-ending love was so big that they always supported me in my choices in my career, although they had to endure being separated from me for many years and never uttered a single word of complaint, but always encouragement and belief. I was also separated from my husband who was at CERN while I was at Fermilab, on and off, but he was always there for me. He is not only my dear love, but also my best colleague, whom I could not do without. They all deserve thanks in Turkish as well. That is what is below. Oh, and, one last thanks to something else, which better remains written in Turkish, because, Kepler, I am still "hopping and skipping" down that road...

Hayatta iyi ve güzel ne elde edebildiysem, bunu sevgili aileme ve canım NGU'ma borçluyum. Bir de içimdeki hiç büyümeyecek çoçuğa...

Addenda: **1.** During the frenzy of trying to finish up this dissertation before its deadline, thanks to the members of my thesis committee, Prof. Dave Buchholz and Prof. André de Gouvêa were mistakenly left out. I thank them here now. **2.** I now dedicate this work to my late brother, who passed away in August. A sorrowful fact I could learn only after my thesis was submitted...

We thank the Fermilab staff and the technical staffs of the participating institutions for their vital contributions. This work was supported by the U.S. Department of Energy and National Science Foundation; the Italian Istituto Nazionale di Fisica Nucleare; the Ministry of Education, Culture, Sports, Science and Technology of Japan; the Natural Sciences and Engineering Research Council of Canada; the National Science Council of the Republic of China; the Swiss National Science Foundation; the A.P. Sloan Foundation; the Bundesministerium fuer Bildung und Forschung, Germany; the Korean Science and Engineering Foundation and the Korean Research Foundation; the Particle Physics and Astronomy Research Council and the Royal Society, UK; the Russian Foundation for Basic Research; the Comision Interministerial de Ciencia y Tecnologia, Spain; in part by the European Community's Human Potential Programme under contract HPRN-CT-20002, Probe for New Physics; and by the Research Fund of Istanbul University Project No. 1755/21122001.

Contents

List of Figures

List of Tables

Chapter 1

Theory Introduction

"We dance around in a ring and suppose,

but the "secret" sits in the middle and knows."

Robert Frost

1.1 Motivation

The "Standard Model" (SM) of elementary particle physics has been the prevailing theory of quarks and leptons and their electromagnetic, weak and strong interactions. However, the current description of the subatomic world, mostly governed by the Standard Model, has important unanswered questions: the composition of the universe, its energy and matter density; the number of particles and the origin of

their masses; the origin and the variance of the strength of particle interactions. Elementary particle physicists have achieved a profound understanding of matter and physical laws, but the mystery(ies) of the universe remains to be solved.

In addition to the theoretical questions, there are recent important developments in particle physics that point toward new phenomena beyond the SM, such as: neutrino mixing, the puzzling dark matter and energy dominance in the universe, briefly described below:

1. *Neutrino Masses:* The recent results from the atmospheric,solar and reactor neutrino experiments point to evidence for oscillations between neutrino families which may explain the observed deficit in the solar electron neutrino flux and the atmospheric muon neutrino flux [1]. The indications of inter-species oscillations of neutrinos is the non-zero and non-degenerate neutrino masses, which may be accommodated in physics beyond the SM.

2. *Dark Matter and Energy:* Only a small fraction of the universe is made up of ordinary matter (particles predicted by the SM). Recent results from cosmological measurements, such as cosmic microwave radiation background measurements from WMAP [2], provide strong support for the existence of dark matter and dark energy, which fills the rest of the universe. Dark matter could be a particle or particles that have not yet been observed [3]. One interpretation for

the dark energy is first postulated by Einstein as a cosmological constant that may account for more than 60% of the universe [4].

3. *Baryon (matter-antimatter) Asymmetry of the Universe:* The question of why there is a baryon asymmetry in the universe is still unexplained by today's experiments and observations. Sakharov suggested solutions which are to a great extent accommodated by grand unified theories. However, the details of the mechanism is not yet clear [5, 6].

The above-mentioned developments and the yet-unanswered questions bring us to the verge of discovering more fundamental laws of nature. They also lead theorists to come up with models with implications that can be tested at the present and future experiments. Most of these models predict massive particles that are not forbidden to exist by current knowledge. Such particles may decay into a fermion pair and may manifest themselves as deviations from SM expectations. The observation of such phenomena often requires large data samples and high center of mass energy in collisions.

In this study, we search for new particles decaying into two highly energetic muons in the data from the Collider Detector Experiment at Fermi National Laboratory (CDF). The direct evidence of massive particles would be a significant excess in the number of observed events in the dimuon data for a high invariant mass sample.

Historically, lepton pair production have been one of the best signatures for observation of new signals in high energy physics. The J/ψ, Υ, and the Z boson were all discovered in the dilepton channel. The current search has been for spin-0 (R-parity violating Supersymmetry $\widetilde{\nu}$), spin-1 heavy gauge bosons and Technicolor mesons (Z$'$, Techni-$\omega_{\rm T}$ and $\rho_{\rm T}$) and spin-2 bosons (Randall-Sundrum graviton). The categorization with respect to the particle spin properties allows for a more general approach toward model independent searches. The dimuon search channel is also complementary to the similar searches that can be performed using the dielectron channel [7]. Furthermore, dimuon and dielectron channel results can be combined into a dilepton result to increase search sensitivity.

In the following sections of this dissertation, we introduce the theoretical background, describe the data and simulation samples, the background predictions and the techniques used. We present the results obtained for new physics and outline the implications of the results for various models that are explored during this study. The results for dilepton channel are also presented.

1.2 Standard Model of Elementary Particles

The Standard Model (SM) of elementary particles is a gauge field theory which is described by the symmetry group $SU(3) \otimes SU(2) \otimes U(1)$. The non-Abelian

$SU(2) \otimes U(1)$ is the electroweak group which unifies the electromagnetism and the weak interactions. It is also called the Glashow-Salam-Weinberg theory [8]. The $SU(3)$ group represents the gauge theory for strong interactions, the Quantum Chromodynamics (QCD) [9].

Fundamental particles known to exist within the SM can be classified into two groups in the particle physics "periodic table": fermions and bosons. The fermions, which form the matter in the universe are grouped as left-handed doublets and right-handed singlets and are summarized in Figure 1.1. The force carrier SM bosons are listed in Figure 1.2. The electroweak fields are the Z, W and γ vector bosons and the strong interactions are carried by the massless gluons. The fermions are characterized by their quantum numbers of weak isospin, I and third component, I_3, and the weak hypercharge, Y. The relation of the $SU(2) \otimes U(1)$ quantum numbers and their electric charges, Q, are given by the Gell-Mann-Nishijima relation:

$$Q = I_3 + \frac{Y}{2} \quad . \tag{1.1}$$

The formulation of the electroweak SM is driven by the empirical facts that depend on these fermions and vector bosons. The observed non-zero masses, m_Z and m_W, of the weak force carriers is the central question of the electroweak physics. Demanding local gauge invariance of the electroweak Lagrangian requires massless

	Generation I	Generation II	Generation III	Q	T	T_3	Y
leptons	$\begin{pmatrix}\nu_e\\ e\end{pmatrix}_L$	$\begin{pmatrix}\nu_\mu\\ \mu\end{pmatrix}_L$	$\begin{pmatrix}\nu_\tau\\ \tau\end{pmatrix}_L$	$\begin{matrix}0\\ -1\end{matrix}$	1/2	$\begin{matrix}+1/2\\ -1/2\end{matrix}$	−1
	e_R	μ_R	τ_R	−1	0	0	−2
quarks	$\begin{pmatrix}u\\ d\end{pmatrix}_L$	$\begin{pmatrix}c\\ s\end{pmatrix}_L$	$\begin{pmatrix}t\\ b\end{pmatrix}_L$	$\begin{matrix}+2/3\\ -1/3\end{matrix}$	1/2	$\begin{matrix}+1/2\\ -1/2\end{matrix}$	+1/3
	$\begin{matrix}u_R\\ d_R\end{matrix}$	$\begin{matrix}c_R\\ s_R\end{matrix}$	$\begin{matrix}t_R\\ b_R\end{matrix}$	$\begin{matrix}+2/3\\ -1/3\end{matrix}$	0	0	$\begin{matrix}+4/3\\ -2/3\end{matrix}$

Figure 1.1: Properties of SM fermions.

Boson	Mass(GeV/c^2)	Q	Spin	Interaction (Strength)	
Z	91.188 ± 0.002	0	1	**Weak**	(E−7)
W	80.423 ± 0.004	+1/−1	1		
γ	0	0	1	**QED**	(E−2)
g	0	0	1	**QCD**	(E+0)
H	> 114 (@95% CL) < 193 (@95% CL)	0	0	**Yukawa**	
G		0	2	**Gravity**	(E−40)

Figure 1.2: Properties of SM bosons and graviton. Higgs mass limits are from [10].

spin-1 fields. The non-zero masses of the W and Z bosons implies that a mechanism should break the electroweak symmetry and that the consistency of the theory with the measurements should be satisfied. The mechanism is the "spontaneous symmetry breaking" of the electroweak through the scalar Higgs field. The gauge-invariant field theory with spontaneous symmetry breaking can be constructed via an electroweak interaction Lagrangian [11]:

$$\mathcal{L} = \mathcal{L}_{gauge} + \mathcal{L}_{fermions} + \mathcal{L}_{Higgs} \tag{1.2}$$

The first term describes the pure gauge field self-interactions:

$$\mathcal{L}_{gauge} = -\frac{1}{4} W^i_{\mu\nu} W^i_{\mu\nu} - \frac{1}{4} B_{\mu\nu} B_{\mu\nu} \quad , \tag{1.3}$$

where the field strength tensors are given by:

$$\begin{aligned} W^i_{\mu\nu} &= \partial_\nu W^i_\mu - \partial_\mu W^i_\nu - g_2 \epsilon^{ijk} W^j_\mu W^k_\nu \quad , \\ B_{\mu\nu} &= \partial_\nu B_\mu - \partial_\mu B_\nu \quad , \end{aligned} \tag{1.4}$$

where g_2 is the weak-isospin coupling. The $U(1)$ Abelian hypercharge coupling is g_1.

The second term in Equation 1.2 is the fermion-gauge boson interactions:

$$\mathcal{L}_{fermion} = \sum \bar{f}\, i \not{D}\, f \tag{1.5}$$

with the sum running over the left- and right-handed field components of the leptons and quarks. Depending on the fermion species, the covariant derivative takes the form:

$$D_\mu = \partial_\mu - i g_2 I^i W^i_\mu + i g_1 \frac{Y}{2} B_\mu \quad . \tag{1.6}$$

The third term, $\mathcal{L}_{Higgs}$, summarizes the Higgs interactions with gauge bosons, fermions (Yukawa couplings) and the Higgs self-interaction terms. The Higgs field ($\Phi = [\phi^+, \phi^0]$) couples to the gauge fields to break the $SU(2) \otimes U(1)$ to leave the electromagnetic gauge subgroup $U(1)_{em}$ unbroken.

$$\mathcal{L}_{Higgs} = (D_\mu \Phi)^\dagger (D^\mu \Phi) - V(\Phi) + \mathcal{L}_{Yukawa} \quad , \tag{1.7}$$

where the Higgs field self-interaction is:

$$V(\Phi) = -\mu^2 \Phi^\dagger \Phi + \frac{\lambda}{4} \left(\Phi^\dagger \Phi \right)^2 \quad , \tag{1.8}$$

and the Yukawa term is:

$$\mathcal{L}_{Yukawa} = -m_f \overline{\psi}_f \psi_f - \frac{m_f}{v} \overline{\psi}_f \psi_f h \quad , \tag{1.9}$$

In the unitary gauge, the Higgs field has the form:

$$\Phi = \frac{1}{\sqrt{2}} \begin{pmatrix} 0 \\ \\ v + h \end{pmatrix} \quad , \tag{1.10}$$

where h is the field of a physical neutral scalar particle, the Higgs boson, with mass $m_H = \mu\sqrt{2}$, and v is the vacuum expectation value (vev).

The physical fields and parameters of the electroweak SM can be derived from the Lagrangians. A transformation from the fields W_μ^i, B_μ to the physical fields in the Higgs-gauge field interaction yields:

$$\begin{aligned} W_\mu^\pm &= \frac{1}{\sqrt{2}} \left[W_\mu^1 \mp i W_\mu^2 \right] \\ Z_\mu &= \cos\theta_W W_\mu^3 + \sin\theta_W B_\mu \\ A_\mu &= -\sin\theta_W W_\mu^3 + \cos\vartheta_W B_\mu \end{aligned} \tag{1.11}$$

where the physical masses become

$$m_W = \frac{1}{2} g_2 v \quad , \quad m_Z = \frac{1}{2}\sqrt{g_1^2 + g_2^2}\, v \quad , \quad m_\gamma = 0 \quad , \tag{1.12}$$

and the mixing angle (θ_W, Weinberg angle), in the rotation Equation 1.11, is related to the gauge boson masses, given by:

$$\cos\theta_W = \frac{g_2}{\sqrt{g_1^2 + g_2^2}} = \frac{m_W}{m_Z} \quad . \tag{1.13}$$

The electric charge e can be expressed in terms of the gauge couplings in the following way:

$$e = \frac{g_1 g_2}{\sqrt{g_1^2 + g_2^2}} = g_2 \sin\theta_W = g_1 \cos\theta_W \quad . \tag{1.14}$$

Finally, from the Yukawa coupling terms, the fermion masses are obtained:

$$m_f = g_f \frac{v}{\sqrt{2}} = \sqrt{2}\frac{g_f \sin\theta_W}{e} m_W \quad . \tag{1.15}$$

The relations above replace the theory parameters (g_2, g_1, λ, μ and g_f) with the physical parameters (e, m_W, m_Z, m_H and m_f) that can, in principle, be measured in experiments. The only parameter that is unmeasured in this list is the mass of the Higgs particle, m_H, whose existence is yet to be proved.

1.3 Resonance Production at Colliders

A resonance is an unstable particle produced as part of a hard processes; its decay treatment normally is also part of the hard process. The hard scattering cross section of a resonance is given by $\hat{\sigma}(\tau) \propto \delta(\tau - \tau_R)$, where τ_R is defined as the scaled mass $\tau_R = m_R^2/s$, as a fraction is the resonance mass and the total squared center-of-mass energy of the system. This is the zero-width approximation. For a resonance where the finite width is Γ_R, the δ function can be replaced by a Breit-Wigner [12] distribution:

$$\delta(\tau - \tau_R) \to \frac{s}{\pi} \frac{m_R \Gamma_R}{(s\tau - m_R^2)^2 + m_R^2 \Gamma_R^2} \quad , \tag{1.16}$$

This is the most common description of a resonance [37] An improved description of resonance shapes is obtained if the width is made mass-dependent (or $\hat{s}$-dependent if $\hat{s}$ is the the resonance mass).

In the section below, we concentrate in the Drell-Yan process, which is the main SM process that yields inclusive muon pair production through a resonance at the Tevatron.

1.3.1 Drell-Yan Process

The inclusive hadronic interaction

$$a + b \rightarrow \ell^+\ell^- + x \tag{1.17}$$

where $\ell^+\ell^-$ represents massive lepton pairs (e^+e^-, $\mu^+\mu^-$and $\tau^+\tau^-$), is known as the Drell-Yan (DY) process. The mediator of these interactions is a virtual photon ($\gamma*$) or a Z-boson, within the known particles of the Standard Model. The name DY is after S. D. Drell and T. M. Yan, who provided the first successful description of lepton pair production in the context of the parton model (leading order in QCD) [13]. The first experiment to study Drell-Yan process was carried out by the Columbia-BNL group in 1970 [14]. Later on, the discovery of the Z boson in dilepton final state at CERN [15] gave an empirical evidence in strong support of SM.

The general form of the $p\bar{p}\rightarrow\ell^+\ell^-+x$ cross section, as a function of the lepton invariant mass, M, the rapidity, y and the $\cos\theta^*$ of the center of mass frame scattering angle, may be represented by [16]:

$$\frac{d\sigma}{dMdyd\cos\theta^*} = \sum_q \left[g_q^S(y,M)S_q(M)(1+\cos^2\theta^*) + g_q^A(y,M)A_q(M)2\cos\theta^*\right] \tag{1.18}$$

where $S_q(M)$ and $A_q(M)$ involve the vector and axial couplings of fermions to the

gauge bosons, $g_q^s(y, M)$ and $g_q^A(y, M)$ are the parton distribution functions of the $p\bar{p}$ beams and the sum is over the quarks. The parton distribution functions (PDF) describe the probability to find a quark (parton) q inside the (anti)proton with the q carrying a fraction x of the total (anti)proton momentum. Parton distributions also depend on momentum scale Q^2 that characterizes the hard process [17].

The $\cos\theta^*$ dependence in Equation 1.18 reflects the spin structure of the interaction, the y dependence gives the hadron structure function dependence. Usually one or more of these dependencies are integrated out. However, it is possible to study various aspects of the production using these dependencies, especially once a signal is observed.

One can compute the QCD corrections to the DY process using the principles of perturbative QCD. Discrepancies found in the measurements compared with the tree level calculations, necessitated improving the accuracy of such calculations. Especially, the next to leading order (NLO) corrections turned out to be rather large (about 30% for CERN Sp$\bar{p}$S). Therefore, an overall correction factor, the K-factor is introduced to represent the higher order effects in α_s to the DY production:

$$K_{NLO} = \frac{\sigma_{NLO}}{\sigma_{LO}} \quad , K_{NNLO} = \frac{\sigma_{NNLO}}{\sigma_{LO}} \quad . \tag{1.19}$$

The NLO correction to the leading order DY process can be expressed numerically

by [18]:

$$K_{NLO}(\alpha_{\rm s}) = 1 + \frac{4}{3}\frac{\alpha_{\rm s}}{2\pi}\left(1 + \frac{4}{3}\pi^2\right) \tag{1.20}$$

Therefore, once a resonance in DY channel is observed, it can also be used as a test of perturbative QCD.

1.4 Beyond the Standard Model

The hints for physics beyond the SM was introduced in Section 1.1. Here, we list the classes of new models proposed in attempt to solve the existing problems of the particle physics.

Grand Unified Theories

The Grand Unified Theories (GUTs) arise as a natural extension of the SM. The idea in a GUT theory is to consider the $SU(3)$, $SU(2)$ and $U(1)$ as subgroups of a larger gauge symmetry group, G, and the quarks and leptons belong to the same multiplets of this group. The symmetry is unbroken above some very large mass scale, M_{GUT} (10^{16} GeV). The two popular extended gauge groups are $\rm E_6$ [19] and $SO(10)$.

The GUT theories attempt to solve the hierarchy between the strong and electroweak forces by unifying them at a new scale. However, this brings in a new hierarchy problem which is the existence of a gap between the electroweak scale ($\rm M_{EW} \approx 10^3$ GeV) and the GUT scale itself.

Supersymmetry

The one-loop corrections to the mass renormalization of the Higgs boson from the bosons and fermions yield quadratic divergences. Avoiding the divergences require a fine-tuning of the order of the hierarchy between the electroweak and GUT scale. SuperSymmetry (SUSY) is a model that is based on the symmetry that relates particles of different spins ("superpartners"). By generating a symmetry between fermions and bosons, the divergences in the Higgs mass corrections may be eliminated due to the additional negative contributions from the superpartners [20]. Therefore, the fine-tuning problem can be solved by the proposed SUSY theories [1]. If minimal supersymmetric models exist, the unification of the strong and electroweak forces can be made nearly equal at the GUT scale, as shown in Figure 1.3.

Dynamical Symmetry Breaking (Strong Dynamics)

The idea of dynamical symmetry breaking is that the dynamics of the fundamental gauge interactions will generate scalar bound states and that these will assume the role assigned to the Higgs field in the SM. This phenomenon is similar to the formation of bound states of elementary fermions in a superconductive phase transition: the Cooper pair of electrons. Two models that are explored in this category are Technicolor and little Higgs models.

- Technicolor: Technicolor models attempt to replace the Higgs scalar by com-

[1] Numerous variations of SUSY models exists, which are beyond the scope of this work.

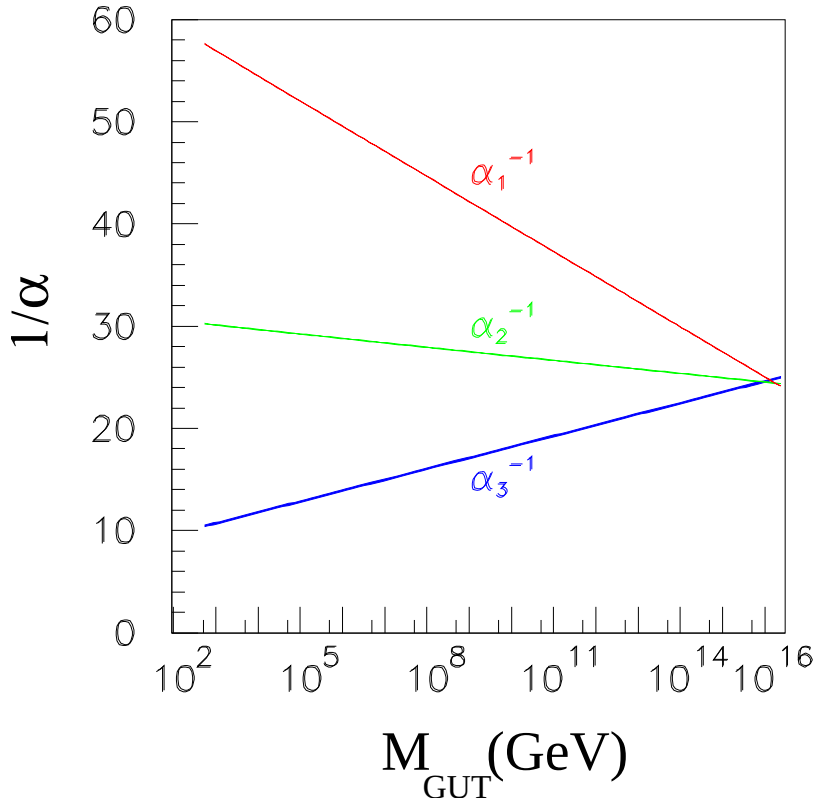

Figure 1.3: Unification of the gauge coupling strengths including supersymmetry [21].

posite meson bound states of a new interaction between additional fermions. It is essentially a scaled up version of QCD. Similar to the pion decay constant which is of the order of Λ_{QCD}, a new "techni-pion" determines that the hadrons of the new strong interaction will be at TeV energies. The earliest literature on Technicolor can be found in [22].

- Little Higgs Models: The little Higgs model emerged recently in the literature as one of the new models attempting to resolve the known hierarchy and fine-tuning problems between the electroweak scale and the Planck scale (M_{Pl}). The little Higgs model predicts the existence of new gauge bosons and fermions at the TeV scale to cancel quadratic divergences of SM at one loop in the calculation of the Higgs mass. The model introduces light Higgs bosons without supersymmetry and allows the scale of the underlying strong dynamics giving rise to composite particles to be as large as 10 TeV, therefore, solving the hierarchy problem.The introduction to the formalism of the little Higgs model can be found in [23].

Extra Dimensions (ED)

The hierarchy problem between the Planck scale and the electroweak scale (M_{EW}) (a factor of about 10^{16}) has motivated a number of extensions to the Standard Model, which involve the interactions of massive gravitons with SM particles. Models in

which particles can propagate in additional spatial dimensions have been proposed.

- Large Extra Dimensions: In the model proposed by Arkani-Hamed, Dimopoulos and Dvali (ADD) [24, 25], SM particles are confined on to a 3-D spatial membrane and gravity is allowed to propagate in the n extra dimensions. In the $(4+n)$-D world which corresponds to the fundamental Planck scale, $M_{\rm S}$ (sometimes called as the string scale), gravity is as strong as other gauge forces. However, gravity is weak in the Planck scale ($\rm M_{Pl}$ $\sim 10^{19}$ TeV) in 4-D. The relation between the two Planck scales is governed through the size, R, of the compactified extra dimension:

$$M_{\rm Pl}^2 \sim R^n M_{\rm S}^{n+2} \quad , \tag{1.21}$$

  which can be large. Assuming $M_{\rm S}$ is near the TeV range, R becomes as large as $\sim 10^{18}$ km, which is already ruled out by the classical description of gravitational force. The gravitational field in the $(4+n)$-D space can be represented in series of Kaluza-Klein (KK) towers.

- Warped Extra Dimensions: Randall and Sundrum (RS) propose a non-factorizable geometry in 5-D space to addresses the hierarchy problem. The extra dimension is warped by an exponential factor, $\exp(-2kr_c\phi)$, where k is the curvature

scale and r_c is the size of the 5th dimension [26]. The existence of the warp factor solves the hierarchy problem by bringing the scale of the gravitational force near the TeV scale.

- Other ED models: A third model, TeV^{-1} ED, is proposed to achieve gauge coupling unification at a scale much lower than the GUT scale [27]. In this model, matter resides on a p-brane (p $>$ 3), with chiral fermions confined to the ordinary 3-D world and SM gauge bosons also propagating in the extra dimensions, all of which are internal to the p-brane. The last model is the Universal ED [28] in which all particles are allowed to propagate in the extra dimensions.

1.5 The Models

Beyond the Standard Model theories have predicted particles that can be observed at the Tevatron. In this section, we describe the models, for which a search has been conducted in this analysis, in more detail. These models include extended electroweak gauge groups, Technicolor, Randall-Sundrum warped extra dimensions and R-parity violating Supersymmetry. A brief history of the previous results for each of the model is also given.

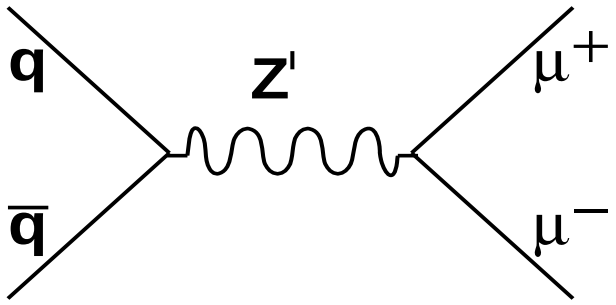

Figure 1.4: Leading order Feynman diagram for dimuon production through Z′ resonance decay.

1.5.1 Extra $U(1)$ and $SU(2)$ Neutral Gauge Bosons (Z′)

New, massive and neutral gauge bosons are a common feature of physics beyond the Standard Model. Any larger group, G, that extends the SM may have predictions of additional Z bosons, the Z′. The smallest group that predicts at least one extra gauge boson is $G = SO(10)$ [2]. The mass of the Z′ is, in general, not constrained by theory. However, it can naturally have a mass of about one TeV, especially in some supersymmetric GUTs [29]. Therefore, a Z′ can be observed at the current and next generation of colliders. In what follows, we will describe models with additional Z′s which can be detected directly in the dimuon decay channel. Figure 1.4 shows the lowest order Feynman diagram for dimuon production through Z′ resonance decay.

[2]The number of n neutral gauge bosons of a GUT is given by $n = rank[G]$. The rank of $SO(10)$ is five, so it predicts one additional neutral gauge boson [29].

1.5.1.1 SM-like (Sequential) Z′

The Sequential (SM-like) model Z′ (Z'_{SM}) is an extra $U(1)$ gauge boson which is defined to have the same couplings to fermions as the SM Z boson. Therefore, the production and decay properties of the Z'_{SM} is similar to that of the SM Z boson. In this model, the three-vector boson couplings (i.e., the bosonic decays of a Z′) is neglected since they are suppressed by a factor of $m_Z^2/m_{Z'}^2$ [30]. This is true in many extended gauge models, including E_6. The fact that the bosonic decays are suppressed for a heavy Z′ means that the total width of the Z′ is a linear function of its mass. The total Z'_{SM} width is about 3% of its mass, same as SM Z boson (see Figure 6.20 in Section 6).

We would like to point out a few issues that make a search for Z'_{SM} in CDF Run II Data reasonable. Generally, such a boson is not expected in the context of gauge theories unless this boson has different couplings to exotic fermions than the ordinary Z. However, a generic Z′ search forms a perfect baseline for other resonance searches which use the same final state particles. It also gives a means to cross-check the Run II data and results against the published Run I search results performed in similar manner. Moreover, it could also play the role of an excited state of the ordinary Z in models with extra dimensions at the weak scale [31].

We also point out that the production cross section increase of a resonance is sub-

stantial with the 8.8% increase in the Tevatron's $p\bar{p}$ center-of-mass energy. Figure 1.5 compares the cross sections for a SM-like Z′ for Run I and Run II center of mass energies. The increase in cross section is more than 40% above a mass of 600 GeV/c^2. Therefore, one can say that the sensitivity to new particles has increased by about 50% in the high mass region.

Previous Results: CDF experiment pioneered the Z′ searches at the Tevatron in Run I. The combined dilepton (dimuon) channel data of 110 pb^{-1} placed a lower mass limit of 690 (590) GeV/c^2 [32, 33]. The DØ experiment have searched for a Z'_{SM} in Run I only in the dielectron channel with a mass limit of 670 GeV/c^2 at 95% CL [48]. The highest indirect lower mass limits for the Z'_{SM} is derived from bounds on contact interactions in a global electroweak analysis and is 1.5 TeV/c^2 [34].

1.5.1.2 E_6

The E_6 model is a superstring inspired GUT theory which can contain additional $U(1)$ groups. Since E_6 is a GUT theory, it will breakdown into various subgroups one of which is the SM. The low energy gauge groups resulting from E_6 breaking leads to additional Z′. Let us consider the following breakdown of E_6 [29]:

$$E_6 \rightarrow SO(10) \otimes U(1)_\psi$$
$$\rightarrow SU(5) \otimes U(1)_\chi \otimes U(1)_\psi$$

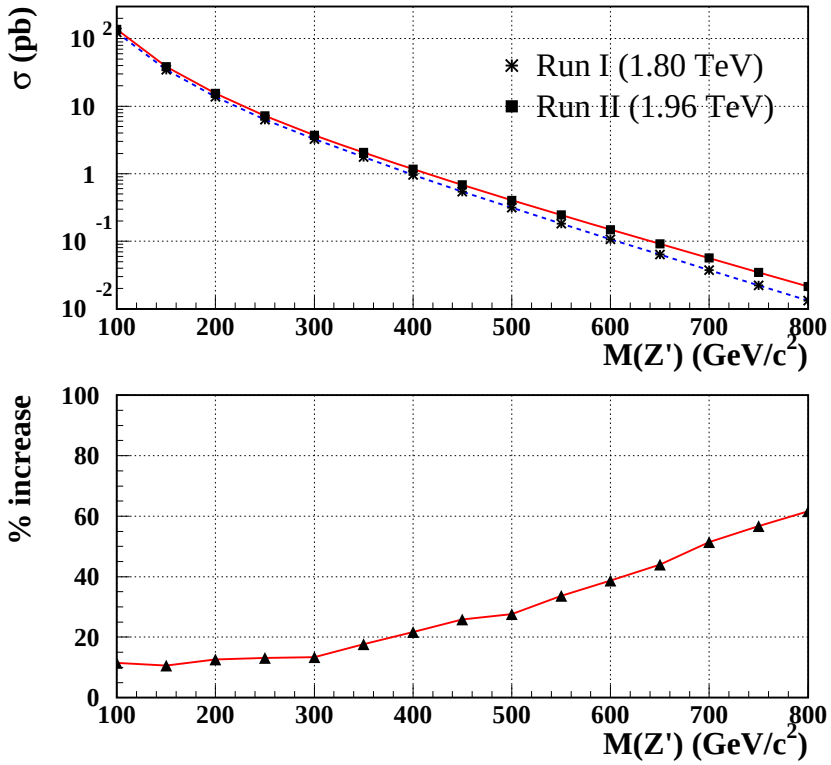

Figure 1.5: $\sigma \cdot BR(\mathrm{Z'_{SM}} \to \mu^+\mu^-)$ for Run I (dashed line) and Run II (solid line) as a function of the $\mathrm{Z'_{SM}}$ mass. The fractional increase of the cross section due to the $\mathrm{p\bar{p}}$ center of mass increase is also shown (bottom plot).

$$\rightarrow SU(3) \otimes SU(2) \otimes U(1) \otimes U(1)_{\chi} \otimes U(1)_{\psi}$$

In this gauge breaking scheme, E_6 first breaks down into $SO(10)$ and a $U(1)_{\psi}$. This breakdown gives the first $U(1)$ symmetry, which is called the Z'_{ψ}. The $SO(10)$ further breaks down into the smallest extended group, $SU(5)$ in which the known SM is contained, and an additional $U(1)_{\chi}$, giving the corresponding Z'_{χ}. The physically observable states of the new bosons can be expressed through a linear mixing of Z'_{ψ} and Z'_{χ}, with the mixing angle θ:

$$Z'(\theta) = Z_{\psi} \cos\theta + Z_{\chi} \sin\theta \tag{1.22}$$

Most common additional Z′ has been predicted for specific values of mixing angle [3]. These are Z'_{ψ}, Z'_{χ}, Z'_{η} and Z'_{I}, which correspond to θ values of 0, $\pi/2$, $\sin^{-1}\sqrt{3/8}$ and $\sin^{-1}\sqrt{5/8}$, respectively.

For the case of decays of Z′ into only SM particles, the most generic partial decay width to a fermion pair $f\bar{f}$ is given by [29]:

$$\Gamma(Z' \rightarrow f\bar{f}) \equiv \Gamma^{f0} = N_f \mu M \frac{g^2}{12\pi} \left\{ \left[v_f^2 + a_f^2 \right] \left(1 + 2\frac{m_f^2}{M^2} \right) - 6a_f^2 \frac{m_f^2}{M^2} \right\} \quad , \tag{1.23}$$

[3] More general analyses have also been performed earlier [29].

where N_f is the color coefficient, *i.e.*, $N_f = 1(3)$ for $f = l(q)$ and μ is the phase space factor due to the massive final fermions, $\mu = \sqrt{1 - 4m_f^2/M_n^2}$. Under the assumption that the final state fermions are massless compared to mass of Z′, M, the partial width is linearly dependent on M.

Previous Results The direct bounds on the masses of the various extra E_6 Z′ bosons come from the CDF Run I experiment [32]. The limits obtained from this analysis are listed in Table 7.6. The indirect expermental bounds for the E_6 Z′s are as low as 350 GeV/c^2, depending on the model. We list the indirect limits as of 2004 PDG [4] values on some of the Z′ models below:

- Z'_ψ: 350 GeV/c^2.
- Z'_η: 619 GeV/c^2, derived using electroweak data assuming a Higgs mass of 100 GeV/c^2.
- Z'_χ: 680 GeV/c^2, derived in an similar manner to that of a Z'_{SM} (Section 1.5.1.1).

1.5.1.3 Little Higgs Model

A model based on the idea of the little Higgs (LH) models, called the *"littlest Higgs model"*, is proposed in [35]. The model begins with $SU(5)$ global symmetry, which, at scale Λ_S, is broken down to its subgroup $SO(5)$ via a *vev* of order f. f is the

[4] The Particle Data Group compiles particle physics information on an annual basis [34].

"decay constant" of the pseudo-Goldstone boson of the theory and is necessarily of the order of TeV scale. For phenomenological studies, the Lagrangian of this theory is linearized as described in [36]. The spontaneous gauge symmetry breaking gives masses of order f for the gauge bosons, where the mass eigenstates are given by:

$$\begin{aligned} W &= sW_1 + cW_2, & W' &= -cW_1 + sW_2, \\ B &= s'B_1 + c'B_2, & B' &= -c'B_1 + s'B_2, \end{aligned} \tag{1.24}$$

and the mixing angles are defined as

$$s = \frac{g_2}{\sqrt{g_1^2 + g_2^2}}, \qquad s' = \frac{g_2'}{\sqrt{g_1'^2 + g_2'^2}}, \tag{1.25}$$

where g_i' and g_i are the couplings of the $[SU(2) \otimes U(1)]_i$ groups (i=1,2). The W and B are the massless SM gauge bosons, with couplings given by

$$g = g_1 s = g_2 c, \qquad g' = g_1' s' = g_2' c', \tag{1.26}$$

which are related numerically by

$$\frac{1}{g_1^2} + \frac{1}{g_2^2} = \frac{1}{g^2} \approx \frac{1}{0.43}, \qquad \frac{1}{g_1'^2} + \frac{1}{g_2'^2} = \frac{1}{g'^2} \approx \frac{1}{0.12}. \tag{1.27}$$

The electroweak symmetry breaking gives rise to further mixing between the gauge bosons. The final mass eigenstates for charged gauge bosons are: W_L (light) and W_H (heavy). Similarly, the neutral gauge bosons are: A_L, A_H, Z_L and Z_H, where the mass of A_L is zero. This means there are one charged boson, W_H, and two neutral bosons, A_H and Z_H, in addition to the SM bosons, W_L, A_L and Z_L. Figure 1.6 shows the spectrum of the particles within the LH model.

To leading order, the new gauge bosons have the following couplings to the SM fermions:

$$\text{for } Z_H: \; g_V = -g_A = \frac{g}{2}\, T_3 \cot\theta; \qquad \text{for } W_H: \; g_V = -g_A = \frac{g}{2\sqrt{2}} \cot\theta, \tag{1.28}$$

where g_V and g_A are the vector and axial couplings and T_3 is the third component of the weak isospin ($+(-)1/2$ for up(down) type fermions). $\cot\theta$ is the mixing angle which, in the context of Ref. [36], taken to be

$$\frac{1}{10} \leq \cot\theta = \frac{c}{s} \leq 2. \tag{1.29}$$

As can be seen from the above equations, the gauge boson couplings to SM fermions are universal to all fermions and depend linearly on the parameter $\cot\theta$ (which means that the cross sections will scale as $cot^2\theta$). The couplings are also purely

left-handed.

We concentrate on the neutral $SU(2)$ vector boson, Z_H , which can be observed at hadron colliders via the Drell-Yan process $q\bar{q} \to Z_H \to \ell^+\ell^-$. Figure 1.7 shows the decay branching fractions for Z_H versus $\cot\theta$. The fermionic decays of Z_H dominate over its bosonic decays (e.g. to ZH or WW) when $\cot\theta \gtrsim 1/2$. The branching fraction to one flavor of quark pair is also equal to the solid curve in this figure ($b\bar{b}$ given as an example), which holds true for the $t\bar{t}$ channel as well, up to a phase space factor. One other decay channel that can be considered is the non-SM decays of Z_H to $A_H H$, which becomes significant at low values of $\cot\theta$. The phenomenology of this model at the Tevatron and its implementation in Pythia event generator [37] framework is discussed in more detail in Chapter 7.

Previous Results: Since little Higgs models have been recently formulated, there are no results for Z_H from previous collider experiments in direct searches. Limits on the scale of the littlest Higgs model exist, derived from CDF Run I high mass search results and electroweak fits, which imply that significant fine-tuning may be needed in order for this model to solve hierarchy problem [40]. No bounds on the little Higgs models are listed in 2004 PDG.

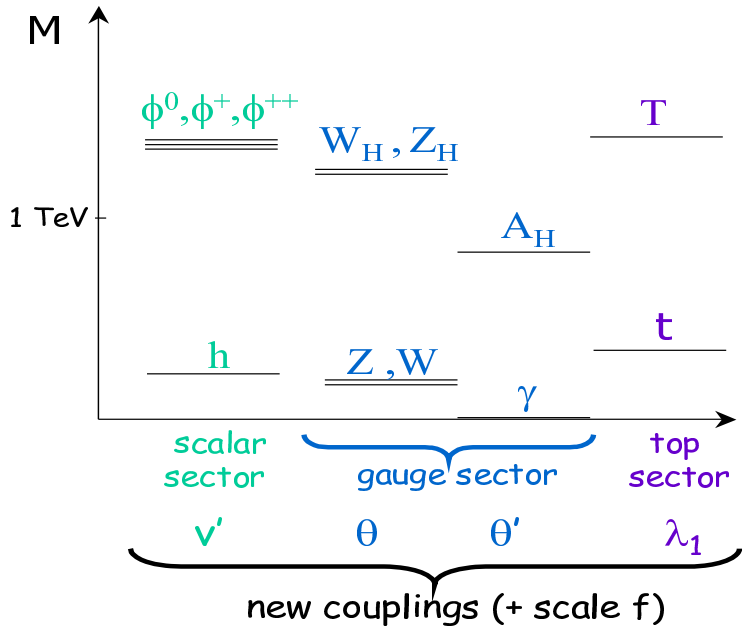

Figure 1.6: Spectrum of little Higgs Model particles [38].

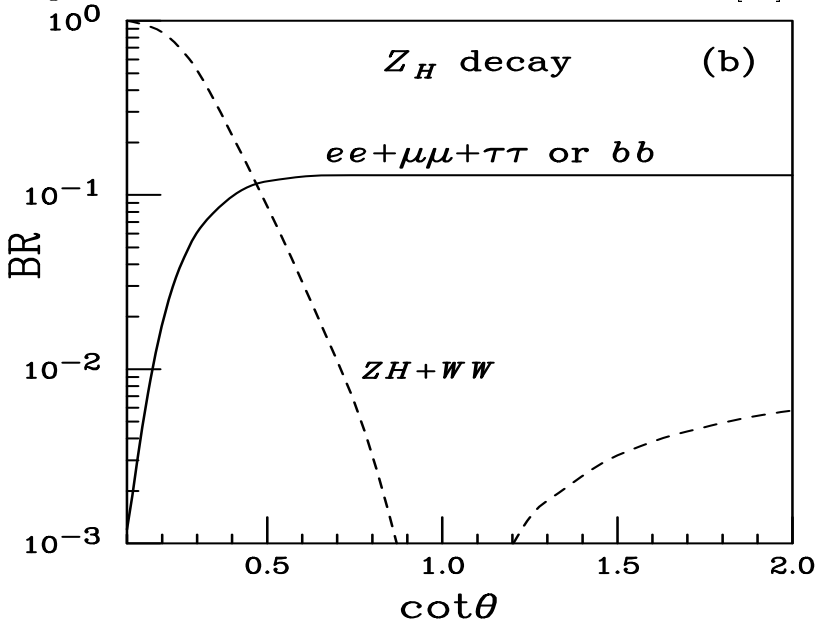

Figure 1.7: Z_H branching fractions as a function of $\cot\theta$ [36, 39].

1.5.2 RS Warped Extra Dimension

In the extra dimension theory, proposed by Randall and Sundrum, 5-dimensional non-factorizable geometry, based on a slice of AdS_5 spacetime exist [41]. Two 3-branes, one being visible with the other being hidden, with opposite tensions reside at S_1/Z_2 orbifold fixed points, taken to be $\phi = 0, \pi$, where ϕ is the angular coordinate parameterizing the extra dimension. The solution to Einstein's equations for this configuration, maintaining 4-dimensional Poincare invariance, is given by the 5-dimensional metric

$$ds^2 = e^{-2\sigma(\phi)}\eta_{\mu\nu}dx^\mu dx^\nu + r_c^2 d\phi^2 \,, \tag{1.30}$$

where the Greek indices run over ordinary 4-dimensional spacetime, $\sigma(\phi) = kr_c|\phi|$ with r_c being the compactification radius of the extra dimension, and $0 \leq |\phi| \leq \pi$. k is a scale of order the Planck scale and relates the 5-dimensional Planck scale M to the cosmological constant. RS model yields [26]:

$$\overline{M}_{\rm Pl}^2 = \frac{M^3}{k}(1 - e^{-2kr_c\pi}) \tag{1.31}$$

for the "reduced" (modified) 4-D Planck scale. Assuming that we live on the 3-brane located at $|\phi| = \pi$, it is found that a field on this brane with the fundamental mass parameter m_0 will appear to have the physical mass $m_n = kx_n e^{-kr_c\pi}$, where x_n are

simply the roots of the J_1 Bessel function. The graviton KK towers masses are not equally spaced (contrasted to ADD model, for example), can be of the order of a TeV and be detected as massive resonances at the collider experiments.

The phenomenology of the RS model is governed by the ratio of k to $\mathrm{M_{Pl}}$ (or $\overline{M}_{\mathrm{Pl}}$), $\mathrm{k/M_{Pl}}$, which can be defined as the dimensionless coupling parameter. This parameter enters linearly in the graviton mass and quadratically in all partial widths of the excited graviton resonance. For the first excited state of the RS graviton, $m_G \propto \sqrt{2} x_1 k/\overline{M}_{\mathrm{Pl}}$, where $x_1 \approx 3.83$ is the first zero of the J_1 Bessel function. The expression for the full width of the RS graviton can be found in [42].

Figure 1.8 shows the spectra of graviton resonance production expected at the Tevatron [41]. Since gravitons couple to gluons as well, the initial state will also include gluon fusion, given by the Feynman diagram in Figure 1.9. Figure 1.10 shows the $\mathrm{q\bar{q}}$ and gluon-gluon (gg) contribution to RS graviton production at 1.96 TeV $\mathrm{p\bar{p}}$ center of mass energy. The gg process decays faster as a function of the resonance mass and it dominates at energies below 200 $\mathrm{GeV/c^2}$. The different initial states will also contribute differently to the angular distribution of the graviton production at the Tevatron [45], as shown below:

$$\begin{aligned} q\bar{q} \to G \to \ell^+\ell^- &\propto 1 - 3\cos^2\theta^* + 4\cos^4\theta^* \\ gg \to G \to \ell^+\ell^- &\propto 1 - \cos^4\theta^* \end{aligned} \tag{1.32}$$

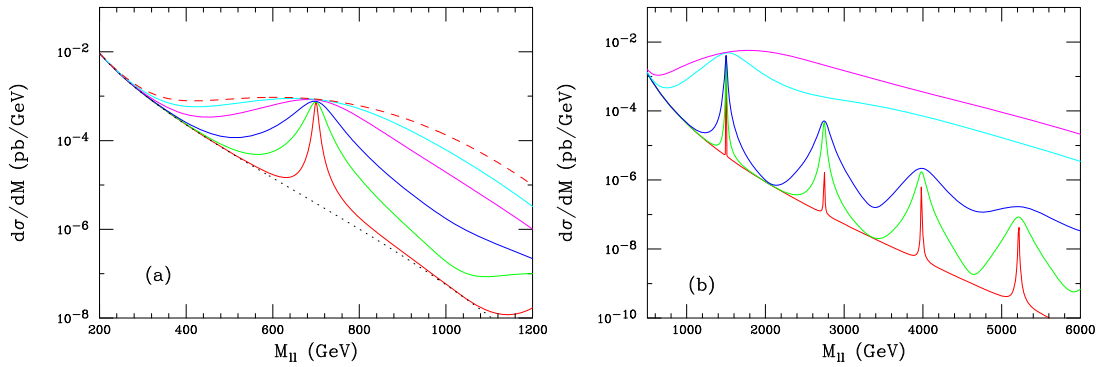

Figure 1.8: Drell-Yan production of a (a) 0.7 TeV Kaluza-Klein graviton at the Tevatron with k/M_{Pl} = 1, 0.7, 0.5, 0.3, 0.2, and 0.1, respectively, from top to bottom; (b) 1.5 TeV KK graviton and its subsequent tower states at the Large Hadron Collider [43]. The curves are for k/M_{Pl} = 1, 0.5, 0.1, 0.05, and 0.01, respectively, from top to bottom.

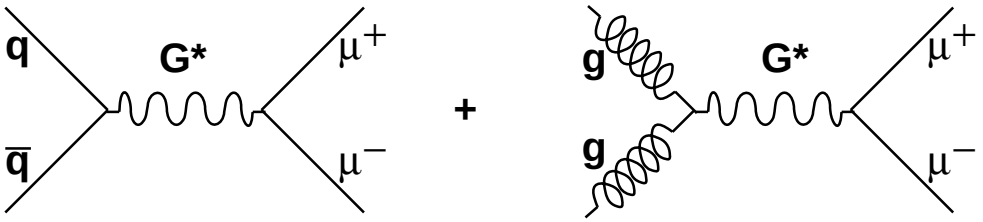

Figure 1.9: Leading order Feynman diagram for dimuon production through graviton resonance decay.

Previous Results: There are no results published from experiments for RS gravitons. Some feasibility studies exist in literature using the Run I CDF high mass search results [41]. The values of k/M_{Pl} can not be too large (> 0.1) for the bulk metric to be trusted and too small (<0.01) from the constraints on the magnitude

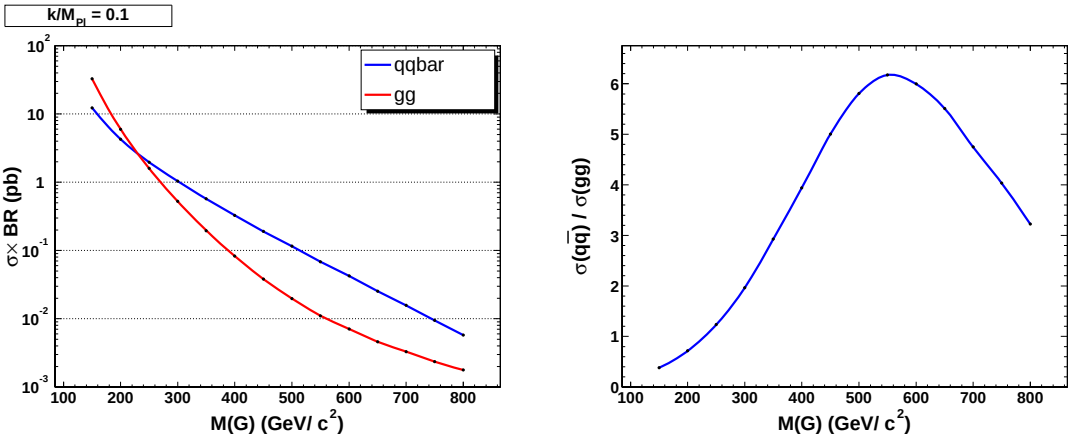

Figure 1.10: Production mechanisms for $\sigma \cdot BR(\mathrm{G} \rightarrow \mu^+\mu^-)$ (left) and ratio of $\mathrm{q\bar{q}}$ annihilation to gluon fusion contribution (right) as a function of the graviton mass.

of the 3-brane tension [41].

1.5.3 R-parity Violating ($\not{R}_P$) sneutrino

The general superpotential of a generic SUSY theory contains terms where the conservation of the baryon or the lepton number is violated. In order to assure conservation, a new symmetry, called R-parity is introduced:

$$R_p = (-1)^R = (-1)^{3(\mathrm{B}-\mathrm{L})+2S} \tag{1.33}$$

for a particle with spin S and baryon and lepton number, B and L. It is a multiplicative quantum number where all the particles of the Standard Model have positive

R-parity, while their superpartners have negative R-parity:

$$R_p \;=\; (-1)^R \;=\; \begin{cases} +1 & \text{for ordinary particles,} \\ -1 & \text{for their superpartners.} \end{cases} \tag{1.34}$$

A single SUSY particle cannot decay into just SM particles if R-parity is conserved which means the lightest superpartner (LSP) is absolutely stable. Astrophysical considerations imply that a stable LSP should be electrically neutral. The best candidates for an LSP, are the lightest neutralino, the sneutrino $\widetilde{\nu}$, or the gravitino. Presently, neither experiment nor any theoretical arguments demand R-parity conservation, so it is natural to consider the most general case in which R-parity is broken. The R-parity violating (RPV, $\not{R}_P$) terms which can contribute to the superpotential are:

$$W_{\not{R}_P} = \lambda_{ijk} L^i L^j \bar{E}^k + \lambda^{'}_{ijk} L^i Q^j \bar{D}^k + \lambda^{''}_{ijk} \bar{U}^i \bar{D}^j \bar{D}^k + \epsilon_i L_i H_2 \quad , \tag{1.35}$$

where i, j, k are generation indices (1,2,3), $L^i_1 \equiv \nu^i_L$, $L^i_2 = \ell^i_L$ and $Q^i_1 = u^i_L$, $Q^i_2 = d^i_L$ are lepton and quark components of $SU(2)_L$ doublet superfields, and $E^i = e^i_R$, $D^i = d^i_R$ and $U^i = u^i_R$ are lepton, down and up– quark $SU(2)_L$ singlet superfields, respectively. The unwritten $\mathrm{SU}(2)_L$ and $\mathrm{SU}(3)_C$ indices imply that the first term is antisymmetric under $i \leftrightarrow j$ interchange, and the third term is antisymmetric under

$j \leftrightarrow k$. Therefore, $i \neq j$ in $L^i L^j \bar{E}^k$ and $j \neq k$ in $\bar{U}^i \bar{D}^j \bar{D}^k$. The coefficients λ_{ijk}, $\lambda^{'}_{ijk}$, $\lambda^{''}_{ijk}$, and ϵ_i are Yukawa couplings, and there is no *a priori* generic prediction for their values. The first two terms in $W_{\not R_P}$ violate L and the $\bar{U}\bar{D}\bar{D}$ term in $W_{\not R_P}$ violates B. To take into account the constraints imposed by the non-observance of the proton decay, B is considered a good symmetry of the theory and $\lambda^{''}_{ijk}$ are taken as zero. The remaining interaction Lagrangian expanded as a function of the superfield components in the four-component Dirac notation is [44]:

$$\begin{aligned}\mathcal{L}_{\not R_P} = \lambda_{ijk} \left\{ \tilde{\nu}^i_L e^j_L \bar{e}^k_R + \tilde{e}^i_L \nu^j_L \bar{e}^k_R + (\tilde{e}^k_R)^* \nu^i_L e^j_L + h.c. \right\} \\ + \lambda^{'}_{ijk} \Big\{ \tilde{\nu}^i_L d^j_L \bar{d}^k_R - \tilde{e}^i_L u^j_L \bar{d}^k_R + \tilde{d}^j_L \nu^i_L \bar{d}^k_R - \tilde{u}^j_L e^i_L \bar{d}^k_R + \\ (\tilde{d}^k_R)^* \nu^i_L d^j_L - (\tilde{d}^k_R)^* e^i_L u^j_L + h.c. \Big\} \quad .\end{aligned} \tag{1.36}$$

In SUSY GUT scenarios, the third generation sfermions are generally expected to be lighter than the sfermions of the first two generations. The flavor violation may also be expected to be minimal in the third generation and the low-energy limits for the third generation sfermions are not very restrictive. Therefore, the searches at the Tevatron may be concentrated on $\widetilde{\nu}_\tau$ resonance formation. As can bee seen from Equation 1.37, a non-zero $\lambda^{'}_{ijk}$ can lead to resonant sneutrino production at a hadron collider and a non-zero λ_{ijk} can lead to dileptonic decays of sneutrino. The

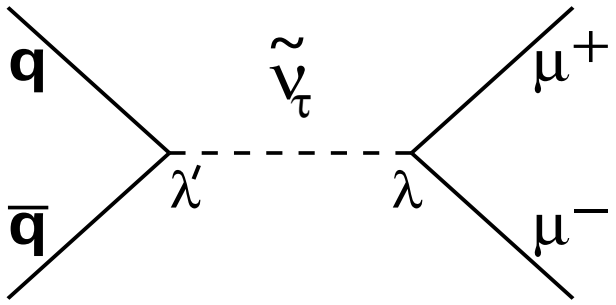

Figure 1.11: Leading order Feynman diagram for dimuon production through $\widetilde{\nu}$ resonance decay.

differential cross section for a $\widetilde{\nu}_\tau$ production is from only $d\bar{d}$ annihilation [44]:

$$\frac{d\hat{\sigma}[\tilde{\nu}_\tau]}{d\cos\theta} = \frac{1}{3}\frac{\pi\alpha^2 s}{4}\frac{(\lambda_{232}\lambda'_{311}/e^2)^2}{(\hat{s}-m^2_{\tilde{\nu}_\tau})^2+\Gamma^2_{\tilde{\nu}_\tau}m^2_{\tilde{\nu}_\tau}} \quad , \tag{1.37}$$

where λ_{232} is the $\widetilde{\nu}_\tau \to \mu^+\mu^-$coupling. The partial width for the $\widetilde{\nu}_\tau \to \mu^+\mu^-$decay is $\Gamma(\mu\mu) = \frac{\lambda^2_{232}}{16\pi}M_{\tilde{\nu}_\tau}$. Figure 1.11 shows the Feynman diagram for dimuon production at hadron collisions through $\widetilde{\nu}_\tau$ decay.

Previous Results: Previous results for $\not{R}_P$ SUSY models have concentrated on the Yukawa couplings as well as the superparticle masses. The upper bounds on couplings depend on the mass of the superpartners and the limits are presented as a functional dependence. For λ_{232} and λ'_{311} in Equation 1.37, the current (indirect)

limits are [45]:

$$\lambda_{232} < 0.07 \times \frac{M_{\tilde{\mu}_R}}{100\ \mathrm{GeV}/c^2} \quad , \quad \lambda'_{311} < 0.11 \times \frac{M_{\tilde{d}_R}}{100\ \mathrm{GeV}/c^2} \quad . \tag{1.38}$$

For a superpartner mass scale of 200 GeV/c^2, present data allow $\lambda_{232}\lambda'_{311} \lesssim 0.03$. The mass limits are usually parameter dependent, however, the highest mass limit on a sneutrino, within MSSM, is $m_{\tilde{\nu}} > 94$ GeV/c^2 [46]. More $\not{R}_P$ $\widetilde{\nu}_\tau$ specific limits are usually lower [34]. The strict bounds from cosmology on $\not{R}_P$ SUSY are generally not considered because they are model dependent [45].

1.5.4 Technicolor Particles (ω_{T} andρ_{T})

Technicolor (TC) is an alternative way to manifest the Higgs mechanism in giving masses to the W and Z bosons using strong dynamics instead of weakly–coupled fundamental scalars. One adaptation of Technicolor is the "Straw-man's" model (TCSM) [47]. This is a model that describes the phenomenology of color–singlet vector and pseudoscalar technimesons and their interactions with SM particles. The two techni-mesons, the isosinglet, ω_{T}, and the neutral member of the techni-ρ isotriplet family, ρ_{T}, can be produced at p$\bar{\mathrm{p}}$ collisions and may decay into two muons.

The main model parameters are listed below:

$$Q_u = Q_d + 1 = \frac{4}{3}$$

$$M_A = M_V = M_T$$

$$M(\omega_{\mathrm{T}}) \simeq M(\rho_{\mathrm{T}}) = M(\pi_{\mathrm{T}}) + 100 GeV/c^2 \tag{1.39}$$

The first formula is the relation between the technifermion charges, to which the $\sigma_{\omega_{\mathrm{T}}}$ is sensitive. The second formula reflects a choice on M_T, which effects both the production cross section of the vector mesons and the rate $\omega_{\mathrm{T}} \rightarrow \gamma + \pi_{\mathrm{T}}$. The third formula relates the ω_{T} and ρ_{T} masses to that of π_{T}. The ω_{T} and ρ_{T} masses are approximately degenerate, since the techni-isospin is likely to be a good approximate symmetry.

Previous Results: The Technicolor model has not been bound by dimuon results from previous experiments. The DØ experiment has results from dielectron channel using Run I data, although these limits are not very stringent [48]. Masses of ω_{T} andρ_{T} have been excluded up to 203 GeV/c^2 for $M_T) > 200$ GeV. The decays of ω_{T} andρ_{T} have also been explored in associated production of π_{T} with a W boson or γ in CDF Run I. The highest mass limits ω_{T} and ρ_{T} for various decay channels

and for various model parameters range about 200-300 GeV/c^2 [34].

Chapter 2

Experimental Apparatus

The data for the analysis described here is taken at the Collider Detector at Fermilab (CDF) experiment located at the Fermi National Accelerator Laboratory (Fermilab), Batavia, Illinois, USA. The data used in the analysis is taken during 2002–2003 at $\sqrt{s} = 1.96$ TeV center of mass energy of proton-antiproton ($p\bar{p}$) collisions produced on the Tevatron accelerator. The period in which the data was taken is referred to as the Run II of Tevatron and the experiment is referred as CDF II. In the following sections, we outline the Fermilab accelerator complex and the CDF II detector with its components.

2.1 The Accelerator

Fermilab, which can be seen in Figure 2.1, is the largest US laboratory for research in high energy physics. It is the home to the world's current highest energy accelerator, the Tevatron. The Tevatron, with a circumference of about 6 km, is the world's first superconducting synchrotron and became operational in 1983. Two of the collision points on Tevatron host two $p\bar{p}$ colliding beam experiments: DØ and CDF. Both experiments took data during the 80's and 90's. Starting in 1996, both the accelerator and the experiments underwent significant upgrades. Data taking began in 2001 with the upgraded accelerator and experiments.

The center-of-mass energy (E_{cm}, $\sqrt{s}$), for the Tevatron proton and antiproton collisions is 1.96 TeV. The acceleration of beams to 0.98 TeV occurs in many stages in the Fermilab accelerator complex. The rest of this section describes the stages of the accelerator chain in detail, which is illustrated in Figure 2.2. The other important parameter of colliders, the measure of the potential number of interactions for the colliding beams ("luminosity"), will be defined at the end of this section. Most of the information provided in this section can be found in Fermilab's Run II Handbook [49].

Proton Source

The starting point for the acceleration before collisions can occur in the Tevatron is the Cockcroft-Walton accelerator which is a source of 750 keV negative hydrogen

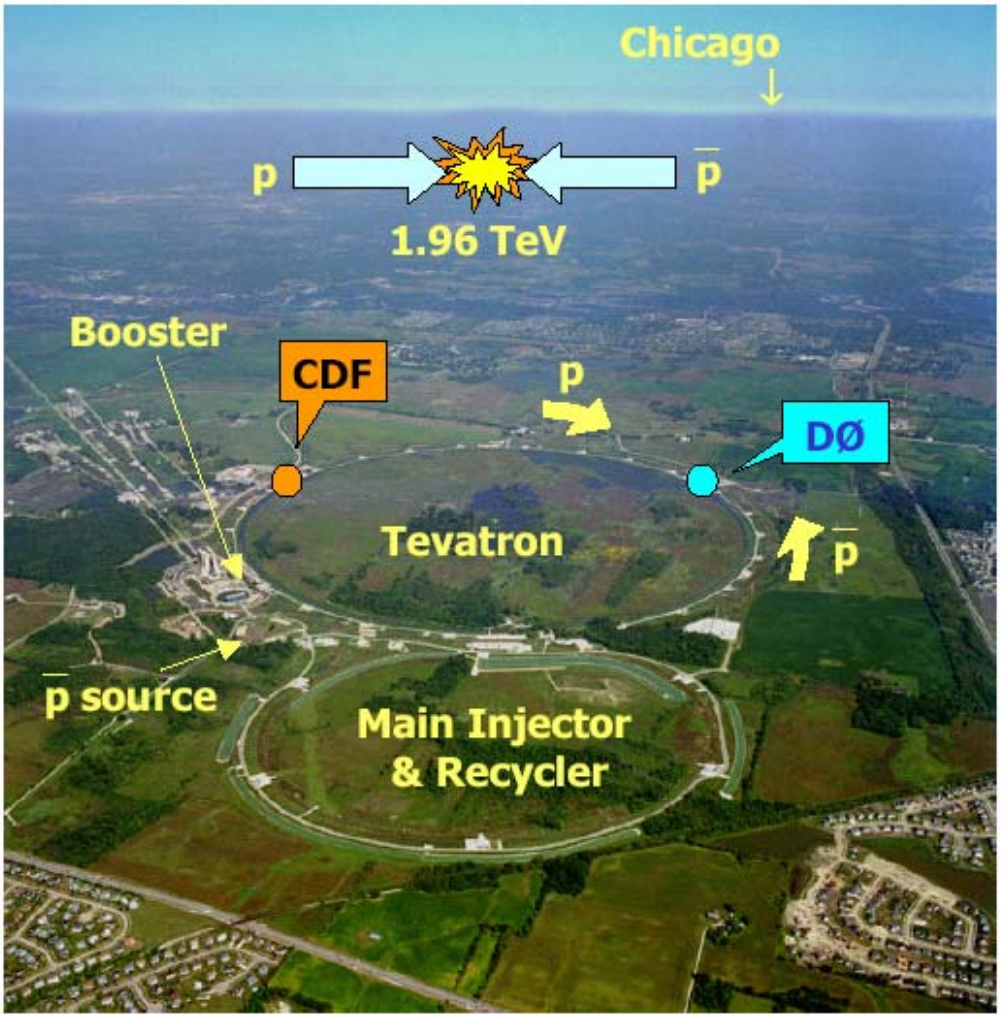

Figure 2.1: Aerial view of Fermilab.

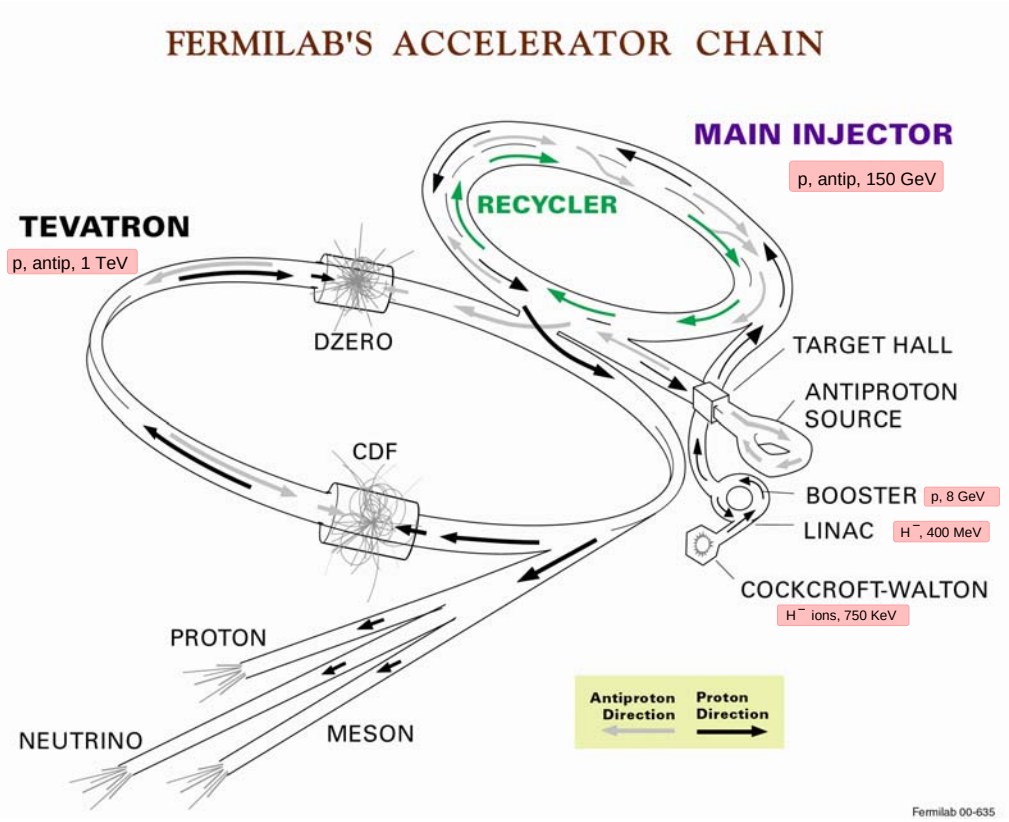

Figure 2.2: The Fermilab Accelerator Chain.

ions (H^-). The H^- ions enter a 150 m long Linear Accelerator (Linac). The Linac uses a radio-frequency field, running at about 800 MHz, to further accelerate the H^- ions to an energy of 400 MeV.

Upon leaving the Linac, the H^- ions enter into the Booster, the first synchrotron of the accelerator chain at Fermilab. During this transmission, the ions are passed through a carbon foil and the electrons are stripped, leaving the bare protons to be accelerated to 8 GeV in the 75m radius Booster. Protons emerge from the Booster in 84 bunches (1 bunch = 1 RF "bucket") spaced by about 19 ns. The design specifications of the Booster for Run II is a total intensity of 6×10^{10} protons per bunch, which is a 20% improvement over Run IB performance.

Main Injector

The Tevatron's old injector, the Main Ring, was incapable of matching the luminosity requirements for Run II. The Main Injector, a synchrotron of about 3 km in circumference, was designed and built to reduce the limitation of the Main Ring and became operational in 1998. The Main Injector accelerates both protons and antiprotons from 8 GeV to 150 GeV . Both beams are also coalesced into smaller number of bunches. The coalesced bunches are finally injected into the Tevatron (36 bunches per beam in total), where they will be further accelerated to their final energies, 980 GeV (the "shot" procedure).

Antiproton Production

One major advantage of a p$\bar{\text{p}}$ collider is that the p and $\bar{\text{p}}$ beams can circulate in opposite directions sharing the same magnet and vacuum system. One major disadvantage of using $\bar{\text{p}}$ beams is the cost of their production. At Fermilab, the antiprotons are produced using the Main Injector protons. A proton pulse of 120 GeV is incident onto a nickel target to produce antiprotons. The produced antiprotons are collected and focused by a "lithium lens" and separated from the other by-products of the proton-nickel scattering using a bending magnet. The system has a wide acceptance around $\bar{p}$ energies of 8 GeV.

Exiting the collection lens, the antiprotons are bunched (preserving the structure of the initial protons). However, they have a large spread of momentum in longitudinal and transverse directions. Before bringing them back to 150 GeV to prepare for proton collisions, they go through the process of stochastic cooling[1]. This task is performed in two steps: the $\bar{\text{p}}$ beam is transformed into a continuous beam and cooled both transversely and longitudinally in the Debuncher ring, and the antiprotons are further cooled and "stacked" in the Accumulator. The stacking of anti-protons takes between half or a full day depending on the desired beam intensity. At this point, the antiprotons are still 8 GeV, but with a momentum spread smaller than one per cent and are rebunched. When a sufficient number of antiprotons is available, they

[1]Simone van der Meer was awarded the Nobel prize for the invention of stochastic cooling in 1984.

are sent either to the Main Injector for further acceleration to 150 GeV or to the Recycler, which we describe below.

The improvements to the Debuncher and Accumulator stochastic cooling systems and the increase in the number of protons per pulse from the Main Injector along with a faster repetition rate are designed to increase the stacking rate by at least a factor of four in Run II as compared to that of Run I.

Recycler: The Recycler Ring is installed in the Main Injector enclosure as a storage ring for antiprotons[2]. It will be used as a post-Accumulator ring. Its main purpose is to recycle the antiprotons which are not used at the end of the Tevatron stores[3] (about 75% of the original injection quantity). At the end of a store, the antiprotons, instead of being dumped as in Run I, will be decelerated, re-cooled, stored and will be sent back to the Main Injector to be used again in the next store. This recycling procedure will essentially provide a factor of two in luminosity that is attainable by the accelerator.

Tevatron

The final stage for the acceleration for the $p\bar{p}$ beams is the 6 km long Tevatron ring. The 36 proton and antiproton bunches are received from the Main Injector at 150 GeV. The general steps of a "shot setup" (the procedure of increasing 150 GeV

[2]Recycler is first used in January, 2004

[3]A store is when stable circulation of $p\bar{p}$ beams obtained in the Tevatron ring.

beams to 980 GeV ones and getting ready for collisions at CDF and DØ) can be outlined in a few steps.

- **Beam Injection:** The protons are sent into the F- section of the Tevatron in 36 coalesced bunches. At this time, the Tevatron magnets [4] are already set to circulate 150 GeV energy beams in anticipation of the injection. The antiprotons are loaded after all the protons are injected. Before antiproton injection, a set of electrostatic separators are used to create a pair of non-intersecting closed helical orbits with the protons circulating on one strand of the helix and antiprotons on the other. This provides transverse separation of the proton and antiproton bunches as they pass each other and reduces the beam-beam tune shift from head-on collisions. The tune shifts arise from beam-beam interactions due to the protons' electromagnetic field affecting antiprotons traveling in opposite directions.

- **Acceleration:** Both protons and antiprotons circulate in three trains of 12 bunches with bunches in each group spaced 396 ns and the three trains are separated by about 2.6 μs ("abort gaps"), as schematically shown in Figure 2.3. The beams are accelerated up to 980 GeV each.

- **Low Beta Squeeze:** After the beams are accelerated to 980 GeV, the β^* [5]

[4] The Tevatron dipole magnets are operated at 4 K and 4.2 Tesla magnetic field.

[5] Given the position-velocity phase space (x, x') profile of the beam is an ellipse of semiaxes, σ

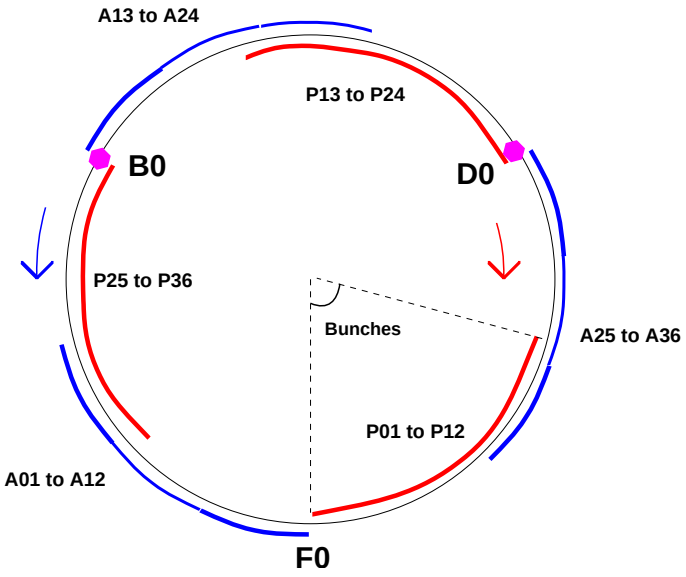

Figure 2.3: Schematic representation of Tevatron bunch orientation.

in the CDF and DØ interaction regions is reduced from about 2 m to 30 cm. The transverse size is reduced from about 1 mm to about 25 μm. The change in the Tevatron lattice is obtained by ramping up the currents in the low-β quadrupole magnets at the two sides of the detectors in the collision hall.

- **Beam Halo Scraping:** The Tevatron beams begin to produce luminosity when the beams have been brought into collisions. At this stage, the proton and antiproton beam halo are scraped to reduce backgrounds in the detectors. This operation is usually done automatically using the scraping collimators around the ring.

and σ', the beta function, β, is defined as the ratio σ/σ' and the beam **emittance** as the phase volume, $\epsilon = \pi\sigma\sigma'$. β^* is beta function as measured at the collison points.

Once the beams are ready for data taking, CDF and D0 detectors initialize their luminosity counters and turn on their detectors for taking data during the Tevatron store until it is dumped/aborted.

The Tevatron luminosity, in the absence of a crossing angle or beam position offset, is given by the expression:

$$L = \frac{f\mathrm{B}N_pN_{\bar{\mathrm{p}}}}{2\pi(\sigma_p^2+\sigma_{\bar{p}}^2)}F(\sigma_l/\beta^*) \tag{2.1}$$

where f is the beam revolution frequency, B is the number of bunches in each beam, N_p ($\mathrm{N}_{\bar{\mathrm{p}}}$) is the number of protons (antiprotons) in a bunch, σ_p ($\sigma_{\bar{p}}$) is the RMS proton (antiproton) beam size at the interaction point and $F\sigma_l/\beta^*$) is a form factor which depends on the ratio of the bunch length, σ_l, to the beta function at the interaction point, β^*. The *integrated* luminosity, defined as $\mathcal{L} = \int \mathrm{L}dt$, is more relevant to physics processes in $\mathrm{p\bar{p}}$ collisions [6]. The measurement of the luminosity at CDF is described in Section 3.4.

[6] The rate of occurrence for interactions is directly proportional to the cross section of the process, σ, ($[cm^2]$) and to $\mathcal{L}$ ($[cm^{-2}]$). For rates we observe in high energy collisions, the preferred unit is a "barn" ($[10^{-24}cm^2]$).

2.1.1 Tevatron at Run II

As mentioned earlier, the Fermilab accelerator complex underwent a series of upgrades to increase energy and luminosity for Run II. In Table 2.1, we summarize the Run II design parameters and compare them to those of Run I. The design parameters for the accelerator was not reached instantaneously as the machine was turned on in 2001. One technical issue impeding the increase in the luminosity is the availability of antiprotons. One other factor is the learning curve of operating brand-new components. As of writing this thesis, the Tevatron is achieving instantaneous luminosity values of about 6×10^{31} $cm^{-2}s^{-1}$. The integrated luminosity per week has reached to values above 10 pb^{-1} routinely. The store duration has well increased, exceeding 24 hours. In Figures 2.4 and 2.5 we illustrate the evolution of the integrated and instantaneous luminosity, respectively. These plots corresponds to about 200 pb^{-1} CDF data collected up to September 2003.

2.2 The CDF II Detector

The Collider Detector at Fermilab (CDF) is a cylindrical-shaped, general-purpose apparatus located at the B0 interaction region of the Tevatron and is designed to study particles outcoming from the $p\bar{p}$ collisions. The CDF experiment went through a series of data taking periods starting from the date the first collisions were produced

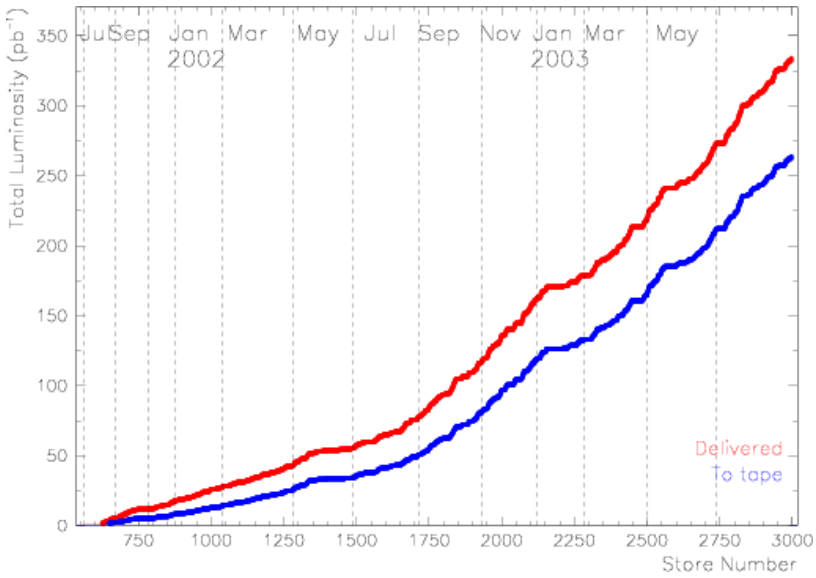

Figure 2.4: Total integrated luminosity delivered and recorded.

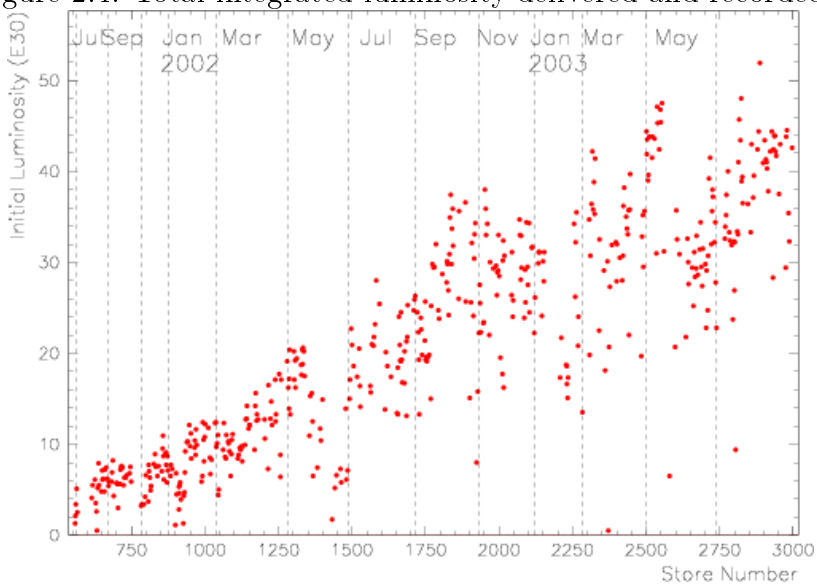

Figure 2.5: Initial luminosity per Tevatron store.

Parameter	Run IB (1993-95)	Run II >2000
p/bunch (10^{10})	23	27
$\bar{p}$/bunch (10^{10})	5.5	2.5
Number of bunches	6	36
$\bar{p}$ stacking (10^{10}/hr)	6	20
p emittance (mm-μrad)	23π	20π
$\bar{p}$ emittance (mm-μrad)	13π	15π
Beam energy (GeV)	900	1000
Bunch length (rms, m)	0.60	0.37
Form Factor	0.59	0.75
Luminosity (10^{31} cm^{-2}s^{-1})	0.16	0.7
Bunch spacing (ns)	$\sim$3500	396
Crossing angle (μrad)	0	0
Interactions/crossing	2.7	1.9

Table 2.1: Comparison of Tevatron Run I parameters with the Run II design goals. Run IB column represents average of 32 stores over the period March-April in 1995

and detected in October, 1985. The history of CDF data taking is summarized in Table 2.2. The CDF experiment provided the first evidence for the existence of the top quark using Run I data [50]. The upgrade preparations for CDF II started in 1996 [51]. An isometric view of the CDF II detector can be seen in Figure 2.6.

CDF uses a cylindrical system of coordinates as is shown in Figure 2.8. The

Run	**Period**	**Integrated Luminosity (pb^{-1})**
–	1987	0.025
Run 0	1988-1989	4.5
Run IA	1992-1993	$\sim$19
Run IB	1994-1996	$\sim$90
Run IIA (sep, 03)	2001-2003	$\sim$ 200

Table 2.2: CDF p$\bar{p}$ data taking history.

center of the coordinate system coincides with the center of the detector (interaction point). The $+z$-axis lies along the proton beam direction and the $+y$-axis points upward, perpendicular to the Tevatron plane. According to the right-hand rule, $+x$-axis points radially outward from the Tevatron ring center. From the proton's point of view coming into the CDF detector (going eastward), the $+x$-axis would be the 9 o'clock with azimuthal angle, ϕ, increasing in the clockwise direction. The polar angle, θ, is measured from the $+z$-direction. One common re-parametrization of the polar angle is the pseudo-rapidity, η, defined below:

$$\eta = -\ln\left(\tan\frac{\theta}{2}\right) \quad . \tag{2.2}$$

Figure 2.7 illustrates the dependence of η of the polar angle. η is a very good approximation to the physical variable, rapidity, y, given by:

$$y = \frac{1}{2}\ln\left(\frac{E + p_L}{E - p_L}\right) \quad . \tag{2.3}$$

The longitudinal momentum of the particle, p_L, is defined to be $p_L = p\cos\theta$. In the high energy approximation ($E \sim p$) rapidity reduces to pseudorapidity. The variable η usually replaces y when the mass and momentum of the particle is unknown. Pseudorapidity is also preferred to describe the detector acceptance and physics

capabilities.

CDF II can be divided into three main components: a tracking system for momentum and charge measurement, a calorimetry for energy measurement and muon systems for identifying muons. There also exists a time-of-flight system to identify particles for flavor tagging. The following subsections outline the detector parts starting from the innermost regions and progressing radially outward.

2.2.1 Tracking System

The CDF detector is a powerful magnetic spectrometer which consists of a several-component tracking system, as shown seen in Figure 2.7. The inner core is a set of silicon strip detectors whose main purpose is to perform precision vertexing. Surrounding the silicon tracker is a multiwire drift chamber whose main purpose is to provide charged particle momentum measurement within the magnetic field of the CDF solenoid coil. The CDF magnetic field is provided by a 5-meter long superconducting solenoid coil. The magnet is operated to provide a field strength similar to Run I. The field strength has a central value of 1.41 Tesla and is uniform to 0.1% in the region $|z| < 150$ cm and $|r| < 150$ cm. The solenoid is built from Al-stabilized NbTi conductor with a maximum field strength of 1.5 Tesla and operating current of 5 kAmps at liquid-He temperatures of about 4.7° K.

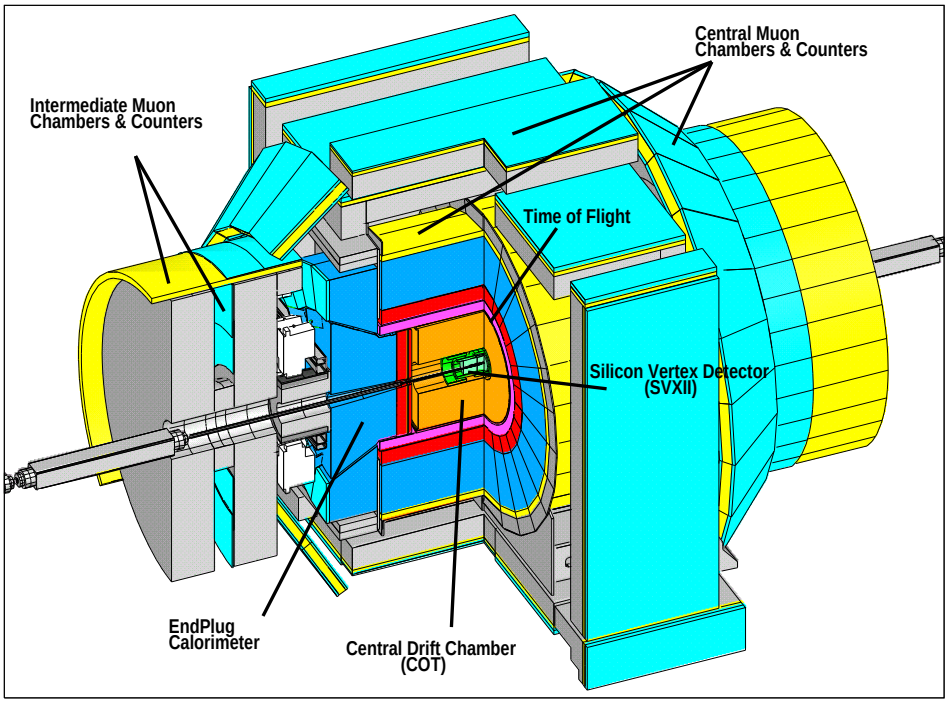

Figure 2.6: Isometric view of the CDF II Detector.

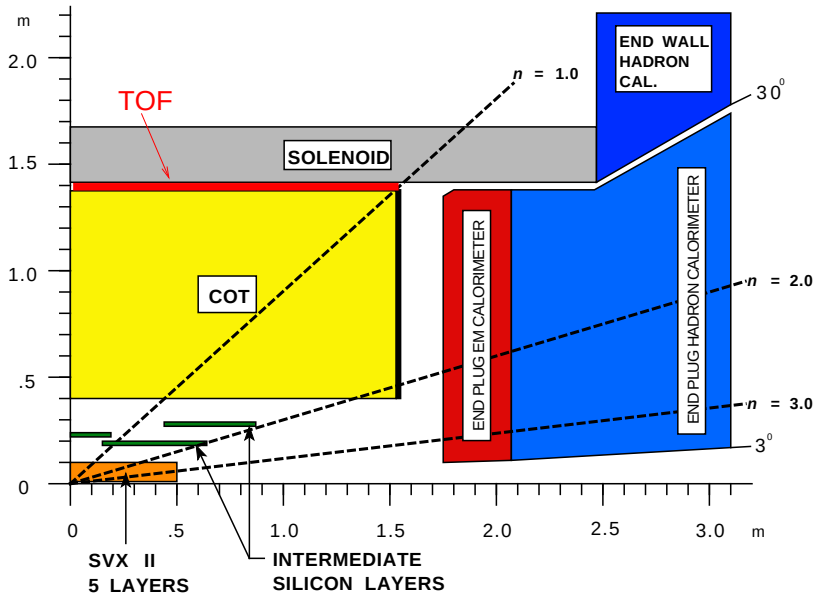

Figure 2.7: One quadrant of the CDF II Tracking System.

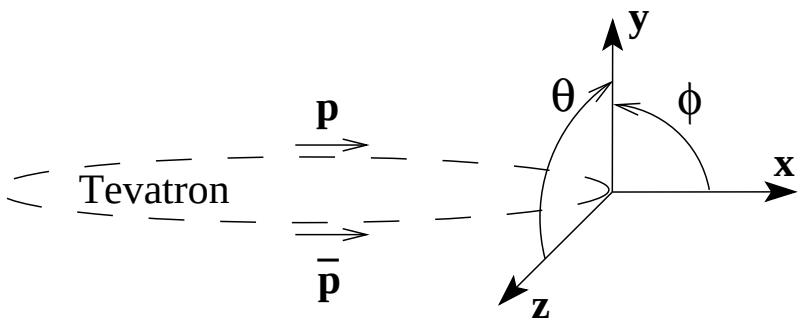

Figure 2.8: CDF detector coordinate system.

2.2.1.1 Inner Tracker: the Silicon System

At the very center of the CDF detector lies the silicon tracking system, which consists of three concentric systems: "Layer 00" (**LØØ**), the Silicon Vertex Detector (**SVX**) and the Intermediate Silicon Layer (**ISL**). The system replaces the vertex time projection chamber and silicon vertex detector systems which were successfully used for vertexing and tracking during Run I [52]. The new silicon system is designed for a larger geometrical coverage as high as $|\eta|$ <2 and to be less radiation-sensitive. An improved pattern recognition is also implemented along with a faster readout scheme. The detector parameters of the silicon system are given in Table 2.3. The $r-z$ view of CDF silicon tracking system is shown in Figure 2.9 and the $r-\phi$ view is shown in Figure 2.10.

The innermost layer of silicon tracker system is LØØ. This single-sided, radiation-hard silicon sensor is placed immediately outside the beam pipe at a minimum radius

of 1.35 cm. Inclusion of LØØ in the tracking serves to improve the track impact parameter resolution.

The SVX II is 90 cm long centered on the CDF origin. It is composed of three 29 cm long cylindrical barrels. Each barrel is divided into 12 pieces (wedges) in azimuth with each wedge containing five layers of double-sided silicon microstrip detectors between radii of 2.4 cm and 10.7 cm. The outermost three layers combine an $r - \phi$ measurement on one side with 90° stereo measurement on the other. The innermost two layers of SVX combine $r - \phi$ information with small angle stereo at 1.2°. The stereo angle information from the layers is used to form a three-dimensional track. The silicon microstrips are supported by carbon fiber rails in assemblies called "ladders". Each ladder hosts four pieces of silicon sensors in two half-ladders. There are 12 ladders in ϕ and a total of 60 ladders in each barrel which are mounted between two beryllium bulkheads which also carry the water cooling lines for the readout electronics. The more than 400,000 channels in the system are connected to readout chips (SVX3) which reside on the surface of the silicon detectors. Each chip digitizes 128 channels. A parallel fiber optic-based data acquisition system reads out the entire detector in approximately 10 μs.

The ISL consists of three separate silicon layers situated at radii of 20, 22 and 28 cm, respectively with respect to the beamline. Each layer is made up of double-sided microstrips as in SVX, only without the 90° stereo measurement. The ISL

SVX II	
Radial coverage	2.4 to 10.7 cm, staggered quadrants
Number of barrels	3
Number of layers per barrel	5
Number of wedges per barrel	12
Readout coordinates	$r-\phi; r-z$
Readout pitch	60-65 μm $r-\phi$; 60-150 μm stereo
Resolution per measurement	12 μm (axial)
Total length	96.0 cm
Rapidity coverage	$\mid \eta \mid < 2.0$
Number of channels	405,504
Material thickness	3.5% X_0

Table 2.3: Detector parameters of the SVX.

readout electronics are also similar to SVX, with the 30° wedge segmentation in readout being the same. ISL has more than 250,000 channels in readout.

2.2.1.2 Central Outer Tracker

Surrounding the silicon system is the Central Outer Tracker (COT), the main tracking volume for CDF II [53]. The COT is a cylindrical drift chamber covering the radial region of 40-138 cm from the beam pipe and is about 3 m long, corresponding to an $|\eta|$ coverage of <1.0. The COT is the replacement of the Run I wire chamber, CTC, as a faster and improved version. Table 2.4 summarizes the detector parameters for the COT.

COT is segmented into eight concentric superlayers and each superlayer is divided into cells in ϕ. A cell consists of a sense plane for 12 sense wires and 17 field shaping

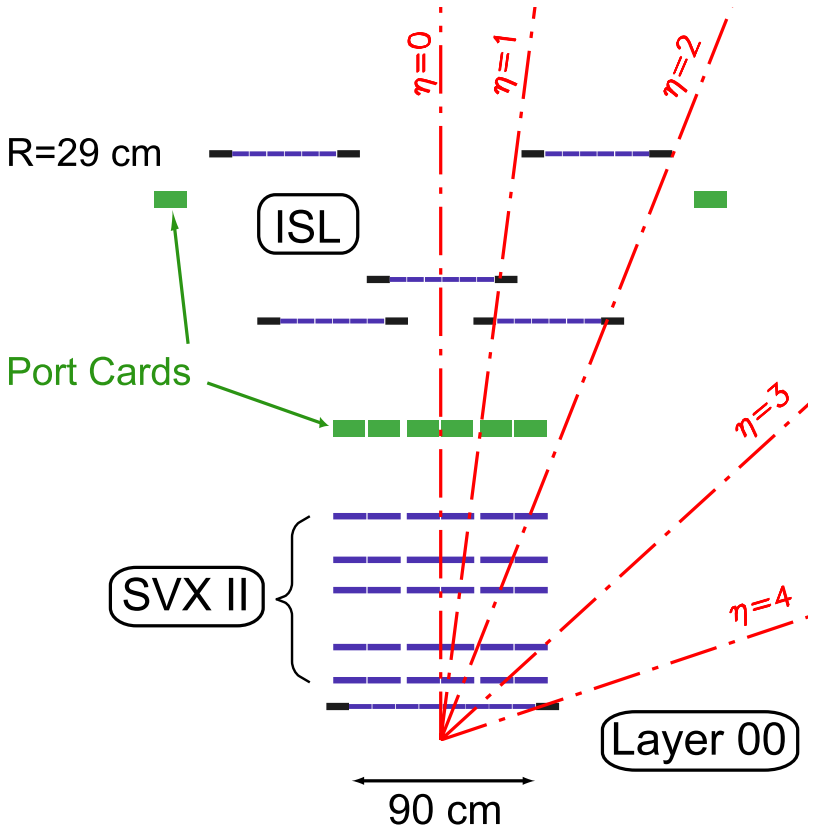

Figure 2.9: The $r-z$ view of CDF silicon tracking system.

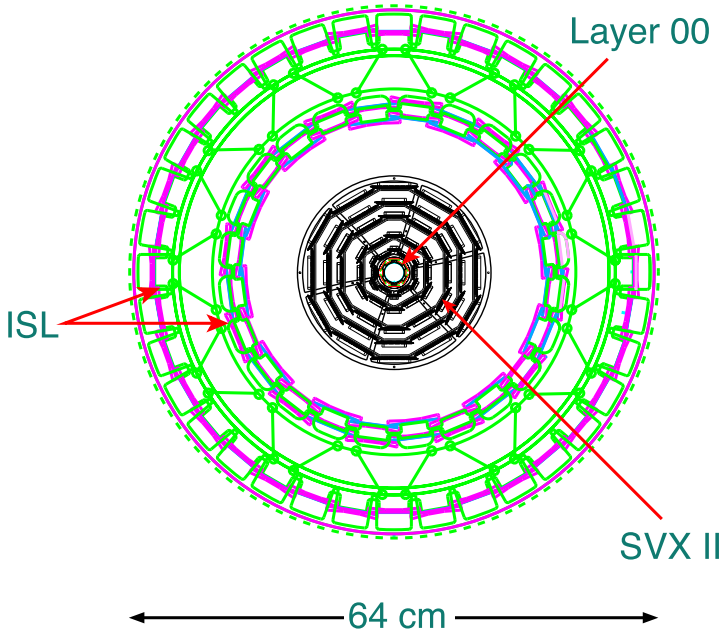

Figure 2.10: The $r - \phi$ view of CDF silicon tracking system.

and potential wires and of two adjacent grounded field (cathode) sheets. Figure 2.12 shows a detail of the configuration for a COT cell showing the cell and wire layout. The sense wires are 40 μm gold-plated tungsten wire and the main body of the field sheets is 6.35 μm gold-coated mylar. Figure 2.11 is a portion of the COT endplate showing cell counts in the superlayers. The superlayers alternate between stereo and axial, the innermost layer being stereo. The difference of a stereo layer to an axial one is that the stereo cell wires and field planes are strung with a 6 cell slot offset between the two endplanes. This allows for a stereo angle of $\pm 3^\circ$ in stereo wires. The tracking combines axial and stereo information to measure the z position. Axial

superlayers only provide $r - \phi$ information.

The COT is filled with Ar/Ethane(50:50). Due to the magnetic field, the electrons produced during the ionization of the Ar/Ethane gas from the passage of the charged particle drift with a Lorentz angle of about 35°. To accommodate the Lorentz angle, the cells are tilted with respect to the radial direction. The chamber is designed to have a fast drift time to cope with Run II beam crossing rates and has operated at a drift velocity of about 50 μm/ns [54].

The momentum resolution of the tracks in the COT chamber is dependent on the p_{T} of the track [7]. During the Run II upgrades, the p_{T} resolution was extensively studied and was estimated to be $\Delta p_{\mathrm{T}}/p_{\mathrm{T}}^2 \sim 0.3\%$ GeV/c^{-1}. The momentum resolution of the COT chamber as a function of p_{T} obtained in this study is shown in Figure 2.13. The measured p_{T} resolution of the COT tracker for the data sample used in the analysis described here is measured to be $\sim 0.15\%$ GeV/c^{-1} with a corresponding hit resolution of about 170 μm [55] [8]. The p_{T} resolution for the Run I CTC chamber was $\sim 0.2\%$ GeV/c^{-1} [57].

[7] The p_{T} of tracks measured in COT tracking volume is given in Equation 2.5.

[8] The most up-to-date number for the hit resolution is $\sim 140\mu$m which is obtained with the latest tracker alignment corrections in CDF offline software [56].

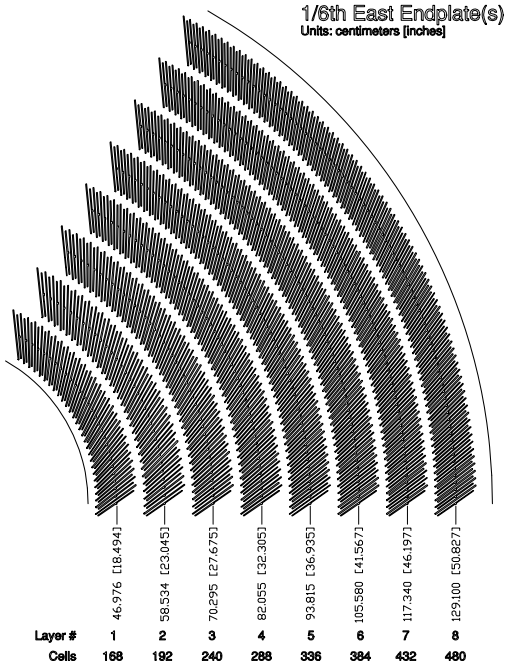

Figure 2.11: Endplate layout of COT. The average radii are given for the superlayers.

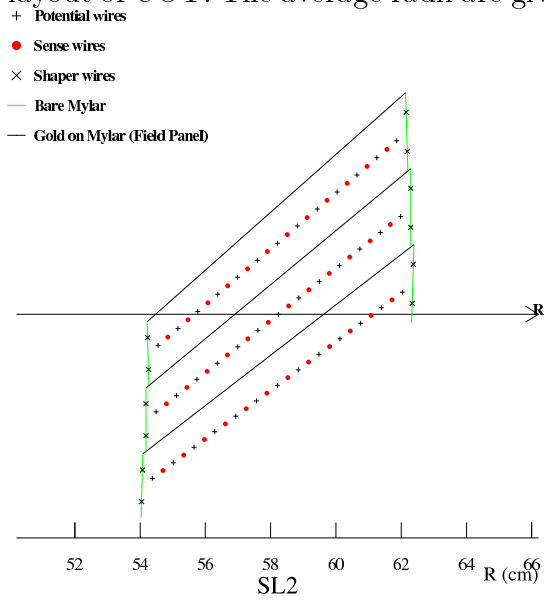

Figure 2.12: Single cell layout of COT.

COT	
Radial coverage	44 to 132 cm
Number of superlayers	8
Layers per superlayer	12
Stereo Angle (°)	+3, 0, -3, 0, +3, 0, -3, 0
Maximum drift distance	0.88 cm
Maximum Drift Time	100 ns
Lorentz Angle	35°
Resolution per measurement	180 μm
Rapidity coverage	$\mid \eta \mid < 1.0$
Number of channels	30,240
Material thickness	1.3% X_0

Table 2.4: Detector parameters of the COT.

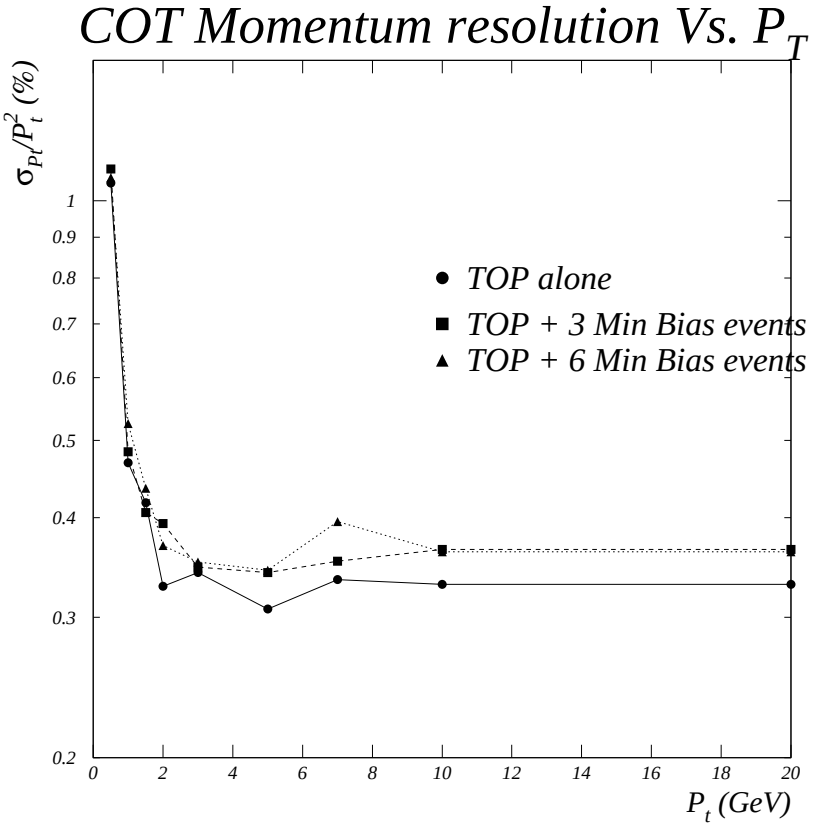

Figure 2.13: COT momentum resolution versus p_{T} for three luminosities.

2.2.2 Time-of-Flight Detector

A new Time-of-Flight (TOF) detector system was installed into the CDF detector during the CDF II upgrade. The main motivation for the TOF is to improve particle identification for flavor tagging. The TOF is located in the space between the COT and the solenoid cryostat at a radius of 138 cm from the beamline, as shown in Figure 2.7. It lies at a radius of 138 cm from the beamline. The system consists of 216 scintillator bars with dimensions of 4×4×279 cm. Each scintillator is read out by a photomultiplier tube (PMT) (Hamamatsu R7761) on each end, which provides time and pulse height measurements. Comparison of the results from each pair of PMTs gives the time and z coordinate information for the particle at the scintillator bar. Since the PMTs operate in the magnetic field of the CDF solenoid, their gain is reduced by a factor of 500 from the nominal gain of 10^6.

The time-of-flight, t, of the particle is defined to be difference between the arrival time at the TOF scintillator and the collision time t_0. Similarly, the path length, L, of the particle is calculated in between the scintillator and the beam collision point. Using this information and the momentum of the particle, one can infer the mass of the particle using the formula below:

$$m = \frac{p}{c}\sqrt{\left(\frac{ct}{L}\right)^2 - 1} \quad . \tag{2.4}$$

The time-of-flight resolution of the system is on the order of 100 ps. The matching of a scintillator information to a track is done by an extrapolation. The summary of the most up-to-date TOF reconstruction can be found in [58].

2.2.3 Calorimeters

Surrounding the CDF tracking volume (outside of the solenoid coil) are a series of calorimeters. CDF uses scintillator sampling calorimeters, which provide a coverage up to about 3.64 units in $|\eta|$. In Run I, CDF calorimeters played an important role in the physics program by measuring electron, photon and jet energies. For Run II, the readout electronics for the central calorimetry system were upgraded. The forward region (endplug) went through a full upgrade and the previous (gas) calorimeter has been replaced by a new system to better accommodate the higher crossing rates for Run II.

The CDF calorimeter system is a complex structure with four subdetectors to allow for maximum possible hermeticity. We describe each subdetector below and summarize the characteristics of the CDF II calorimeter system in Table 2.5. The system forms a uniform pattern of projective towers of electromagnetic (EM) and hadronic (HAD) calorimeters. The segmentation is given in Table 2.6.

2.2.3.1 Central and End-wall Calorimeters

The central calorimeter is divided into two halves at $|\eta|$ =0 and each half consists of 24 wedges in azimuth. The central electromagnetic (CEM) calorimeter wedges consist of alternating layers of lead and polystyrene scintillator. The light signal is wavelength-shifted and carried by light guides to the PMTs (two per EM tower), which measure the number of scintillation photons produced in an EM shower that is formed during the particles' passage through the detector. The energy resolution of CEM is measured to be $\sigma/E = 13.5\%/\sqrt{E_{\mathrm{T}}}$ [59]. During the Run II upgrades, this value is estimated to be at most $14\%/\sqrt{E_{\mathrm{T}}}$ taking into account a scenario where the light yield is 25% less then expected. One wedge of central calorimeter with details of the electromagnetic part is given in Figure 2.14.

To record the position of an EM shower, proportional chambers of wire and strips are embedded near the shower maximum (about 6 radiation lengths) deep into the EM calorimeter. The shower-track matching is performed using these chambers (CES), which helps electron, γ and π^0 identification and reduce fake electron rates. The CES is shown in Figure 2.14 as "strip chamber". Another set of wire chambers is the preshower detector (CPR) which is located right in front of the CEM and uses the tracker and the solenoid coil as radiators. CPR is useful for pion-photon and electron separation.

The central and endwall hadron calorimeters (CHA, WHA) use iron as the radiator and PMMA napthtalane scintillator. The energy resolution of CHA is $\sigma/E = 75\%/\sqrt{E} \oplus 3\%$. The endwall hadron calorimeter consists of modules mounted to the solenoid flux return to provide coverage from 30° to 45 ° on both east and west sides of the CDF detector. The hadronic segmentation and readout scheme matches that of the CEM.

2.2.3.2 Forward (End-plug) Calorimeter

The end-plug (plug) calorimeter is one of the major upgrade projects of CDF II. The old plug calorimeters, being gas-based, had a time response that would be incapable of matching the Run II Tevatron rates. The new plug calorimeter, which covers the $|\eta|$ region from 1.1 to 3.6 (polar angle from 37° to 3°), also matches better the segmentation and the projectivity of the central calorimeters. The calorimeter consist of EM and HAD parts, as is the case of its central counterpart. A section of the plug calorimeter is shown in Figure 2.15.

The plug EM calorimeter is composed of 23 layers of lead/scintillator units. At normal incidence, this corresponds to a thickness of about 21 X_0. The energy resolution is $\sigma/E = 14\%/\sqrt{E} \oplus 1\%$ [60]. The first layer of units are used as a preshower detector (PPR) similar to CPR. As in the CEM, a shower-max detector (PES) exists in the plug calorimeter. The PES and PPR uses scintillating fibers read-out by

	CEM	CHA	WHA	PEM	PHA
$\|\eta\|$ coverage	< 1.1	< 1.1	< 1.3	$1.1<\|\eta\|<3.6$	$1.3<\|\eta\|<3.6$
Total Channels	956	768	676	960	864
Scintillator	5 mm	6 mm	6 mm	4 mm	6 mm
Absorber (inches)	Pb (0.13)	Fe (1)	Fe (2)	Pb (0.18)	Fe (2)
Yield (pe/GeV)	160	~ 40	40	300	39
Thickness	$19X_0$, $1\lambda_I$	$4.5\lambda_I$	$4.5\lambda_I$	$21X_0$, $1\lambda_I$	$7\lambda_I$
Position Res.	0.2×0.2	10×5	10×5		N/A
Energy Res.	$14\%/\sqrt{E_T}$	$75\%/\sqrt{E}\oplus 3\%$	N/A	$14\%/\sqrt{E}\oplus 1\%$	$80\%/\sqrt{E}\oplus 5\%$

Table 2.5: Design parameters and characteristics of CDF II calorimeters. The position resolution (in $(r-\phi)\times z$ cm) is measured at 50 GeV incident energy. CEM resolution is obtained using CES chambers.

$\|\eta\|$ Range	$\Delta\phi$	$\Delta\eta$
0.0 - 1.1 (1.2 HAD)	15°	~ 0.1
1.1 (1.2 HAD) - 2.1	7.5°	~ 0.1 - 0.16
2.1 - 3.64	15°	0.2 - 0.6

Table 2.6: CDF II Calorimeter Segmentation in $\eta - \phi$.

multi-anode PMTs. The plug hadron calorimeter design aims at optimizing detector performance for various physics in the forward region. Its design resolution is $\sigma/E = 80\%/\sqrt{E} \oplus 5\%$, which is dominated by the sampling fluctuations from the absorber plates. Similar to the EM section, it is composed of 23 layers, but of iron sandwiched scintillators.

2.2.4 Muon Detectors

The radially outermost component of CDF II is the muon system which consists of sets of drift chambers and scintillators. There are 4 muon subsystems in CDF

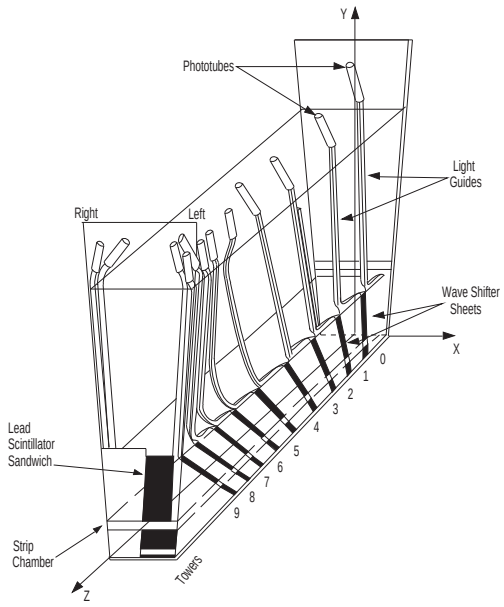

Figure 2.14: One wedge of the CDF central calorimeter.

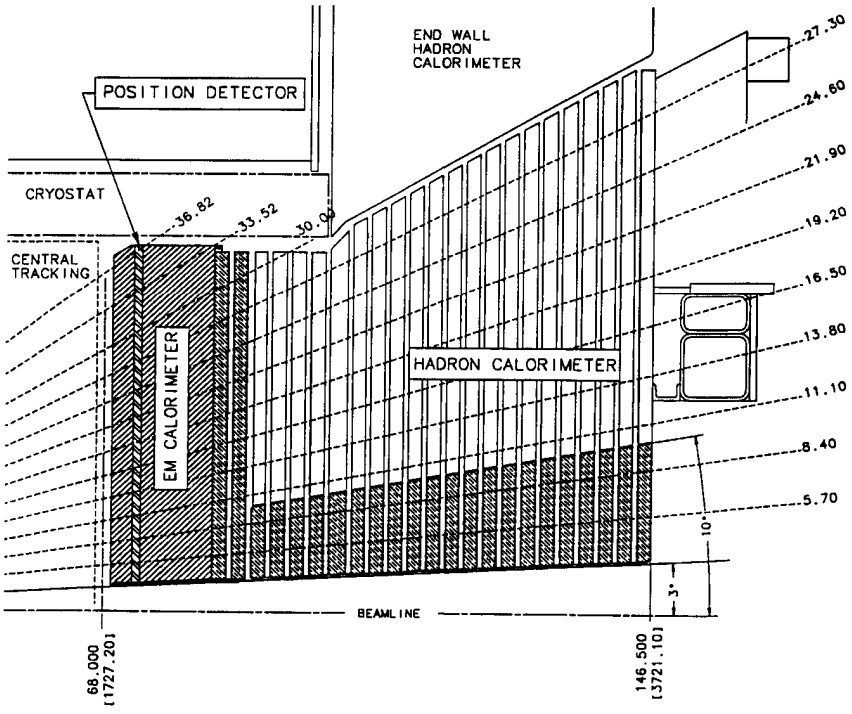

Figure 2.15: Cross section of upper part of the Run II end-plug calorimeter.

II: the Central Muon Detector (CMU), Central Muon Upgrade Detector (CMP), Central Muon Extension Detector (CMX) and Intermediate Muon Detector (IMU). The central part of the system is similar to Run I, except upgrades to improve readout and geometrical coverage. The IMU is new to Run II. The $\eta - \phi$ coverage of the muon system for Run II is shown in Figure 2.16. The design parameters of CDF II muon system is outlined in Table 2.7.

2.2.4.1 Central Muon Detectors

The central muon system covers $|\eta|$ region of up to $\gtrsim 1.0$. The innermost section is CMU, surrounded by the rectangular CMP. CMU and CMP systems cover $|\eta|<0.6$. The details of muon triggering and muon reconstruction using CDF central system is covered in Section 2.3.3.

CMU

The CMU detector is located right behind the hadron calorimeter at a radius of about 350 cm and has a cylindrically symmetric structure. The CMU is the first muon detector built for the CDF experiment [61]. The calorimeters act as absorbers for almost all of the particles, except muons which do not shower as the electrons and photons. Figure 2.17 shows the location of one wedge of CMU chambers behind the CHA. Each wedge covers 12.6° and calorimeter towers cover 15° , so there exists a gap of 2.4° between wedges. Each CMU wedge consist of three modules (stacks)

with four layers of 4 rectangular drift cells as shown in Figure 2.18. The cells have 50 μm sense wire at the center of the cell, running parallel to the z-xis. They are filled with Ar/Ethane(50:50) with some alcohol added.

CMP

The CMP detectors were added during Run I to be mainly used in combination with CMU chambers to further improve the purity in muon identification. It forms a rectangular box around the detector and is located behind 60 cm steel. Due to the geometry of the detector, the $|\eta|$ coverage varies with ϕ, as can be seen in Figure 2.16. The ϕ coverage of CMP was increased in Run II, with the addition of the section referred to as the "bluebeam".

As in CMU, the CMP stacks consist of four layers of drift cells, but they are staggered by half cell per layer. The cells cannot provide information along the z-direction. On top of the outermost layer of CMP are the Central Scintillator Upgrade (CSP) system, consisting of a single layer of rectangular scintillator tiles.

CMX

"The most beautiful of the muon detectors" [62], the CMX, is an extension to the central muon which started during Run I, to cover $0.6<|\eta|<1.0$. It is a conical arrangement of drift tubes similar to those of CMP cells and a sandwich of scintillators (CSX) system. The Run I CMX system, called the "arches" cover 240° in ϕ. The Run II upgrades for CMX includes the extension of ϕ coverage at the west top section

(the "keystone") and the 90° gap at the bottom on both sides (the "miniskirts"). The east 30° gap at the top is filled with the instrumentation for the solenoid cryogenic system. The CMX detector layout can be seen in Figure 2.19.

The CMX segmentation in wedges is 15° in azimuthal angle. Each wedge has 8 layers of rectangular tubes in radial direction and and 6 cells neighbor in each other in ϕ. The eight layers are grouped in pairs to form four continuous layers, each of which is half-staggered with respect to each other. The layout of CMX is given in Figure 2.20. The conical structure of CMX arches allows CMX z coordinate to be independent of ϕ on east and west sides of the CDF detector. This is not true for the miniskirt section, which has no curvature along its width.

The CSX system consist of single layers of scintillator tiles on both sides of the CMX wedges in the arches. The miniskirt scintillation system (MSX) has only one layer of scintillator counters [63]. The system is used in coincidence with the chambers to further improve the timing of the system and reduce the fake rates due to accidental muons (due to beam splashes, for example). In Run I, the pair of layers of CSX were used to time-in to the passing muon, in Run II, information from either of the layers is sufficient [9].

[9] In Run I, CMX detector suffered from high trigger rates due to secondard particles produced in far forward parts of the beamline and scattering into the detector. A ring of steel ("snout") is welded in the inner surface of the IMU toroids (see Section 2.2.4.2) for CMX shielding during the Run II upgrades. Another ring of shielding also added on the toroids ("nostral") near the beampipe for further protection of calorimeters and muon detectors.

2.2.4.2 Intermediate Muon Detector

Muons in the region $1.0 \gtrsim |\eta| \gtrsim 1.5$ are detected by the Intermediate Muon Detector (IMU). This system is the new addition in CDF which uses the toroid steel of old Forward Muon System to mount its chambers and scintillators. The toroid barrels are moved as close to the interaction region as possible to provide a continuous muon detection in $|\eta|$. The upgrades in CDF tracker system and triggers make it possible to trigger and reconstruct IMU muons.

The main parts of IMU are the chambers (BMU) and the scintillator layer (BSU) at the outermost radious of thetoroid structure. The chambers are designed such that they are similar to those of CMU, both in readout and structure. There is also the Toroid Scintillator Upgrade (TSU) system which is made up of trapezoidal scintillators and is mounted in the innner face of the toroid, perpendicular to the beamline. IMU is expected to be prone to beam-related backgrounds at the rear-end, where it is less shielded against the beam halo coming into the CDF interaction point.

2.2.5 Luminosity Monitor

The CDF II luminosity is measured using a set of Čerenkov luminosity counters (CLC) [64]. There are two CLC modules located in the 3-degree holes between

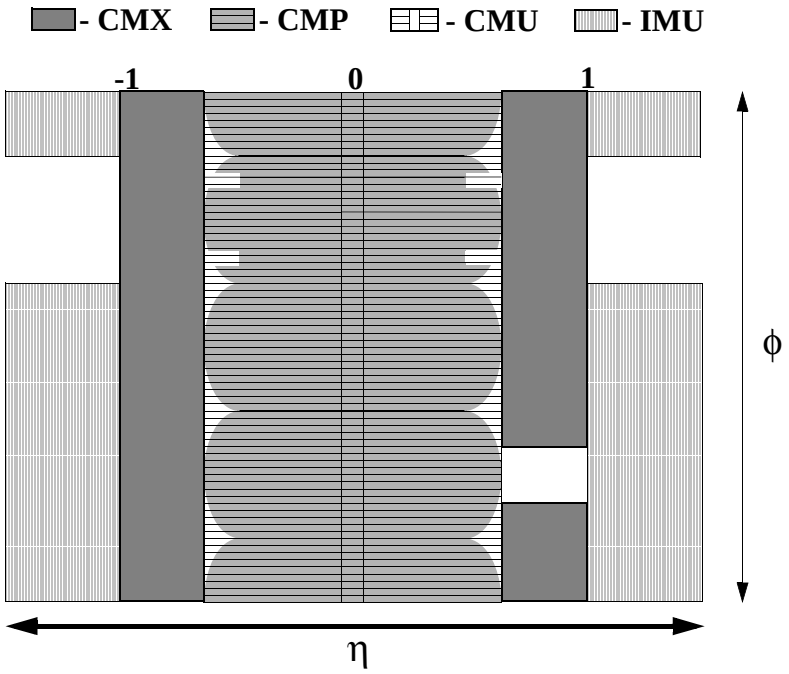

Figure 2.16: Schematic drawing of the location of the muon components in ϕ and η for Run II.

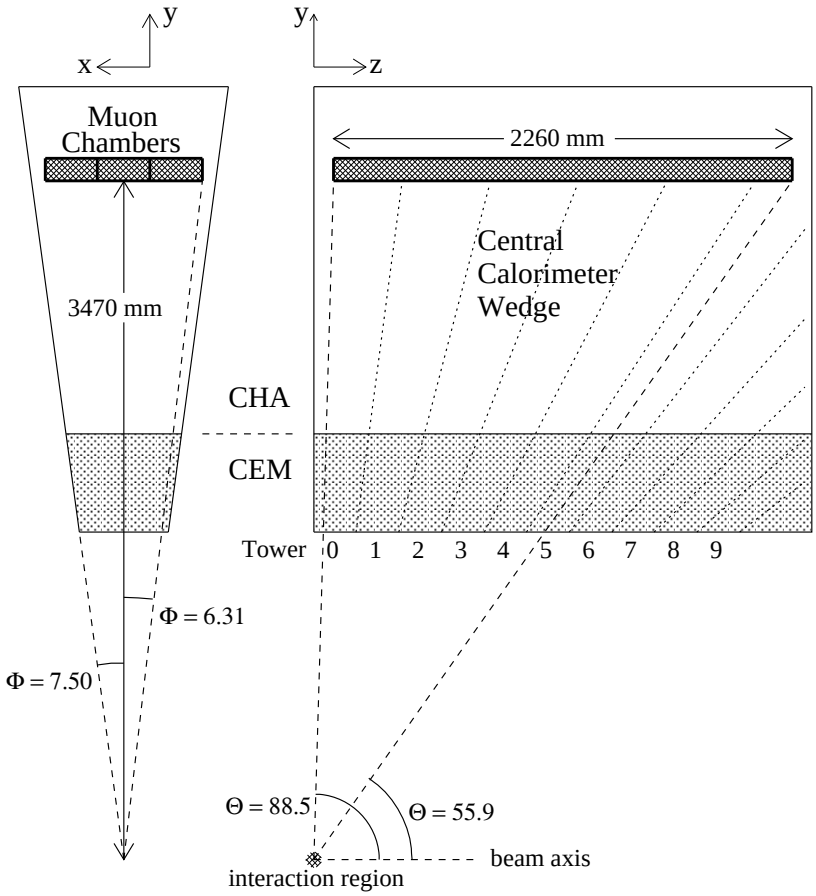

Figure 2.17: Location of CMU chambers.

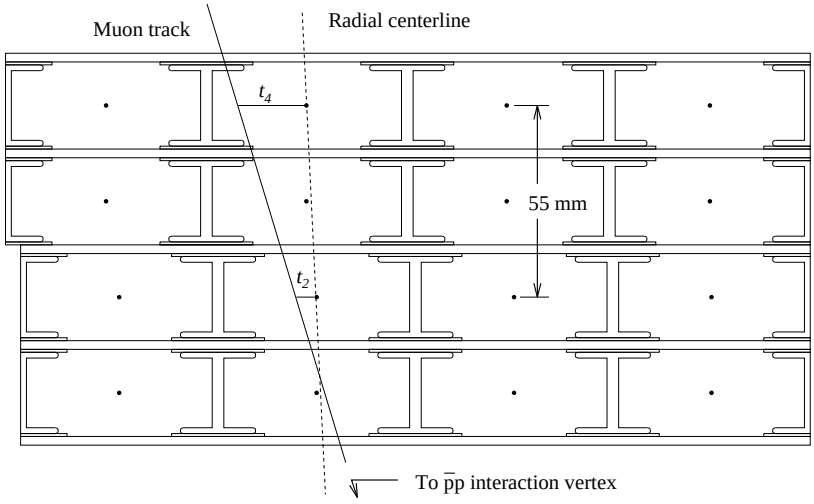

Figure 2.18: A drawing of CMU tower showing a muon track.

	CMU	CMP/CSP	CMX/CSX	IMU
$\|\eta\|$	$\|\eta\| \leq\sim 0.6$	$\|\eta\| \leq\sim 0.6$	$\sim 0.6 \leq \|\eta\| \leq\sim 1.0$	$\sim 1.0 \leq \|\eta\| \leq\sim 1.5$
Drift tube cross-section	2.68 x 6.35 cm	2.5 x 15 cm	2.5 x 15 cm	2.5 x 8.4 cm
Drift tube length	226 cm	640 cm	180 cm	363 cm
Max drift time	800 ns	1.4 μs	1.4 μs	800 ns
Total drift tubes (Run I)	2304	864	1536	none
Total drift tubes (Run II)	2304	1076	2208	1728
Scint. counter width	–	30 cm	30-40 cm	17 cm
Scint. counter length	–	320 cm	180 cm	180 cm
Scint. counter thickness	–	2.5 cm	1.5 cm	2.5 cm
Total counters (Run I)	–	128	256	none
Total counters (Run II)	–	274	324	864
Pion interaction lengths	5.5	7.8	6.2	6.2-20
Min. detectable μ p_{T}	1.4 GeV/c	2.2 GeV/c	1.4 GeV/c	1.4-2.0 GeV/c
Multiple scattering resolution	12 cm/p (GeV/p)	15 cm/p	13 cm/p	13-25 cm/p

Table 2.7: Design parameters of the CDF II muon detectors [51]. Pion interaction lengths and multiple scattering are computed at a reference angle of $\theta = 90^\circ$ in CMU and CMP/CSP and at an angle of $\theta = 55^\circ$ in CMX/CSX, and show the range of values for the IMU.

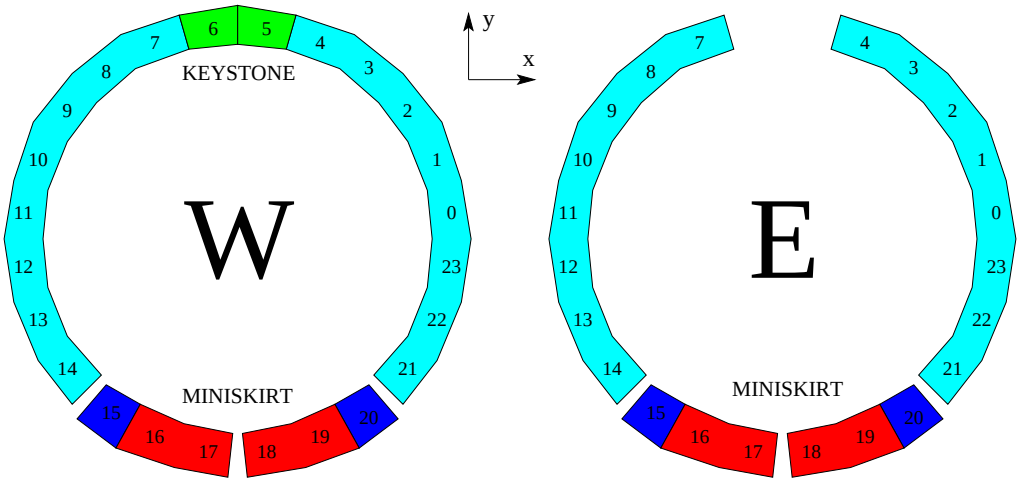

Figure 2.19: CMX detector layout. The arches are represented by cyan (light), keystone green (darker), miniskirt red (30° sections) and blue (darkest) (10° sections). The 10° wedges in blue have not been installed for Run IIA. Wedge 0 starts with $\phi = 0$ line on both west and the east sides.

each endplug calorimeter and the beam pipe. The modules cover the region $3.7 < |\eta| < 4.7$. Each module consists of 48 isobutane-filled Čerenkov counters which are conical in shape. The counters surround the beam pipe in three concentric layers and point to the CDF interaction region. The counters have varying cross-sections and lengths. The cross sections ranges between 2 and 6 cm in diameter. The lengths for the two outermost layers are 180 cm long and the inner four layers are 110 cm long. This arrangement is due to geometrical constraints. The counters are read out by PMTs. The detector type, geometry and material allows for large acceptance, radiation hardness. The CLC is also less sensitive to secondary particles which can scatter into the CLC, as compared with scintillator based monitors. This effect is

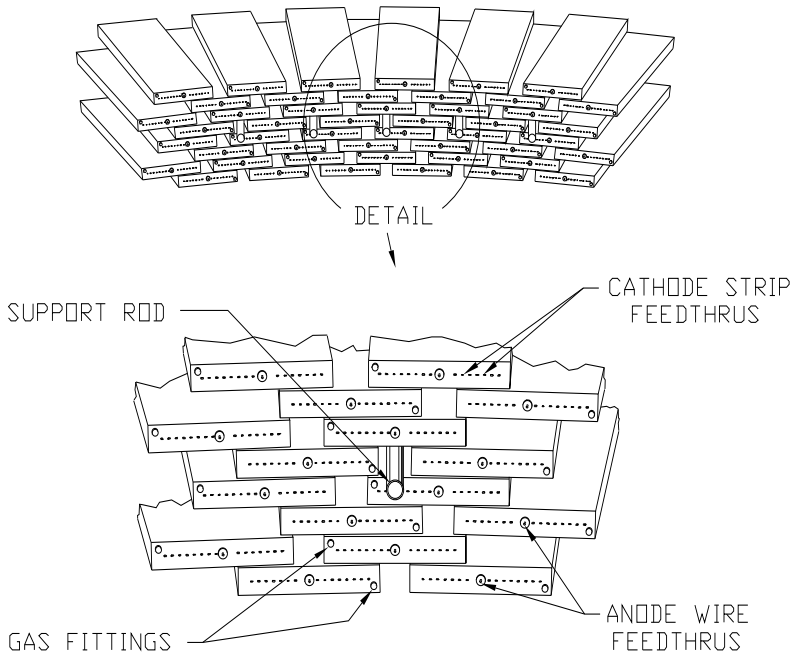

Figure 2.20: Drift tube layout in a CMX module covering 15° in azimuth. The 8 layers of tubes are logically grouped in pairs to form four continuous layers each of which is half-cell staggered with respect to the next layer. Neighboring modules nest together to form a contiguous conical surface.

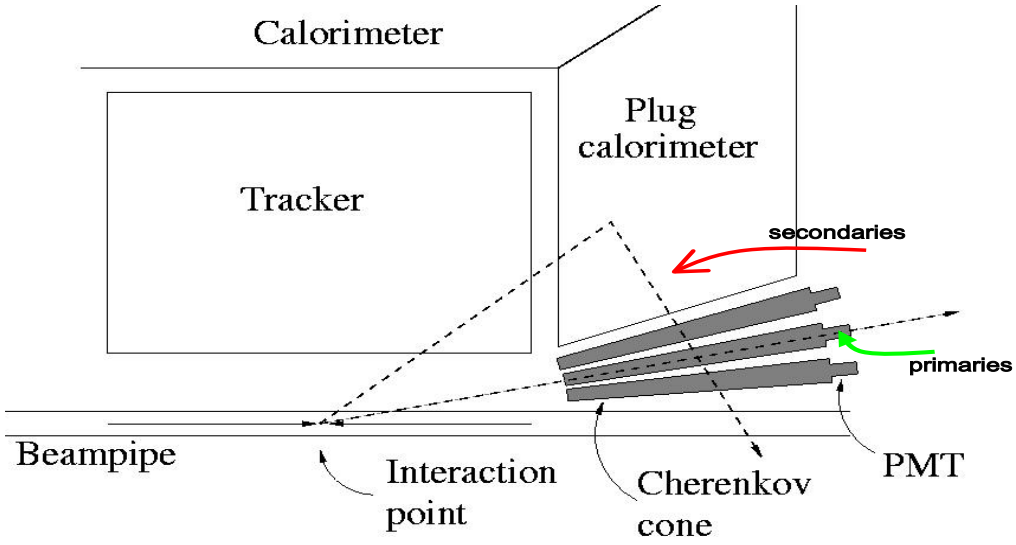

Figure 2.21: CLC detector layout [65].

represented in Figure 2.21.

2.2.6 Forward Detectors and Beam Monitoring

Similar to CLC, other detectors are placed along the Tevatron beamline, at small angles relative to the beam-pipe [66]. Such detectors can be used both as a part of the forward physics program to measure diffractive processes, and as a part of the Tevatron beam monitoring, such as beam losses and beam halo. The Beam Shower Counters (BSC) are sets of scintillator counters which are positioned along the Tevatron magnet system at $z \sim \pm$ 6.5, 23, 32, 56 m (the farthest BSC unit is not present on the east side [67]). The closest of the BSC units to the B0 interaction

point measures the proton and antiproton losses. In addition, a series of scintillating fibers are placed on the west side of CDF as the furthermost components. These tracking detectors are placed in the Tevatron vacuum in movable "Roman Pots" and are used in the diffractive physics program which is beyond the scope of this work.

CDF has undergone an enormous effort to understand the beam conditions at the beginning of Run II, since unexpected beam losses and halo effected the quality and continuity of the data-taking. One of such efforts resulted in installation of a set of monitors at CDF, called the Beam Halo Monitors (BHM). These are arrays of scintillator counters and provide measurements of proton and antiproton beam halo [68]. In addition to scintillator counters listed above, a set of ionization chambers, the Beam Loss Monitors, are also used to monitor the losses from the Tevatron beams. All these monitors are a routine and important part of the data-taking at CDF and are connected to alarms to notify the control room crew in case of undesired beam conditions.

2.2.7 Data Acquisition and Trigger Systems

In this section, we describe the CDF Data Acquisition (DAQ) and trigger systems. For any experiment, both systems are, in general, coupled to each other and share a common infrastructure for data taking.

Data Acquisition System (DAQ)

The reduced separation between the Tevatron bunches requires the readout and DAQ of the CDF II system to be faster. Therefore, the DAQ was altered from the Run I configuration, although the basic architecture remained the same as in Run IB. Improvements were also made to make use of the most up-to-date state-of-the-art developments in electronics and computing.

The DAQ system is responsible for collecting data fragments from front-end electronics systems for events satisfying the trigger criteria up to the final stage of the trigger (Level 3) in which complete event records are formed and sent to mass storage. The schematic diagram in Figure 2.22 summarizes the data flow in CDF DAQ system. The front-end and trigger electronics are packaged as VME modules that reside in about 120 crates in the system. Each crate contains at least one processor board (Motorola, MVME 2301 or higher) for hardware initialization and event readout. The MVME boards run under the VxWorks operating system. In addition to the processors, all crates (except those for the silicon system which has other controllers) contain a "TRigger And Clock + Event Readout" (TRACER) module [69]. The TRACER provides the interface between the VME modules and the Trigger System Interface (TSI). TSI serves as the bridge to the hardware trigger (Level 1 and Level 2). It is this interface that receives the trigger decisions and forwards them to the front-end electronics through the TRACER. The CDF data is digitized

synchronous to the Tevatron clock to ensure proper triggering to the collisions at the CDF interaction point. The global synchronization is provided to the electronics and to trigger by the CDF "Master Clock" [70]. The interface of the Master Clock to the readout crates is the TRACER module.

The data from the front-end crates are transmitted to the L3 trigger by the Event Building Network. The event builder system is constructed around a commercial Asynchronous Transfer Mode (ATM) network switch [10]. The data are first received by the VME Readout Boards (VRB) and, through the switch, are sent to a set of PCs running Linux, so that the events are assembled for shipment to the L3 processing nodes. L3 farms consist of more than a hundred dual-processor nodes [11]. The design input rate into L3 is about 300 Hz. The rate is reduced using the filter algorithms within CDF C++ code, to about 75 Hz(20MB/s). The filtered events are sent to the data logger, which logs the data into several data streams. The streams store collections of datasets (set of events with common physics properties, usually determined by the L3 criteria). The streams are written to tapes in the Feynman Computing Center, to get ready to be read for analysis offline. The processing of the data is performed in the CDF production farms, which produces the data samples and reconstructs physics objects (electrons, muons, photons, jets, ...) (see Section 2.2.8).

[10] The Run IIB upgrades includes the replacement of the ATM switch by a Gigabit-ethernet network.

[11] The farms have been upgraded to cope with the demands of the increasing event sizes and rates.

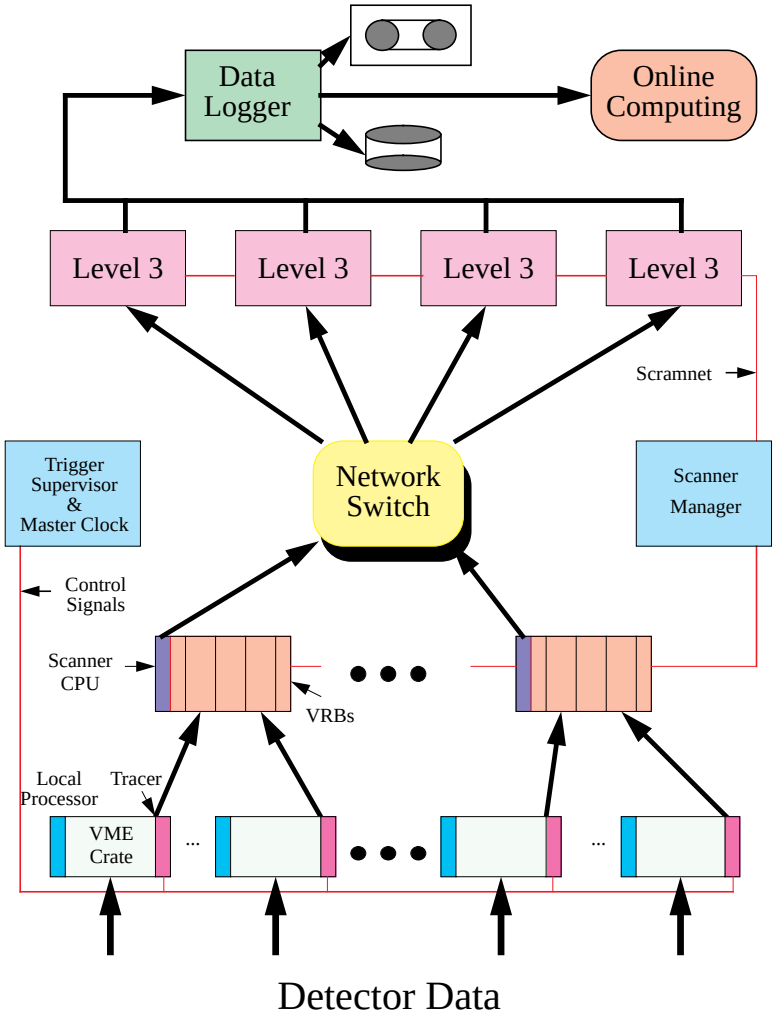

Figure 2.22: CDF II Data Acquisition system. The schematic shows data flow from the front-end and trigger VME crates to the Online Computing system.

An outline of the CDF DAQ system described here can be found in [71].

Trigger System

In state-of-the-art hadron collider experiments triggering becomes especially critical for two reasons: the high beam crossing rates and the large number of final state particles due to underlying events and multiple interactions. To be able to extract the most interesting physics events from the large number of minimum bias events[12], CDF has adapted and implemented a new and faster triggering structure in Run II. The CDF trigger system has a three level architecture. Having described the software part of the trigger, Level 3, earlier, we outline the hardware trigger systems, Level 1 and Level 2, in the following paragraphs. The functional block diagram of the CDF II data flow is shown in Figure 2.23 and the description of CDF II trigger system is given in Figure 2.24.

Level 1

The first decision and filtering level of CDF is the Level 1 trigger. This is a synchronous hardware system which is custom designed to reduce the event rates from about 7.6 MHz to less than 50 KHz. The decision time is about 4 μs, however, the pipelined readout scheme makes the Level 1 "deadtimeless"[13].

At Level 1, the data from the various components of CDF II detector is examined

[12]total di-top cross section is about ten orders of magnitude smaller than the total $p\bar{p}$ cross section

[13]DAQ deadtime occurs anytime a trigger for incoming data is disregarded due to a busy DAQ or trigger system.

(with the exception of silicon). All elements of L1 trigger are synchronized to 132ns clock by the Global L1 trigger with every other cycle rejected automatically to collect data at every 396 ns bunch-crossings.

- XFT: The triggering to tracks at Level 1 is performed by the eXtremely Fast Tracker system [72]. A coarse transverse measurement of momentum and azimuthal direction of a track is formed by using hits in axial superlayers of the COT chamber using what is essentially a fast lookup table. The first step of XFT track finding is to search for track segments in each of the four axial superlayers of COT and the second step is to search for four-out-of-four match among segments in the four axial layers. If not track is found, the search is performed on a three-out-of-three match among segments in the innermost three layers. The XFT configuration allows for up to three missed wire planes in an axial superlayer for the finding of the track segments. The XFT information is distributed to L1 muon and calorimeter systems using the XTRP (Extrapolator) System [73]. The XFT is efficient for transverse momenta above 1.5 GeV.

- L1CAL: This is the calorimeter trigger which triggers on calorimeter objects (electrons, photons, jets) and global event variables (missing transverse energy and event transverse energy). The bulk of L1 processing occurs in boards, called DIRAC (Digital Information Receive And Compare). DIRAC receives

information from XTRP for track-wedge matching.

- L1MUON: The muon trigger uses the information from the CDF muon chamber and scintillator system along with the XTRP unit information to trigger on high and low p_{T} muons. The track matching is performed at the granularity of about 2.5°.

Level 2

L2 inputs information from L1 and silicon system and applies similar (and additional) criteria on data as in L1, but with higher precision. L2 uses dedicated hardware processors to make decisions based on more information about the events. The system has four asynchronous buffers which means events remain in buffer until accepted or rejected. This may cause deadtime at high luminosities. CDF aims to keep the deadtime to less than 10%. For this purpose, L2 is a combination of two steps of 10 μs each. The first step is used to examine the event for the following generalized conditions [14]:

- SVT: The SVX 2-D fast tracking is performed at this level including the measurement of the impact parameter, d_0, which makes it possible to trigger on secondary vertices in SVX. This capability is an important addition to CDF b-physics program in Run II [74].

[14] L2MUON trigger implementation has been carried out during 2004.

- L2CAL: This is where the clustering of towers are performed to be able to form jets and reduce the rates.

- XCES: The calorimeter shower maximum chambers can be further used to refine the track matching (position and momentum)with XFT and reduce the fake electron and photon rates. The segmentation of XCES trigger is about 2° in azimuth.

The second step of L2 is further event topology characterization and tighter requirements performed in the Alpha processors. There are about 100 triggers in L2 and output rate of L2 is about 300Hz at maximum. After L2, the entire event data is passed onto the L3 farms, which perform the filtering at software reconstruction level.

2.2.8 CDF Analysis Framework

CDF reconstruction and analysis framework is built upon an object-oriented concept, similar to the DAQ and online system. The coding language is C++. The framework is specifically called AC++ which is a family of classes and its main infrastructure is based upon modules, paths and streams. An AC++ "module" is a piece of code typically to carry out a single well-defined task, such as event reconstruction in a particular subdetector, for example, muon reconstruction in the muon system. The

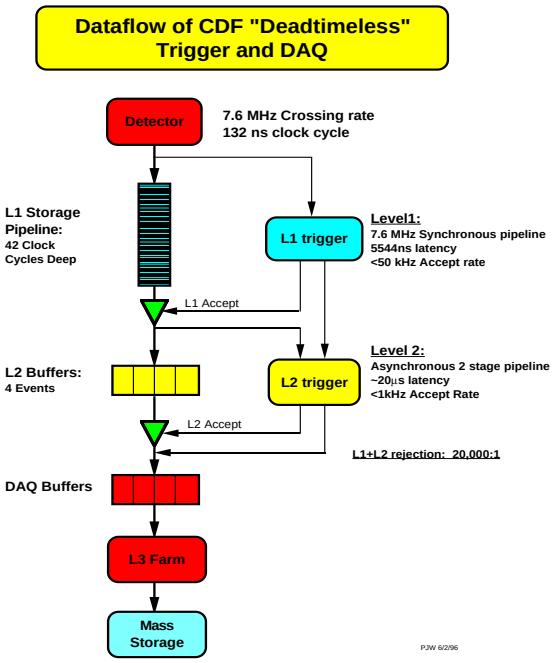

Figure 2.23: Functional block diagram of the CDF II data flow.

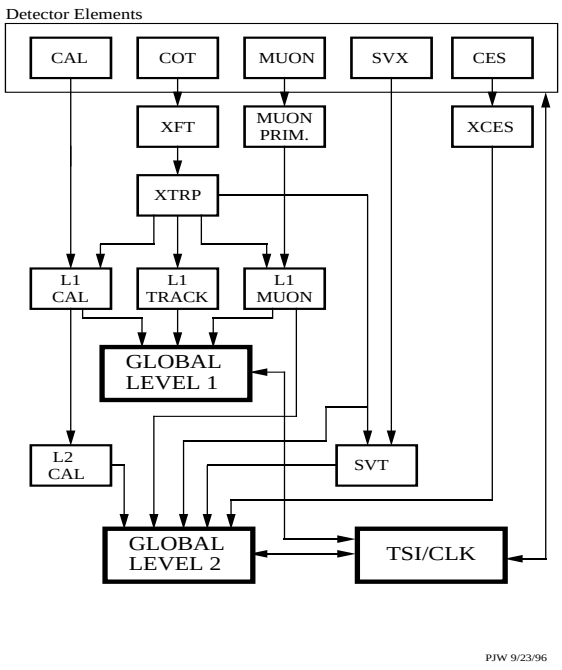

Figure 2.24: Block diagram of the CDF II trigger system.

order and choice of modules a user would like to have in the analysis code is done through defining a "path" in his/her executable. Associated with a path can be a "stream", which is the specific output file for the analysis job. The storage of of data for each event within memory or resident on a disk is described by a model called the "event-data-model" (EDM). The underlying structure of EDM uses ROOT [75] file format. The event record within EDM format makes full use of object-oriented language concepts. The numerous data structures that are contained in the event record are defined by C++ classes. Following the nomenclature of C++, we call these data structures as *"objects"*, which are uniquely defined by a number in the event record. The end user at CDF does not need to know what these numbers are, but rather use the name of the class itself. The event record holds the raw detector data in "StorableBank" classes. This information is used to create higher-level objects for making the final analysis-level objects. A muon object, for example, will have a track and usually a stub associated with it. A "link" can give the necessary information to point to a track used for reconstructing the final muon particle, for example. Similar to muons, there are other objects used in CDF for data analysis. The most common ones are tracks, calorimetry objects, electrons, photons and taus. The CDF framework was designed to make many of the object similar in their form and usage. An "electron object", which typically contains a "track object" also carries a link to it, similar to the muon. We give more information on the creation of the "CDF muon

object" in the following sections. Finally, we should mention that the CDF analysis code has improved constantly during the period of data taking which is presented in this work.

2.3 Muon Detection, Trigger and Reconstruction

In the following sections, the muon detection and identification (ID) at CDF is briefly described, with a possible emphasis given to CMX detector. CDF detector uses a collection of single-wire, gaseous drift chambers and organic scintillator tiles for muon detection and triggering, as briefly introduced in Section 2.2.4. In the following sections, we outline the basics of drift chambers, readout, trigger and reconstruction and identification. An elaborate discussion of the concepts introduced here can be found in [76] (detectors) and in [77] (reconstruction).

2.3.1 Basics of muon detection

A drift chamber is a type of gas chamber detector which are based on direct collection of the ionization of electrons and ions produced in a gas by a passing charged particle. A single-wire drift chamber with a rectangular cross section is shown in Figure 2.25. A penetrating muon ionizes gas inside the chamber with negligible energy loss (minimum ionizing particle, MIP). The chamber sustains a net positive

voltage difference between the anode (sense) wire and the cathode (field) plates. The positively charged ions drift toward the cathode field, the ionization electrons drift toward the anode wire. The electrons create an avalanche of charge as they come nearest to the wire and produce a pulse as the charge hits in the wire. The pulse is sent to the readout electronics and collected as signal. The distance, D, of the muon to the wire is measured using the drift time of the pulse and the drift velocity, v_d. The drift velocity of a chamber is dependent on the grid voltage (uniform) and the gas content. CDF muon uses Ar/C_2H_6 bubbled through isopropyl alcohol. Argon is the noble gas. Ethane (C_2H_6) is the quencher. The role of a quencher is to absorb photons emitted from Ar, through vibrational and rotational degrees of freedom. It also helps tune drift velocity and signal gain. It has been shown that the usage of alcohol, as the additive vapor, helps as a quenching agent to prevent breakdowns, glow discharges and aging [78]. Most drift chambers employ a field shaping to get almost a constant drift velocity across the chamber. The details of the voltage grid of the CMP and CMX chambers can be found in [76].

Figure 2.26 illustrates the readout chain of a muon chamber [15]. The signal collected at the anode wire is first passed through a preamplifier (Radeka, [79, 76]), for signal amplification. The analog signal is then carried to the ASD [79] modules in

[15]There exist slight variations on the electronics and DAQ of the different CDF muon subdetectors, however, the principles of readout is similar.

the collision hall. The ASD (Amplifier-Shaper-Discriminator) card further amplifies the signal and converts to to an ECL signal, which for which the width of the signal is proportional to the time measured over some threshold. Representative analog and ECL signals are shown in Figure 2.27. The ASD modules also have the task of distributing the calibration signals to the preamplifiers. The different modes of operation of an ASD card is shown in Figure 2.28 and the electronic circuitry for one ASD channel is shown in Figure 2.29. The differential ECL signal coming out of the ASD is sent through to the counting room outside of the collision hall, to be read by the TDC modules [51], where the signal arrival times and the widths of the signals are digitized and can be further used for storing the information or for triggering purposes. The TDC sampling is 1 ns with window of 2 μs and they are programmed to read, at most, eight consecutive signals from the chambers [16]. In CMU detector, the neighboring chamber are ganged together such that the relative amounts of charges collected in the resistive anode wires can be used to measure the position of the muon along the wire (z). Similar measurement can also be performed for the BMU detector.

Operating gaseous chambers is a difficult task. The most common problem in operating chambers is the breakdown process. A breakdown occurs when the volt-

[16] A chamber with high frequency noise will thus has a high possibility to yield event hit multiplicities of eight.

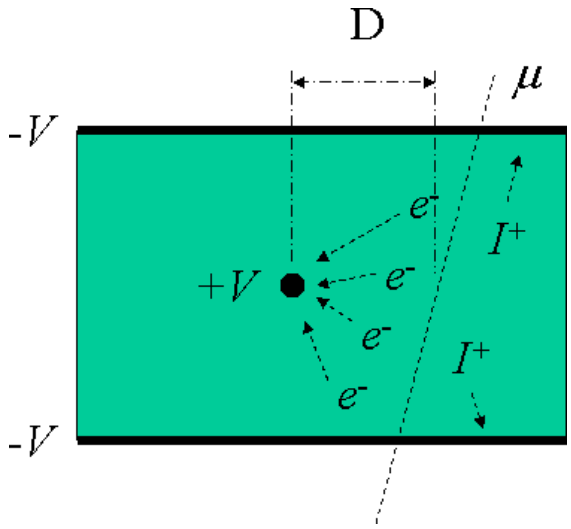

Figure 2.25: Drift chamber principles [62].

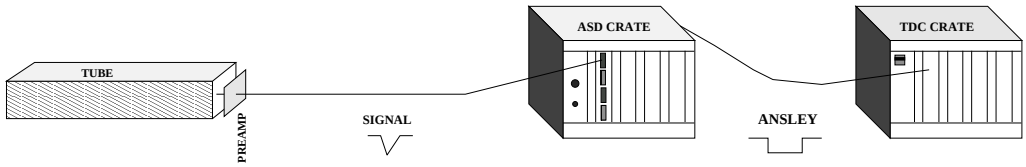

Figure 2.26: Readout chain for the CMX/CMP muon detectors.

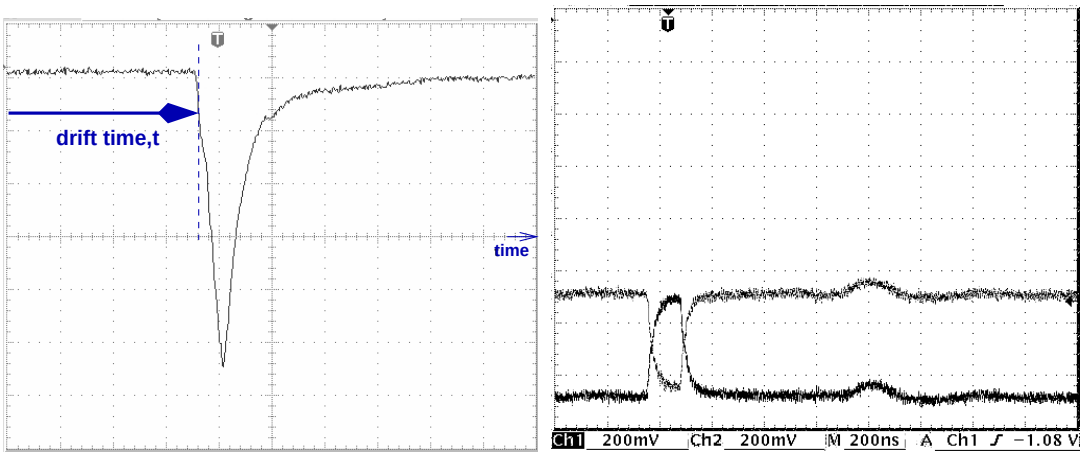

Figure 2.27: Typical signal shapes for a CDF drift chamber. Left is the analog output from the chamber, right is the ECL output that is input into the TDC for the CMX detector.

age across the cathode and anode gap drops by a processes which produces a high conductivity between cathode and anode [80]. The mechanisms of breakdown in wire chambers are usually related to the chemical reactions of the particles, such as electrons, ions, molecules and photons, within the chamber plasma and with their interactions with the cathode. It has been especially observed that when ultraviolet photons from excitations of the gaseous medium are not completely quenched. Self-sustaining discharges often occur for the gaseous chambers, such as "sparks" which are complete breakdowns of inter-electrode gap. "Glow discharges" occur when self-sustained currents develop and dark-current rates increase. Under sustained irradiation wire chambers can "age", which is a degradation of operating characteristics, commonly as a result of formation of deposits of molecules on the anode wires or

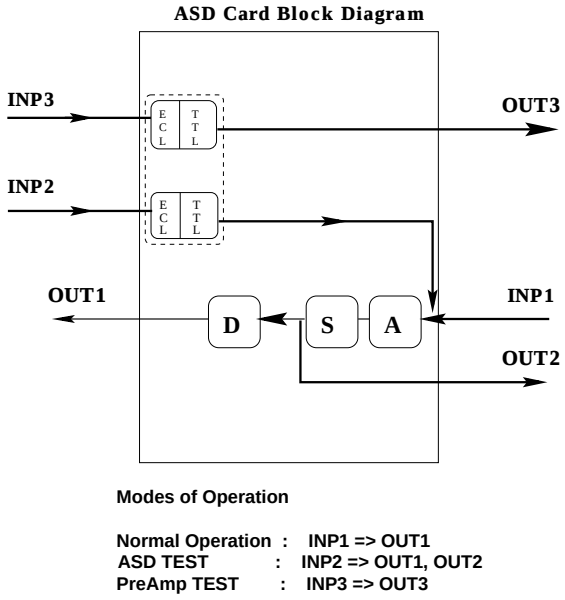

Figure 2.28: ASD card block diagram for CMX/CMP detectors.

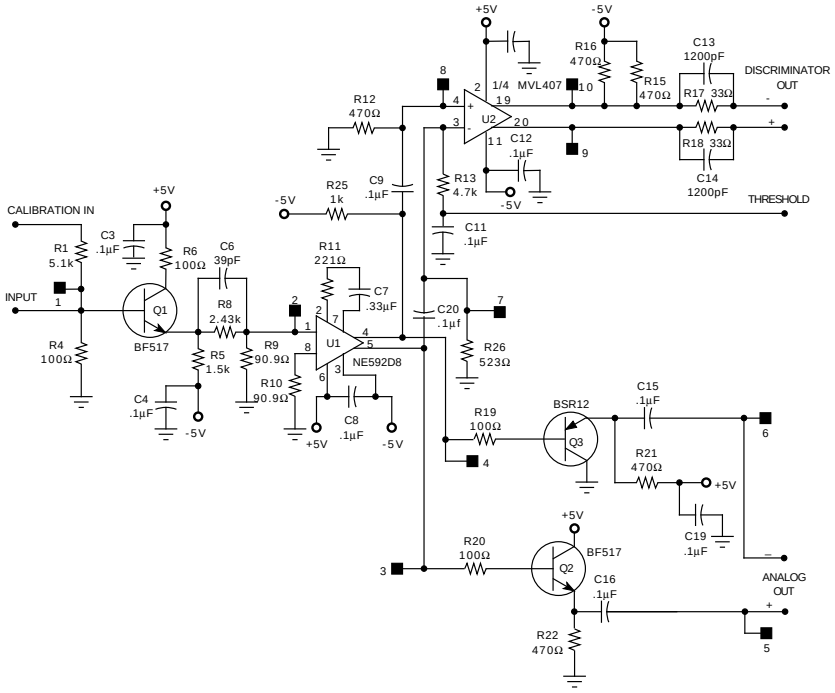

Figure 2.29: CMX/CMP ASD circuit.

cathode plates changing the gain of the chamber. Some details of problems observed in the CMX chambers is outlined in Section E.

2.3.2 Muon Trigger

The muon detector information can be triggered on at the Level 1 of CDF triggering system. The muon stub information is obtained in bitwise information in the transverse momentum of the particle that is passing through it. Arrangement of the anode (sense) wires within a muon chamber permits a lower bound on the p_{T} of a particle to be determined [61]. The angle between a particle track and the radial line passing through the anode wires can be determined by measuring the difference in arrival times of the drift electrons (Δ_t). A further relationship can be derived between this angle and the angle of deflection due to the magnetic field surrounding the tracker, which is in turn related to the p_{T} of the passing muon track. Therefore, a crude measurement of the muon p_{T} can be performed by using the Δ_t information. This relation is derived for the CMU chambers, but in principle, may be applied to all the muon detectors.

Figure 2.30 shows the trigger-pair of the CMX system. The trigger-pair chambers are selected to be the the pair of chambers that lie at the same ϕ. If the drift time difference between a trigger pair is < 124 ns, the L1 muon "primitive" trigger

fires a "High p_{T} stub" if it is less than 396 ns (beam crossing time), then it is a "Low p_{T} stub". For the CMX and IMU systems the scintillator information is also attached to the trigger. As of this writing, the CSP scintillators are not used. The CMP detector information is obtained through a specific pattern finding using four layers of drift tubes. The IMU system also makes use of the HAD calorimeter timing information to further bring down the trigger rates down [62]. Figure 2.31 shows the diagram of the Level 1 muon trigger in Run II. The high p_{T} muon track identification in the COT is accomplished in the XFT processor at Level 1, as discussed in Section 2.2.7. The information of the track trigger (XTRP) and the muon stub information is matched in the Muon Matchbox card over an entire 30° azimuthal wedge of the CDF detector. From then on, the information can be passed to the Level 2 trigger.

2.3.3 Muon Reconstruction and Identification

The high p_{T} muon data that are collected need to be reconstructed with the CDF offline software with very loose reconstruction requirements and with the calibrations and corrections applied. The CDF muon system is very complicated, consisting of many parts with different capabilities. Therefore, we will not go into the details of individual subsystem calibrations here. The common calibrations are the global

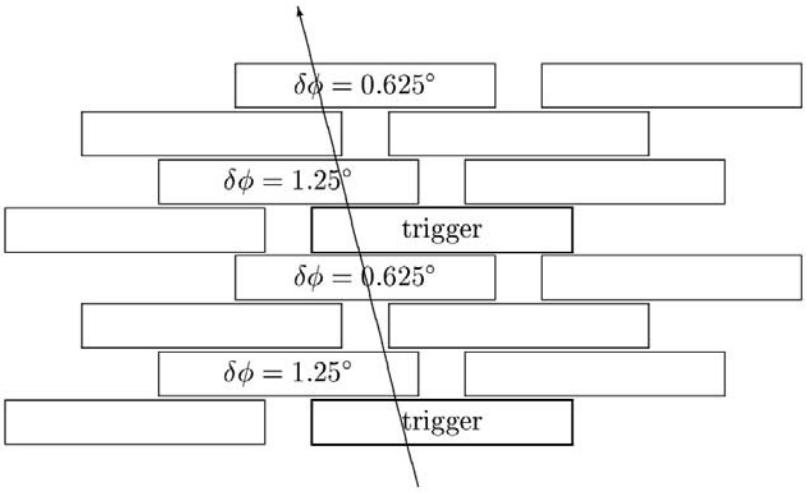

Figure 2.30: Schematic drawing of the CMX trigger [81].

alignment of the detectors with respect to the central tracker, the drift velocities for a correct measurement of drift distances.

The passage of a muon in CDF detector and hitting CMU and CMP chambers is schematically shown in Figure 2.33. The muon track parameters are measured in the tracking volume and the 4-momentum of a CDFMuon comes from its track. The calorimeters, in principle, act like absorbers and they give the measure of the EM and HAD energies. The muon then passes through the muon chambers (in this case, the CMU and CMP), such that muon chamber tracking (forming "stubs") can later on be performed. A muon stub is formed using the hit information and stub finding and fitting algorithms for the subdetectors. The output of the fits are the stub position and direction vectors [77]. A muon stub has at least 3 hits associated

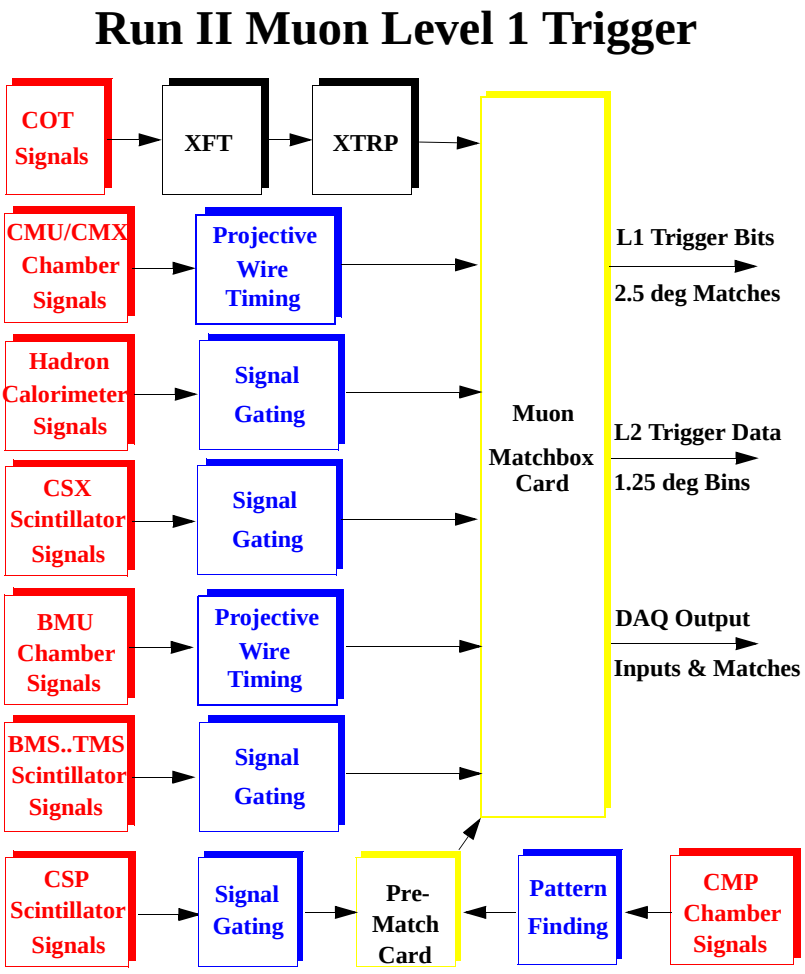

Figure 2.31: Data flow for the Run II L1 muon trigger [82].

to it.

The muon track helices are parameterized at the point of closest approach to the origin in $x-y$ plane of the CDF detector [83]. The axial $(r-\phi)$ parameters are the impact parameter (d_0), azimuthal angle (ϕ_0), and the curvature (p_{T}). The stereo $(r-z)$ parameters are the z position (z_0) and the $\cot\theta$, of the angle with respect to the z-axis at the point of origin. The $\cot\theta$ is defined as p_z/p_{T}. The curvature is defined as $c = 1/2R$ where R is the radius of the curvature of the track. For a negatively charged particle, the curvature has a negative sign. The relation between p_{T} and curvature is:

$$p_{\mathrm{T}} = \frac{B}{2c_l} \times \frac{1}{c} = \frac{0.002117}{c} \quad , \tag{2.5}$$

where c_l is the speed of the light. For a tracking volume of fixed magnetic field, p_{T} is only a function of c (or R).

If the tracks use only the COT information, they are usually "beam-constrained" (BC) at the analysis level, since they are reconstructed with respect to the z-axis of the CDF detector. This is performed refitting the track by using the measured position of the beamline. This procedure improves the momentum resolution of the tracks, as will be discussed in Section 4.

The muon tracking stops at the face of the COT. From then on, a procedure should be applied to match a stub candidate in the muon chambers to the muon

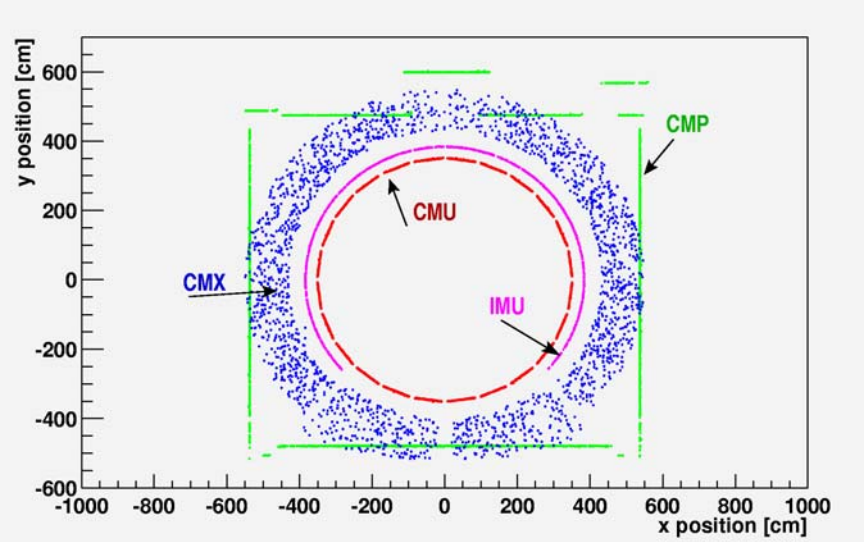

Figure 2.32: The $x - y$ distribution of hits from simulation. $x, y = 0$ cm is the detector center.

track candidate. Also the path of the muon inside the calorimeters is not measured. Therefore, "extrapolators" are used to extrapolate the track to the stub. The measure of this quantity in $r - \phi$ plane, usually called Δx, is one of the basic criteria for selecting a muon candidate in the CDF detector (Section 4).

Figure 2.32 shows the proton eye's view of the CDF muon detectors as outlined by using the hits in a single muon event simulation of 40 GeV/c muons. The large spread of CMX detector hits is due to its conical structure. The miniskirt section hit occupancies have also been plotted in this figure.

Table 2.8 summarizes the criteria for reconstructing a CDFMuon in the CDF offline code. The criteria is taken as applied in the version of CDF software used in

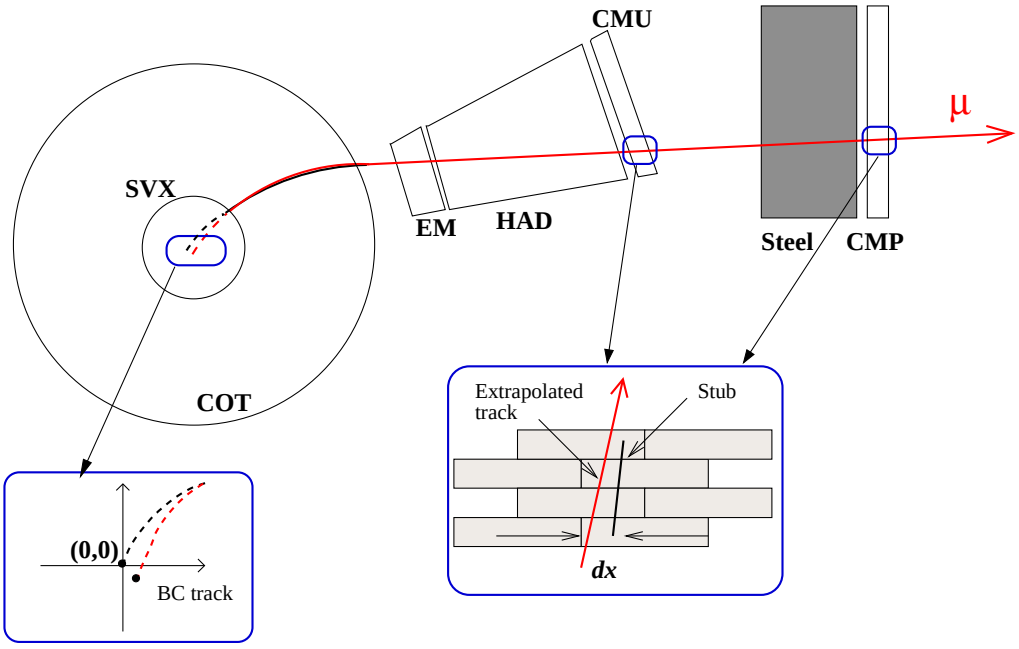

Figure 2.33: Passage of a muon through the CDF detector.

parameter	Criteria
p_{T}	> 1.3 GeV/c
	> 10 GeV/c(Stubless)
$\lvert z_0 \rvert$, $\lvert d_0 \rvert$	< 200 cm, < 6 cm
Track hits (N_{axial})	≥ 10
$\lvert \Delta x \rvert$(cm)	< 30 (CMU)
	< 60 (CMP)
	< 50 (CMX)
	< 90 (BMU)
$\lvert \Delta z \rvert$(cm)	< 250 (CMU)
	< 330 (CMP)
	[325, 550] (CMX)
	[440, 840] (BMU)

Table 2.8: Muon reconstruction criteria.

this analysis. For CMX and BMU detectors, the track-stub matching quantities are applied to the tracks and stubs on the same side of the detector (east ($+z$-axis) or west). For CMU this criteria is applied only if z_0 is > 20 cm.

Chapter 3

Data Sample

The first step in every analysis is to choose the appropriate dataset; the trigger, that is best suited for the desired physics signature to be studied. In this chapter, we describe the data sample used for the high mass dimuon physics searches.

3.1 Inclusive Muon Sample

For the high mass physics searches in the dimuon final state, we use the dataset that contains at least one high p_{T} central muon (p_{T}>18 GeV/c, $|\eta| \lesssim 1.0$) This dataset is called the "inclusive" high p_{T} muon dataset and is obtained by splitting off the events from the data stream satisfying the triggers discussed below. The data stream is referred to as "Stream B" and includes all high p_{T} lepton trigger datasets. Stream

	CMUP Path
	MUON_CMUP_18
L1	L1_CMUP6_PT4
L2	L2_AUTO_L1_CMUP6_PT4 (run < 152951) L2_TRK8_L1_CMUP6_PT4
L3	L3_Muon_CMUP18

	CMX Path
	MUON_CMX_18
L1	L1_CMX6_PT8 (run < 152951) L1_CMX6_PT8_CSX
L2	L2_AUTO_L1_CMX6_PT8 (run < 152951) L2_AUTO_L1_CMX6_PT8_CSX
L3	L3_Muon_CMX18

Table 3.1: Trigger paths used for the high mass dimuon analysis.

B, therefore, serves as a most generic data sample for many analysis including the leptonic decays of W, Z bosons either produced directly or as decay products from other particles, such as the top quark.

The events that make up the dataset are determined by the trigger requirements which are tabulated for each CDF physics run [1]. The global high p_{T} central muon dataset consists of three trigger paths. In this analysis, we use only the two trigger paths listed in Table 3.1 [2]. The naming convention for levels of each trigger is such that the level specification, object description and main thresholds are indicated. For example, L1_CMUP6_PT4 means a Level 1 trigger requiring a CMUP muon with

[1] A run is a continuous data-taking and recording period of the detector. CDF runs are identified by incremental integer numbers.

[2] The trigger paths are enforced at the dimuon selection level as described in Chapter 4.

trigger p_{T} greater than 4 GeV/c and L1_CMX6_PT8_CSX means a level 1 trigger requiring a CMX muon with trigger p_{T} greater than 8 GeV/c and an associated CSX signal.

The trigger requirements for the CMUP high p_{T} muon path is:

- Level 1: A high p_{T} CMU muon stub primitive matched to an XFT track with p_{T} >4 GeV/c and a matching pattern in CMP chambers.
- Level 2: No requirements before run 152951, and requirement of a standalone XFT track with p_{T} >8 GeV/c thereafter.
- Level 3: Software reconstruction of muon track with p_{T} >18 GeV/c with CMU and CMP stubs satisfying the track-stub matching condition as listed in Table 3.2.

The trigger requirements for the CMX high p_{T} muon path is:

- Level 1: A high p_{T} CMX muon stub primitive matched to an XFT track with p_{T} >8 GeV/c. Starting with run 152951, matching scintillator information from either tile of the CSX sandwich is required.
- Level 2: The events are "auto-accepted", *i.e.*, no requirements at this level of trigger. To accommodate the L1 change at run 152951, trigger name has changed.

Trigger	Requirement
L1	CMU_STUB_PT = 6 GeV/c
	REQUIRE_CSP = 0
	REQUIRE_CMP = 1
	CMU_XFT_PT = 4.09 GeV/c
L2	XFT_PT = 4 GeV/c (No req. for run < 152951)
L3	cmpDx = 20 cm
	cmuDx = 10 cm
	minPt = 18 GeV/c
	nMuon = 1
	selectCMUP = true

Table 3.2: Requirements for the CMUP high p_{T} trigger path.

Trigger	Requirement
L1	CMX_STUB_PT = 6 GeV/c
	CMX_XFT_LAYERS = 4
	REQUIRE_CSX = 1 (= 0, for run < 152951)
	CMX_XFT_PT = 8.34 GeV/c
L2	No req.
L3	cmxDx = 10 cm
	minPt = 18 GeV/c
	nMuon = 1
	selectCMX = true

Table 3.3: Requirements for the CMX high p_{T} trigger path.

- Level 3: Software reconstruction of muon track with p_{T} >18 GeV/c with the reconstructed CMX stub satisfying the track-stub matching condition as listed in Table 3.2.

There have been changes to the trigger requirements for high p_{T} muon sample during the Run II data taking. Starting with the tests from run 152621, there have been modifications of some of the triggers in the three trigger paths. A L2 trigger

change for CMUP and L1 trigger change for CMX path took place mid-October starting from run 152951. The earlier triggers as labeled by the run number in Table 3.1 officially ceased to be effective after this point in time. Also, starting from 162636, the general XFT track trigger requirements were tightened, as described earlier. The trigger level specifications of the dataset for different versions of the Physics Trigger Tables is tabulated at the CDF database and is also logged by the Trigger and Dataset Working Group [84].

3.2 Secondary Dataset

The inclusive high p_{T} muon sample from Stream B is processed by version 4.8.4 of CDF offline production code and is a combination of two datasets (with identifiers: bhmu08 and bhmu09) corresponding to two time periods: before and after January 2003 shutdown. The data in this collection includes data until Fall 2003 Tevatron Shutdown which took place between September 8, 2003, to November 16, 2003, and is processed to be in time for Winter 2004. We refer to this sample also as the "Winter 04" sample. The total data volume in the Stream B, high p_{T} muon sample, is too large to be analyzed by an average CDF user and is also contaminated by fake triggers (there is no MIP requirement at the trigger level) and by cosmic ray events (see Section 5.3 for a discussion of the main backgrounds). Therefore, the

data sample is stripped with the application of "loose" muon identification (ID) requirements ("cuts") [85] and a secondary data sample is generated. The events are filtered to assure the presence of at least one muon and that muon passes the loose ID requirements listed in Table 3.4. The requirements are tighter than the online trigger criteria, but much looser as compared to analysis level cuts, which are described in Chapter 4. The corresponding filtered datasets are btop1g and btop1j, which are skimmed using a 4.8.4+ stripping module ("StripMods" module). About half of the muon events remain in the secondary dataset after this stripping process. It sometimes happens that the production of datasets occur before the calibrations and final corrections can be applied to it. Therefore, the secondary datasets are further re-processed [85] using version 4.11.1 release to correct for updated tracking and calorimeter calibration to pick up the latest calibration constants available for the calorimeter system. Tracking is reprocessed excluding LØØ hits in the track reconstruction. Section 3.3 summarizes the calorimeter corrections in detail.

The high level objects, such as electrons and muons, were re-reconstructed with these updates taken into account. In this analysis, we are using this inclusive dataset with the final corrections applied. Figure 3.1 illustrate the p_{T} distribution of the CDFMuons. The trigger cut-off around 18 GeV/c is visible. Figure 3.2 shows the COT z-vertex distribution which indicates a longitudinal vertex profile with an RMS of about 30 cm. Both distributions are obtained by using a subsample (≈ 18 pb^{-1})

Requirement	Value
nMuon	≥ 1
p_{T}	≥ 18 GeV
$\mathrm{E_{EM}}$	$< \max(0.5\times6.0,\ 0.5\times(6.0 + 0.028\times(p - 100)))$
$\mathrm{E_{HAD}}$	$< \max(1.5\times6.0,\ 1.5\times(6.0 + 0.028\times(p - 100)))$
Δx	< 5.0 cm (CMU) & < 10.0 cm (CMP) < 20.0 cm (CMX) < 50.0 cm (BMU)

Table 3.4: Stripping cuts for the inclusive muon data.

of the inclusive muon events.

3.3 Calorimeter Corrections

The calorimeter corrections are particularly important for physics objects, such as, jets, $\not\!\!E_{\mathrm{T}}$ [3], electrons and photons. Calibration updates to the calorimeter during reprocessing of the inclusive data were applied using the online and offline database from version 4.11.1 of CDF software. The main corrections applied to the inclusive dataset are:

- Calorimeter tower-by-tower gain variations,
- Time dependent gain and energy scale changes.

[3]The missing transverse energy, $\not\!\!E_{\mathrm{T}}$, is the magnitude of the vectorial sum of the 2-D transverse energy vectors of all calorimeter towers. The direction of $\not\!\!E_{\mathrm{T}}$ points in the negative direction of the total transverse energy vector.

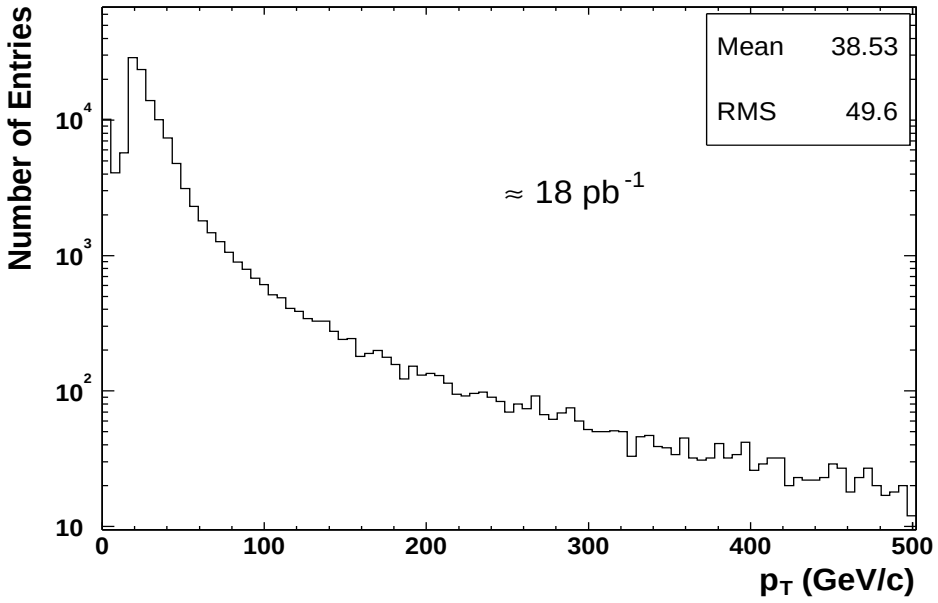

Figure 3.1: p_{T} distribution of muons in the inclusive sample.

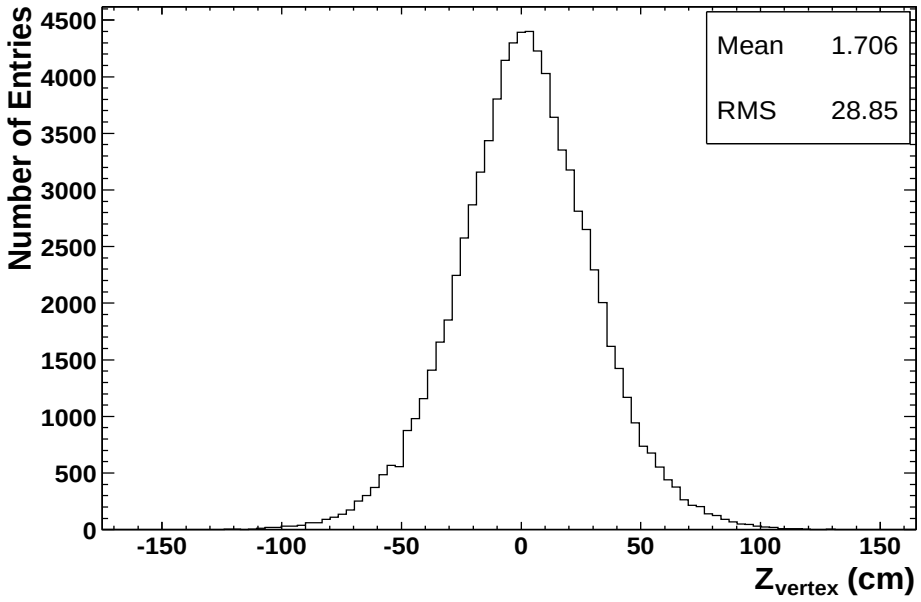

Figure 3.2: Event z vertex profile in the inclusive muon sample.

The calorimeter channel-by-channel gain corrections are kept in the CDF online database as LER's which use information from the laser and source calibration systems. The tower-by-tower calibrations are first obtained by using these online LER's and are further improved upon in offline by using the offline LER's. To obtain the offline corrections for the CEM, E/p of the electrons is used [86]. The gain variations are determined for each tower. The corrections are downloaded to be used online in June 2002. The effect of corrections is a 5% improvement in the energy resolution and a narrower peak in $Z \rightarrow e^+e^-$ invariant mass. The CHA offline LER's were determined using MIP peaks from J/ψ muons and Min-Bias sample [87, 88]. For Plug Calorimeter, a significant drop of gain in PMT's were observed during 2002 and were corrected, mainly, by using laser and source calibrations systems [89].

The energy scale calibrations are stored in the database as the SCL's. For CEM, the energy scale drop versus time is corrected by using the E/p of electrons as a function of run number [88]. The energy scale of CHA is corrected online in September 2002 when it was found to be 4% lower than in Run I using MIP peaks from J/ψ muons [87] and has been stable as a function of time. An outline of the offline calibration of the calorimeter can be found in [90].

3.4 Luminosity Measurement

The total integrated luminosity, $\mathcal{L}$, of $p\bar{p}$ collisions is determined by the rate of inelastic $p\bar{p}$ interactions, via the expression:

$$L = \frac{\mathrm{R}_{in}}{\epsilon_{CLC} \cdot \sigma_{in}} \quad , \tag{3.1}$$

where R_{in} is the rate of $p\bar{p}$ inelastic collisions measured with the CLC detector, ϵ_{CLC} is the CLC acceptance and σ_{in} is the inelastic cross section at 1.96 TeV. The inelastic cross section of 60.7 $\pm$ 2.4 mb is the average of the CDF and E811 Run I measurements scaled by 2.4% to account for the increase in center-of-mass energy of Run II [91, 92].

The CLC acceptance is calculated using data and simulation information from CLC and the Plug calorimeter using the formula:

$$\epsilon_{\mathrm{CLC}} = \frac{\mathrm{N(CLC\ E-W\ coincidence)}}{\mathrm{N(CLC\ +Plug\ tagged\ inelastic)}} \cdot \frac{\mathrm{N(CLC\ +Plug\ tagged\ inelastic)}}{\mathrm{N(inelastic)}} \quad , \tag{3.2}$$

where N(CLC + Plug tagged inelastic) is the number of inelastic events tagged simultaneously by the CLC and Plug calorimeter and N(CLC E-W coincidence) is a subset of those events which pass a certain set of online selection criteria using the two outer layers of CLC detector. The first multiplier in Equation 3.2 is measured

from data using Zero-Bias (Bunch-Crossing) trigger dataset and the second one is estimated from simulation by generating hard and diffractive inelastic collisions. The acceptance is estimated to be 60.2 $\pm$2.4% [93].

The total uncertainty in the CDF II luminosity calculation is 6%. This number is dominated by the CLC acceptance calculation uncertainty and inelastic cross section uncertainty (each about 4%). Factors like, detector stability, calibration, contamination from beam losses and transfer of luminosity to CDF offline from the raw online measurement, each contribute well less than 2% [93].

3.5 Good Run Requirement

The CDF production farms process every run that has more than 10 nb^{-1} data and is approved to be processed by the shift crew taking the data. Information about the quality of the data from the DAQ and detector systems is stored for each run in the CDF database. Selecting a "good" quality for a given set of detectors determines which runs are selected for subsequent analysis. In this analysis, we use the CDF "good run list" version 4 [94]. This list provides common set of good runs for electrons and muons. We use the "no-si" list which ignores the status of silicon good run bits. The criteria applied are listed below:

- More than 10 nb^{-1} data

- Run and trigger type: Physics, beam (no tests allowed)
- CDF Control Room online criteria passed (core detector, luminosity counter and trigger components are good for data analysis)
- Offline validation criteria for detector high p_{T} lepton detector components (CAL, COT, CMU, CMP and CMX) are satisfied.

The good run dataset spans the period from March 23rd, 2002 to September 6th, 2003 including runs in the range 141554-168889. We calculate the integrated luminosity to be 195.4 $\pm$ 11.7pb^{-1}. For this purpose, we run the official code provided by the luminosity group on the inclusive dataset. We include an additional correction factor of 1.019 to this number which reflects a revision of the inelastic scattering cross section [91]. The total integrated luminosity with this factor is $\mathcal{L} = 199.1 \pm 11.9$ pb^{-1}. The details of the CDF luminosity calculation is given in Section 3.4. For the CMX detector, the good run list is separated into two sections: pre-CMX and post-CMX. The pre-CMX data is before run 150145 where we do not require CMX to be good for analysis. The main reason for this is that the last important trigger hardware fix for CMX took place on August 20th, 2002 (run 150145) and also it took considerable efforts for the CMX detector to make it stable due to its high sensitivity to beam conditions (Appendix E). In this analysis, we use CMX detector information for the post-CMX period which leaves us with $\mathcal{L}_{CMX} = 178.6 \pm 10.7$ pb^{-1}.

Chapter 4

Selection of Dimuon Candidates

Chapter 3 described the inclusive dataset filtered with loose clean-up requirements. The following sections describe the selection of the final event sample using tighter muon identification and additional analysis requirements. The aim of the analysis is to impose requirements loose enough to leave smaller room for biases in the final sample as well as increase the sensitivity to observe new physics.

4.1 Selection Requirements

We follow a cut-based analysis for the selection of the high mass dimuon events. We impose the cuts as listed in Table 4.1 to find clean high p_{T} muon pairs from $\mathrm{p\bar{p}}$ collisions and to reject possible backgrounds, while aiming to maintain high efficiency

for our searches. For the triggered muons, we use the full central muon detector which is composed of three parts: CMU, CMP and CMX. The second leg of the pair can be a track (TRK) which is required to be minimum ionizing (MIP) track, isolated in the calorimeter, at the analysis level. All muons selected in this analysis are within the CDFMuon collection which were reconstructed as muons. For this analysis, therefore, a dimuon event can consist of five combinations of dimuons:

- **CMUP-CMUP**: A muon pair in which both muons pass the selection criteria for a CMUP muon.
- **CMX-CMX**: A muon pair in which both muons pass the selection criteria for a CMX muon. A CMX muon is a muon which has a CMX stub in it and has passed the COT exit radius cut (>140 cm).
- **CMUP-CMX**: A muon pair in which one muon passes CMUP and the other one passes CMX muon selection cuts.
- **CMUP(CMX)-TRK**: A muon pair in which one muon passes CMUP(CMX) cuts and the other is neither a CMUP nor CMX muon.

Inclusion of CMX and TRK types of muons in the selection increased the dimuon event yield by about a factor of two as compared to the Run I analysis [33]. This is discussed in more detail in Chapter 6.

There are overlaps with CMX and CMU and CMX and BMU detectors, but we ignore any stub information for the CMX muon other than the CMX stub (i.e., any muon labeled as a combination of CMX and BMU stubs is considered a CMX muon if it passes the selection requirements). This allows to use the full fiducial region of CMX detector. There is no physical overlap between CMUP and CMX detectors, so the two categories are expected to be completely decoupled for high p_{T} muons. The muon stub information from the CMX "miniskirt" and "keystone" and CMP "bluebeam" sections are also ignored. These detectors have not been fully operational due to the beam conditions and readout and trigger problems. The BMU stub information for any reconstructed BMU muon is also neglected and only the TRK selection requirements are applied. The reason that the BMU muons are not used in this analysis is that the BMU trigger commissioning and data monitoring has not been in place for a portion of the data that is used. The CMX acceptance extends outside of XFT region [62]. This is the reason why an exit radius cut of $>$140 cm is placed for a CMX muon. The exit radius value has been chosen to assure the CMX muon passes through all the axial superlayers of the COT, which is the requirement that exist at the L1 trigger level.

The analysis imposes selection requirement on the following criteria:

- Trigger

- Muon ID and Isolation
  - Muon Track-Stub Matching
  - MIP Energy
  - Calorimeter Isolation
- Vertex Fiduciality and Proximity
- Cosmic Ray Rejection

4.1.1 Trigger Requirements

The trigger path for the analysis sample has been described in Section 3.1. All three levels of online trigger conditions are required to be satisfied in an event, for the event to be considered a dimuon candidate. This also helps to reject events which can come from the "MUON_CMUP18_VOLUNTEER_*", which is included in the same inclusive dataset. This trigger path does not have the L1 and L2 criteria applied to the CMUP muon.

The muon tracks are required to have transverse momentum, $p_{\mathrm{T}} > 20$ GeV/c. The transverse momentum of a track is the momentum as measured in the tracking volume in the $x - y$ plane of the CDF coordinate system. In this analysis, COT chambers are used to measure p_{T} of the muon tracks. The tracks are constrained

Cut Variable	Purpose	Type	Condition
L1, L2 & L3	high p_{T} trigger	trigger	CMUP or CMX bits on
p_{T}	high p_{T} muon	trigger,kinematic	$>$ 20 GeV/c (BC, corrected COT-only)
Δ_x(CMU) (CMUP)	track-stub match (r-ϕ)	ID	$<$ 3 cm
Δ_x(CMP) (CMUP)	track-stub match (r-ϕ)	ID	$<$ 5 cm
Δ_x(CMX) (CMX)	track-stub match (r-ϕ)	ID	$<$ 6 cm
$\mathrm{E_{EM}}$ (sliding)	MIP	ID	$<$ max(2, 2+0.0115$\times$(p-100)) GeV
$\mathrm{E_{HAD}}$ (sliding)	MIP	ID	$<$ max(6, 6+0.0280$\times$(p-100)) GeV
$z_{0,\mu}$	vertex fiduciality	fiduciality	$<$ 60 cm
Δ_z	vertex proximity	background veto	$<$ 6 cm
dicosmic bit	cosmic ray	background veto	off
$\mathrm{d_{0,}}_{corrected}$	cosmic ray	background veto	$<$ 0.02 (0.20) cm, SVX (COT-only)
$\mathrm{I_{0.4}}$, fractional	QCD	background veto	$<$ 0.1$\times p_{\mathrm{T}}$

Table 4.1: Selection requirements applied to the data.

to the beam spot as measured with COT detector. This allows for a more accurate measurement of track curvature. The track momentum is further corrected for ϕ dependent curvature after the beam-constraining (BC) applying the formula below [95]:

$$\frac{q}{p_{\mathrm{T}}(corr)} = \frac{q}{p_{\mathrm{T}}(uncorr)} - 0.00037 - 0.00110 \times \sin\left(\phi + 0.28\right) \quad , \tag{4.1}$$

where q is the charge of the track. The curvature correction enhances the invariant mass resolution (RMS) at the Z-peak. This is illustrated in Figure 4.1. The figure shows only a portion of the dimuon data and is for the CMUP-CMUP type of events. For this case, the core Gaussian width reduces from 4.6 GeV/c^2 to 2.5 GeV/c^2 (labeled as $p2$ in the plots). Similar investigations are described in detail in [96]. The track impact parameter, d_0, is also corrected for the beam spot before applying the selection cut on this variable, for background rejection. For this parameter, we use silicon hit information of the track, if available.

4.1.2 Muon ID and Isolation

The muon identification and isolation requirements are the basis of every analysis using muons at CDF. Each analysis may require a different set of requirements on the common muon variables. This is because many are a function of the interaction of

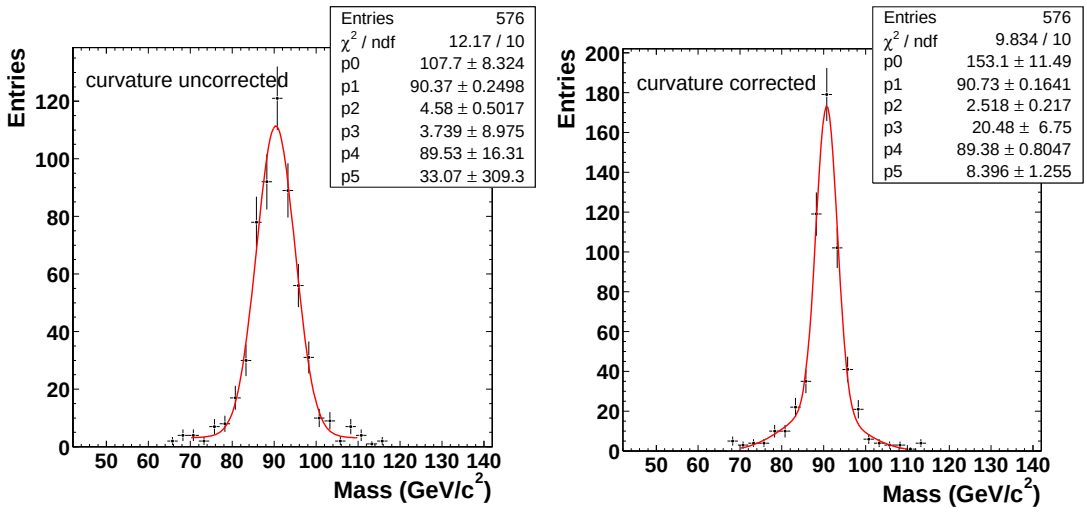

Figure 4.1: Curvature correction effects in dimuon data. The left (right) plot shows invariant mass spectra without (with) curvature corrections.

the muons with the CDF detector as a function of its momentum. As the momentum increases, the mean energy deposition in the EM and HAD calorimeters increases linearly with momentum. At high energies, the dominating processes for energy loss of muons are e^+e^- pair production and bremsstrahlung processes, whereas, at low energies, ionization dE/dx dominates [97]. Therefore, the MIP requirements in CDF calorimeters listed in Table 4.1 are parametrized and optimized in CDF Run I and using CCFR experiment's results [98], [99]. These cuts, also referred to as "sliding cuts", are designed to have a constant efficiency for the muons as a function of momentum and have been determined by using a GEANT [100] simulation modeling

of the CDF I detector [1]. For a muon with p = 200 GeV/c, the maximum energy that a muon can deposit in a CDF hadron calorimeter is 8.8 GeV and in an EM calorimeter is 3.15 GeV. This was shown to be tight enough a requirement to keep the fake background to negligible levels [76].

A charged particle passing through a medium will be deflected by multiple Coulomb scattering. The projection angle while traversing the medium has a width (deflection) inversely proportional to the momentum and directly proportional to the charge of the particle [34]. Therefore, muons with low p_{T} are deflected my multiple scattering in the EM and HAD calorimeters and the deflection in $r-\phi$ plane can be calculated using first principles as a function of p_{T} and $\sin\theta$ [101]. In this analysis, high p_{T} muons are used where the track-stub matching in the $r-\phi$ plane has a better resolution (see Figure A.9, for example). Therefore, p_{T} independent requirements are applied to the Δx variable as listed in Table 4.1.

Prompt muons from the decays of resonances are very isolated. However, the isolation of a muon is dependent on the energy of a muon, which may radiate more in the calorimeter (or in the tracker, for that matter.). The isolation requirement applied to the muons in this analysis is a fractional function of p_{T} of the muon. The main purpose of the isolation requirement is to eliminate fakes from QCD multijet

[1] The total selection efficiency as dimuon mass is illustrated with spin-0,-1,-2 particles Figures 6.6,6.11 and 6.16.

events to the best extent.

4.1.3 Vertex Fiduciality and Proximity

The interaction vertex fiduciality is satisfied by requiring both muons in the event to have the z_0 of their tracks to be within ± 60 cm from the center of the CDF detector. This requirement on the vertex is necessary for keeping the interaction in the luminous region of $p\bar{p}$ collisions [2] as well as constraining it within the fiduciality of the good tracking volume. The requirement automatically helps veto cosmic ray events for which the vertex can be at larger z values at much higher rates than that of a collision event vertex. The z_0 distribution of typical cosmic ray muons is shown in Figure A.1.

The $|\Delta_z| < 6$ cm requirement is applied to the event once a muon pair is found. The value of 6 cm is satisfies that the selection requirement is more than 4σ away from the mean of the wider Gaussian distribution, shown in Figure 4.6. This requirement helps ensure the the muons are close to each other along the beamline as expected from prompt production as a result of a resonant particle decay. It also rejects backgrounds and fakes that can be produced by the processes below:

- The number of multiple interactions increases as the luminosity increases [3].

[2] This is described in more detail when selection efficiencies are discussed

[3] This is one of the reasons that this analysis has a tighter requirement on Δ_z as compared to the value in Run I [33], which was 10 cm.

The chance of associating particles coming out of different vertices to each other as the dimuon pair, therefore, increases.

- Cosmic rays overlap with physics collisions yielding multiple muons/vertices.
- High p_{T} particles, that can be muons or misidentified as muons, may scatter along the beam line as part of the beam losses and may be selected as a second muon in an event.

Figure 4.2 shows such an event observed in CDF data. Both muons in this event pass the selection cuts, however, they fail the vertex proximity requirement. A scan of such events shows that many of such events are selected mainly through the L1 trigger which requires two tracks that have a large opening angle in ϕ.

4.1.4 Cosmic Ray Rejection

As mentioned in Chapter 3, the inclusive high p_{T} sample is heavily dominated by muons from cosmic ray events. The cosmic ray events tend to be isolated and pass the muon ID cuts most of the time [4]. Therefore, we have to apply cosmic ray rejection requirements to the dimuon data sample. In this analysis, we use the "dicosmic" tagger which uses a COT timing algorithm present in the CosmicRayTagger (CRT) module of the CDF analysis software [102]. The dicosmic tagger uses the timing

[4] A dedicated study of properties of cosmic ray muons as detected in the CDF detector is given in Section A.

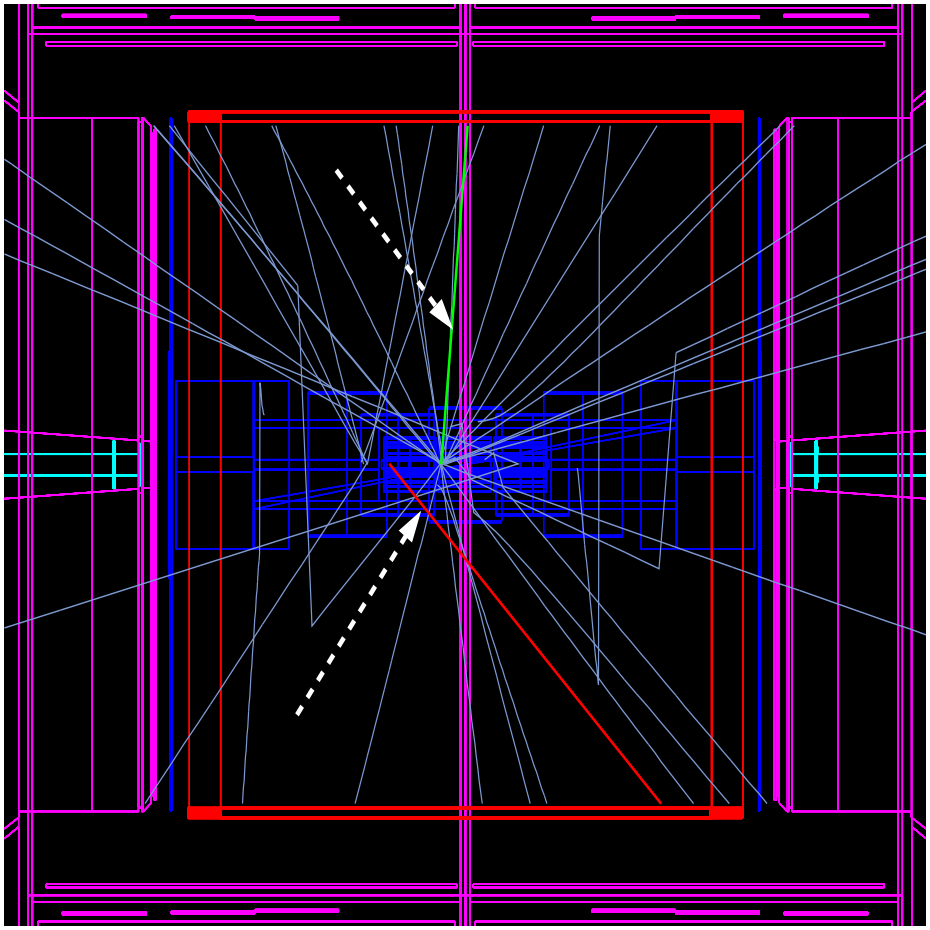

Figure 4.2: Event display showing two muon candidates with large z_0 separation. Arrows point to the two muon candidates in the event.

information of the individual COT hits on the muon tracks to test if the tracks are consistent with coming from the collision point or passing through the CDF detector. The dicosmic tagging follows the algorithm outlined below [103]:

- Start with an input track from the reconstructed CDFTrack collection and call this as the "seed track". Identify the hits associated with this seed track by performing a hit search in a narrow road defined by the track trajectory.

- Refit hits of the seed track with a 6-parameter helix [5] including a floating track t_0, assuming β is +1 or -1. t_0 is the global time shift of all hits and β determines the relative time shifts due to time-of-flight.

- Based on the best fit values, determined by the χ^2/N_{dof}, for the two β options, assign an "incoming" or "outgoing" hypothesis to the track.

- Using the refitted seed track, search for COT hits in the opposite direction to be associated with the second leg of the cosmic ray. If enough hits are found on the other side of COT to make a track, the track is fit similar to the seed track and the track is called the "opposite" track.

- Label the opposite track as incoming or outgoing determined by the fit, similar to the seed track.

[5] The helix parameters are: $\cot\theta$, curvature, z_0, ϕ_0, d_0 and t_0 of the track.

- If both legs are successfully found, perform a simultaneous fit to both sets of hits to a single 6-parameter helix. This final fit is called the "dicosmic" track and the dicosmic fit is repeated for each four combinations of directions of the two legs. The fit with the best hypothesis is selected for the final result of the tagger.

Collision muons have both outgoing tracks from the collision point and should fail to be tagged, if the fits are good. To make the fits better, hits that are more than 0.9 mm away are excluded before refitting [103].

4.2 Candidate Events

After the application of the selection cuts to the inclusive muon data sample, 7775 events remain with 6491 being in Z-peak region ([80-100] GeV/c^2). The total luminosity for the candidates corresponds to approximately 200 pb^{-1}, whereas, the luminosity for candidates that contains a CMX muon is approximately 179 pb^{-1}. The breakdown of the yields with respect to the five dimuon categories are given in Figure 4.3 and the sum of all dimuon candidates in the data sample is shown in Figure 4.4. The data is dominated by the CMUP-TRK muon pairs. The smallest contribution comes from the CMX-CMX category. The yields are cross-checked by using the Z-peak region in Section 5.5. Figure 4.5 shows the $r-\phi$ and $r-z$ views of a

Run/Event	Event Type	$p_T(\mu_1, \mu_2)$ (GeV/c)	$\Delta\phi(\mu_1, \mu_2)$	M (GeV/c^2)
167551/5335217	CMUP/TRK	522.4, 96.6	3.11	500.8
151843/2021616	CMUP/TRK	218.5, 124.3	2.87	346.8
167715/1881653	CMUP/TRK	159.5, 178.6	3.14	337.9

Table 4.2: List of kinematic information for the three highest mass events.

high mass dimuon event where one muon is reconstructed in CMUP detector and the other is in CMX, with both detectors passing the online trigger requirements. The (corrected) transverse momenta of the muons in this event are 104 and 89 GeV/c, and the dimuon invariant mass is 203 GeV/c^2. Table 4.2 lists some characteristic quantities for the highest three events we observe in the dimuon candidates.

4.3 Selection Efficiencies

In Section 4.1, the new resonance search selection criteria applied to the high p_T muon sample is described. To search for a signal, the detection efficiency has to be estimated. The best way to estimate any efficiency is by using data rather than simulation. Therefore, to estimate the efficiencies, muon candidates for particles like Z and W boson, which serve as more background free samples, are used, wherever possible. The following sections outline the procedure and results of the efficiency estimates.

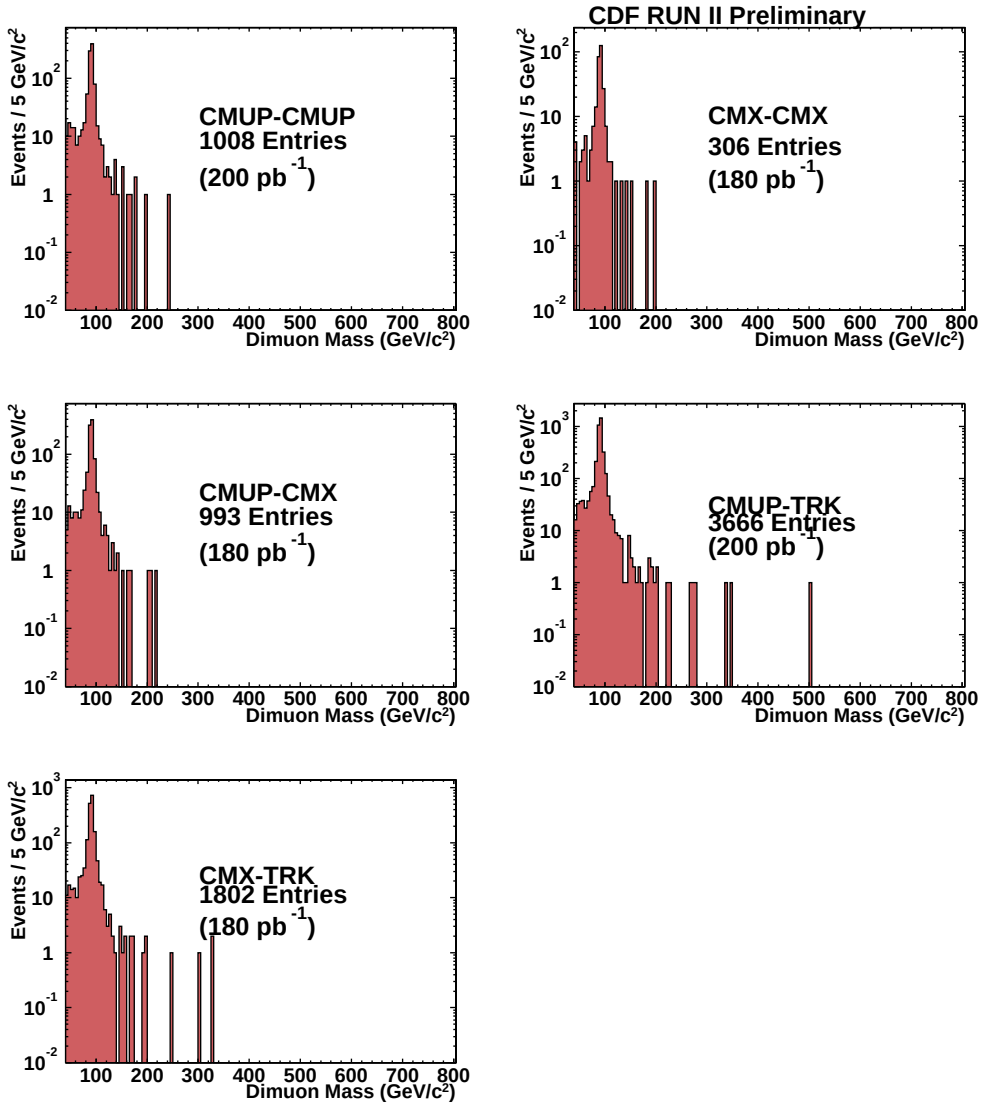

Figure 4.3: Invariant mass distribution for the subcategories of dimuon candidates after the selection cuts applied. The plot is in logarithmic scale in $y-$axis.

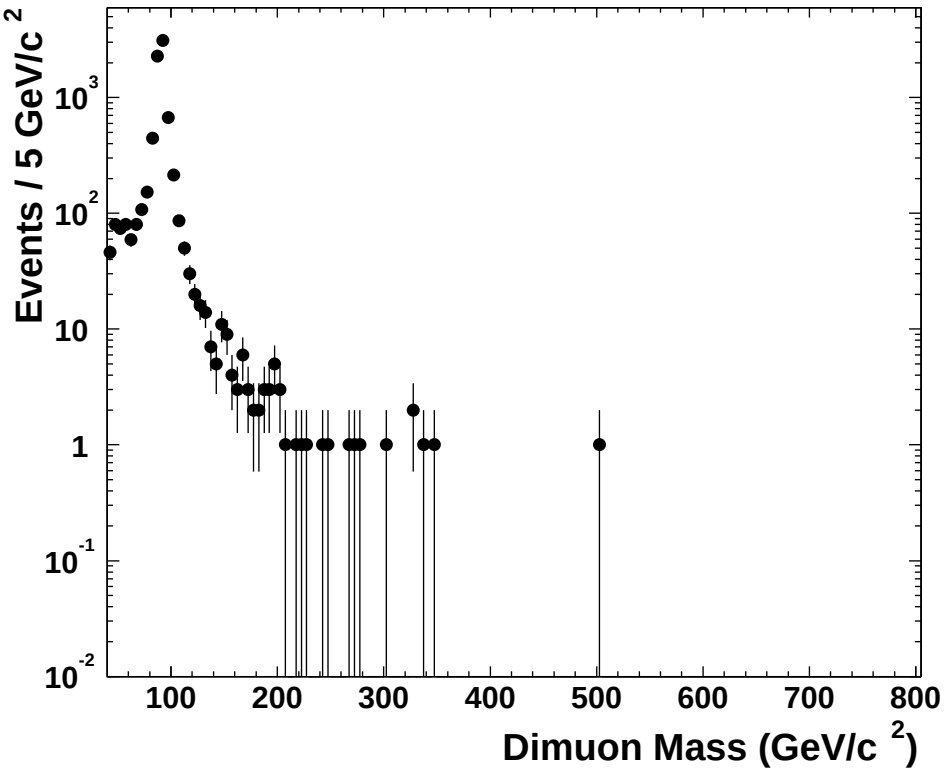

Figure 4.4: Invariant mass distribution for the dimuon candidates after the selection cuts applied.

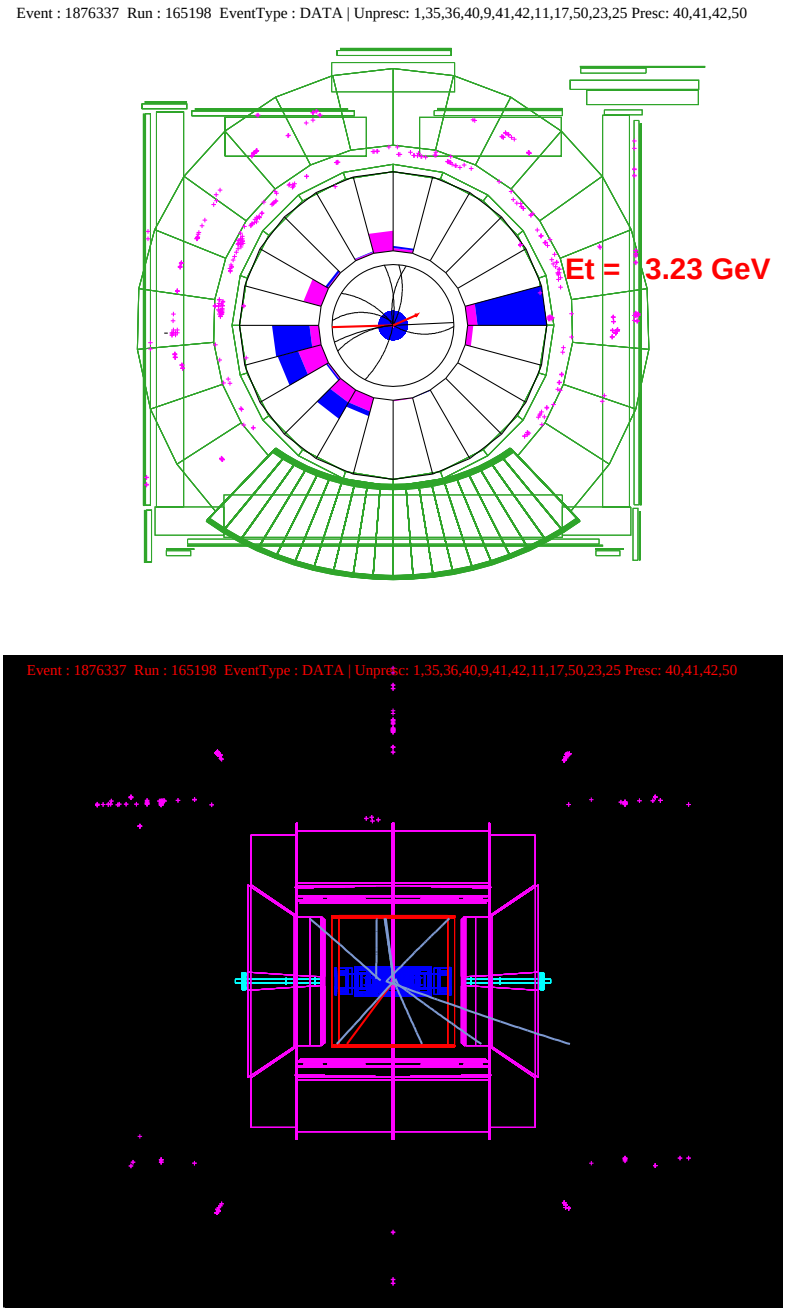

Figure 4.5: Event displays for a high mass $\mu^+\mu^-$ event.

4.3.1 Trigger Efficiency

We calculate the trigger efficiency values for the CMUP and CMX muons using the dimuon candidates that fall in the Z-mass window ([80-100] GeV/c^2). There are two methods that can be used for calculating the efficiencies:

- Method 1: Count the number of existing CMUP (CMX) triggered legs in CMX (CMUP) triggered CMX-CMUP events.
- Method 2: Use the same type (CMX-CMX or CMUP-CMUP) Z candidate events.

We apply the first method and follow the procedure as described in Section 4.3.3.1. We obtain an overall $\epsilon_{trig,CMUP}$ to be 88.4 $\pm$ 1.1% and $\epsilon_{trig,CMX}$ to be 96.9 $\pm$ 0.6%, integrated over the 200 pb^{-1} data. The values listed here are the combined L1$\times$L2$\times$L3 trigger efficiency. The inefficiencies are driven by the L1 triggers from the track trigger (XFT) requirements (Section 3.1). The L2 trigger is fully efficient for CMX muons (no requirements applied) or negligible inefficiency is expected for CMUP muons (8 GeV/c $p_{\rm T}$ requirement). The L3 trigger efficiency is measured to be 99.4 $\pm$ 0.3% for CMUP muons and to be 99.2$\pm$ 0.3% for CMX muons [104].

The trigger efficiency has had slight time dependencies during the data taking. The changes that took place are outlined in Section 3.1. For example, a comparison of CMUP trigger efficiencies after the L1 XFT configuration change in October 2002

with a sample taken before December 2003 showed that the efficiency dropped from 90.0 ±2.3% to 86.7 ± 3.6% [105], although the two values are consistent within the Binomial errors. As again mentioned earlier, the CMX L1 trigger was included a CSX hit requirement in October 2002 as well. The CDF Run I CSX tag efficiency for CMX muons were about 85%, which required coincidence of the two sandwich layers. Dropping the coincidence requirement in Run II, the CSX triggers are expected to be about 99% efficient [62]. This is also checked by using a subsample of the CMUP-CMX Z muons by counting which CMX muon pass the CSX requirement that already passed the other trigger requirements. The efficiency is found to be ϵ_{CSX}=99.3 ±0.5% [106].

4.3.2 Muon ID and Isolation Efficiencies

The efficiency of identifying a high p_{T} isolated muon is calculated using the method described in Section 4.3.3.1. The efficiency for each requirement is also calculated for each muon variable as well as the total ID and isolation efficiencies. The results are listed in Table 4.3, for CMUP, CMX and TRK type muons. The largest contribution to the inefficiency in ID requirements is from the transverse track-stub matching of the CMUP muons. The results from data is compared with Drell-Yan simulation in the following section.

SAME TYPE	**CMUP**		**CMX**	
	Efficiency	Error	Efficiency	Error
HAD energy	0.984	0.003	0.980	0.006
EM energy	0.969	0.004	0.979	0.006
Δx match	0.932	0.006	0.973	0.007
ϵ_{ID}	0.889	0.008	0.933	0.011
ϵ_{Iso}	0.989	0.003	0.980	0.006

MIXED TYPE	**CMUP**		**CMX**		**TRK**	
	Efficiency	Error	Efficiency	Error	Efficiency	Error
HAD energy	0.986	0.002	0.983	0.002	0.983	0.002
EM energy	0.978	0.002	0.983	0.002	0.975	0.002
Δx match	0.947	0.004	0.985	0.002	1.000	0.000
ϵ_{ID}	0.892	0.005	0.932	0.004	0.959	0.003
ϵ_{Iso}	0.976	0.003	0.980	0.002	0.979	0.002

Combined ϵ_{ID}	0.892	0.005	0.932	0.004
Combined ϵ_{Iso}	0.983	0.002	0.980	0.003

Table 4.3: Muon ID and isolation efficiencies.

4.3.3 Method for Calculating Efficiencies

This section describes the method to calculate the muon ID and isolation efficiencies. We follow two approaches: one is the canonical approach in which a minimum of one muon is required to pass all the muon selection cuts in an event and another muon that passes the cut(s) in question is searched for. This method, which we call "1-leg" or "tight-loose" method, allows for a better sample isolation from possible fakes. The results of this method are used in the final calculations of the analysis. The second method is to test the cuts on both of the muons which could be considered as an "event" or a "2-leg" cut. To have the most background free sample, we require the invariant mass of the dimuons to be within [80-100] GeV/c^2 window in both cases. We also apply the cosmic ray rejection cuts and common event selection cuts to further clean the sample. We do not make a charge sign requirement for the muons.

4.3.3.1 "1-leg based" Method

This method uses same type (CMUP-CMUP or CMX-CMX) and mixed type (CMUP-(CMX/TRK) and CMX-(CMUP/TRK)) events to estimate the muon ID and isolation efficiencies. Starting with a base sample of events (R_{tot}) to which neither the muon ID nor isolation cuts are applied, the existence of a muon which passes all the individual ID and isolation cuts (a total of "i" many of them) is required. This muon

is called a "tight" (T) muon and will be the first leg of the Z dimuons. Then, we apply the cuts to the other Z leg candidate and see whether it passes the cuts or not. By convention, we call this test muon "Loose" (L). When we look at the same–type events. we will have both T and L muon of the same type, whereas, mixed type means using the opposite type of muon of the Z candidate is always tight. We define the event yield of when all cuts applied are passed by the muon as R_0. This set consists of TT events ($R_0 \equiv$ TT), so it is related to R_{tot} via the following equation:

$$R_0 \;=\; \prod_i \epsilon_i{}^2 \cdot R_{tot} \quad . \tag{4.2}$$

The different event yields are defined as R_i for each one of the cuts, which we compare to R_0. R_i is a superset of R_0, since it is obtained by applying all the other cuts to R_{tot} except the i'th cut. This set can consist of all T and L combinations for cut i ($R_i \equiv$ TT+TL+LT), so it has a different relation with R_{tot}:

$$R_i = \epsilon_i \cdot (2 - \epsilon_i) \cdot \prod_j \epsilon_j{}^2 \cdot R_{tot} \;, \quad (j \neq i) \quad , \tag{4.3}$$

where we have taken into account possible T and L combinations [6].

[6] The total probability of such combinations are given by $\epsilon_i^2 + \epsilon_i \cdot (1 - \epsilon_i) + (1 - \epsilon_i) \cdot \epsilon_i$. Simple manipulation yields the factor in Equation 4.3.

Using the ratio R_0/R_i, one can solve for the individual efficiencies:

$$\epsilon_i = \frac{2 \times R}{1 + R} \quad , \tag{4.4}$$

where $R \equiv R_0/R_i$. We calculate the errors on each efficiency by using the relation given below:

$$\sigma_\epsilon{}^2 = \left(\frac{\delta\epsilon}{\delta R}\right)^2 \cdot \sigma_R{}^2 \quad . \tag{4.5}$$

In reality, R is a function of TT and TL types of events, so we can write ϵ_i as below:

$$\epsilon_i = \frac{2 \times TT}{2 \times TT + \widetilde{TL}} \quad , \tag{4.6}$$

where $\widetilde{TL}$ represents both the TL and LT types. This equality is obtained by substituting the definition of R_0 and R_i in Equation 4.4. Therefore, we can obtain σ_ϵ using Equations 4.5 and 4.6, which becomes, written in terms of R:

$$\sigma_\epsilon = \frac{\epsilon \cdot R}{(1 + R)} \sqrt{\frac{(1 - R)}{R_0}} \ . \tag{4.7}$$

We report the final value of muon ID efficiency as obtained from application of all the contributors simultaneously. We cross-check these results against the multiplication of individual efficiencies, which assumes zero or small correlation.

In the case of the mixed category of events, the CMUP (CMX) efficiencies are calculated using:

$$\mathrm{R}_0 = \prod_i \epsilon_i \cdot \mathrm{R}_{\mathrm{tot}} \quad , \tag{4.8}$$

$$\mathrm{R}_i = (\epsilon_i + (1 - \epsilon_i)) \cdot \prod_j \epsilon_j \cdot \mathrm{R}_{\mathrm{tot}} \ , \quad (j \neq i) \tag{4.9}$$

to account for a T and L CMUP (CMX) muon with a T CMX (CMUP) muon. Upon manipulation, one sees that, $\mathrm{R} = \mathrm{R}_0/\mathrm{R}_i = \epsilon_{\mathrm{CMUP}}$ and the individual ID efficiencies can be estimated right away. The errors are equal to the binomial error on R. The calculation of total ID efficiency is as described for the same-type muon category. Lastly, we combine the results from same and mixed type events by treating them as separate measurements and we take into account the errors in the weighing of the measurements accordingly.

4.3.3.2 "2-leg based" Method

This method utilizes the same type muon pairs (CMUP-CMUP) or (CMX-CMX) to calculate the muon ID and isolation efficiencies and requires the two muons to pass the selection criteria at the same time. This means whether both muons pass the ith requirement simultaneously is checked. This gives different event yields (R_i) for each one of the cuts, which we eventually compare with the yield when all cuts are applied (R_0), as is in the 1-leg method case. In the terminology of "tight-loose", this

set would be the TT set, $R_0 = \prod_i \epsilon_i{}^2 \cdot R_{tot}$. The yield for individual cuts is, then, given by:

$$R_i = \prod_j \epsilon_j{}^2 \cdot R_{tot} \ , \quad (j \neq i). \tag{4.10}$$

It is obvious why R_i is independent of ϵ_i; it is measured over all combinations of muons, including LL, thus, the cut efficiency is equal to one. Note that this means, for this method, we start with an initial sample that is less pure and may be more sensitive to fakes. Although, requiring same-type muons with stubs yields a pure enough sample, as compared to stubless muons. A same-sign event subtraction can also be considered to further clean the sample, which is not performed here.

Using the ratio R_0/R_i, one can calculate the efficiencies as listed in Table 4.4. These numbers are obtained using the first 72 pb^{-1} data. The errors on each efficiency is calculated using:

$$\sigma_\epsilon = \frac{1}{2 \times R} \cdot \sigma_R \quad , \tag{4.11}$$

which is derived using Equation 4.5. σ_R is the binomial error on R. The total muon ID efficiency is obtained as in Section 4.3.3.1.

We would like to compare the 1-leg and 2-leg method efficiencies obtained from the same-type events since we would like to test the possible impact from the fakes and calculate the difference of the efficiencies of the two methods ($\delta(\epsilon)$). The comparison has been performed using 72 pb^{-1} data, as described in [105] and listed in

	CMUP		CMX	
	Efficiency	Error	Efficiency	Error
HAD energy	0.982	0.006	0.988	0.008
EM energy	0.977	0.006	0.972	0.012
Δx match	0.932	0.010	0.983	0.010
ID efficiency	0.893	0.013	0.933	0.019
Isolation	0.984	0.005	0.972	0.012

Table 4.4: Efficiencies obtained from the 2-leg method.

Table 4.5. The uncertainty on this quantity (calculated as functions of number of TT, $\widetilde{\text{TL}}$ and LL events following the principles that led to Equation 4.7) is calculated using Mathematica [107]. The identification and isolation efficiency values are also calculated using the $Z/\gamma^* \to \mu^+\mu^-$ MC simulation, for the cross-check. Using the the MC sample described in [105], we obtain the results listed in Table 4.6. We observe that the data and simulation agree well for CMX muons. This is not the case for the CMUP ID efficiency values. The simulation has considerably higher efficiency compared with the data. We have observed that the CMU stub finding is inefficient in data compared with MC which is the main factor for this discrepancy [108]. The $\delta(\epsilon)$ values are an order of magnitude smaller in MC than in data. However, the errors on these values turn out to be also a large fraction of the central values. We do not quote a systematic error on the efficiencies by using the calculated $\delta(\epsilon)$.

	ID efficiency	value	error
CMUP	$\delta(\epsilon)$	0.002	0.003
CMX	$\delta(\epsilon)$	0.002	0.005
	Isolation efficiency	**value**	**error**
CMUP	$\delta(\epsilon)$	0.003	0.002
CMX	$\delta(\epsilon)$	0.005	0.005

Table 4.5: Comparison of the two efficiency calculation methods.

Drell-Yan MC	ID efficiency	value	error
CMUP	2-leg same-type	0.9367	0.0064
	1-leg same-type	0.9361	0.0067
	$\delta(\epsilon)$	0.0007	0.0010
CMX	2-leg same-type	0.9212	0.0115
	1-leg same-type	0.9216	0.0122
	$\delta(\epsilon)$	-0.0004	0.0025
	Isolation efficiency	**value**	**error**
CMUP	2-leg same-type	0.9768	0.0041
	1-leg same-type	0.9765	0.0041
	$\delta(\epsilon)$	0.0003	0.0001
CMX	2-leg same-type	0.9760	0.0068
	1-leg same-type	0.9757	0.0070
	$\delta(\epsilon)$	0.0003	0.0002

Table 4.6: Results from Drell-Yan MC for same-type efficiencies.

4.3.4 Muon Reconstruction Efficiency

The muon reconstruction efficiency is the probability of the CDF muon reconstruction algorithm to create a CDFMuon object given a reconstructed track and the existence of real muon in an event [7]. The efficiency is calculated using $Z \to \mu^+\mu^-$events in approximately 126 pb^{-1} of the analysis sample (March 23, 2002 to May 27, 2003) and Pythia Drell-Yan simulation sample [109]. The first leg of the muon pair from Z decays should be a tight muon satisfying the trigger requirements (CMUP or CMX muon), selected with the same ID cuts as listed in Table 4.1. There are additional requirements on the number of COT hits for the first leg for this calculation to ensure a more background free sample. The second leg is a CDFTrack that satisfies the minimum track requirements in the muon reconstruction algorithm and passes the MIP calorimeter ID cuts as in the first leg to ensure a muon-like object. Cosmic veto and vertex fiduciality cuts are also applied to the candidate events. Events in which any other CDFTrack with $p_{\text{T}} > 10.0$ GeV/c are also vetoed.

The fraction of the second leg tracks passing the above-mentioned cuts that successfully reconstructs as a CDFMuon which linked to a stub as CMUP or CMX to the total number of tracks passing the cuts gives the reconstruction efficiency. This quantity is, in reality, a measure of the product of the CDF offline software reconstruction efficiency and the efficiency for a stub to be found in the muon chambers.

[7] The COT track reconstruction efficiency is a separate quantity which we report in Section 4.3.5.

The single hit efficiency of a muon chamber is, then, embedded implicitly in this quantity. The calculation is performed for opposite charge muon + track candidates within Z-mass window of [80-100] GeV/c^2 to increase the purity of the sample. An earlier version of the calculation also made use of low p_{T} muons found in J/Ψ decays from a semileptonic B sample collected with a muon and an SVT track requirement [110]. The results of the measurement using J/Ψ decays was slightly different from those of the measurement using the Z-boson decays, due to differences between the datasets and a variation of the cut parameters of the different versions of the calculations. From simulation studies, a 0.3% increase in CMX efficiency is also expected to take place, due to January 2003 shutdown chamber fixes which raises the hit-finding efficiency.

Table 4.7 summarizes the efficiencies for CMUP and CMX muons. The efficiencies correspond to a set of muons selected with a set of loose fiducial cuts to ensure the likelihood of enough number of hits to the muon chambers for a stub to be reconstructed [109]. The dependence of the efficiencies on the variation of fiducial requirements is found to be negligible. Much of the inefficiency is due to geometric effects from the chambers. A few rare cases include events where no sufficient number of hits are found in the chamber. The numbers used for the analysis is ϵ_{Reco} that is the Data vs MC simulation scale factor, as outlined in Table 4.8.

	CMUP	CMX
Data (D)	0.820±0.009	0.916±0.010
Simulation (S)	0.884±0.002	0.923±0.003
ϵ_{Reco} (D/S)	0.927±0.010(stat)±0.003(syst)	0.992±0.011(stat)±0.003(syst)

Table 4.7: Muon reconstruction efficiencies.

4.3.5 Track Reconstruction

Reconstruction of a high p_{T} muon candidate in the CDF detector depends on the efficiency of the track reconstruction. The efficiency of track reconstruction is the ability of the tracking algorithm to reconstruct high p_{T} tracks in a clean and unbiased sample of charged particles with high purity. Such a sample is the "W no-track" sample which is collected with triggers that requires only loose calorimeter electron conditions and large $\not\!\!E_{\mathrm{T}}$. The absence of track requirement in the trigger serves to collect an unbiased sample.

The sample used in the efficiency calculation is reconstructed with CDF offline version 4.11.2 and spans October 2002 to September 2003. The electrons candidates from W decays are identified using information from the calorimeter with a set of electron ID cuts. Further requirements are applied using the calorimeter information mainly to reject backgrounds, which can mimic the calorimeter-only signature, but have no reconstructible charged particles pointing to the calorimeter cluster. Examples of such backgrounds are cosmic-rays, beam-related backgrounds, photons and

chargeless pions. In this analysis, muons have COT tracks, therefore, using tracking information from the silicon detector only can be use to further clean the W sample. An $r-\phi$ position match between the silicon stand-alone tracks and the "electron" clusters determines the final candidates. The COT tracking efficiency can then be calculated as the fraction of such candidates which have a COT track pointing to the electron cluster. A COT track in this analysis satisfies hit requirements (COT *defTracks*). The resulting efficiency is $99.29^{+0.07}_{-0.09}\%$ which includes the binomial statistical uncertainty. As the systematic uncertainty, the effect of silicon stand-alone track selection on the fake rate is considered. The final efficiency is $99.29\pm0.11\%$. The details of the selection cuts and algorithms can be found in [111].

Applying the same cuts described above to a MC sample, a scale factor corresponding to the ratio of COT tracking efficiency in the data to the tracking efficiency in the MC simulation. The number we quote is the scale factor for COT tracks, which is $99.6\pm0.3\%$, where the statistical and systematical errors have been combined.

4.3.6 Vertex Fiduciality and Proximity Efficiency

The luminosity reported by CLC detector is over the full luminous region along the beampipe. Imposing a vertex requirement within ±60 cm, limits the event selection and requires an efficiency calculation. The calculation of the efficiency of the vertex

cut, $|z_{0,\mu}| < 60cm$, involves the study of the longitudinal profile of the $p\bar{p}$ luminous region at CDF interaction point and a calculation of acceptance of COT tracks in this region[112]. Minimum bias data are used to measure the longitudinal profile of the $p\bar{p}$ luminous region. The Tevatron beam profile function is used to estimate the fraction of the luminous region at large z [113]:

$$\frac{d\mathcal{L}}{dz} = N_0 \frac{\exp(-z^2/2\sigma_z^2)}{\sqrt{\left[1+(\frac{z-z_{0,1}}{\beta^*})^2\right]\left[1+(\frac{z-z_{0,2}}{\beta^*})^2\right]}} \quad , \tag{4.12}$$

where N_0 is a normalization and $z_{0,1}$ and $z_{0,2}$ are two independent z_0's for the x and y coordinates. The function, in this form, takes into account the Run II measurements of σ_x and σ_y versus z [114].

The z-vertex distribution is obtained by using the primary vertex found in the events with COT tracks in min-bias sample corresponding to about 200 pb^{-1} data of 2002-2003. The COT track acceptance in z is studied by using the cosmic ray data and HERWIG [115] $W \rightarrow e\nu$ simulation. The z-vertex finding efficiency within $|z| < 60cm$ is flat.

For the dataset used in this analysis, $\epsilon_{fid} = 94.8 \pm 0.3\%$, where the error is dominated by the systematic errors estimated by changing the z-ranges used in the beam profile fit.

The vertex proximity efficiency is calculated using the Z-mass window. The

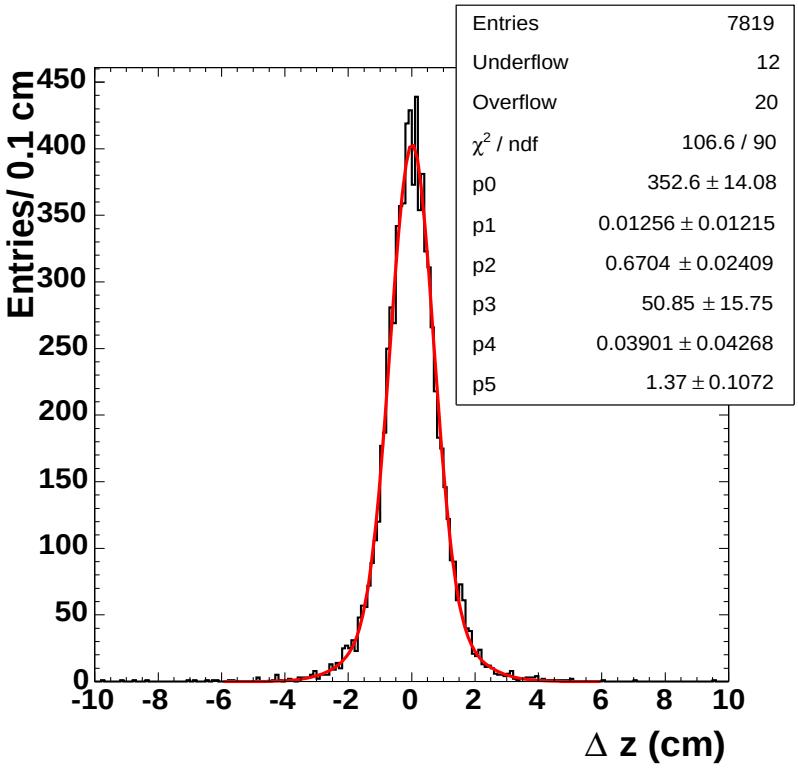

Figure 4.6: Δz distribution of the final muon candidates with no requirement on the Δz variable. The overflow and underflow events are likely to correspond to similar cases given in Figure 4.2.

efficiency obtained is 99.76±0.66%. Figure 4.6 shows the Δz distribution of the final muon candidates, where a requirement on the Δz has not been performed. The distribution is fit to a double Gaussian where the σ values are 0.67 cm and 1.37 cm.

4.3.7 Efficiency of the Cosmic Ray Veto

We use the dicosmic tagger and the impact parameter cut in combination for the cosmic ray efficiency. The efficiency of the dicosmic tagger is reported to be 100 per cent in CDF6457 [116], using the Z boson signal region. We take the impact parameter efficiency as reported in [104] and we use d_0 cut efficiency of TRK type muons as 99.2 $\pm$ 0.6%. We also would like to assign a systematical error to the signal efficiency of the dicosmic tagger. For this, we use the Z boson mass window and count the number of events that are tagged by the dicosmic fit in comparison to those events that are selected as final dimuons. To have a better handle of selecting collision dimuons, we look at events that have number of tracks (p_{T} >1.2 GeV) greater than two since the cosmic rays in general yield only two track events in the high p_{T} muon data. The distributions are shown in Figure 4.7. We obtain a 0.6% error on the dicosmic efficiency by using the ratio of these two distributions.

The optimization of the cosmic ray tagging efficiency and the efficiency of the cosmic ray rejection to keep the signal events from real collisions is an important issue. Various approaches and strategies has been studied in detail. Section A details some of the studies performed. The signal inefficiency (mistag rate) was also studied using samples of Z-boson, Z$'$ and RS graviton both at 500 GeV/c^2. The samples are used to investigate a mass dependence of the dicosmic tagger and a bias

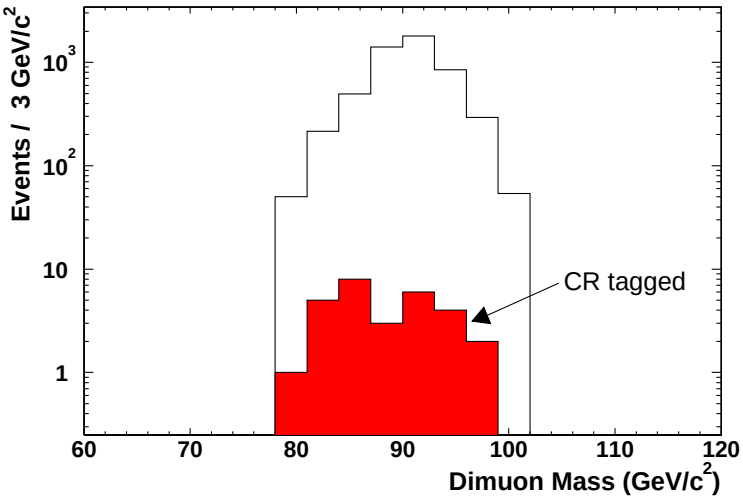

Figure 4.7: Fraction of cosmic events tagged in the Z window as compared to those non-tagged.

between two signal processes. Neither a mass dependence nor a bias was observed. A few cases of mistags were found in the region of forward tracking and are outlined in [96]. The failure level of dicosmic tagger is higher for W decays in muon channel due to the missing second track [102].

4.3.8 Summary of Efficiencies

The selection efficiency for the high p_{T} dimuon sample consists of the combination of the individual selection cuts applied to the data. In Table 4.8, we list the individual efficiency values for the three muon types. The details are outlined under the sections for the individual efficiencies earlier in this chapter. For the TRK ID efficiency,

CDF Run II Preliminary

ϵ (%)	CMUP	CMX	TRK
ϵ_{trig}	88.4 ± 1.1	96.9 ± 0.6	–
ϵ_{CR}	99.6 ± 0.6	99.2 ± 0.6	99.2 ± 0.6
ϵ_{fid}	94.8±0.3		
$\epsilon_{\Delta z}$	99.76±0.66		
ϵ_{track}	99.6±0.3		
ϵ_{ID}	89.2 ± 0.5	93.2 ± 0.4	95.9 ± 0.3
ϵ_{Reco}	92.7 ± 1.0(stat) ± 0.3(syst)	99.2 ± 1.1(stat) ± 0.3(syst)	–
ϵ_{Iso}	98.3 ± 0.2	98.0 ± 0.3	97.9 ± 0.2

Table 4.8: Efficiency summary table for dimuons.

we only consider the efficiencies of the hadronic energy and electromagnetic energy sliding cuts.

To obtain the dimuon selection efficiency, $\epsilon_{\mu\mu}$, five combinations of efficiencies are calculated:

$$\begin{aligned}
\epsilon_{PP} &= (\epsilon^P_{trig} \times (2 - \epsilon^P_{trig})) \times (\epsilon^P_{IDReco})^2 \times \epsilon_{com} \\
\epsilon_{XX} &= (\epsilon^X_{trig} \times (2 - \epsilon^X_{trig})) \times (\epsilon^X_{IDReco})^2 \times \epsilon_{com} \\
\epsilon_{PX} &= (\epsilon^P_{trig} + \epsilon^X_{trig} - \epsilon^X_{trig} \times \epsilon^P_{trig}) \times \epsilon^P_{IDReco} \times \epsilon^X_{IDReco} \times \epsilon_{com} \\
\epsilon_{PT} &= (\epsilon^P_{trig}) \times \epsilon^P_{IDReco} \times \epsilon^T_{ID} \times \epsilon_{com} \\
\epsilon_{XT} &= (\epsilon^X_{trig}) \times \epsilon^X_{IDReco} \times \epsilon^T_{ID} \times \epsilon_{com} \quad , \qquad (4.13)
\end{aligned}$$

CDF Run II Preliminary

ϵ_{PP}= 60.9 ± 1.9%
ϵ_{XX}= 77.1 ± 2.1%
ϵ_{PX}= 68.8 ± 1.7%
ϵ_{PT}= 63.2 ± 1.4%
ϵ_{XT}= 77.5 ± 1.5%

Table 4.9: Dimuon selection efficiencies for five categories.

where we define $\epsilon_{IDReco} \equiv \epsilon_{ID} \times \epsilon_{Reco}$ and $\epsilon_{com} \equiv \epsilon_{CR} \times \epsilon_{fid} \times (\epsilon_{track} \times \epsilon_{Iso})^2 \times \epsilon_{\Delta z}$. The terms for trigger efficiency follows from Section 4.3.3.

Plugging in the numbers from Table 4.8 into Equation 4.13 above, the dimuon selection efficiencies listed in Table 4.9 are obtained. The errors for dimuon efficiencies are obtained using the error propagation method, where the errors listed in Table 4.8 are used in Equation 4.13.

Chapter 5

Background Processes

The search channel in this analysis, which is a final state with two isolated high p_{T} muons ($p_{\mathrm{T}} > 20$ GeV/c), may be produced in known processes. The processes expected to yield dimuons may either directly produce dimuon signatures or mimic one by misidentification or misreconstruction of one or two muons in an event. In order to estimate the new physics (signal) content of the analysis sample, we calculate the contributions from the known processes which are usually referred to be "background" to the signal.

The first category of background processes we consider in this analysis are the dimuon signature of $\mathrm{p\bar{p}}$ collision processes. The second category is the cosmic rays that can penetrate into the CDF detector and that can be misidentified as two muons originating from a collision point. We expected contributions from the below list of

background processes:

- Collision background: Drell-Yan $Z/\gamma^* \to \mu\mu$, DY $Z \to \tau\tau$, WW, WZ, $t\bar{t}$, QCD/Fakes
- Cosmic ray background.

In this chapter, we describe the estimation of the background yields we expect to observe in inclusive dimuon signature and compare it to the observation in CDF II data. The background estimate is further used to determine the final results for the new physics searches.

5.1 Simulation Samples for the Processes

The MC samples for the analysis are generated and simulated based on the official CDF code version 4.9.1. For the detector simulation, a full description of the CDF detector implemented in GEANT [100] simulation package, is used. For a more realistic MC sample, a representative run is selected (run number 151435). This way, a realistic estimate of the beamline alignment and the silicon tracker dead channel information was simulated. The basic beamline parameters used for the background (and signal) simulations is shown below:

The beamline parameter for this run are first obtained from collision data and

beam x = -0.064 cm;
beam y = 0.310 cm;
err x = 0.0025 cm;
err y = 0.0025 cm;
slope x= -0.00021 rad;
slope y= 0.00031 rad;

then corrected to account for the total shift of silicon detector with respect to the beamline which did not exist in simulation.

Due to the composite structure of protons and antiprotons and high luminosity environment of an hadron collider, the hard scattering processes of initial partons are usually accompanied by an underlying structure. The events may include initial and final state radiation, beam-beam interaction remnants and multiple parton interactions. Such effects are often referred to as the "underlying event". A set of parameters in Pythia event generator have been tuned to describe both minimum-bias interactions and the underlying event in hard scattering processes in $p\bar{p}$ collisions with a better match to the observed data [117]. This set of tunes (called "Tune A") have been used uniformly for all MC simulations for CDF analyses. More information on the underlying event studies can be found in [118].

5.2 Collision Backgrounds

We can categorize the collision backgrounds as coming from direct production of muons in electroweak (EWK) processes and from misidentified objects (fakes) dominated by QCD processes.

5.2.1 Standard Model Background

To estimate the expected number of events from EWK processes, we use MC simulation. The main collision background comes from the irreducible DY Z $/\gamma^* \rightarrow \mu\mu$ channel. The list of processes is summarized in Table 5.1. Figure 5.1 shows the invariant mass distributions for dimuon events from non-DY collision backgrounds. Most of these backgrounds have very small contributions to the expected mass spectrum, especially at high mass. The backgrounds taken into account can be listed as:

- DY Z/γ^* production: For the DY Z/$\gamma^* \rightarrow \mu^+\mu^-$ MC sample, the CDF 4.9.1 offline version (zewk2m) which include some corrections and tunings in the simulation for better agreement with data. We utilize about 500k events from this sample. This dataset was reproduced in order to correct for some effects that were not modeled well in the earlier versions of the CDF detector simulation. These corrections include underestimated material in the GEANT

description of the CDF detector, which are mostly important for the electron identification. More information can be found in [119].

- $t\bar{t}$ production: The top quark decays are governed by weak interactions through a W boson in SM. The final state particles are thus determined by subsequent W decays. In $t\bar{t}$ production, if both W bosons decay into a second generation lepton family ($W \to \mu\nu$), there are two muons observed in the final state. The total cross section for dimuon production from $t\bar{t}$ process is 0.07 pb, where the $\sqrt{s} = 2.0$ TeV NLO $t\bar{t}$ production cross section prediction of 6.7 pb ([120]) for m_t of 175 GeV/c^2 is multiplied by the square of BR($W \to \mu\nu$) of 10.2% [34]. Only about 5% of the total $t\bar{t}$ events are observed in the dilepton mode.

  For the background estimation, a sample of $t\bar{t}$ production MC simulation is used. The sample is generated using HERWIG 6.4 [115] with the PDF set CTEQ5L.

- heavy diboson (WW, WZ) production: The hadronic production of a heavy diboson pair, $p\bar{p} \to WW$ or $p\bar{p} \to WZ$ and muonic decays of W and Z may yield dimuon final states observable in CDF data. We use the NLO calculated production cross sections to estimate the $\sigma \cdot BR(WW, W \to \mu\nu)$ of 0.14 pb and $\sigma \cdot BR(WZ, Z \to \mu^+\mu^-)$ of 0.07 pb, respectively. The total diboson production cross sections are the average of calculations repeated with two different PDF's

Table 5.1: Collision background processes other than QCD/Fakes.

Process	N_{gen}	σ.BR (pb)	Simulation Comments
DY $Z/\gamma^* \rightarrow \mu^+\mu^-$	500k	250	$M_{\mu^+\mu^-} > 30$ GeV/c^2
DY $Z/\gamma^* \rightarrow \tau^+\tau^-$, $\tau \rightarrow \mu\nu_\mu\nu_\tau$	10k	7.54	$M_{\tau^+\tau^-} > 30$ GeV/c^2
WW, $W \rightarrow \mu\nu$	5k	0.14	
WZ, $Z \rightarrow \mu^+\mu^-$	5k	0.07	W all decay modes on
$t\bar{t}$, both $W \rightarrow \mu\nu$	5k	0.0697	

and are 13.25±0.25 pb (WW) and 1.98±0.03 pb (WZ) [121].

- $\tau\tau$ production: The $Z/\gamma^* \rightarrow \tau^+\tau^-$ will yield muon pairs if both τ leptons decay weakly into leptons. The branching fraction of ($\tau \rightarrow \mu\nu_\mu\nu_\tau$) is 17.37% [34].

  For the background estimation, a sample of Drell-Yan sample decaying into two τ leptons are simulated using Pythia. The decay of τ leptons are simulated with the Tauola package [122]. The invariant mass of the τ pair, $M_{\tau\tau}$, is required to be greater than 30 GeV/c^2.

5.2.2 QCD/Fakes

QCD background usually arises from the misidentification of hadrons as muons due to punch-through and from low p_T muons coming from processes like semi-leptonic decays of a quark or hadron decays in flight, where the momentum of the low p_T muon may be mismeasured in the tracker. For QCD background determination, two methods can be applied: using same-sign dimuon mass spectrum and using calorimeter

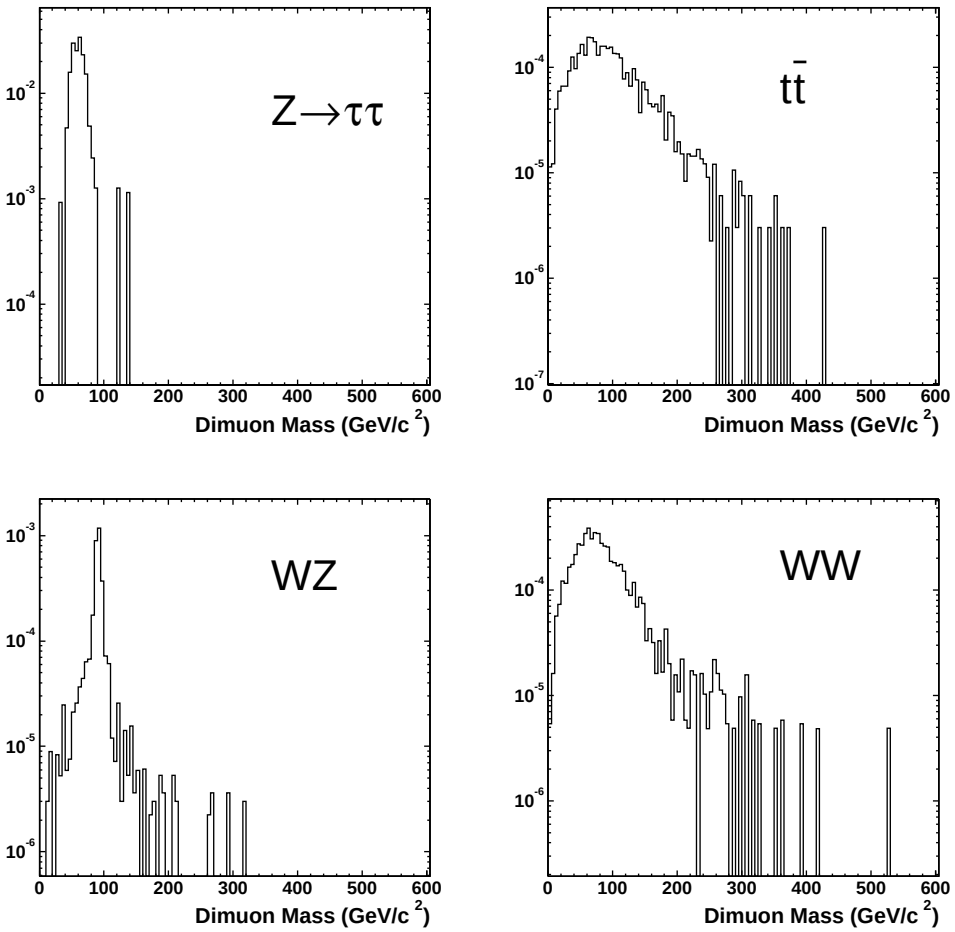

Figure 5.1: Invariant mass distributions for dimuon events from non-DY background.

isolation for the muons. In this analysis, we use the the same sign event hypothesis [1] to get an estimate to our QCD background and use the data for the background contribution estimates instead of MC [2]. The backgrounds from QCD events are charge symmetric, since there is no known reason for these events to be preferentially positive or negative charged. Therefore, the same sign dimuon yield in data is expected to give a good estimate of the total multijet misidentification background. The same-sign dimuons can also arise from charge misidentification of a high p_{T} muon. Simulation studies using 40 GeV/c momentum muons have shown that the misidentification rate is below 10^{-3}.

To estimate the background contamination, we count the number of events which have the same sign muons in the final candidates. To get the shape of the distribution, we use the sample in which we require one tight muon and relax the ID and isolation requirements in the second muon. This gives a higher event yield to which we can fit a function of the form:

$$y = (cst) \times (x - x_0)^{\alpha} \times e^{-\beta(x-x_0)} \quad . \tag{5.1}$$

This function describes both the turn-on of the distribution around 40GeV/c^2 due to muon trigger requirements and the exponential decay of the background as the

[1] Similar approach was used in CDF Run I Drell-Yan cross section measurement [124].
[2] In an earlier version [105] of the analysis, the isolation method was also used as a cross-check.

invariant mass increases. This distribution is normalized to the number of events multiplied by a factor of two, to account for the charge symmetry of the background. The same sign spectrum selected in the dimuon sample is shown in Figure 5.2. In this figure, the darker histogram represents the same-sign events in the final dimuon sample. The fit parameters for Equation 5.1 is also shown on this plot. The fit distribution used in the QCD fakes background estimate is shown in Figure 5.3.

The case of μ+track final state is more prone to contamination from backgrounds that may yield high rate of muon fakes as compared to $\mu + \mu$ case. Hence, we examined some processes like, dijet and W+jet production, using CDF version 4.9.1 ALPGEN+HERWIG [123, 115] MC samples. We also studied the effects of varying requirements on the number of COT track hits in our selection, using these data sets. We have observed that, we obtain only a yield increase in the W+jet sample, which is not related to the background contamination, but is due to an enhancement in CMX detector acceptance.

5.3 Cosmic Ray Background

In Section 4.1.4, we discussed the signal efficiency of the cosmic ray rejection requirements. Here, we estimate the cosmic ray background that remains in the final

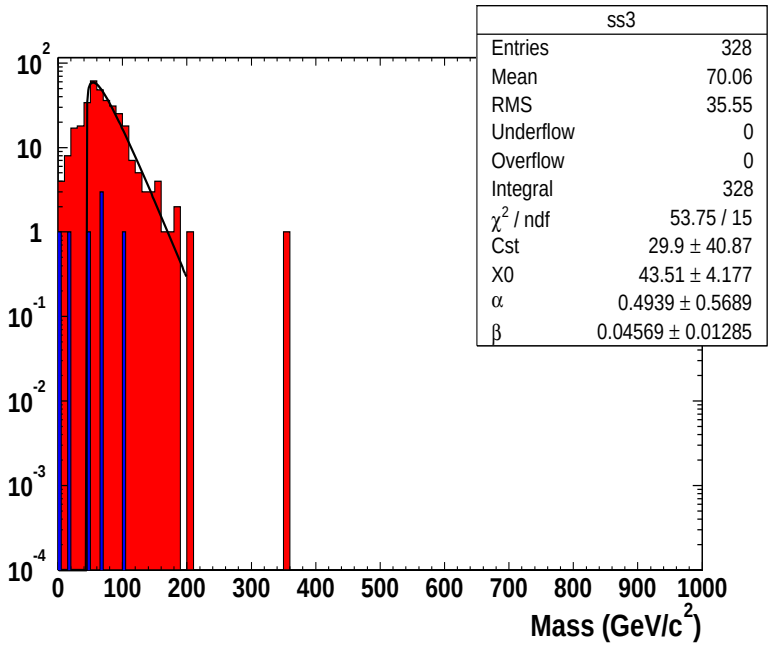

Figure 5.2: Same sign dimuon spectrum in inclusive muon data sample selected by the dimuon cuts.

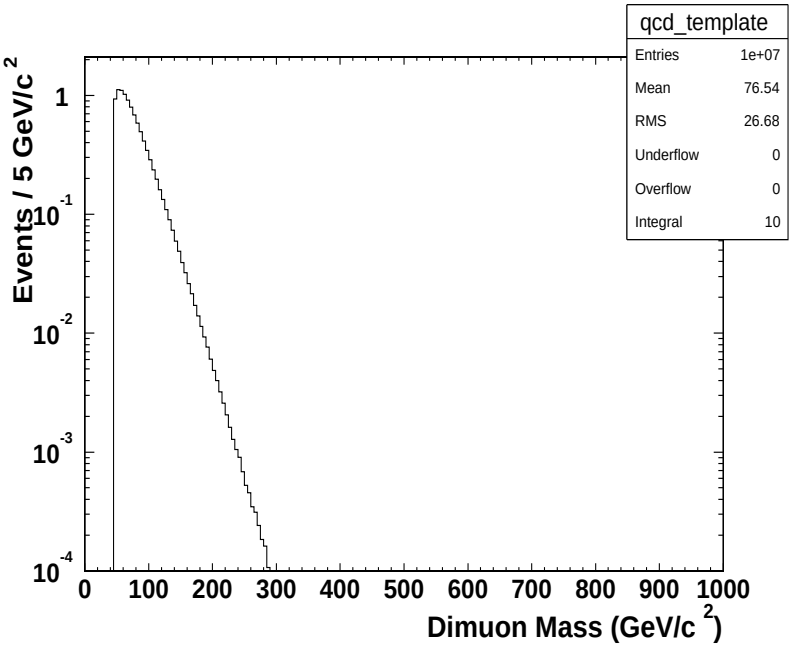

Figure 5.3: Same sign dimuon spectrum used to represent the QCD fakes for this study.

sample, after the requirements applied [3]. We estimate the background contribution as a function of the dimuon invariant mass in our sample. This estimate is used in our cross section limit calculations. We use the dimuon data which is tagged as cosmic rays to describe the shape of our cosmic ray background spectrum. We fit this distribution to double exponentials and plot the distribution used in the calculation in Figure 5.4. To get the normalization, we use the fraction of events that fall in the tail of the d_0 distribution of cosmic ray events to the signal region of the distribution and use this number to calculate the expected background in the selected dimuon sample. Figure 5.5 shows the histogram we used to represent the cosmic background in our sample. We also studied the distribution of events in our final sample that are tagged by the full cosmic ray tagger. The estimate of the background using this distribution, which can be seen in Figure 5.6, gives us comparable results in the high mass region (see Table 5.2, for example). [4].

5.4 Comparison of Expected Background with Data

We compare our data with the expected background contributions from known processes. To calculate the expected number of background events, we first add up

[3] The vetoing power of the cosmic ray tagger is studied on cosmic ray data in detail in Appendix A.

[4] In an earlier version of the analysis, we used a combination of minbias and real cosmic ray data to estimate the cosmic ray background [105].

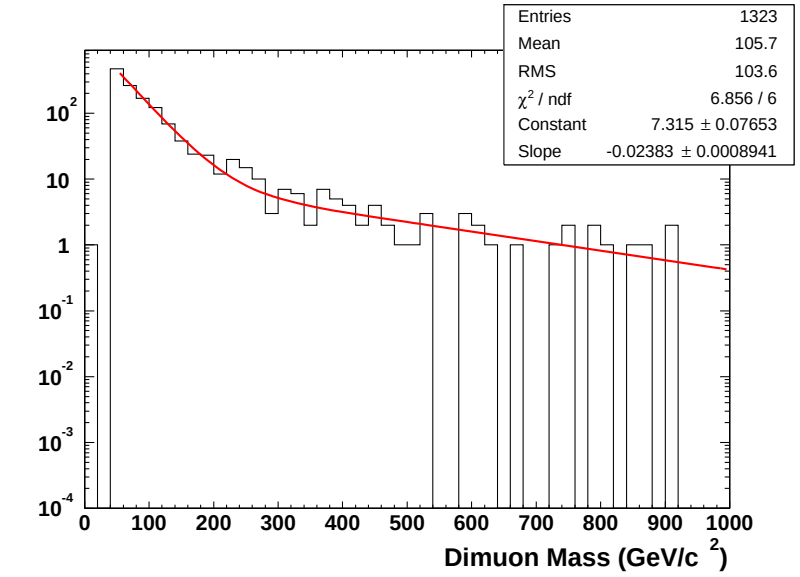

Figure 5.4: Invariant mass of the cosmic ray muons used in determining the cosmic ray background for this study.

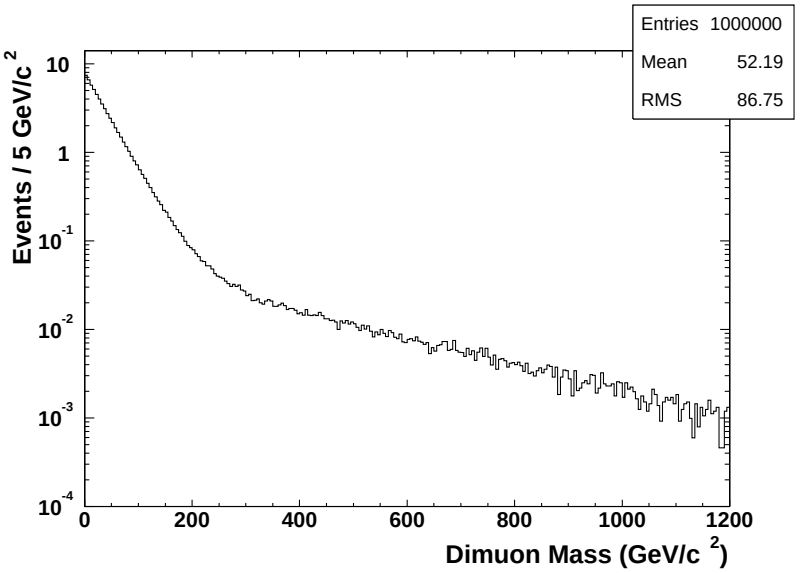

Figure 5.5: The histogram fit to the shape of the invariant mass of the cosmic ray muons used as the cosmic ray background.

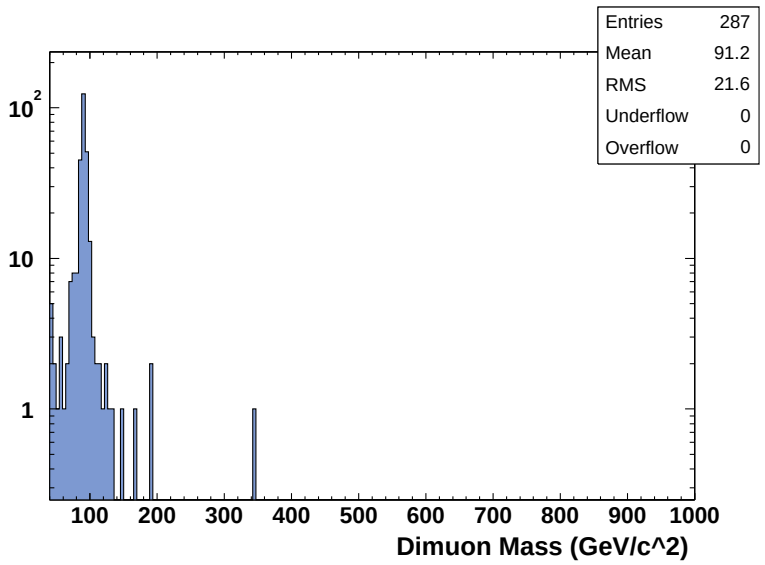

Figure 5.6: Mass distribution of the muons in our final sample that are tagged by the full CR tagger.

the contributions from DY Z $\rightarrow \mu\mu$, DY Z $\rightarrow \tau\tau$, WW, ZZ, $t\bar{t}$ processes. The contributions are calculated by taking into account the efficiencies, acceptances [5] and cross sections. Selection efficiencies are measured from the data, as described in Section 4.3. Acceptances are calculated using MC simulation. Cross sections are as listed in Table 5.1. We then normalize the total number of background events relative to data within the mass window of [80-100] GeV/c^2. In Figure 5.7, we compare data to expected background for all our dimuon candidates in the high $p_{\rm T}$ central muon sample. In Figure 5.8, we compare the $p_{\rm T}$ distribution of selected events with DY/Z MC. The upper plot is for the whole sample, the lower plot is for those events only in

[5] The definition of acceptance is given in Equation 6.1.

the Z mass window. In Figure 5.9, we show the breakdown of the comparison with respect to various categories of dimuons. We also perform a simple KS test for these distributions as shown in the figure. In Table 5.2, we list the observed number of events and the comparison with the expectations integrated above different masses.

In Figure 5.10, we show a portion of the high mass spectrum in the range [110, 300] GeV/c^2. There are two regions in the mass spectra where one can observe a slight excess: 150 and 200 GeV/c^2. We observe 29 events in data to be compared with 23.0 expected background events for 150 GeV/c^2 in [140-160] GeV/c^2 mass region and 17 events to be compared with 11.0 expected background events for 200 GeV/c^2 in [180-210] GeV/c^2 mass region. Simple counting gives us less than 1σ (2σ) discrepancy between data and background in 150 (200) GeV/c^2. The excess around 200 GeV/c^2 is interesting. However, at this point in time, we cannot consider this excess to be statistically significant. We believe that 180–200GeV/c^2 mass region of the invariant mass spectrum should be re-examined when more data is available.

The polar angle distribution of the dimuons in data is also compared to that of expected from Drell-Yan background. The DY background is the same MC sample used in the mass spectrum comparison. We define the Lorentz-invariant polar angle of

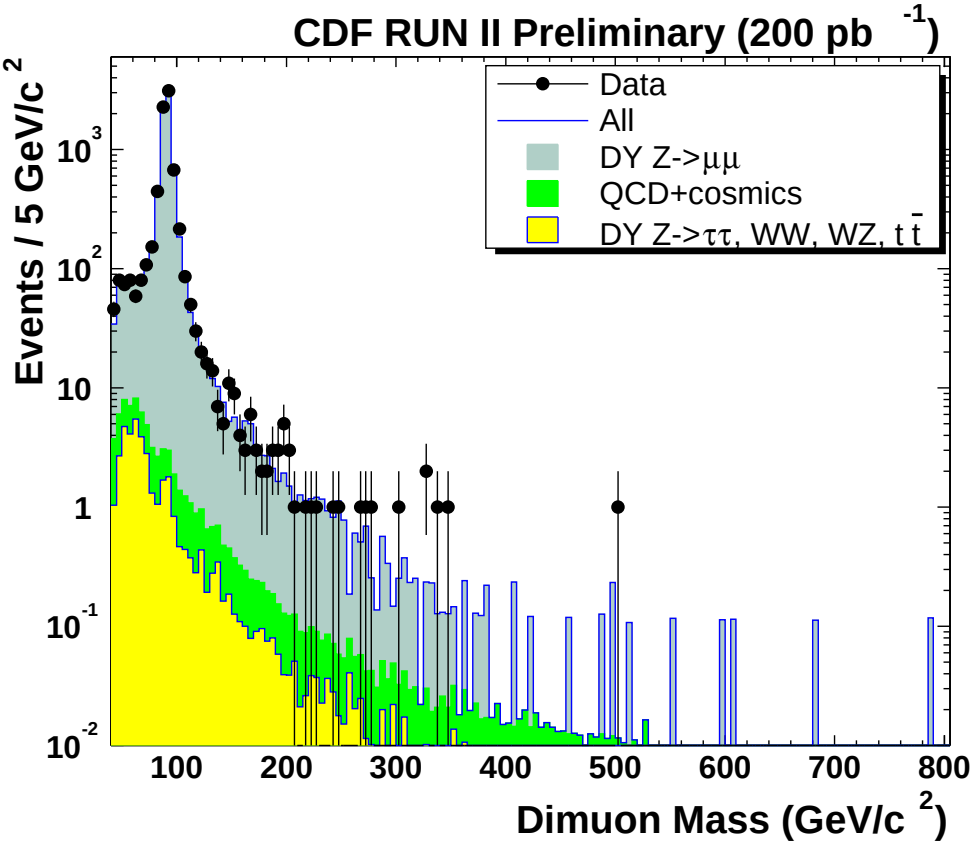

Figure 5.7: Data compared with expected background for dimuon invariant mass spectrum.

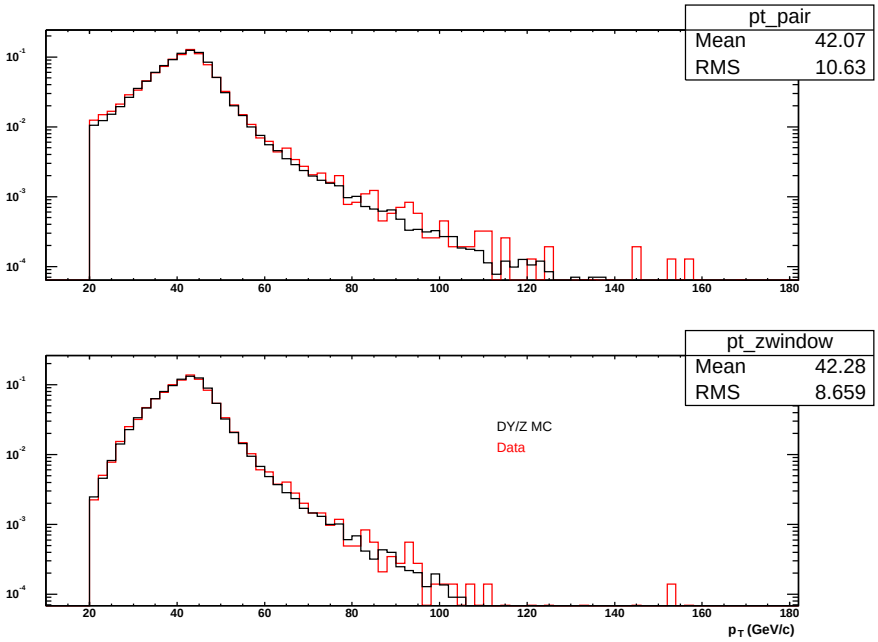

Figure 5.8: Data (light, red) comparison with expected Drell-Yan background (dark, black) for muon p_{T} distribution.

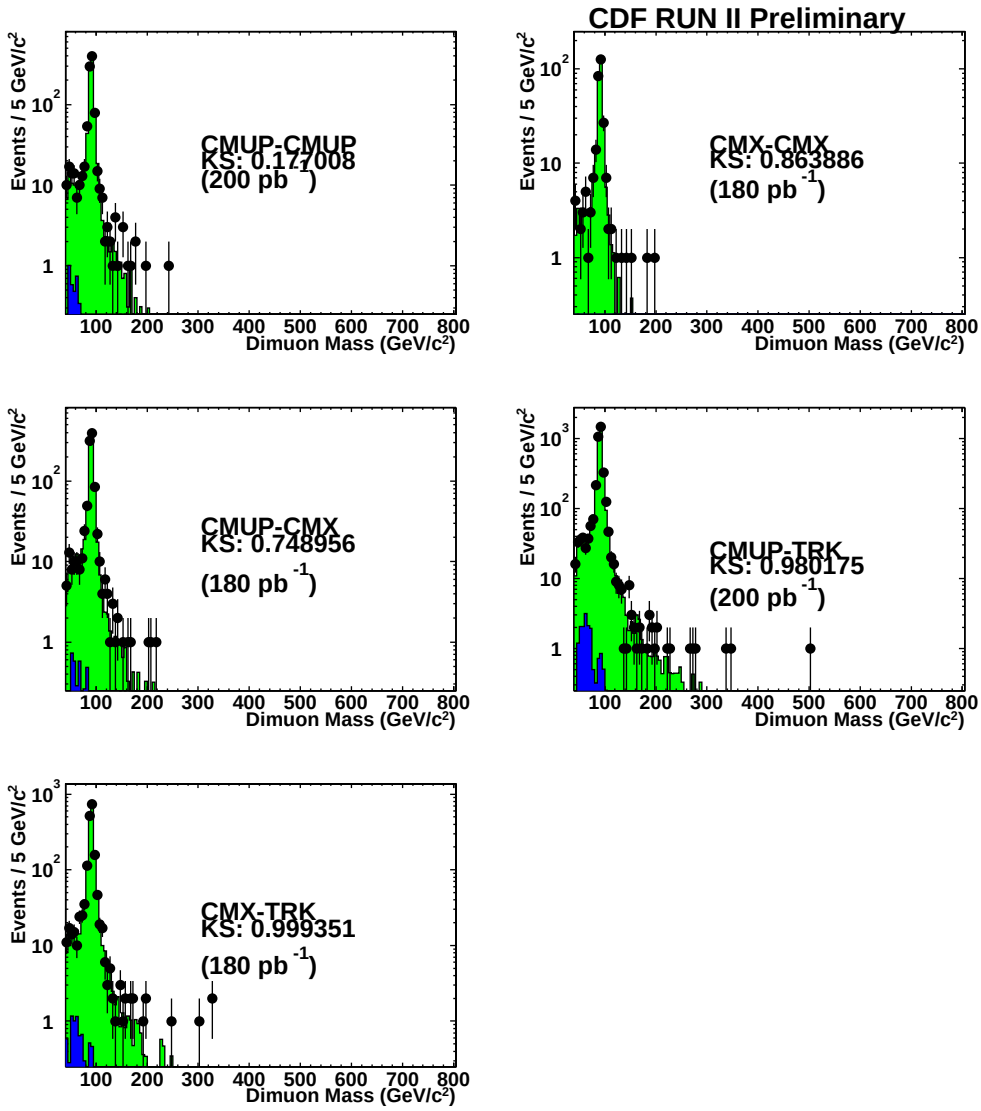

Figure 5.9: Data comparison with expected background for dimuon invariant mass. KS tests are also shown for each category.

CDF Run II Preliminary (200 pb^{-1})

Mass (>)	Data	Direct	Fake	Total
150	58	51.54+/-2.37	3.70+/-0.80	55.25+/-2.50
200	18	18.70+/-0.86	2.17+/-0.45	20.88+/-0.97
250	9	7.86+/-0.36	1.59+/-0.33	9.44+/-0.49
300	6	3.97+/-0.18	1.25+/-0.26	5.22+/-0.32
350	1	2.20+/-0.10	1.03+/-0.21	3.23+/-0.24
400	1	1.42+/-0.06	0.86+/-0.18	2.28+/-0.19
450	1	1.08+/-0.05	0.71+/-0.15	1.79+/-0.16
500	1	0.64+/-0.02	0.59+/-0.12	1.24+/-0.13
550	0	0.54+/-0.02	0.49+/-0.10	1.03+/-0.11
600	0	0.33+/-0.01	0.41+/-0.08	0.73+/-0.09
650	0	0.22+/-0.01	0.33+/-0.07	0.56+/-0.07
700	0	0.11+/-0.00	0.27+/-0.05	0.38+/-0.06
750	0	0.11+/-0.00	0.21+/-0.04	0.33+/-0.04
800	0	0+/-0	0.17+/-0.03	0.17+/-0.04

Table 5.2: Data comparison with expected background integrated above the masses as shown.

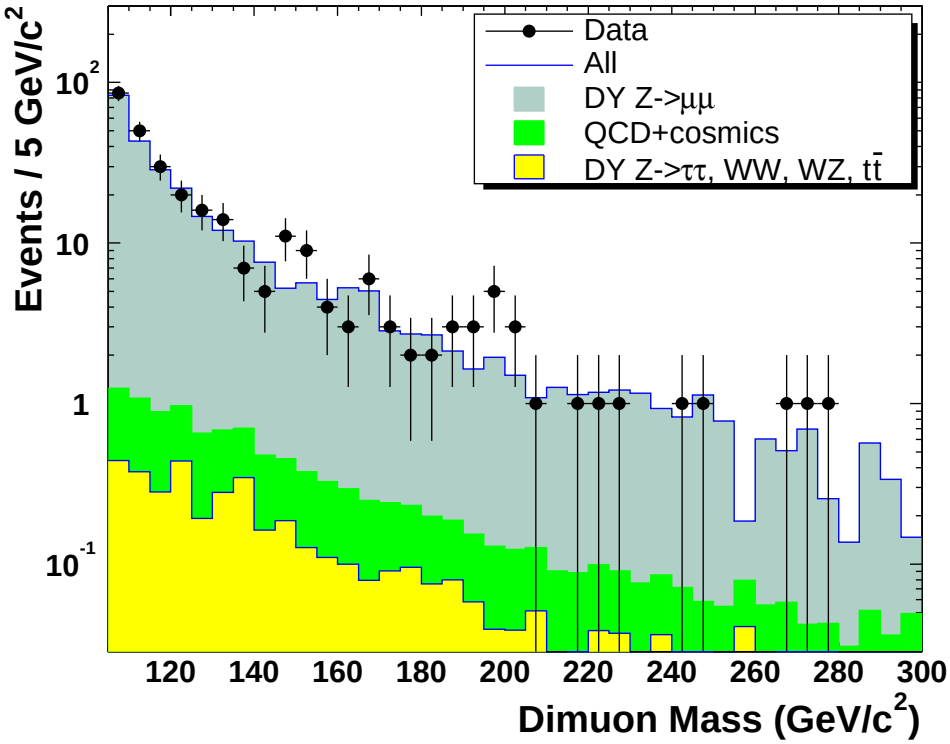

Figure 5.10: Data comparison with expected background for high mass region and for $M_{\mu\mu} < 300$ GeV/c^2.

the dimuons, $\cos\theta^*$, in the Collins-Soper frame [125]. We use the following expression:

$$\cos\theta^* = \frac{2}{M\sqrt{M^2+P_T^2}}\left(\ell_1^+\ell_2^- - \ell_1^-\ell_2^+\right) \quad ,\ell_i^{\pm} = \frac{1}{\sqrt{2}}(\ell^0 \pm \ell^3) \quad ,i = 1,2 \quad . \tag{5.2}$$

where M is the mass of the dimuon (dilepton) pair, P_T is the transverse momentum of the muon pair, ℓ^0 and ℓ^3 are the energy and the third momentum component of the muon ($i = 1$) or antimuon ($i = 2$), respectively. We use the unsigned value to make the equation independent of the lepton charge. The Collins-Soper formalism allows one to reduce the uncertainty in $\cos\theta^*$ that is introduced by the transverse momentum of the incoming partons to a negligible level.

Figure 5.11 shows a comparison of the data with the expected Drell-Yan distribution from simulation and Figure 5.12 shows the same distribution for the mass region above 150 GeV/c^2. There is good agreement between data and simulation. The $\cos\theta^*$ distribution is not used in the fit for the search analysis. Therefore, a numerical comparison has not been performed on these distributions.

5.5 Cross-check with Z boson Cross Section

The Standard Model Z boson gives us the control region with which a cross-check of the acceptance and efficiency estimates can be performed. For this, we calculate

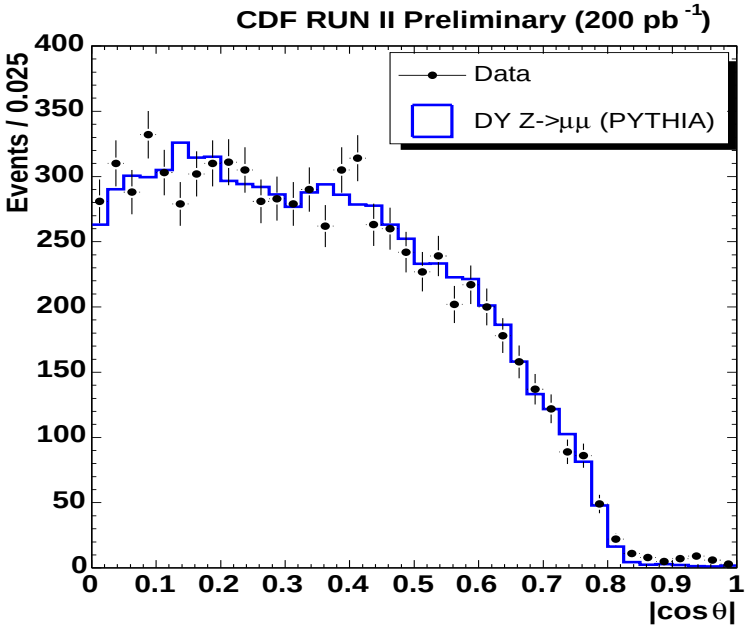

Figure 5.11: Data compared with expected DY background for dimuon $\cos\theta^*$ distribution. The MC distribution is normalized to the total data number of events.

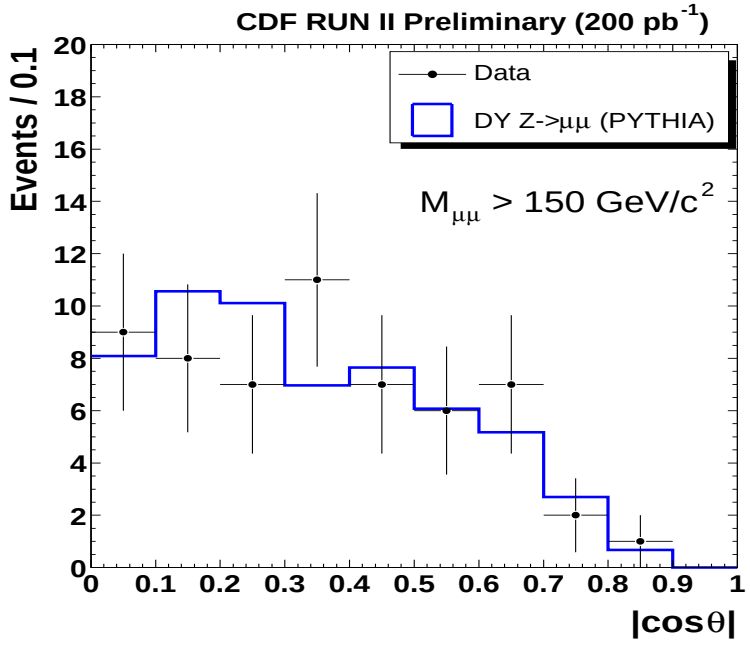

Figure 5.12: Data compared with expected DY background for dimuon $\cos\theta^*$ distribution for events with $M_{\mu\mu} > 150$ GeV/c^2. The MC distribution is normalized to the total data number of events.

the Z cross section using the number of observed events in 200 pb^{-1} data within a dimuon mass range of [80,100] GeV/c^2. The cross section is calculated using the following formula:

$$\sigma \cdot BR(\mathrm{Z} \to \mu^+\mu^-) = \frac{N_{obs} - N_{backgr}}{A(\mathrm{Z}) \times \epsilon_{\mu\mu} \times \mathcal{L}} \quad . \tag{5.3}$$

The MC acceptance of the Z mass window is normalized using the 500k events in the DY/Z sample. The negligible $< 0.5\%$ difference due to γ^* interference effect in the cross section in mass range of [80,100] GeV/c^2 is not corrected for the final $\sigma \cdot BR$ result. For the acceptances, an explicit requirement of at least one muon tagged by a stub and the dimuon tracks satisfying the kinematic cut of $p_{\mathrm{T}} > 20$ GeV and passing the track reconstruction cuts of $N_{ax} > 20$ and $N_{st} > 16$. Table 5.3 summarizes the results for all the dimuon subcategories included in the analysis. The luminosity measurement error is separated from the other uncertainty contributions. The results are in agreement with the theory prediction. The theory prediction for the cross section is 250.2 pb for Z mass of [66-116] GeV/c^2 [126]. CDF also measured the cross section of Z boson in muon channel using the [66-116] GeV/c^2 mass range and with slightly tighter selection criteria, smaller acceptance and 72 pb^{-1} muon data. The cross section measurement[127] is in very good agreement with theory calculations.

	CMUP-CMUP	CMX-CMX	CMUP-CMX	CMUP-TRK	CMX-TRK
N_{obs}	827	251	842	3051	1520
N_{backgr}	0.6±0.0	0.1±0.0	1.0±0.0	2.4±0.0	1.3±0.0
A(Z)	0.029±0.001	0.0071±0.0	0.028±0.001	0.098±0.003	0.046±0.001
$\epsilon_{\mu\mu}$	0.609±0.02	0.771±0.020	0.687±0.02	0.632±0.02	0.775±0.02
$\mathcal{L}$ (pb^{-1})	199.1±11.9	178.6±10.7	178.6±10.7	199.1±11.9	178.6±10.7
σ.BR (pb)	235±14±14	256±18±15	245±14±15	247±12±15	239±10±14

Table 5.3: Calculated DY-Z cross section in dimuon channel in Z boson peak.

Chapter 6

Signal Acceptances

The most important factor that determines the sensitivity of an analysis to a signal process is to maximize the number of events that may be observed within the detector. This may be performed either via increasing the luminosity, efficiency or optimizing the potential observation of signal by increasing the geometrical coverage or maximizing the available center-of-mass energy in a detector. The latter is usually related to the acceptance of the detector. In this chapter, we describe the Monte Carlo simulation samples that are used in estimating the CDF detector's acceptance to spin -0, -1, -2 particles in dimuon channel and comment on the various signal simulation related issues.

6.1 Monte Carlo Samples and Acceptances

The acceptance for the signal processes is estimated using an event generator and a realistic simulation of the CDF detector. The samples are generated and simulated using the official CDF code version 4.9.1. The event generator is Pythia version 6.203 [37]. The choice of the simulation parameters (such as PDF functions, Pythia tunings, alignments and calibrations) are the same as the background processes and are discussed in Section 5.1. For the kinematics of the signal processes, we use PDF set which is CTEQ5L [129] and we impose no further restrictions on the kinematic variables during generation. Pythia uses "parton shower" evolution [134], in order to take higher than leading order QCD effects into account in the simulation of physics processes [1]. The implementation of the parton showers allows for better modeling of the overall structure and kinematics of the generated events. Validation of Pythia vector boson acceptance and mass spectra shape estimates have been performed by various groups [135, 136].

To determine our signal acceptances for the three different spin hypotheses, 5000 events are generated for each mass value from 150 GeV/c^2 to 800 GeV/c^2 in 50 GeV/c^2 intervals. The dimuon final states are reconstructed with similar requirements as applied to the data. The acceptance is determined by making the kine-

[1] The cross sections are calculated in leading order in Pythia. Section 7.4 describes the corrections to the cross sections.

matic and geometric requirements on the reconstructed muons. The minimum p_{T} requirement of 20 GeV/c determines the total kinematic acceptance. The geometrical acceptance is determined by requiring five types of dimuons as described in Section 4 and a minimum number of axial (>20) and stereo (> 16) hits in the COT. The definition of acceptance, A_i, where i runs up to the number of reference signal masses generated, is given as:

$$A_i = \frac{N^i_{reconstructed}(p_T > 20\ GeV/c^2\ \&\ COT\ fiducial\ cuts)}{N^i_{generated}} \quad . \tag{6.1}$$

The polar angular distribution of a particle with zero angular momentum depends on its spin and mass. The more massive the particle gets, the smaller the boost and the massless decay products gain larger energy in the transverse direction. Therefore, the final state becomes more "central". The spin of the particle determines the shape of the polar angular distribution in the production, which also affects the acceptance. For a spin-0 particle, the distribution of $\cos\theta$ is flat. For a spin-1 particle, the polar angular distribution is quadratic in $\cos\theta$ and for a spin-2 particle, the distribution is quartic. The angular dependence of Drell-Yan production is given in Equation 1.18. For an RS graviton, the dependence is more involved, due to two different production channels, as shown in Equation 1.32. An illustration of these distributions obtained using MC simulation are given in Figure 6.1.

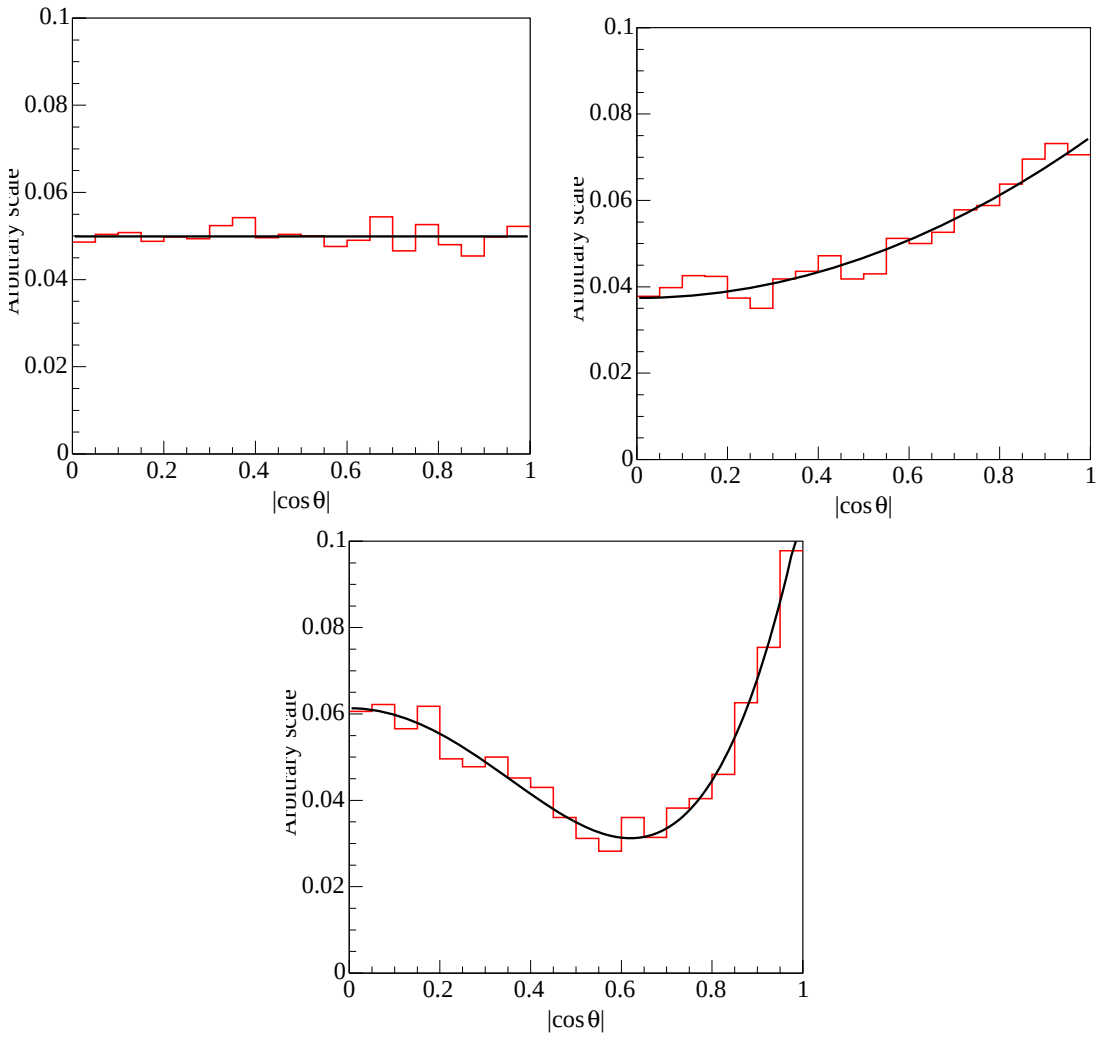

Figure 6.1: Spin dependence of spin-0,-1,-2 resonance angular distribution for generator level kinematic acceptance for dileptons [137].

In the sections below, we report on the estimated acceptances for Sequential Z′, RS Graviton and Higgs scalar, representing the three different spin categories. We also study the dimuon selection efficiency in MC as a function of resonance mass. The systematic uncertainties related with the acceptance estimates are given in Section 7 where the the search results are presented.

6.1.1 Spin-0 (Higgs)

We simulate the production of SM Higgs particle to estimate the Spin-0 acceptances. We generate a heavy Higgs (H) within the MSSM formalism [138] and include only the the dimuon decay channel. At very high masses, the Higgs particle does not have a resonance-like structure, rather, it is produced as a continuum, as generated in Pythia, with default settings in the program for Higgs decays [2]. Figure 6.2 shows a comparison between a 200 GeV/c^2 and 600 GeV/c^2 Higgs $d\sigma/dM$ distribution. For the purposes of acceptance calculations, the model is generated with a $\pm$20 GeV/c^2 mass window around the reference Higgs masses to represent resonances. The choice of the mass window is consistent with the widths of a heavy Z'_{SM}, as can be seen in Figure 6.20. The resulting reconstructed mass distribution is shown in Figure 6.3. Also shown in the plots are the 3σ lower bounds on the fits

[2] Studies have been performed for Higgs mass spectra in [132]. We believe the treatment of Higgs width to boson pairs at high masses is responsible for this behavior.

to illustrate the effect of the momentum resolution in the distribution. The dimuon mass resolution dominates over the width of the Higgs mass window as the mass increases. The MC $\cos\theta$ distributions of the dimuons for various masses of the Higgs particle is shown in Figure 6.4. The $\cos\theta$ distributions are normalized to unity.

The geometric and kinematic acceptance for Higgs particles is shown in Figure 6.5, for the five categories of muon types as a function of Higgs mass. The largest contribution to signal acceptance comes from the CMUP+TRK dimuon category. The smallest contribution comes from CMX+CMX dimuons, this is due to the smaller polar and azimuthal acceptance of the CMX detector. There is also a constraint on the polar opening angle between the two muons for them to be both in the CMX detector. The total acceptance for a Higgs particle is about 60% at the highest masses. The MC selection efficiency (except cosmic timing cuts) is shown in Figure 6.6. The efficiency is independent of the Higgs mass and is flat within the statistical errors [3]. The combined MC selection efficiency is about 75%.

6.1.2 Spin-1 (Z')

The only degree of freedom in the sequential (SM-like) Z' model (Z'_{SM}) is the mass of the boson itself. This is because Z'_{SM} has its couplings fixed to those of the SM Z^0 and

[3] All acceptance and efficiency statistical errors are calculated binomially for all the signal MC samples.

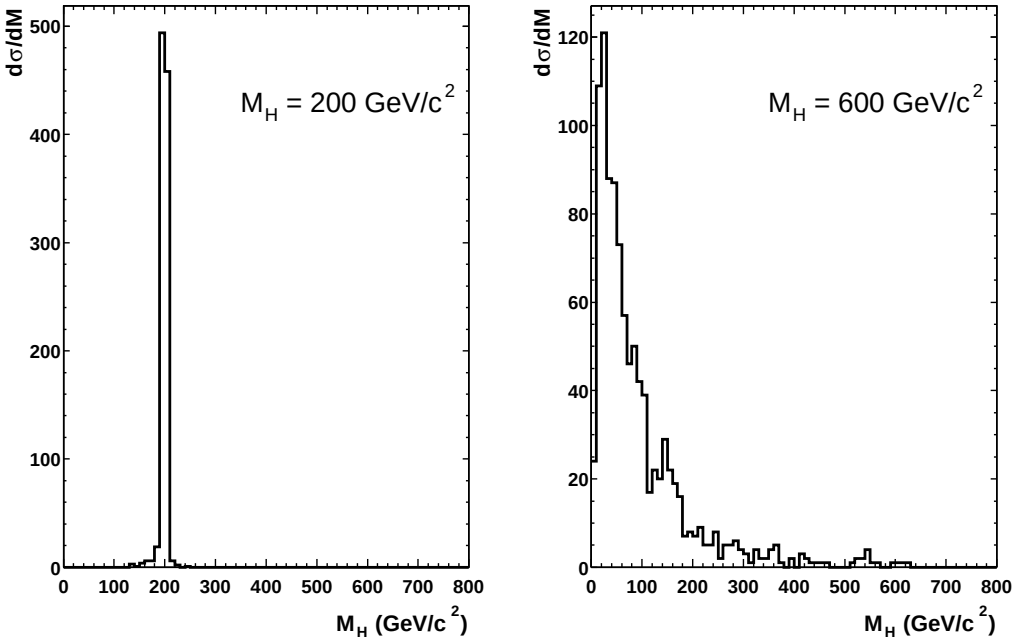

Figure 6.2: $d\sigma/dM$ calculated in Pythia for a 200 GeV/c^2 and 600 GeV/c^2 Higgs particle.

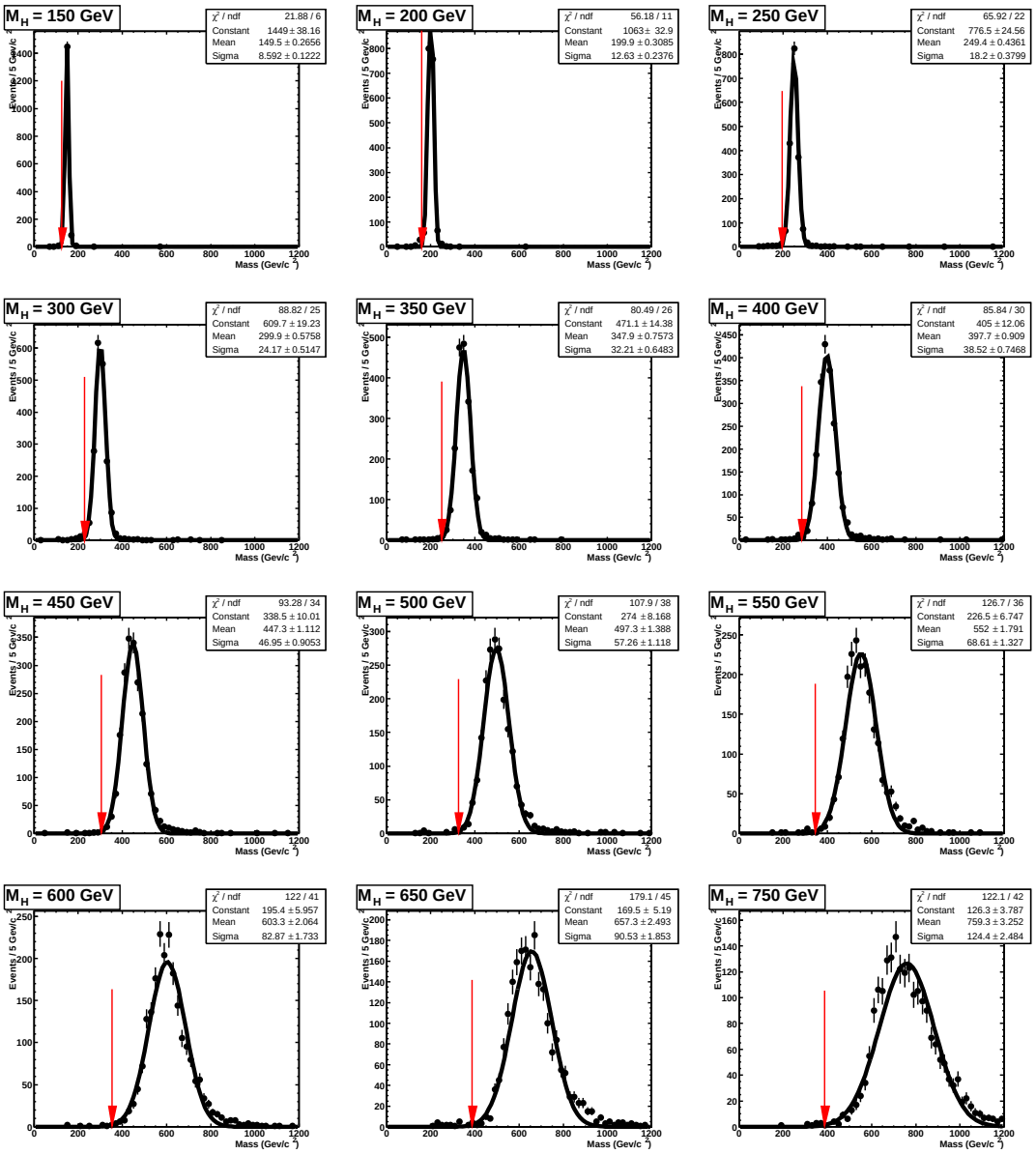

Figure 6.3: Reconstructed dimuon invariant mass distributions for H$\rightarrow \mu^+\mu^-$. Also shown are the Gaussian fit results. Arrows point to the lower 3σ bounds for the individual reconstructed mass means.

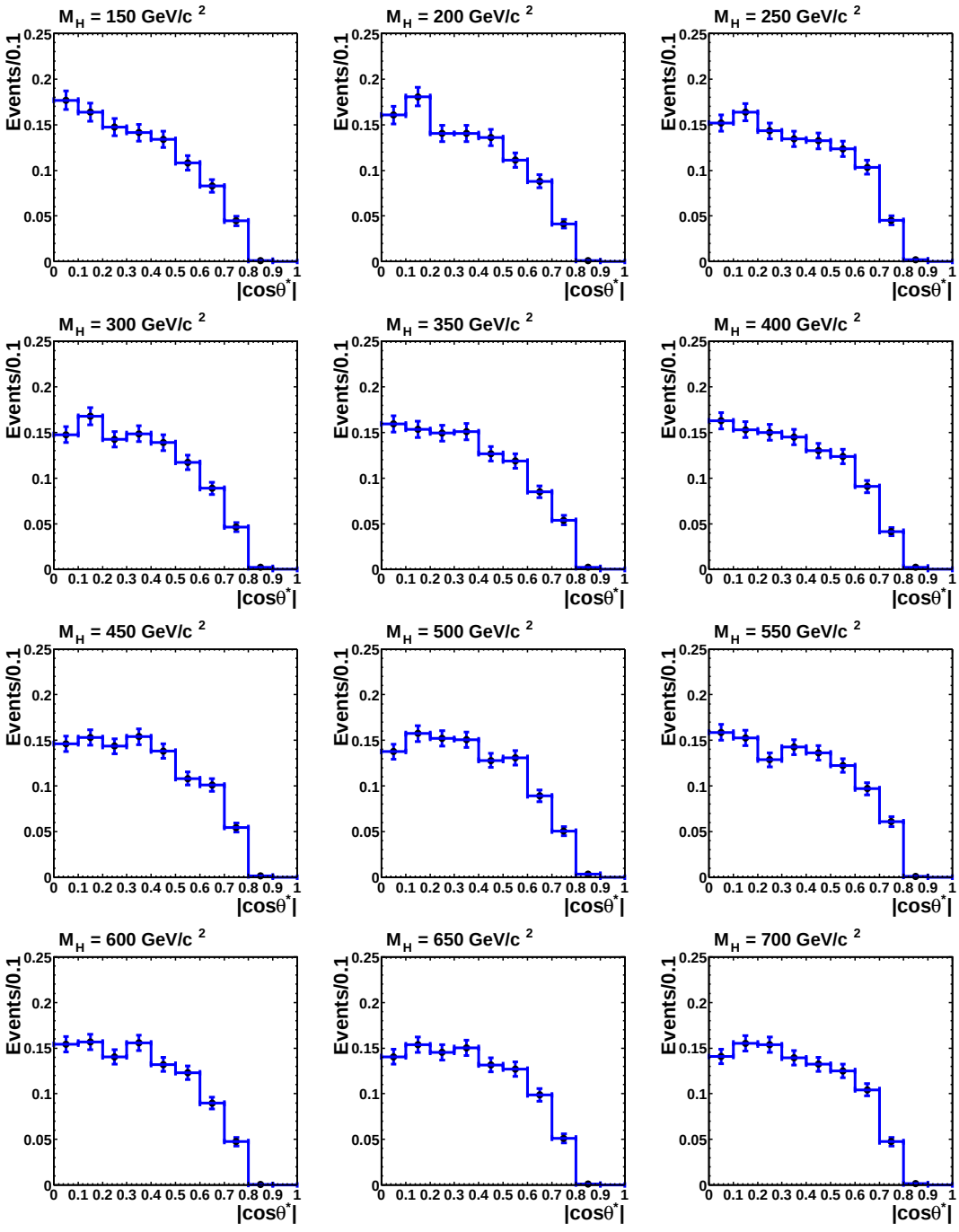

Figure 6.4: $\cos\theta^*$ distributions for various Higgs particle masses.

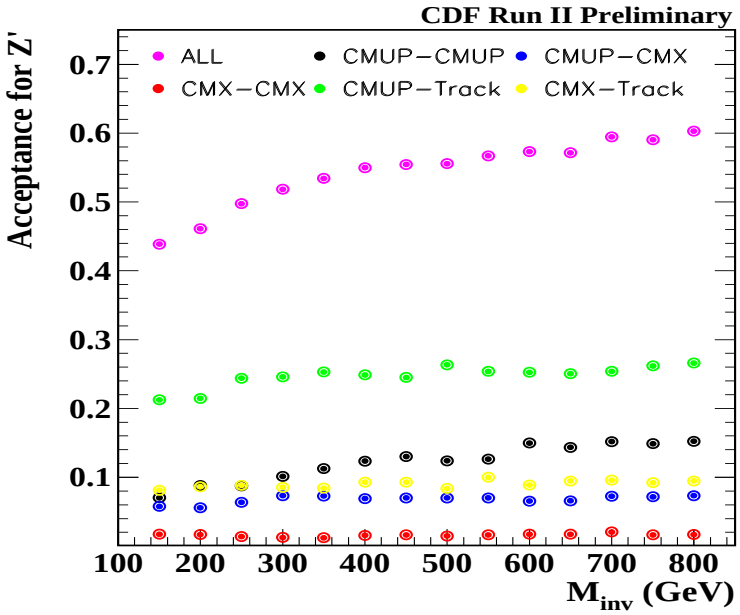

Figure 6.5: Dimuon acceptance as a function of Higgs mass.

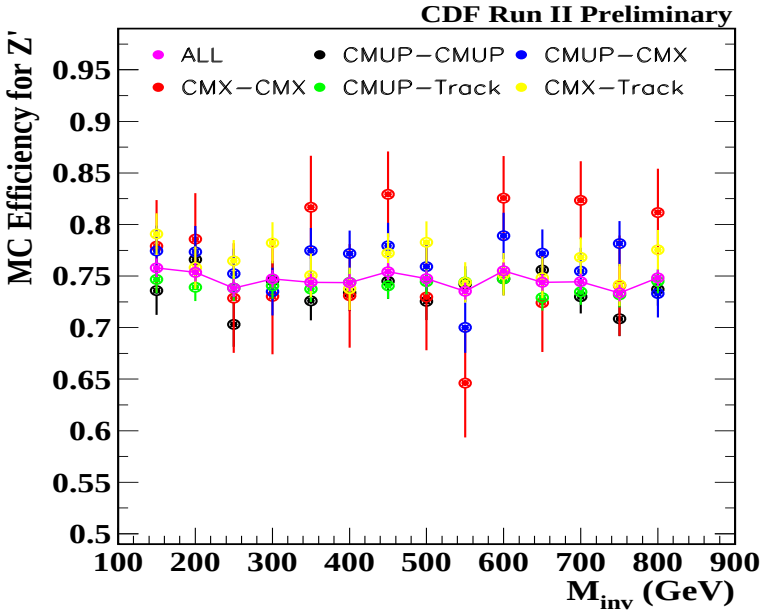

Figure 6.6: Mass dependence of the selection efficiency for Higgs.

has an intrinsic width proportional to its mass (Figure 6.20). The Z′ are generated with no interference with SM neutral gauge bosons. Figure 6.7 illustrates resonance shapes for 200, 500 and 800 GeV/c^2 Z′. We observe that as mass nears the E_{cm}, the low end tails of the mass distribution increases, with respect to the peak. This behavior is mainly an effect of the PDF distribution of the proton and antiprotons where the resonance mass approaches the $p\bar{p}$ center of mass energy and its width becomes wider. Figure 6.8 shows the reconstructed dimuon mass distributions for the reference Z′ masses. Each sample consists of 5000 Z'_{SM} events generated. The low-mass tail is visible as Z′ mass gets higher. Figure 6.9 shows the dimuon $\cos\theta$ distributions for various masses of the Z′. We do not observe a strong dependence of the distribution to the mass of Z′.

Figure 6.10 shows the expected combined geometrical and kinematic acceptance for the five categories of muon types as a function of generated Z′ masses. We observe that the CMUP-CMUP category, yields more acceptance as the Z′ mass gets larger, as expected. The contribution from CMX-only category is not substantial. However, CMUP-CMX category of dimuons increase the acceptance by more than a factor of two for some generated Z′ masses. In Figure 6.11, we plot the MC efficiency of the selection cuts (no cosmic timing cuts) as a function Z′ mass. The distribution is flat within the errors. Figure 6.12 compares the acceptance×efficiency of the dimuon selection to that of the earlier stage of the analysis where only muons

with stubs were included in the final selection. Except for some negligible, minor differences, the main selection requirements were the same in both estimates. We note approximately a factor of two increase in the total acceptance at high masses when the current algorithm is applied, improving the sensitivity for the searches.

6.1.3 Spin-2 (RS Graviton)

The RS graviton is a spin-2 boson. The resonance is expected to have a slightly different detector acceptance than a that of a Z′ or a Higgs particle. The correct angular distributions are included for decays to a fermion pair in the lowest-order processes As in the case of the other models, the mass of the RS graviton is a free parameter. The other degree of freedom of the RS model is the dimensionless coupling parameter (k/M_{Pl}) which enters quadratically into the calculation of the intrinsic width of the graviton, as mentioned in Section 1. Figure 6.20 shows the width of RS graviton as a function of its mass. Decays of the graviton to a fermion pair ($f\bar{f}$), gg, $\gamma\gamma$, ZZ and W^+W^- contribute to its total width. We use $k/M_{Pl} = 0.1$, which defines the upper bound of the search region, for our acceptance calculations. In Figure 6.13, the reconstructed dimuon masses are plotted for the RS Graviton signal. The high mass RS graviton resonances have larger tails in the low mass region as compared to those of Z′ boson (Figure 6.8). This is mostly due to the gluon fusion component

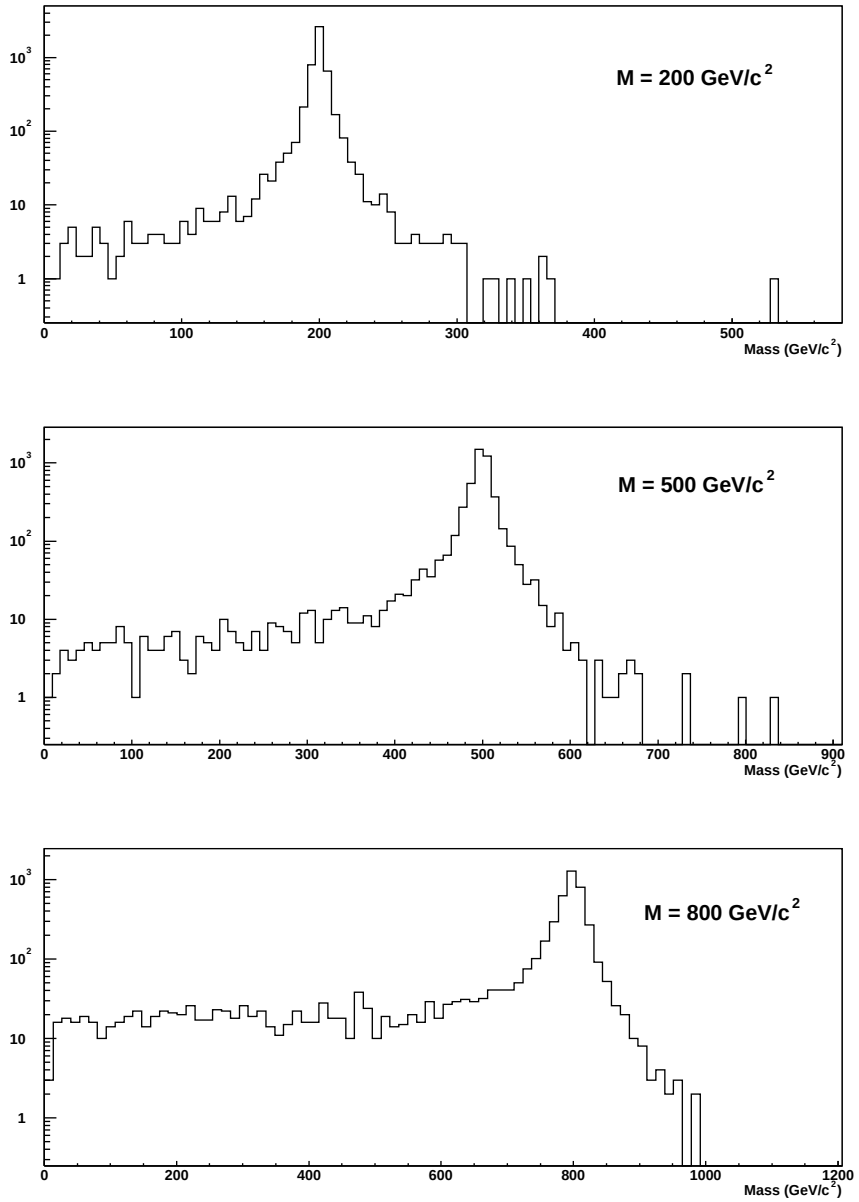

Figure 6.7: Resonance shapes for three different Z′ masses (200, 500, 800 GeV/c^2, top to bottom) at generator level.

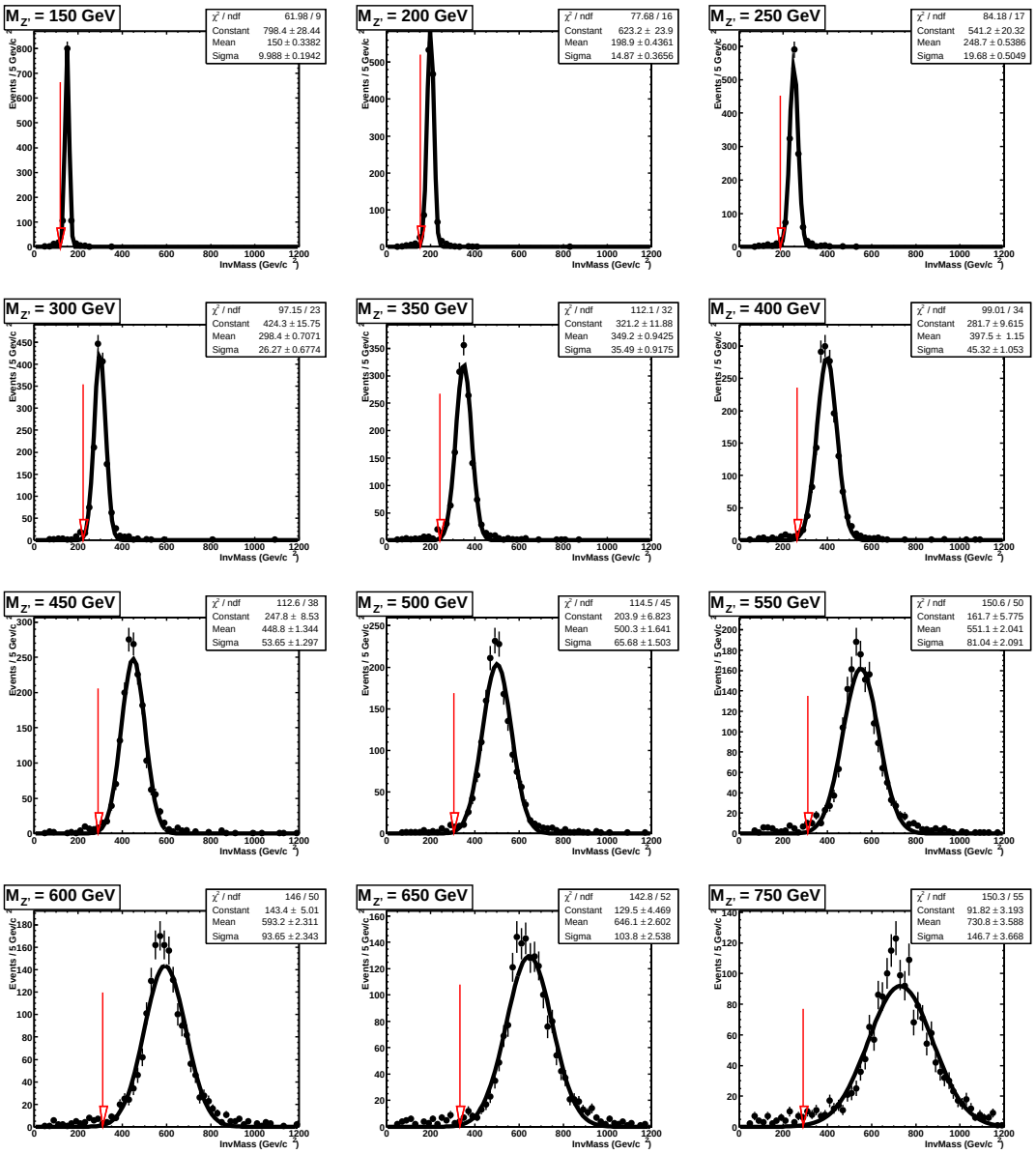

Figure 6.8: Reconstructed dimuon invariant mass distributions for $Z' \to \mu^+\mu^-$. Also shown are the Gaussian fit results. Arrows point to the lower 3σ bounds for the individual reconstructed mass means.

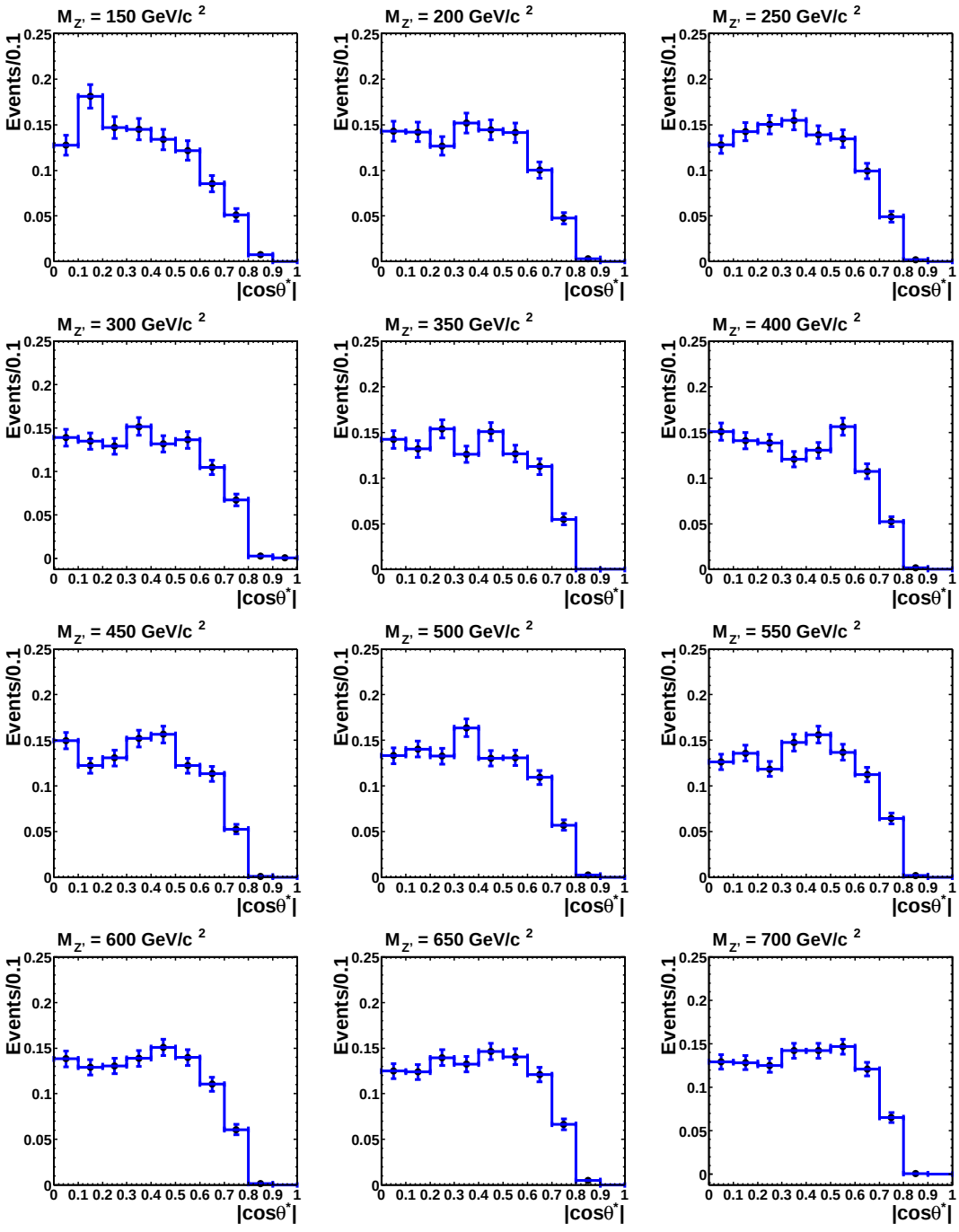

Figure 6.9: $\cos\theta^*$ distributions for Z′ for various reference masses.

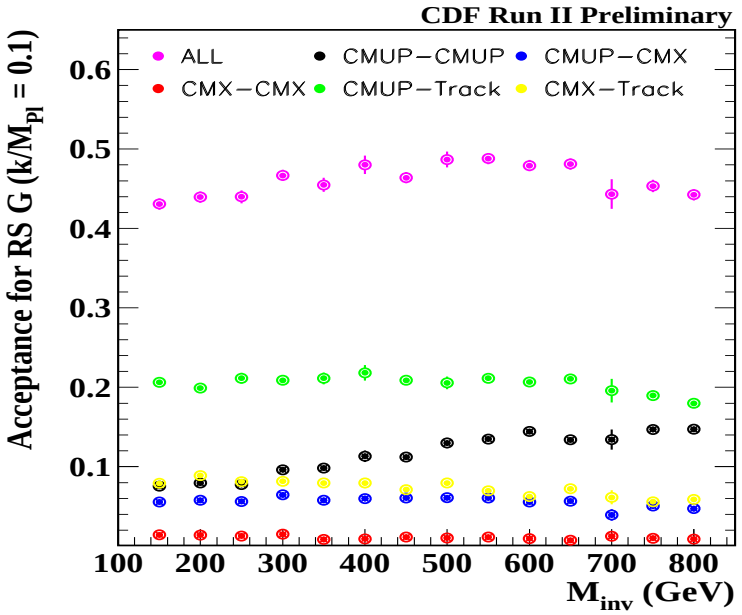

Figure 6.10: Dimuon acceptance as a function of Z′ mass.

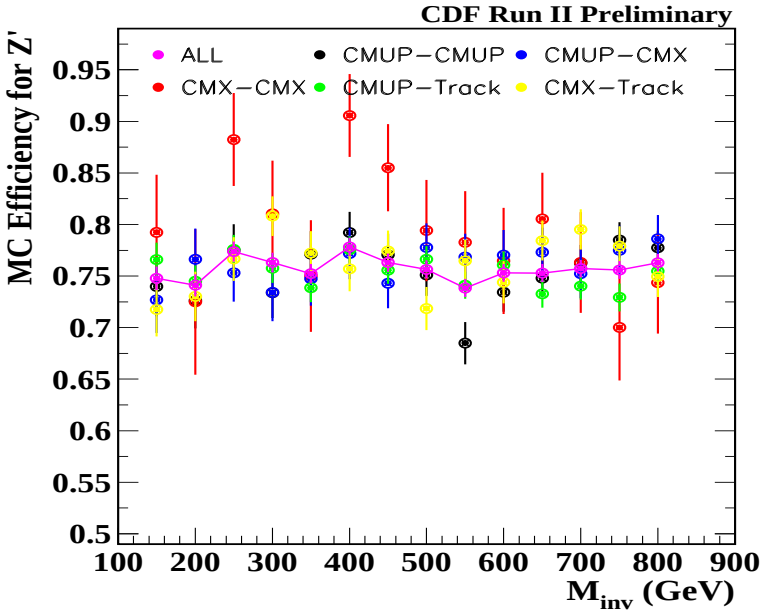

Figure 6.11: Mass dependence of the selection efficiency for Z′.

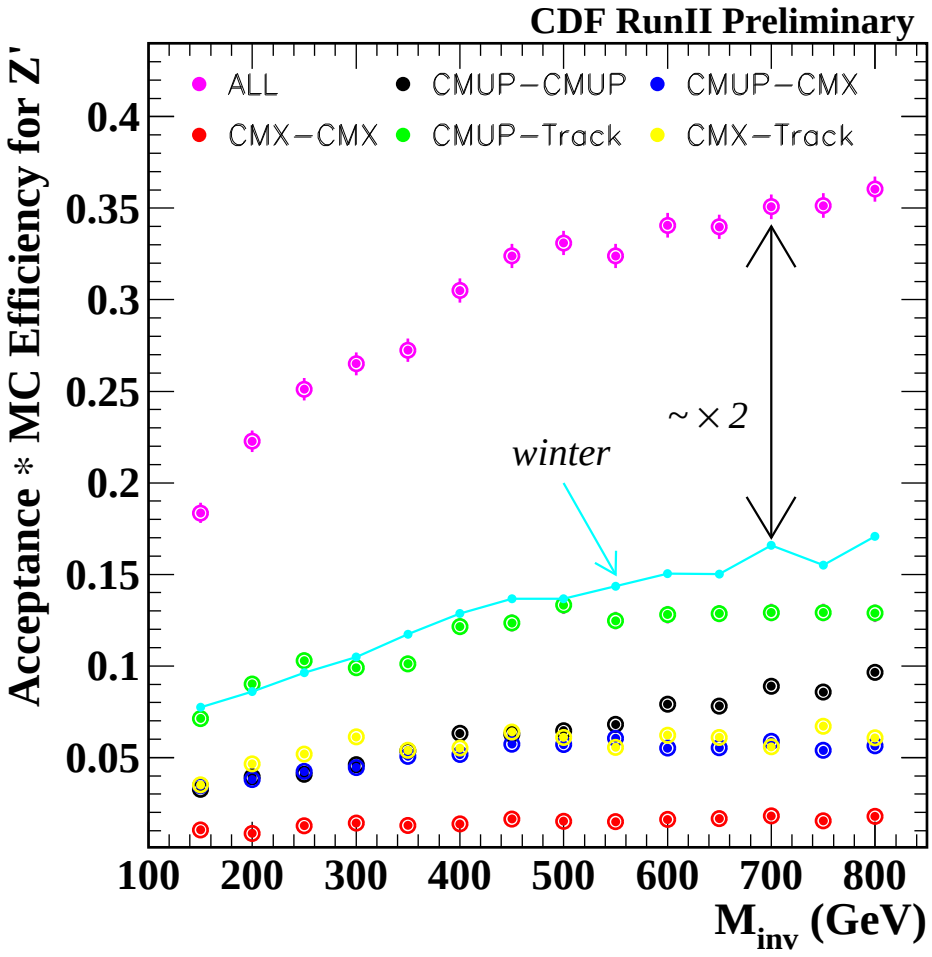

Figure 6.12: Comparison of the acceptance to an earlier version. Note the significant increase due to inclusion of tracks without stubs in the dimuon selection.

in the graviton production at $p\bar{p}$ collisions (Figure 1.10). In the Pythia event generator, the cross sections are calculated as a function of graviton mass. Since the high mass region behavior is dictated by the PDF and the probability of finding a pair of gluons with a given center-of-mass energy is even more a rapidly falling function at that energy, a larger tail in the low mass region is expected to be observed [4]. Figure 6.14 shows the $\cos\theta$ distributions for the dimuons, for various RS graviton masses. The signal is populated at low $\cos\theta$ values with a steep decrease as a function of $\cos\theta$. This is a distinctive behavior of $\cos\theta$ for spin-2 resonances and holds also true for graviton production in Large Extra Dimension models [133]. Figure 6.15 shows the expected acceptance of dimuons to an RS graviton signal as a function of the generated RS graviton mass. Mass dependence of the selection efficiency estimated via simulation for RS Graviton is shown in Figure 6.16. Figure 6.17 shows the acceptance as a function of RS Graviton mass[5]. The acceptance is almost flat within the statistical errors for different k/M_{Pl} values. We choose the value of k/M_{Pl} (= 0.1) corresponding to a large graviton resonance width that should result in a more conservative mass limit for RS graviton model.

[4] Comparisons of Pythia with another generator, HERWIG, has been performed earlier [42]. $d\sigma/dM$ for a graviton generated by HERWIG has shorter tails in the low mass region, due to the fact that the cross section is calculated at the resonance maximum and then smeared according to the Breit-Wigner distribution. For wide resonances, such as an 800 GeV/c^2 graviton (k/M_{Pl}=0.1), the approximation of Pythia is suggested to be more valid.

[5] This plot is produced using only the muons in $|\eta| < 1.1$ region. The result is independent of this choice.

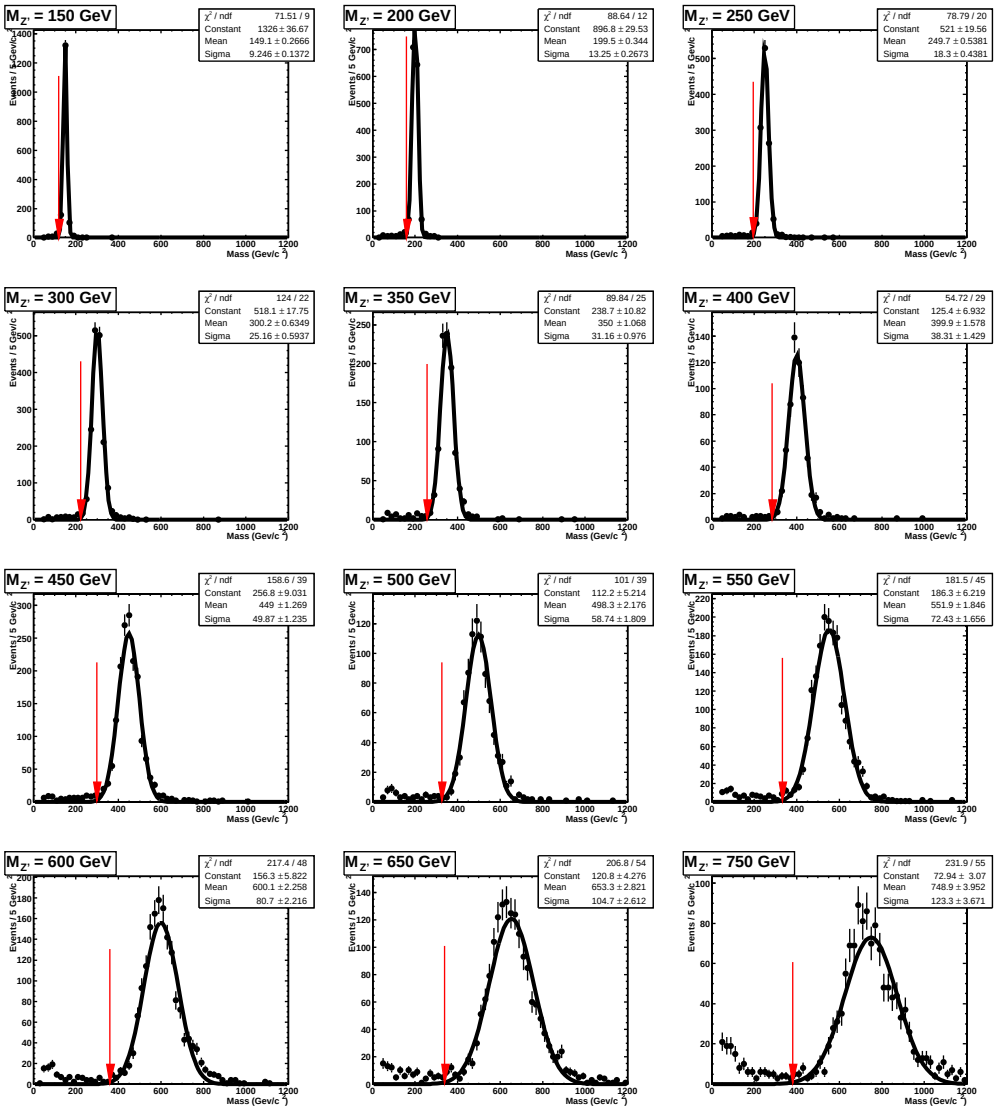

Figure 6.13: Reconstructed dimuon invariant mass distributions for G$\rightarrow \mu^+\mu^-$. Also shown are the Gaussian fit results. Arrows point to the lower 3σ bounds for the individual reconstructed mass means.

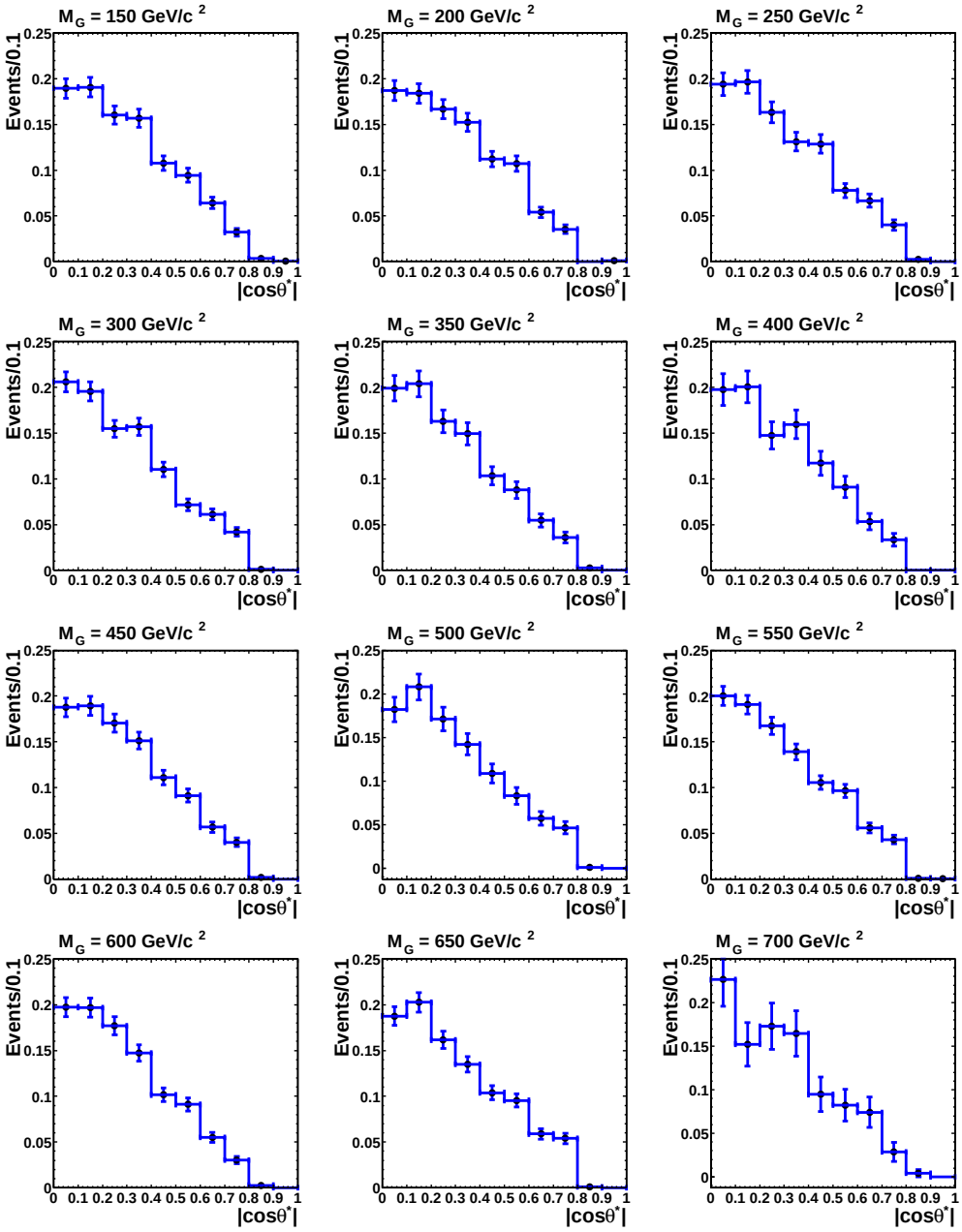

Figure 6.14: $\cos\theta$ distributions for various RS Graviton masses.

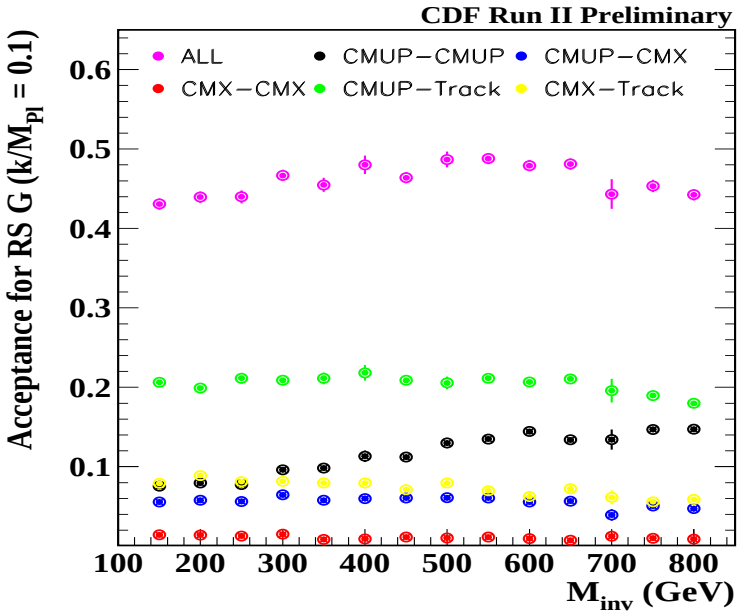

Figure 6.15: Dimuon acceptance as a function of graviton mass.

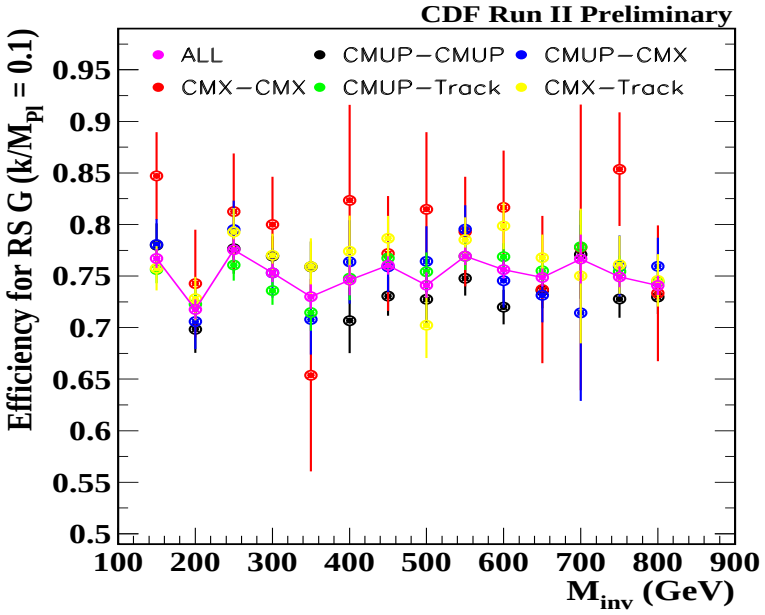

Figure 6.16: Mass dependence of the selection efficiency for RS Graviton.

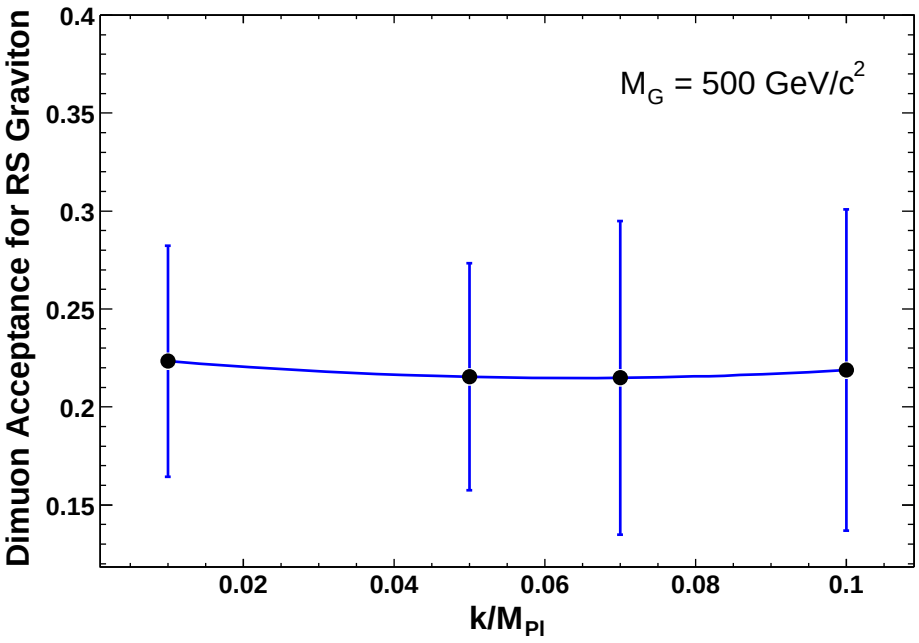

Figure 6.17: k/M_{Pl} dependence of the acceptance for RS Graviton.

6.2 Investigation of Various Acceptance Issues

6.2.1 Interference Effects

For the acceptance and cross section estimates, signal-only Z′ distributions are used. However, signal and background processes can interfere that may effect both the total cross section and the shape of the invariant mass spectrum. Here, a comparison of the signal-only Z'_{SM} cross section to the $\gamma^*/Z/Z'$ interference cross section is presented. For the comparisons, we use a 10,000 sample of each sample (interference on and off) generated using Pythia. A minimum center of mass value for the final state dimuons in the interference spectrum is taken to be 120 GeV/c . This cut-off allows a reasonable MC sample size without the necessity to generate many events (since the Z_0 resonance would dominate the spectrum at low mass), in the signal region. Figure 6.18 shows the invariant mass distributions for seven reference Z′ masses allowing interference. The reference masses cover the range [150-750 GeV/c^2] with 100 GeV/c^2 intervals. The cross section comparison is performed by calculating the ratio of the number of generated events of the signal-only sample (N_s) to the interference sample (N_i) within a mass window around the reference signal mass. The procedure is performed for two different mass windows corresponding to five

and three σ of the generator level resonance widths:

$$R = \frac{N_s}{N_i} \quad , \quad N_{s,i} = \sigma_{s,i} \cdot \frac{N^w_{s,i}}{N^t_{s,i}} \quad , \tag{6.2}$$

where N^w is the number of events in five or three σ windows and N^t is the total number of events generated corresponding to cross section, $\sigma_{s,i}$. Figure 6.19 shows the ratio of the signal-only Z′ cross section to the interference cross section. A correction for a FWHM to Gaussian sigma is not performed for the intrinsic widths since our mass windows are wide enough to take that effect into account. The errors in these plots are calculated by propagation of errors applied to Equation 6.2.

The 5σ and 3σ windows yield results that are in agreement with each other within the errors. A shift is generally expected in the mass peak of the resonance with respect to the pole mass, due to $\gamma^*/\mathrm{Z}/\mathrm{Z}'$ interference effects. Along with an asymmetric mass window, this accounts for a portion of the slight discrepancy observed in the comparisons. Small signals in the highest mass points also contribute to the large calculation uncertainties. We conclude that interference effects are negligible for the purposes of the results of the analysis presented here. The acceptances calculated without interference are used for the search results.

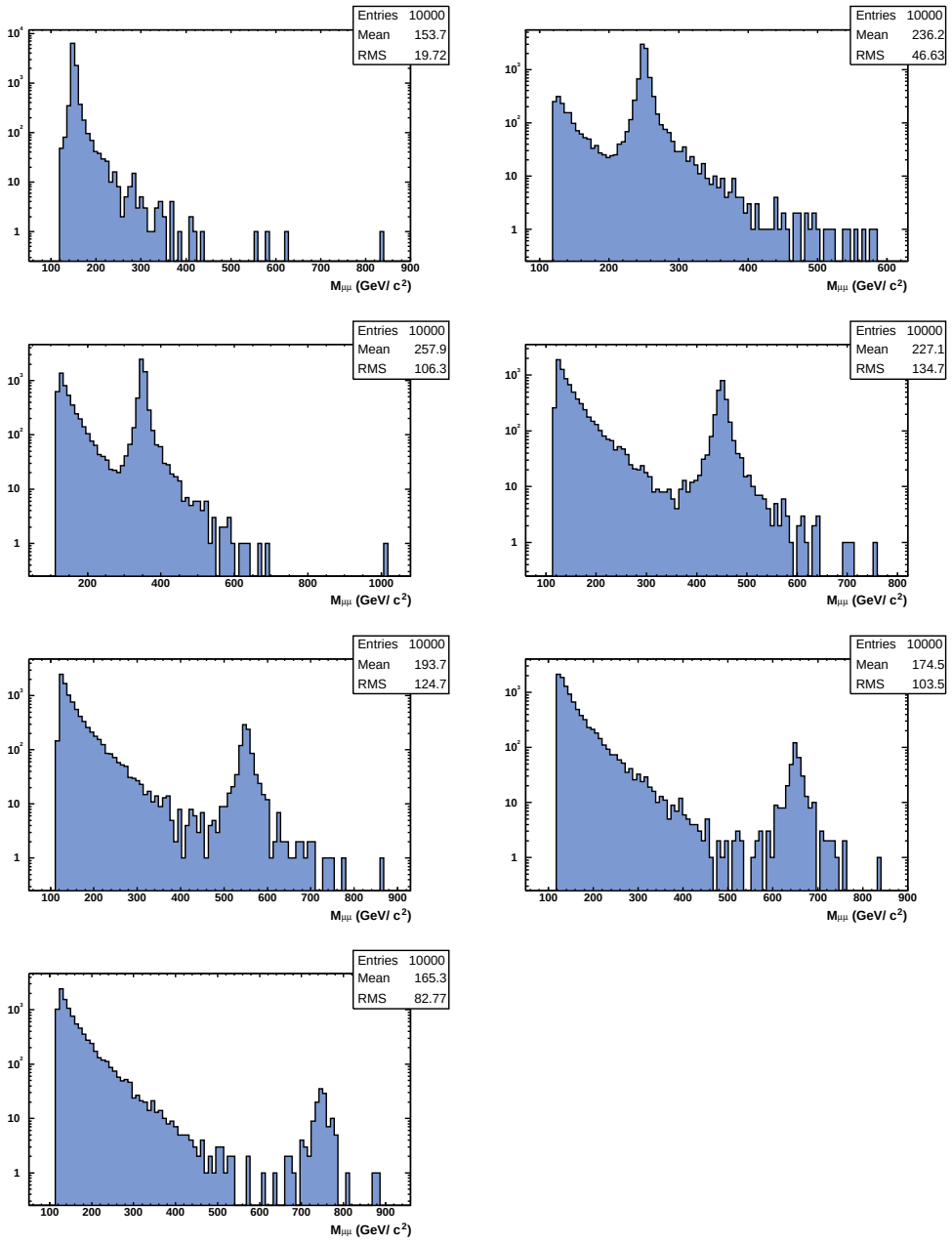

Figure 6.18: Generator level mass distribution for $\gamma^*/Z/Z'$ interference. There is a lower cut-off value at 120 GeV/c for each generated mass. The plots are in logarithmic scale in $y-$axis. The reference masses cover the range [150-750 GeV/c^2] with 100 GeV/c^2 intervals.

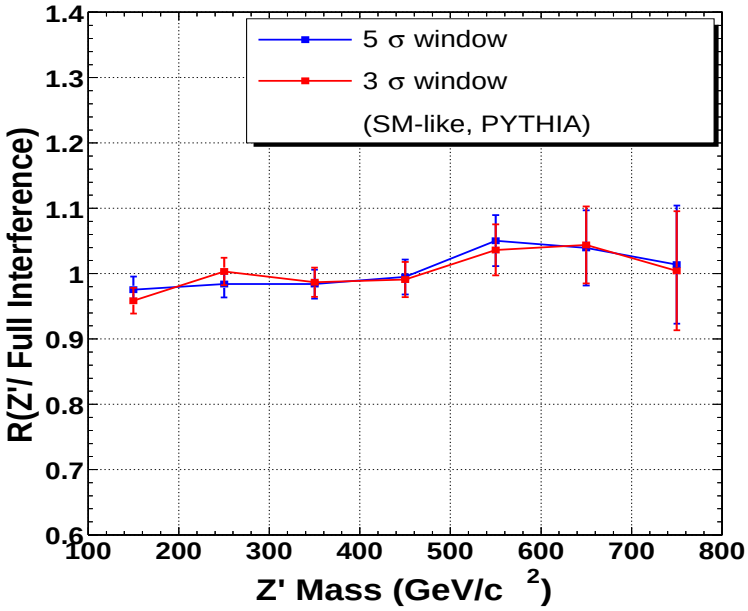

Figure 6.19: Ratio of the signal-only Z′ cross section to the full γ^*/Z/Z′ interference cross section, as a function of mass. The two curves represent the two different mass windows taken for the cross section calculation.

6.2.2 Intrinsic Widths of Resonances and Mass Resolutions

We describe here the comparison of the dilepton mass resolution to the intrinsic width of the resonance. To estimate the detector mass resolution as a function of resonance mass, we use the Z'_{SM} and RS graviton MC samples. We separate out the intrinsic full widths of the resonances (as calculated by Pythia) from the reconstructed mass resolution in the dilepton final states:

$$\sigma^2_{resolution} = \sigma^2_{reconstruction} - \sigma^2_{intrinsic} \quad . \tag{6.3}$$

The value of $\sigma_{intrinsic}$ is calculated using the relation:

$$\sigma_{intrinsic} = \frac{\Gamma_{intrinsic}}{\sqrt{2}} \quad , \tag{6.4}$$

which is obtained by fitting a resonance curve to a Gaussian distribution. Figure 6.20 shows the intrinsic widths of Z′ and RS graviton as a function of the particle mass. The RS graviton width corresponds to $k/M_{Pl} = 0.1$, the largest with that is considered for this particular model. The width of a 800 GeV/c^2 Sequential Z′ is about twice that of a RS graviton at the same mass. Figure 6.21 compares various graviton widths to electron and muon detector resolutions. The reconstructed mass resolution values for the dielectrons are taken from CDF Note 6343 [140]. In the calculations of

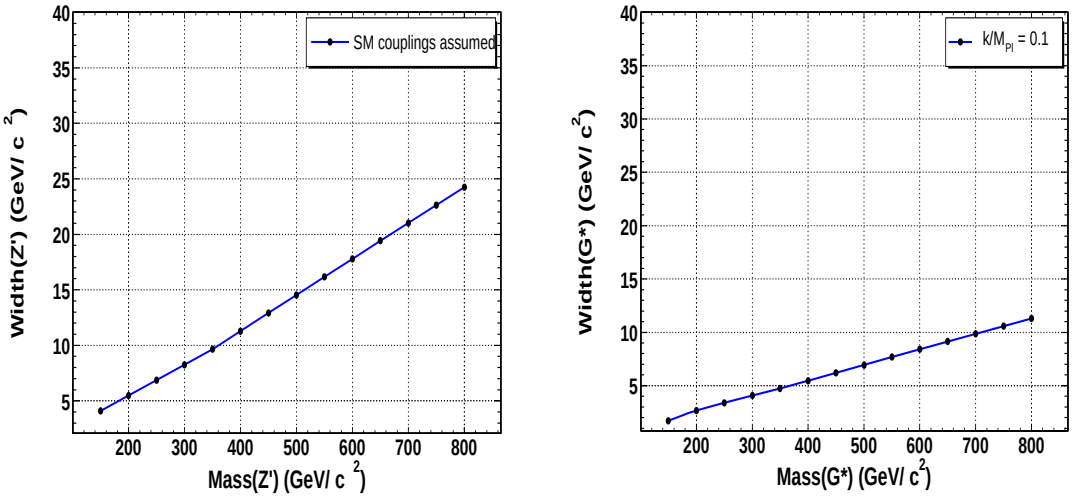

Figure 6.20: Mass vs full width of Z′ (left) and RS Graviton for $k/M_{Pl} = 0.1$ (right). For RS Graviton, the width is dependent on the second power of k/M_{Pl}.

detector resolutions using the reconstructed mass resolution and the intrinsic widths, no errors on the theoretical widths and the reconstructed widths are taken into account. One must keep in mind that the mass distributions are not exactly described by perfect Gaussians as the width of the resonance grows larger. The comparisons are insensitive to this effect as can be seen from the fit results in Figures 6.8 and 6.13. The detector resolution dominates the intrinsic mass width of the RS Graviton for our choices of k/M_{Pl} values. Dimuon mass resolution is worse than the dielectron mass resolution, which is measured using the EM energy. This is a consequence of the momentum resolution of the muon tracks in COT (Section 2.2.1.2) and the energy resolution of electrons in the calorimeter (Table 2.5).

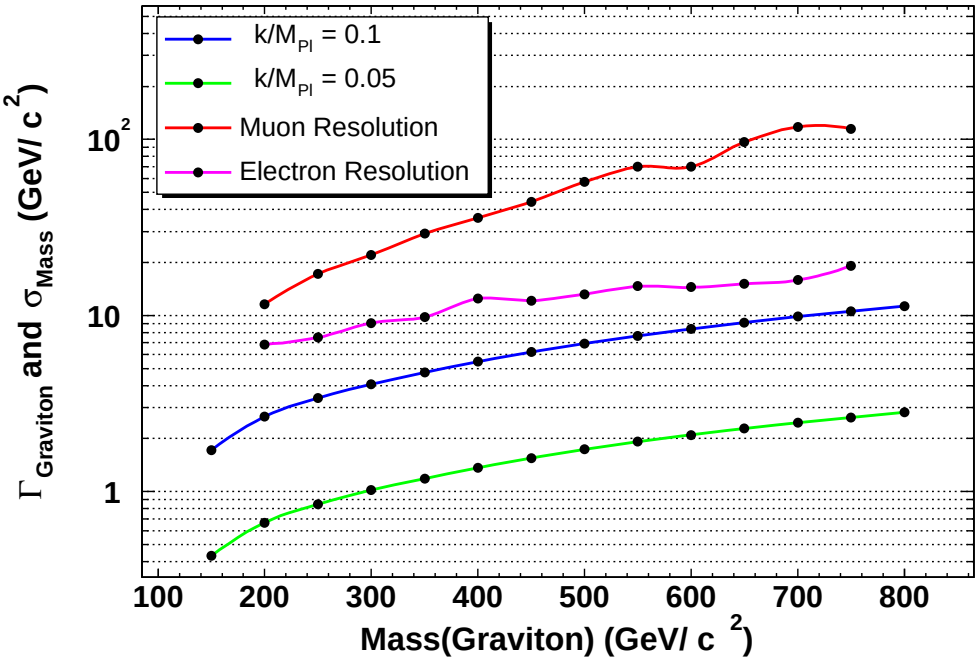

Figure 6.21: Mass resolutions for dielectrons and dimuons overlaid with the width of RS graviton for two different k/M_{Pl} values. Reconstructed mass resolutions of the graviton corresponding to k/M_{Pl} of 0.1 is used to extract the plotted detector resolutions.

Chapter 7

Results

This chapter describes the final results of the high mass dimuon analysis, and the methods used in obtaining the results. In the absence of a significant excess in the observed data with respect to the predicted background as described in Chapter 5, limits can be placed on the production cross section of resonant particles as a function of dimuon invariant mass. Further limits on the masses of various particles within the models described in Chapter 1.

7.1 Method for Setting Limits

To set the upper limits on $\sigma \cdot BR(\mathrm{Z}'/\mathrm{G} \to \mu^+\mu^-)$ at 95% confidence level and lower limits on the masses, we use a binned likelihood method[1]. The binned likelihood method starts with each bin considered as a separate data sample and its contents treated with Poisson statistics. Assuming the presence of a signal, each bin consists of a combination of the predicted signal and background events. For purposes of searches, the cross section of the signal process is usually the main quantity when one uses the event rates for the likelihood. For this, one may assign a coefficient, α, to represent the signal event rate, N^{signal} and it is this parameter that one can use to formulate a likelihood function and calculate the desired confidence limit. The likelihood is the product of the the individual bin probabilities. and it becomes a function of α. In case of errors on α, one may convolute the distribution with a Gaussian which has the mean α and width $\Delta\alpha$. The desired confidence limit on α is then calculated using this likelihood method. This limit can then be converted into a limit on cross section using the expected cross section value. The relevant formulae are summarized below:

[1]Previously, we used a single counting Bayesian limit calculation for the results which used a smaller integrated luminosity of Run II [147]. The method is outlined in Appendix G.

Poisson probability associated with each bin, i, is:

$$P_i(n_i, \mu_i) = \frac{\mu_i^{n_i} e^{-\mu_i}}{n_i!} \tag{7.1}$$

where $\mu_i = \alpha\, N_i^{signal} + N_i^{bgrnd}$. In our search, we compare only the high mass search region, above 110 GeV. The total likelihood for all channels, M, as a function of α is,

$$\mathcal{L}(\alpha) = \prod_{i=1}^{M} P_i(n_i, \mu_i) = \prod_{i=1}^{M} \frac{\mu_i^{n_i} e^{-\mu_i}}{n_i!} \quad . \tag{7.2}$$

The limits are obtained via integrating the Equation 7.2 up to the desired confidence level as below:

$$\mathcal{L}(\alpha_{95}) = (\text{norm.}) \int_0^{0.95} \mathcal{L}(\alpha) d\alpha \quad . \tag{7.3}$$

Using the below equation for the cross section:

$$N_{95} = \sigma_{95}(M) \times BR(M) \times \mathcal{L} \times A(M) \times \epsilon = \alpha_{95} \times N \quad , \tag{7.4}$$

we get Equation 7.5 below, from which 95%CL cross section limits, σ_{95}, are estimated:

$$\sigma_{95} = \alpha_{95} \times \sigma^{signal} \quad , \tag{7.5}$$

where σ^{signal} is the predicted cross section for the signal. Equation 7.5 is used to

convert the likelihoods to posterior probability densities in the cross section times branching ratio (σ). The distributions, as a function of σ, are illustrated in Figure 7.1 for various masses. There are a few effects that may be observed in these plots. One is that the likelihoods typically maximize near zero values for α or σ, if there is no apparent excess in data to support a non-zero α hypothesis (*e.g.*, $\mathcal{L}(\sigma)$ at 250 GeV/c^2). A peak in the distribution can be interpreted as a sign of excess in the data (*e.g.*, $\mathcal{L}(\sigma)$ at 300 GeV/c^2).

7.2 Pseudo-experiments

Before including the effects of systematic uncertainties on the limits, 1000 pseudo-experiments have been performed to check the statistical reliability of the experimental $\sigma \cdot BR$ limit results. The pseudo-experiments are generated using the Poisson variations of the predicted background and checked against the original prediction from which 1000 limit results are obtained. The observed limits (estimated using CDF dimuon data) are compared to the mean expected limit from the pseudo-experiments. The results are presented in Figures 7.2, for spin-1, spin-2 and spin-0 experimental limit curves. The 1, 2 and 3σ errors on the mean of the expected limit are also plotted. For spin-0, fake background contribution is also taken into account. The plots can be used to observe excesses observed in data as a function of dimuon mass,

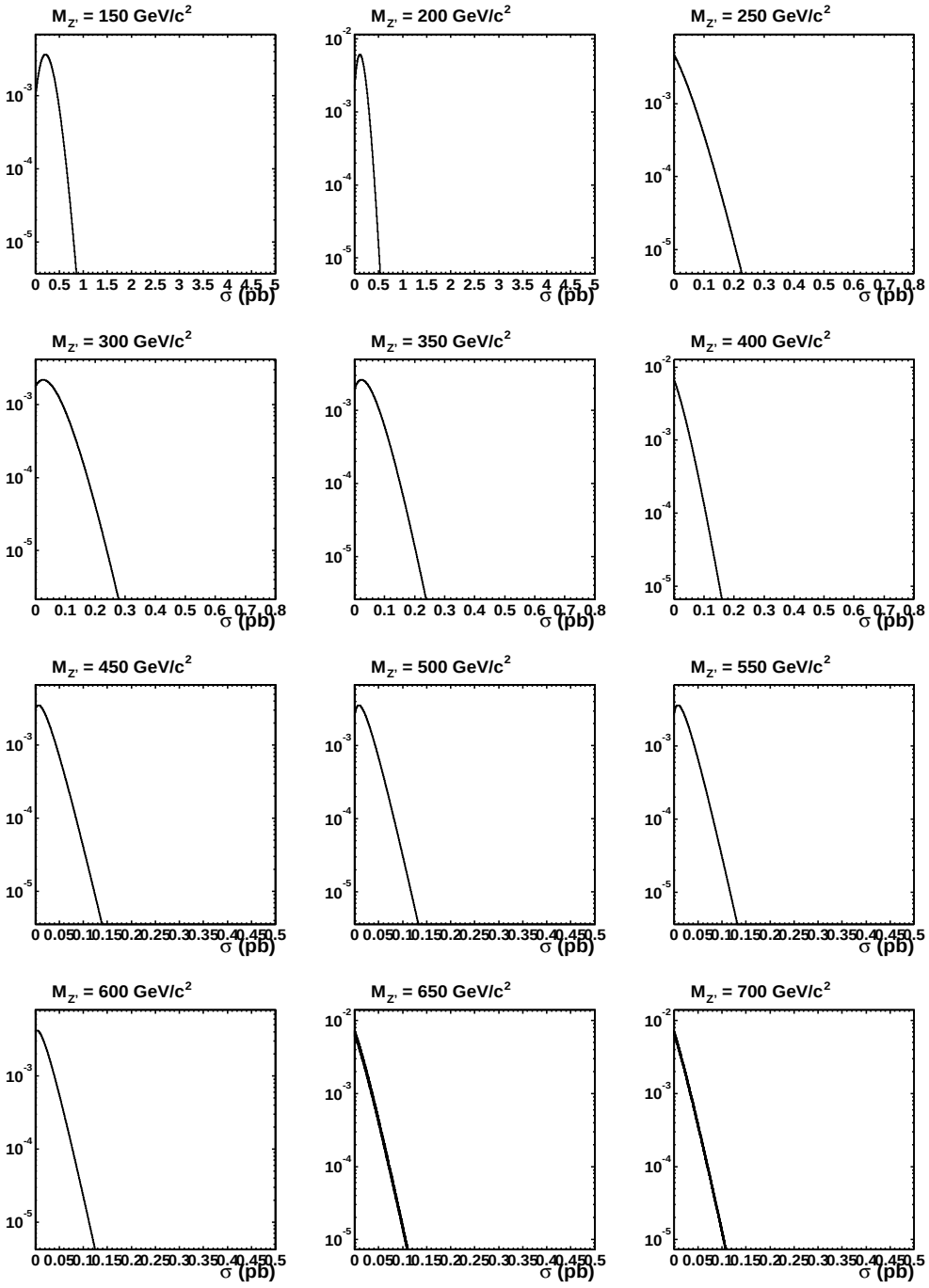

Figure 7.1: Posterior density distributions in cross section (σ, pb) without systematic errors for spin-1 particle dimuon masses.

where the observed limits are expected to be less constraining than the expected limits using the background predictions. For example, this comparison is in agreement with the slight excess of data observed 300-400 GeV/c^2 dimuon mass spectrum.

7.3 Systematic Uncertainties

To obtain the final limits, we need to assign systematic uncertainties in our calculation of signal and background events. In this analysis, we consider contributions from the sources listed below and we assume acceptance uncertainties to be uniform for all dimuons.

- Uncertainty on Acceptance: The acceptance depends on the kinematics of the physics processes and the geometry of the detector. The contributions we consider for the uncertainty in the acceptance are listed as: the choice of PDF, the momentum resolution and scale of the dimuons.

  –Choice of PDF: We estimate the error on the choice of PDF by using the acceptance changes with respect to the Z′ mass for three different choices of PDF sets. We compare the default CTEQ5L used in the acceptance calculations to other leading order PDF sets (CTEQ3L and MRST) and present the relative error on the acceptance in Figure 7.3. The average deviation for our choices is about 2% and is quoted as a mass independent PDF choice uncertainty on our

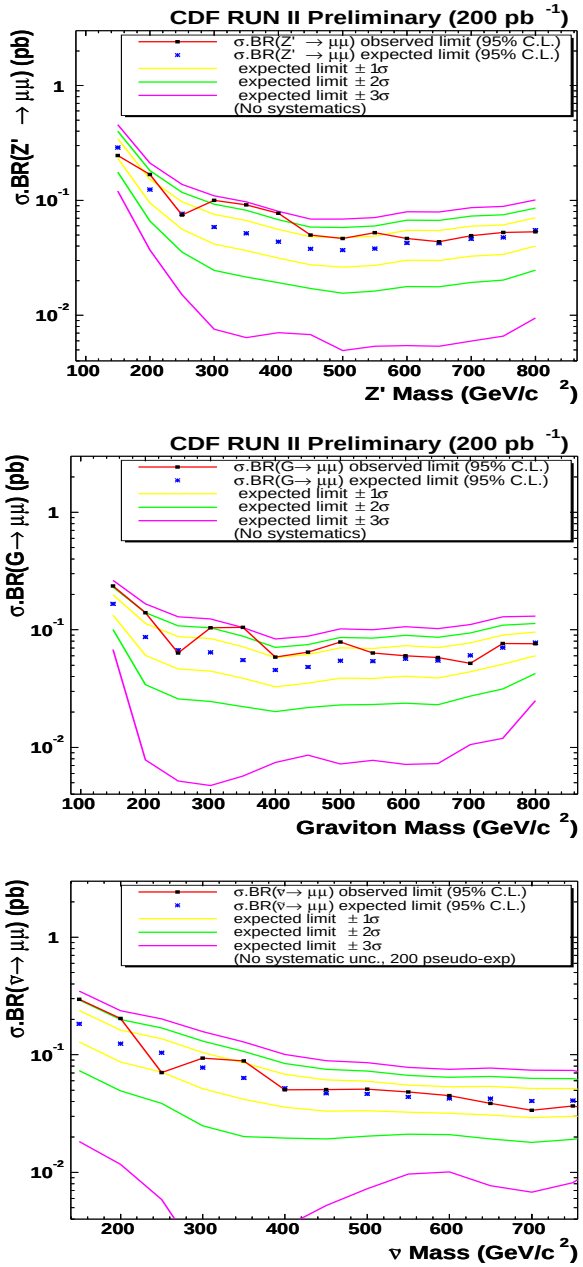

Figure 7.2: 95% C.L. upper limit expectation from pseudo-experiments with statistical errors overlayed with the observed limit for three spins.

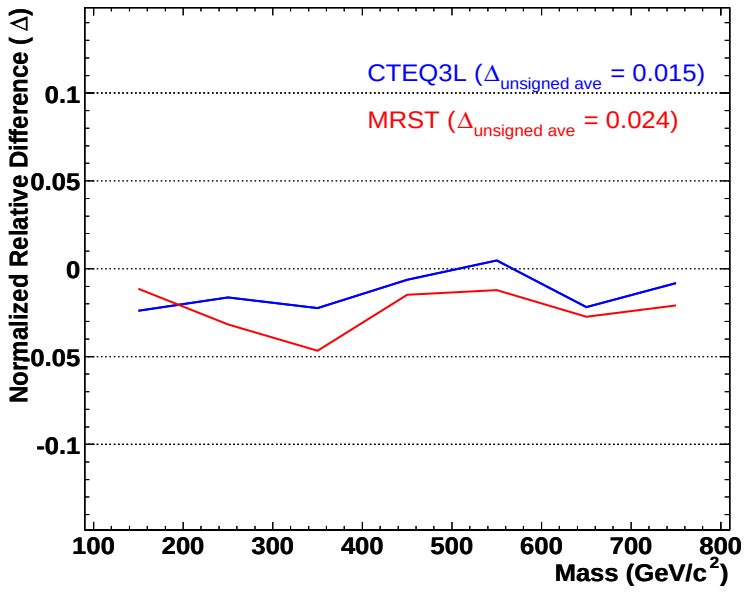

Figure 7.3: Mass dependence of the PDF uncertainty for 10k Z′ MC events.

results.

–Momentum resolution and scale: We use the invariant mass in the Z peak to determine the systematic difference between MC and data. We obtain 3.6% using the Gaussian fits to the spectra in Figure 7.4.

- Uncertainty on Efficiency: We use 2% for the efficiency error to represent the totol dimuon sample as listed in Section 4.3.

- Uncertainty on Luminosity: We use the luminosity error of 6% as described in Section 3.4.

Table 7.1: Systematic Uncertainty Summary Table.

CDF Run II Preliminary

Factor	Relative Error	
	Signal	Direct Background
PDF	0.021	0.021
Track resolution and scale	0.036	0.036
Efficiency	0.02	0.02
Luminosity	0.06	-
δA	0.076	0.046

The total systematic uncertainty is obtained when all the above mentioned contributions are combined. The summary of contributions to the direct backgrounds can be found in Table 7.1. We also consider the statistical uncertainty on the number of fake events as their systematic uncertainties.

To incorporate the systematic uncertainty in our limits, we can use the likelihood smeared (convoluted with Gaussian) by the estimated variations on α:

$$\mathcal{L}(\alpha) = \int_0^\infty \frac{d\alpha'}{\sqrt{2\pi(\Delta\alpha')^2}}\,\mathcal{L}(\alpha')\,e^{\frac{-(\alpha-\alpha')^2}{2(\Delta\alpha')^2}} \tag{7.6}$$

To calculate $\Delta\alpha$, we perform a number of pseudo-experiments by fluctuating the expected background and signal events from some template which corresponds to some nominal α. We find the best fit α for each pseudo-experiment by maximizing the likelihood for α. Another set of pseudo-experiments, with yields 1σ varied up

and down and, gives another sets of α values, by taking the average of the means of the result of the variations. We use the difference between the means of the original set and the varied sets to give the $\Delta\alpha$ for all our masses and uncertainty factors. Figures 7.5 – 7.7 show the mass dependent uncertainties on α. We also plot the total uncertainty which is the obtained through a quadratic sum of the individual uncertainties. An interesting question to ask is how much the systematic errors affect the results of 95% CL upper limits for the cross section. We have used the results of a previous study (Table 4 in [142]) to calculate the percent difference in upper limits when an uncertainty in the signal acceptance is taken into account. For a 10% relative error in the absence of observed events and backgrounds, the value obtained for the difference is 3%. Same acceptance error in the case of one observed and one background event (certain up to 10%) also yields 3%.

7.4 Limits on New Physics

Using the spin-0,-1,-2 experimental $\sigma \cdot BR(\mathrm{X} \rightarrow \mu^+\mu^-)$ limits curves, lower mass bounds on the various particles listed in Chapter 1 can be placed. This is performed by using the intersection of the 95% CL limit curves with the theoretical production curves for the models. Ignoring the PDF effects for the $\mathrm{p\bar{p}}$ collisions, the magnitude of the theoretical cross sections are determined by the partonic and leptonic couplings of

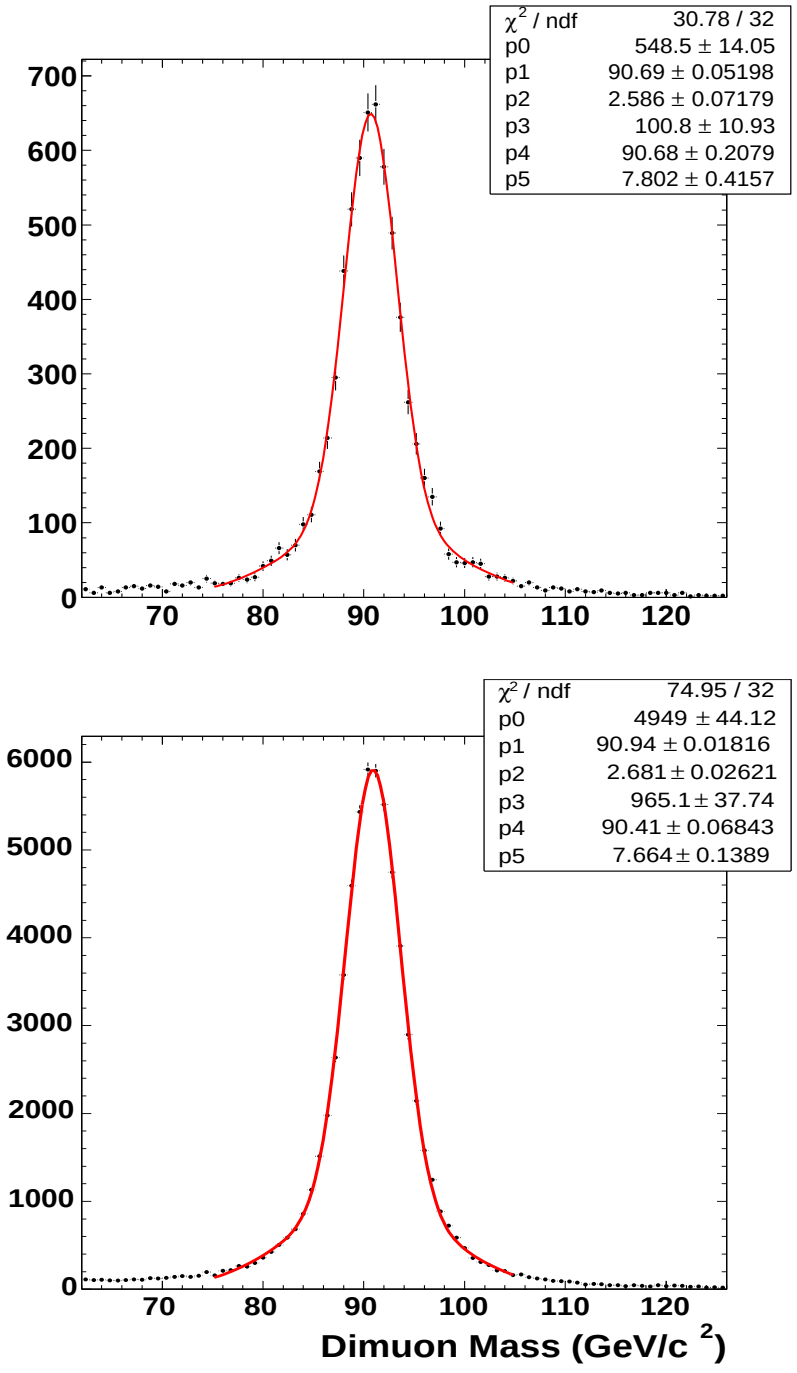

Figure 7.4: Dimuon invariant mass in data (top) and in DY MC sample (bottom).

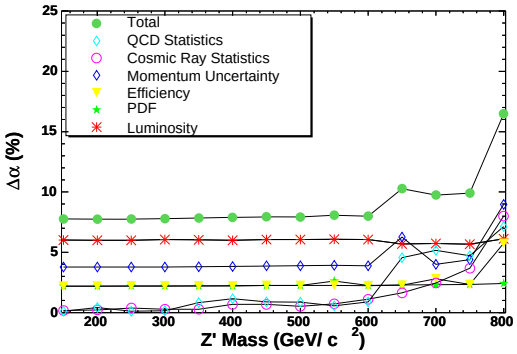

Figure 7.5: Systematic uncertainties on α as a function of Z$'$ mass.

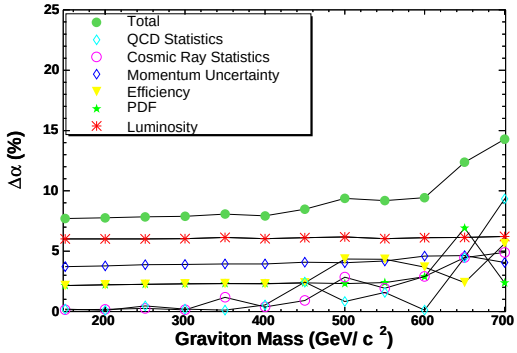

Figure 7.6: Systematic uncertainties on α as a function of graviton mass.

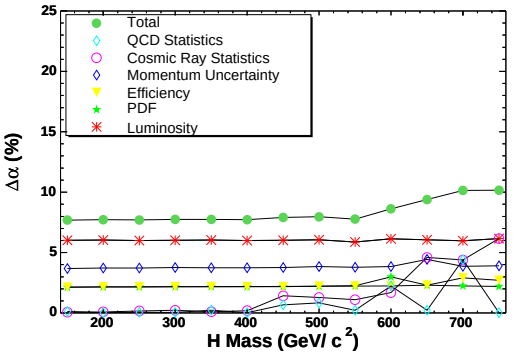

Figure 7.7: Systematic uncertainties on α as a function of Higgs mass.

the resonances which are usually dependent on the, phenomenologically important but mostly unconstrained, parameters of the theory. Such parameters are varied for the models (except the Sequential Z′, for which the couplings are preset) such that various lower mass limits are obtained as a function of these parameters. This approach allows to exclude a region of the parameter space for the models, as will be presented in the following subsections.

7.4.1 Extra Gauge Bosons: Z′

Figure 7.8 shows the 95% CL upper limit on $\sigma \cdot BR(\mathrm{Z'_{SM}} \rightarrow \mu^+\mu^-)$ as a function of dimuon mass. For the theory prediction, Pythia 6.203 is used with CTEQ5L parton distribution function (same simulation as described in Chapter 6, where the acceptance calculations are discussed). The LO calculation of Pythia is multiplied by an overall K-factor. The K-factor is taken to be 1.3, similar to Run I Z′ searches, for all extra gauge bosons that are explored. Some studies have been performed to investigate the mass dependence of the K-factor for a $\mathrm{Z'_{SM}}$. The details of the studies is detailed in Section F. The lower mass bound on a $\mathrm{Z'_{SM}}$ is 735 GeV/c^2. This result can be compared to Run I results and earlier preliminary results from Run II, as listed in Table 7.2. The 16 pb^{-1} dimuon results is described in [141]. We also place limits on the mass of the four $\mathrm{E_6}$ Z′. The cross sections for the $\mathrm{E_6}$ Z′s are

calculated by implementing the couplings of the models outlined in Section 1.5.1.2 into Pythia framework [145]. For the implementation, we followed the formalism detailed in [16]. In principle, the E_6 model places each family of fermions into a 27-plet. Each family includes the ordinary fermions as well as some new exotic particles. In the phenomenology of E_6 Z' , one often constrains the analysis in which the Z' decays only to the known SM fermions. This is the approach followed in the current analysis.

The comparison of the the theory expectations with the 95% CL limit curve is shown in Figure 7.9. The mass limits obtained using this plot are listed in Table 7.3, which is the grand summary for extra gauge boson searches. The most stringent mass limit is obtained for a Z'_η with the highest cross section prediction. The limit results for the Z'_η and Z'_ψ surpass the global PDG limits that are listed in Section 1.5.1.2.

Littlest Higgs Z_H:

We also apply the spin-1 limits to place bounds on the Littlest Higgs Z'. For this purpose, we have implemented the littlest Higgs model described in Section 1.5.1.3 into Pythia framework. At CDF, Pythia event generator is used extensively for many signal and background processes. Therefore, being able to generate this particular model with Pythia allows it to be on the same footing as other MC samples. For the implementation, Pythia version 6.212 with CTEQ5L PDF set was used. We utilized

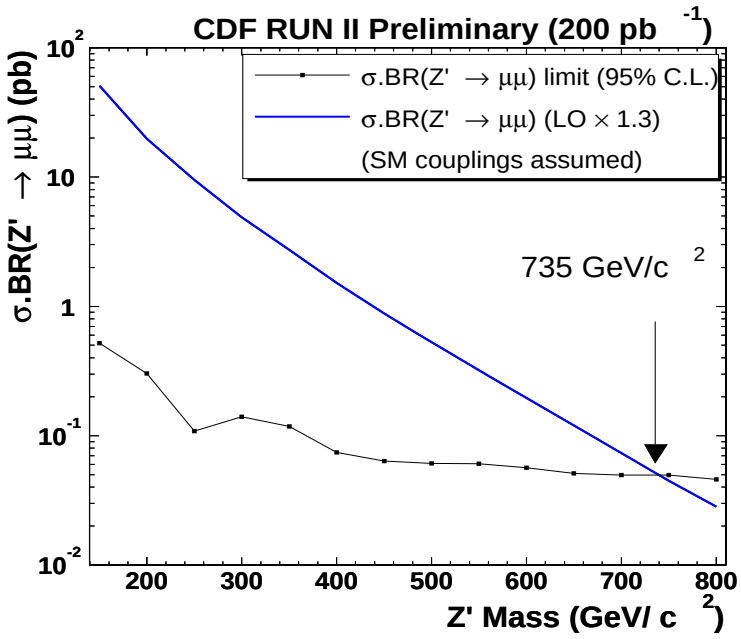

Figure 7.8: 95% C.L. upper limit on $\sigma \cdot BR(Z' \to \mu^+\mu^-)$ as a function of Z′ mass for dimuons with $\mathcal{L}$= 200 pb^{-1}.

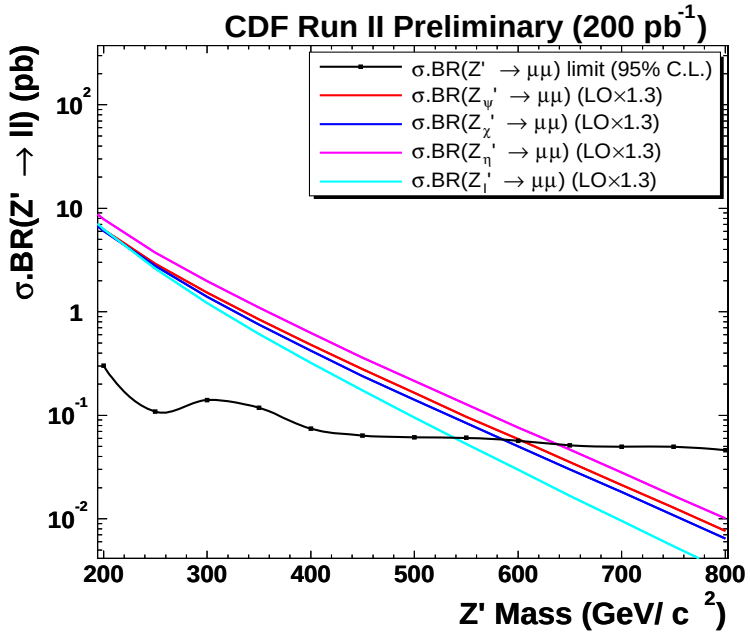

Figure 7.9: 95% C.L. upper limit on $\sigma \cdot BR(Z' \to \mu^+\mu^-)$ as a function of Z′ mass for dimuons with $\mathcal{L}$= 200 pb^{-1}.

the available Z′ that exists in Pythia and replaced the default coupling parameters with those of Z_H given as in Equation 1.28. Only the SM fermionic couplings and decays of Z_H are considered, since we explore the region $0.5<\cot\theta<1.0$ [39]. This region yields the best search sensitivity without having to deal with the other decay modes of Z_H described in Section 1.5.1.3. Figure 7.10 shows the branching fractions of Z_H as a function of its mass, as calculated in Pythia. Also, note that once the mass of Z_H is determined, $\cot\theta$ is the only other parameter for this process. Therefore, following a 2-D search strategy involving the mass and the mixing angle may be a better choice.

Figure 7.11 shows the LO Pythia cross section curve for some reference Z_H masses for $\cot\theta$ =1.0 along with some other cross section curves for comparison. This figure shows that $\sigma \cdot BR(Z_H \rightarrow \mu^+\mu^-)$ for $\cot\theta$ =1.0 is higher than the sequential Z′ cross section and it gives the best sensitivity for the searches. The lowest value of $\cot\theta$ we use yields similar cross section values to those of Z'_η of E_6 model described in Section 1.5.1.2. When we compare the cross section curves that correspond to $\cot\theta$ =1.0, we see that Pythia predicts a slightly smaller slope for the cross section compared to the formalism of [36]. Both curves are calculated taking into account the finite top quark mass in the branching fraction calculations and are produced using the same CTEQ5L PDF sets. Figure 7.12 shows the difference in cross section switching from CTEQ5L to CTEQ4M. The difference is a change in the slope of the

cross section curves.

Figure 7.13 shows the comparison of the width of a Z_H to that of a Z'_{SM} for two values of $\cot\theta$. At a mass of 800 GeV/c^2, $\Gamma(Z_H)$ is about 4 GeV larger than that of $\Gamma(Z'_{SM})$. This additional width is a negligible effect compared with the dimuon mass resolution. Therefore, we obtain lower mass limits on Z_H. The theory cross section predictions on the Littlest Higgs Z$'$ is compared to the spin-1 95% CL cross section limit results in Figure 7.14. The mass limits are calculated for three different values of $\cot\theta$. The best value for the lowest mass bounds corresponds to $\cot\theta = 0.9$, which is 775 GeV/c^2. At this particular value, the cross section expectations are higher for a Z_H as compared to a Z'_{SM}, therefore the mass bounds are stronger. The 2-D exclusion region in mass versus $\cot\theta$ is given in Figure 7.15.

7.4.2 Technicolor: ω_T, ρ_T

The parametrization and description of Technicolor model is given in Section 1.5.4. Since the techni-mesons are spin-1 particles, with narrow resonance predictions, we compare the cross section expectations of these particles with respect to the Z$'$ experimental 95% CL limit results. We obtain the cross sections using Pythia and correct for the higher order effects with the K-factor. The treatment of the model in Pythia V6.203 involves mixing between the γ^*, Z^0, ρ_T and ω_T particles in the Drell-Yan

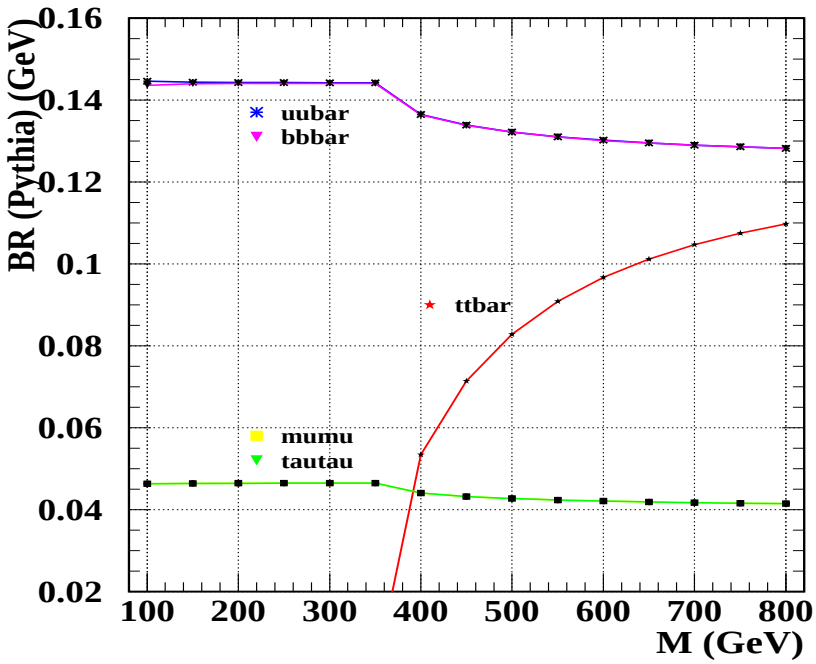

Figure 7.10: Z_H branching fractions as a function of generated mass. The curves corresponding to the leptons selected as examples (μ and τ) overlap over the full mass region.

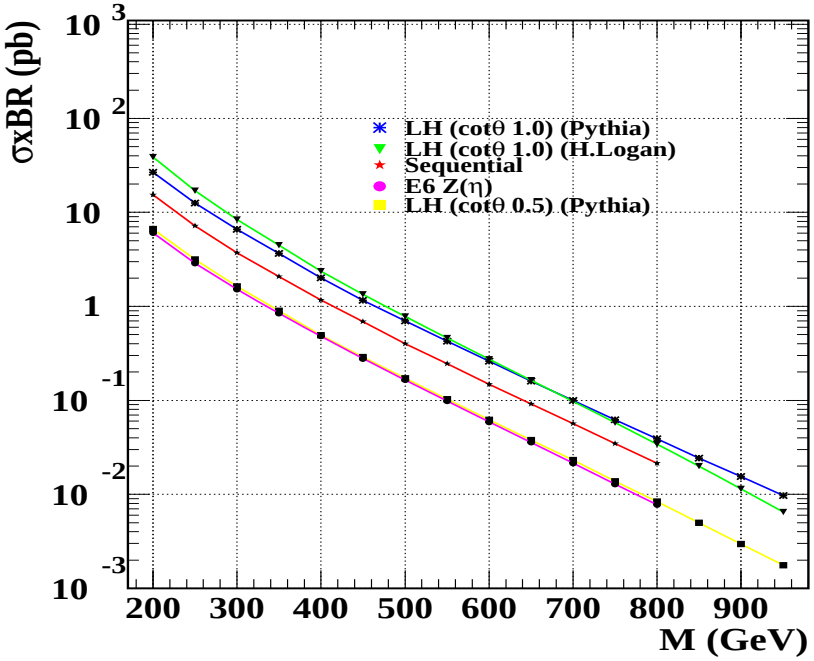

Figure 7.11: Lowest order $\sigma \cdot BR(Z_H \to \ell^+\ell^-)$ for two $\cot\theta$ values compared with various Z′ predicted cross sections. All curves are produced using CTEQ5L PDF set. The green curve is courtesy of [39].

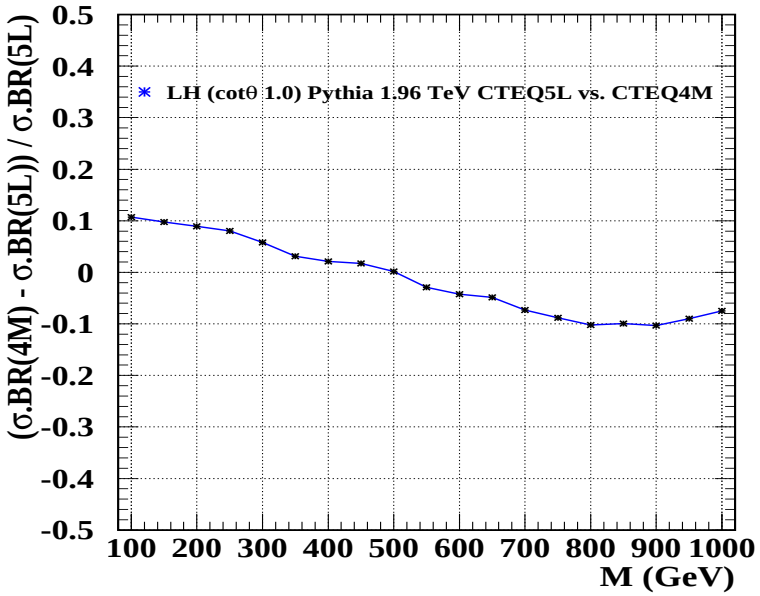

Figure 7.12: Difference in the LO Z_H cross section with respect to different PDF's.

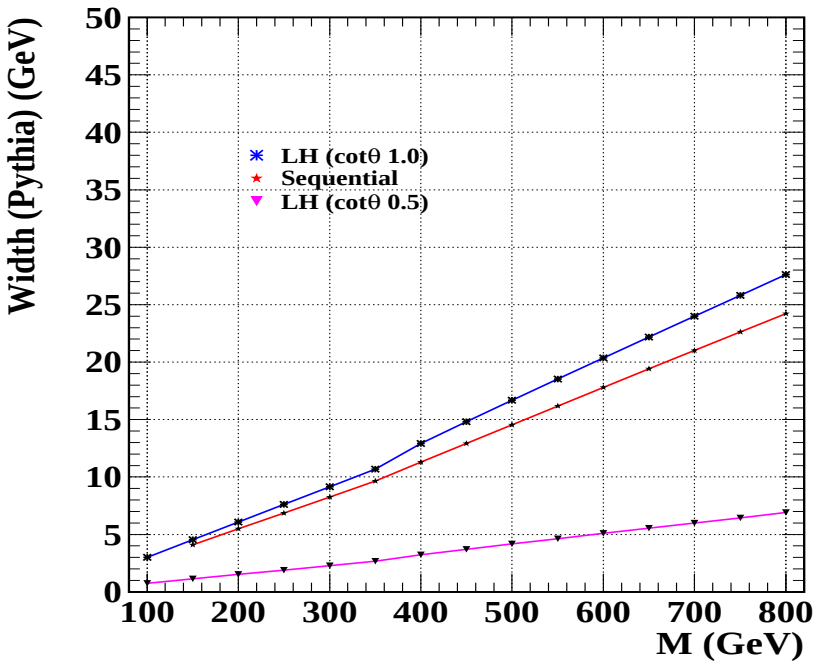

Figure 7.13: Resonance width for the Z_H as a function of mass and for two $\cot\theta$ values compared with the Z'_{SM} width as calculated in Pythia.

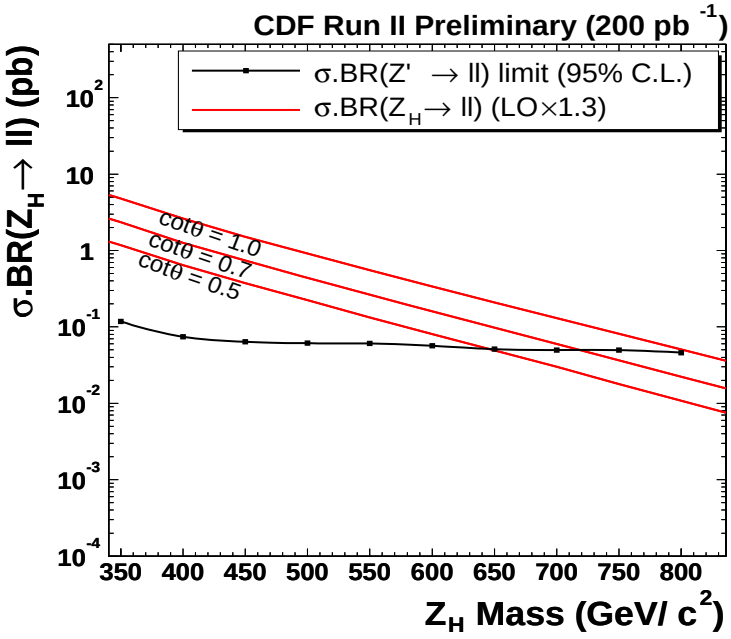

Figure 7.14: 95% C.L. upper limit on $\sigma \cdot BR(\mathrm{Z}_H \to \mu^+\mu^-)$ as a function of mass for dimuons with $\mathcal{L}$= 200 pb^{-1}.

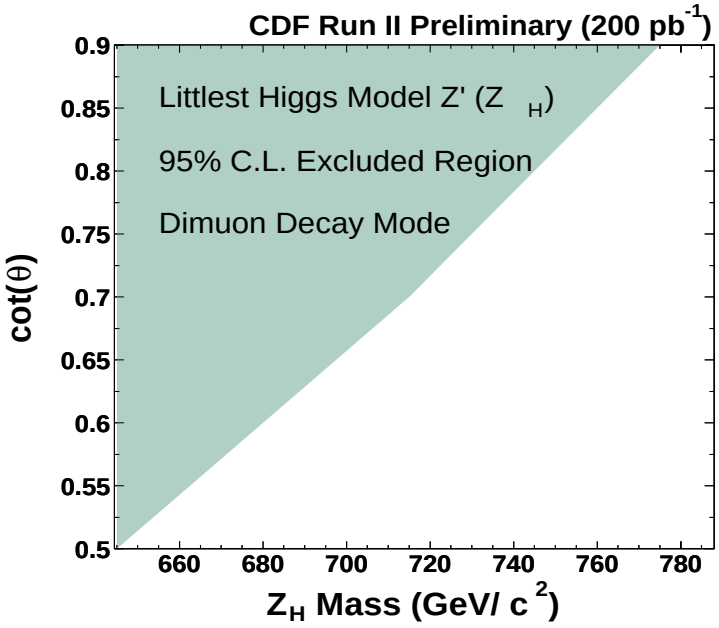

Figure 7.15: 95% C.L. exclusion curve for Littlest Higgs Z′.

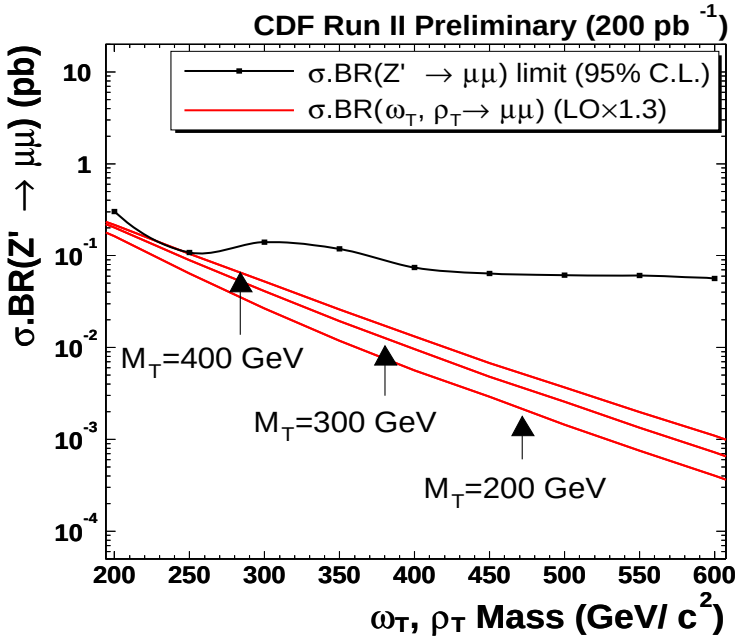

Figure 7.16: 95% C.L. upper limit curve overlayed with $\sigma \cdot BR(\rho_{\mathrm{T}},\omega_{\mathrm{T}} \rightarrow \mu^{+}\mu^{-})$ as a function of mass for dimuons with $\mathcal{L}$= 200 pb^{-1}.

process, as well as a signal-only calculation. To extract the signal contribution with the interference, a mass window around the signal pole mass should be applied and the SM contribution from the total cross section should be subtracted. The $d\sigma/dM$ distributions can be found in [143]. The two calculations yield the same results [144].

7.4.3 Randall-Sundrum Graviton

The limits for a first excited state of RS graviton is obtained by using the spin-2 acceptances calculated as a function of RS graviton mass. Figure 7.17 shows the

CDF Run II Preliminary

CDF Run	Luminosity (pb^{-1})	$M_{Z',95\%C.L}$ (GeV/c)
IA	18.8	440
IB	88.6	575
IIA (summer '02)	16	275
IIA (winter '03)	72.0 (56.0 for CMX)	455
IIA (summer '03)	126 (110 for CMX)	585
IIA (winter '04)	200 (180 for CMX)	735

CDF Run	Luminosity (pb^{-1})	$M_{G,95\%C.L}$ (GeV/c) ($k/M_{Pl} = 0.1$)
IA	–	–
IB	–	–
IIA (summer '02)	16	255
IIA (winter '03)	72.0 (56.0 for CMX)	370
IIA (summer '03)	126 (110 for CMX)	475
IIA (winter '04)	200 (180 for CMX)	605

Table 7.2: History of CDF neutral boson searches (Z′ and RS Graviton) in the dimuon channel.

CDF Run II Preliminary

Model	Mass Limit at 95%C.L (GeV/c)		
	Run I	Run II (summer '03)	Run II (winter '04)
Z'_{SM}	590	585	735
Z'_{η}	520	495	635
Z'_{ψ}	495	465	600
Z'_{χ}	500	455	580
Z'_{I}	480	425	530

Table 7.3: Results for Z′s.

95% CL upper limits on $\sigma \cdot BR(\mathrm{G} \rightarrow \mu^+\mu^-)$ as a function of graviton mass. Currently, there is no higher order QCD correction to the LO RS Graviton production. For RS graviton limits analysis, the K-factor from Drell-Yan production is used. Given that the gravitons can be produced through gluon annihilation and that this cross section is small but not totally negligible (Figure 1.10), it may be possible to further consider a more appropriate higher order correction. In any case, the K-factor for graviton production is not expected to be very much different than the DY K-factor [144]. For the validity of the current approach, Run I Tevatron results for the large extra dimensions searches ([148]) can also be cited.

The mass limits are obtained by using the Pythia LO cross section values multiplied by a K-factor of 1.3 and parameterized in terms of the dimensionless coupling parameter, $\mathrm{k/M_{Pl}}$. The largest mass limits for RS graviton is 605 $\mathrm{GeV/c^2}$, corresponding to $\mathrm{k/M_{Pl}} = 0.1$. The choice of this upper bound of $\mathrm{k/M_{Pl}}$ is driven by considerations to to assure the consistency of the low-energy theory [41]. The excluded parameter space of the RS extra dimensions is shown in Figure 7.18.

7.4.4 $\not{R}_P$ Supersymmetry: $\widetilde{\nu}$ Production

We use the acceptance for spin-0 particle to place limits on the $\not{R}_P$ $\widetilde{\nu}$ which can decay into a muon pair. The phenomenological parameter in this model is $\lambda'^2 \cdot \mathrm{BR}$, which

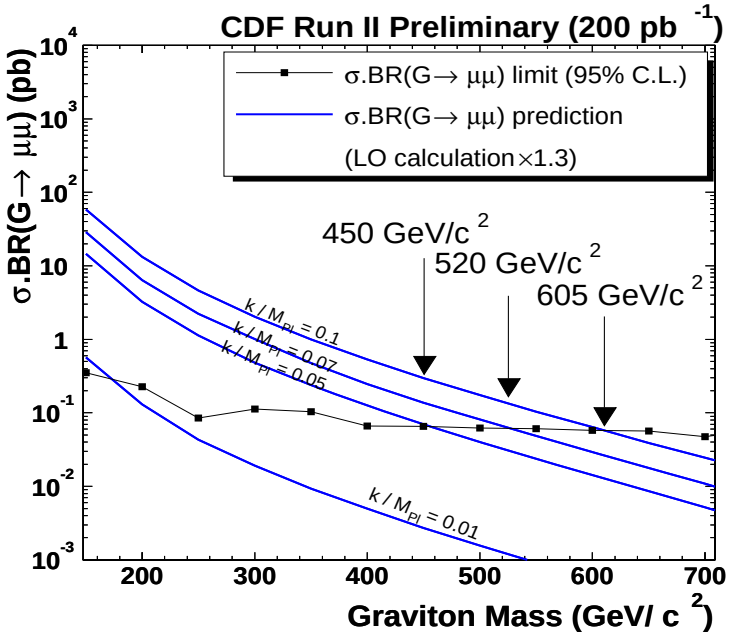

Figure 7.17: 95% C.L. upper limits on $\sigma \cdot BR(\mathrm{G} \to \mu^+\mu^-)$ (pb) as a function of G mass with $\mathcal{L}$= 200 pb^{-1}for various k/M$_{\mathrm{Pl}}$ values.

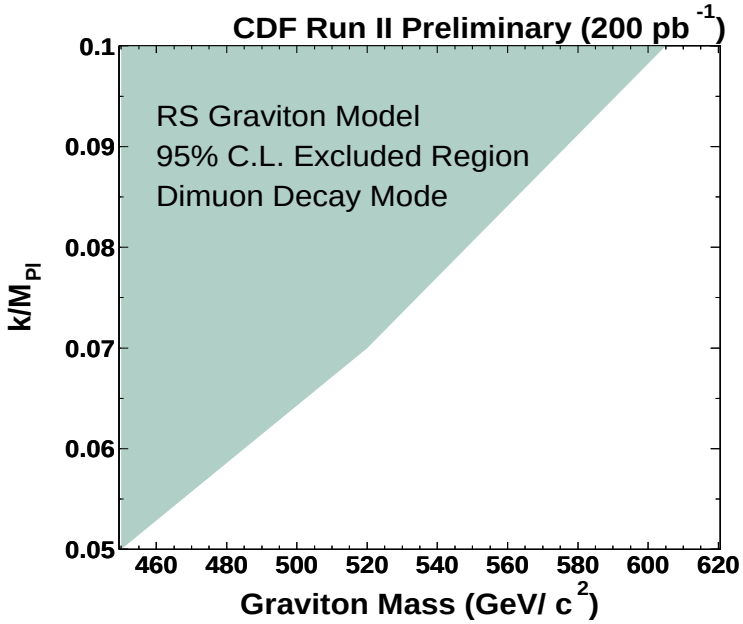

Figure 7.18: 95% C.L. exclusion curve for RS Graviton.

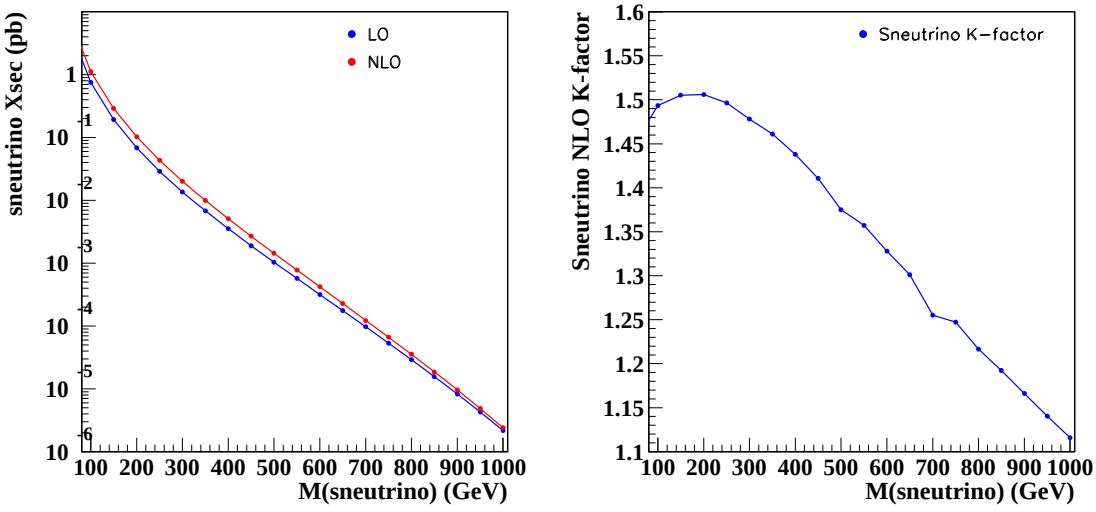

Figure 7.19: NLO and LO cross section and NLO K-factor curves as a function of $\not{R}_P$ $\widetilde{\nu}$ mass.

governs the coupling of the $\widetilde{\nu}_\tau$ to the quark pair and its decay Branching fraction to dimuons, as can be inferred from Figure 1.11. We set limits for various values of λ'^2·BR for the process $p\bar{p}\rightarrow\widetilde{\nu}_{tau}\rightarrow\mu^+\mu^-$. The cross section values are obtained from [149]. The cross sections are calculated using NLO QCD corrections with CTEQ5 PDF set. The cross section values as a function of mass and the corresponding K-factorvalue is shown in Figure 7.19. Figure 7.20 shows the 95% CL upper limits on $\sigma \cdot BR(\widetilde{\nu} \rightarrow \mu^+\mu^-)$ as a function of $\widetilde{\nu}$ mass and for various λ'^2·BR values.

The summary of experimental limits for all spins is represented in Figure 7.22. We illustrate the effect of including systematic uncertainties in our limit calculations in Figure 7.21.

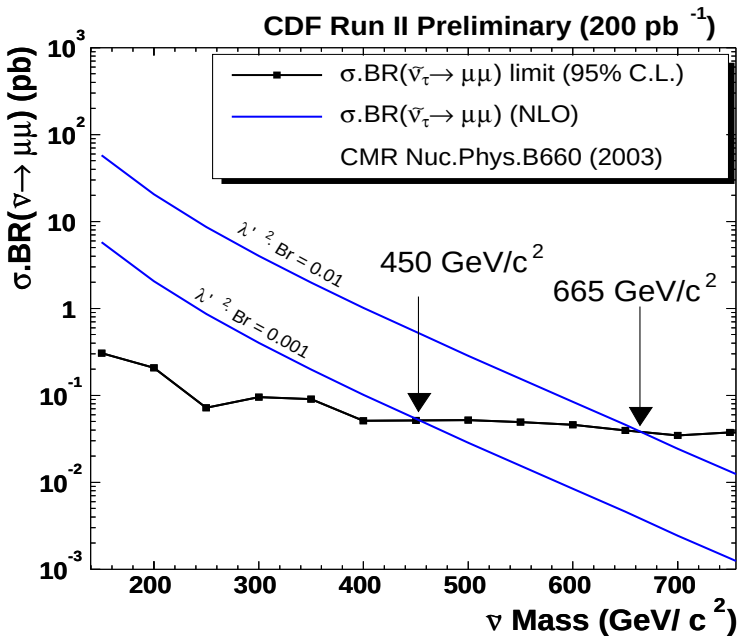

Figure 7.20: 95% C.L. upper limits on $\sigma \cdot BR(\widetilde{\nu} \rightarrow \mu^+\mu^-)$ (pb) as a function of $\widetilde{\nu}$ mass with $\mathcal{L}$= 200 pb^{-1} for various λ'^2·BR values.

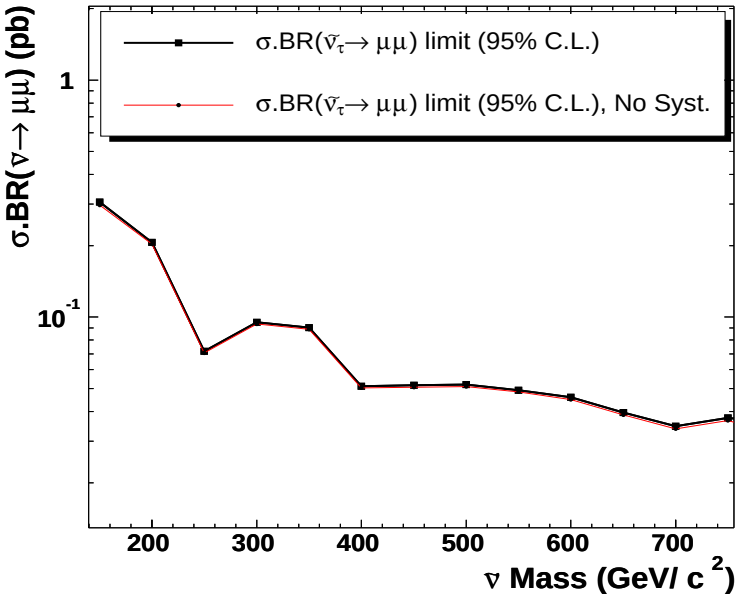

Figure 7.21: 95% C.L. $\sigma \cdot BR(\ \to \mu^+\mu^-)$upper limits on spin-0 particle as a function of mass with $\mathcal{L}$= 200 pb^{-1}. This plot compares the limits with and without systematical errors.

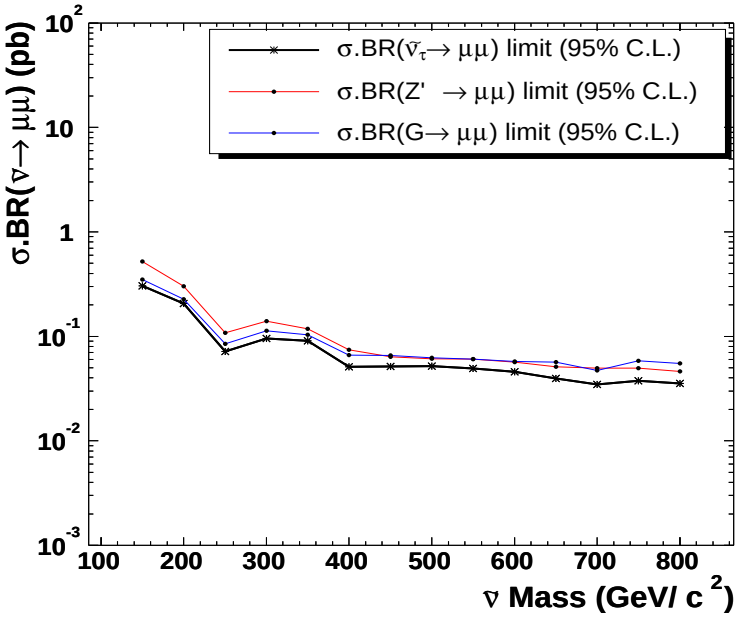

Figure 7.22: 95% C.L. upper limits on spin-0,-1,-2 as a function of reference masses for dimuons with $\mathcal{L}$= 200 pb^{-1}.

7.5 Combined Limits Using Dielectron and Dimuon (Dilepton) Channels

This section describes the combined dielectron and dimuon limits for heavy neutral particles in Spin-0,1,2 states. The dielectron results also used about 200 pb^{-1} high p_{T} and E_{T} data taken during February 2002- September 2003. The individual dielectron results for 95% CL upper limits on the $\sigma_{95\%CL}$.BR and 95% CL mass limits are detailed someplace else [137, 150].

For the combination, correlated and uncorrelated uncertainties between the dimuon and dielectron channels should be considered. The PDF uncertainty on acceptance, the luminosity and the event vertex efficiency uncertainties are considered to be fully correlated between the dielectron and dimuon channels. The likelihoods are smeared according to the uncertainties using Gaussian distribution with $\Delta\alpha$:

$$\mathcal{L}(\alpha) = \int_0^\infty \frac{d\alpha'}{\sqrt{2\pi(\Delta\alpha')^2}}\,\mathcal{L}(\alpha')\,e^{\frac{-(\alpha-\alpha')^2}{2(\Delta\alpha')^2}}\,. \tag{7.7}$$

There are n likelihood functions that need to be smeared, for each reference signal mass considered in the analysis. Here, we use $\mathcal{L}(\sigma.\cdot BR)$ instead of $\mathcal{L}(\alpha)$ via a translation of variables. For the determination of the final uncertainties, we use systematic uncertainty estimates on α ($\Delta\alpha$) as listed in [137, 96]. The $\Delta\alpha$ values are

directly applicable to the likelihoods as a function of σ since they are represented in fractional (percentage) form. The full systematic uncertainty in α is broken into two parts: $\Delta\alpha^{corr}$ and $\Delta\alpha^{uncorr}$. We treat CC (i=1) CP(j=2) and $\mu\mu$ (k=3) as three separate channels for combination. The matrix for the uncertainties, then, is a 3×3 symmetric matrix where the symmetric elements represent the correlated uncertainties among each channel:

$$\begin{pmatrix} c_{11} & c_{12} & c_{13} \\ c_{21} & c_{22} & c_{23} \\ c_{31} & c_{32} & c_{33} \end{pmatrix} + \begin{pmatrix} c_{123} & 0 & 0 \\ 0 & c_{123} & 0 \\ 0 & 0 & c_{123} \end{pmatrix} \tag{7.8}$$

c_{ij} are the coefficients of the uncertainties which are used to Gaussian smear the individual likelihoods. For example, in the case of two channels, the smeared σ' can be written out such as:

$$\sigma'_{11} = c_{11} + c_{11}\Delta\sigma_{11} + c_{12}\Delta\sigma_{11} \tag{7.9}$$

$$\sigma'_{22} = c_{22} + c_{21}\Delta\sigma_{22} + c_{22}\Delta\sigma_{22} \tag{7.10}$$

Figure 7.23 shows the likelihoods used for combination for a 500 GeV/c spin-0 particle. The red lines represent the effect when correlated and uncorrelated systematics are taken into account.

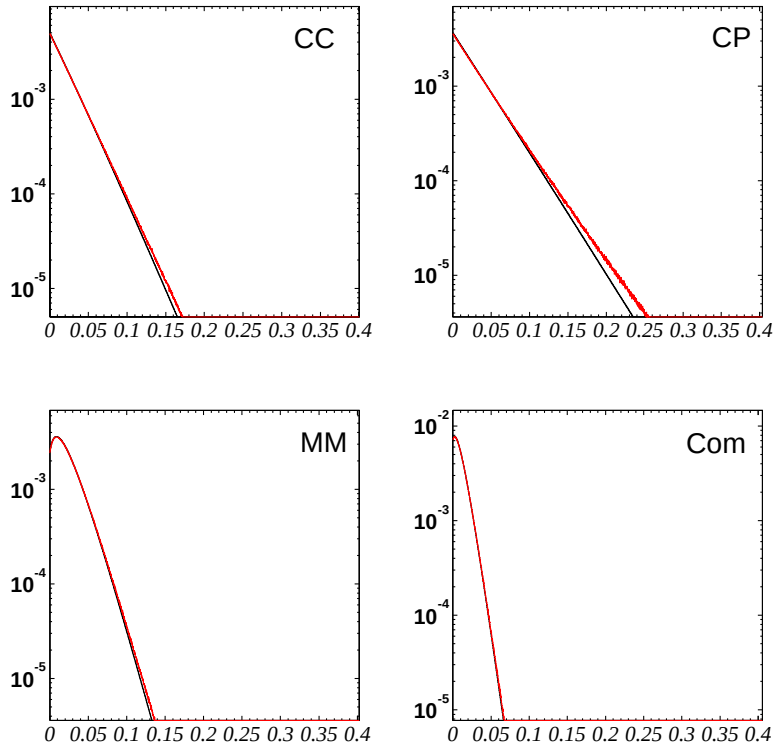

Figure 7.23: Likelihood functions without systematic errors for combination for a 500 GeV/c^2 spin-1 particle.

Results for the upper limits in σ.BR is shown in Figures 7.25, 7.26 and 7.24 for spin-1, spin-2 and spin-0 particles. Table 7.4 summarizes the history of CDF Z'_{SM} searches in the dilepton channel from Run IA ([151]), Run IA+B ([32]) and Run II. Table 7.5 lists the Run II combined results for E_6 Z′s and Table 7.6 shows the comparison of E_6 Z′ results with those from Run I. Tables 7.7 - 7.10 list the results obtained for little Higgs Z′, techni-mesons, RS graviton and $\widetilde{\nu}$, respectively.

CDF Run II Preliminary

CDF Run	Luminosity (pb^{-1})	$M_{Z'_{SM},95\%C.L}$ (GeV/c^2)
IA	18.8	505
IA+B	110	690
IIA	72	665
IIA	126	730
IIA	200	815

Table 7.4: History of CDF Z'_{SM} searches in the dilepton channel.

Model	E_6 Mass Limit at 95%C.L (GeV/c^2)		
	e^+e^-	$\mu^+\mu^-$	$\ell^+\ell^-$
Z'_{SM}	750	735	815
Z'_{ψ}	635	600	690
Z'_{χ}	620	585	670
Z'_{η}	655	640	715
Z'_{I}	575	540	610

Table 7.5: Combined Results for E_6 Z′s.

Model	Mass Limit at 95%C.L (GeV/c^2)	
	Run I	Run II
Z'_{ψ}	495	690
Z'_{χ}	500	670
Z'_{η}	520	715
Z'_{I}	480	610

Table 7.6: CDF Run I and II comparison of combined Results for E_6 Z′s.

$\coth\theta$	Z_H Mass Limit at 95%C.L (GeV/c^2)		
	e^+e^-	$\mu^+\mu^-$	$\ell^+\ell^-$
1.0	810	805	875
0.9	785	780	850
0.7	735	715	800
0.6	700	685	765
0.5	665	640	720

Table 7.7: Combined Results for Littlest Higgs Z′.

M_T	TC Mass Limit at 95%C.L (GeV/c^2)
	$\ell^+\ell^-$
500	320
400	315
300	310
200	225

Table 7.8: Combined Results for Techni-mesons, $\rho_{\rm T}$, $\omega_{\rm T}$.

k/$M_{\rm Pl}$	RS Graviton Mass Limit at 95%C.L (GeV/c^2)		
	e^+e^-	$\mu^+\mu^-$	$\ell^+\ell^-$
0.1	640	610	700
0.05	485	455	525
0.01	200	170	200

Table 7.9: Combined Results for RS Gravitons.

λ'^2·BR	$\widetilde{\nu}_\tau$ Mass Limit at 95%C.L (GeV/c^2)		
	e^+e^-	$\mu^+\mu^-$	$\ell^+\ell^-$
0.1	670	665	725
0.05	615	590	665
0.01	470	455	510

Table 7.10: Combined Results for RPV $\widetilde{\nu}$.

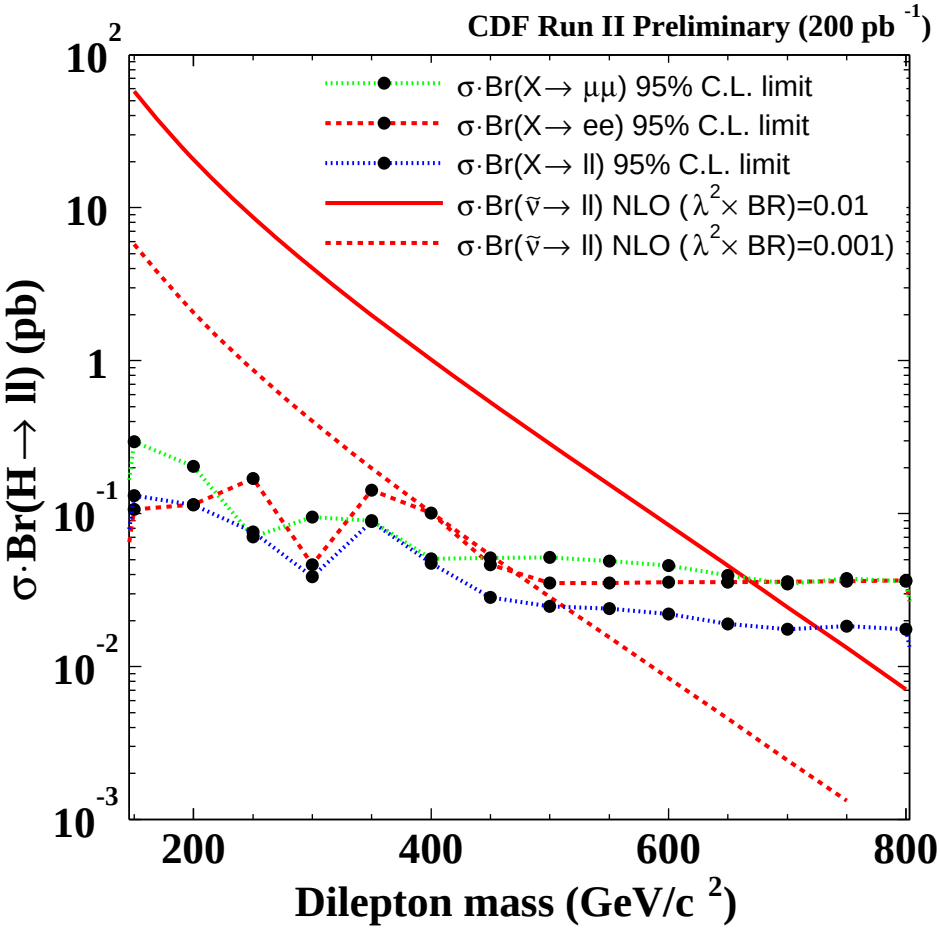

Figure 7.24: 95% C.L. combined limits for spin-0 particles.

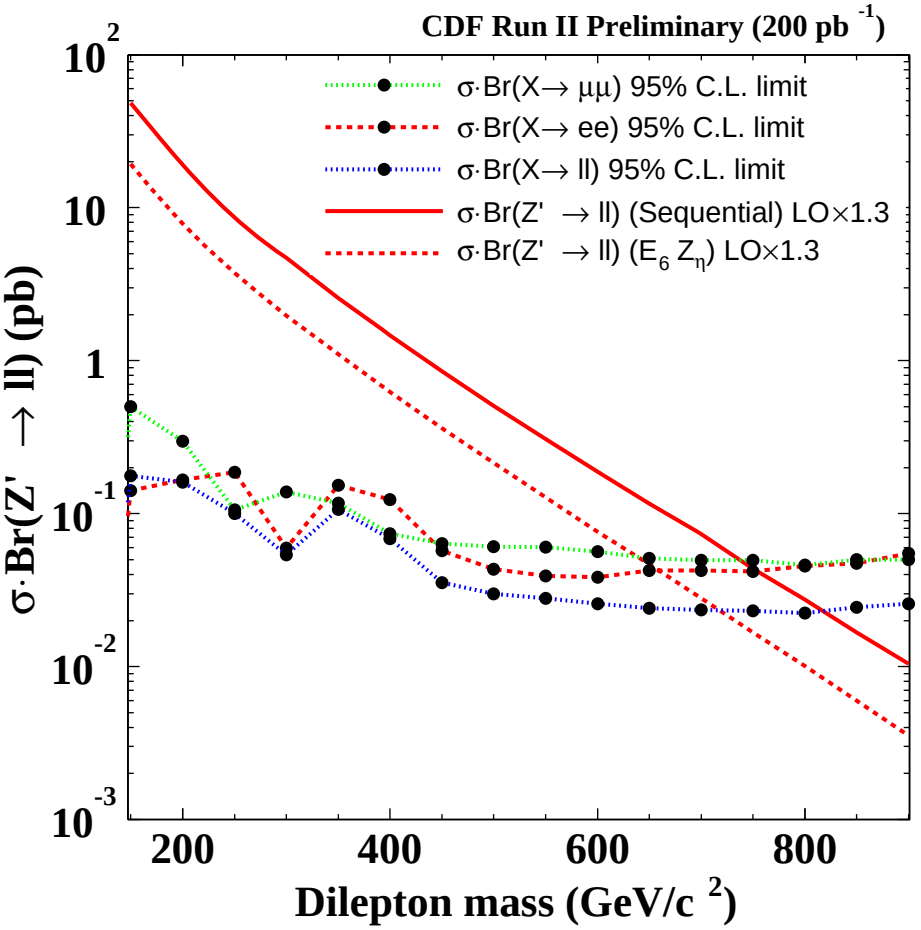

Figure 7.25: 95% C.L. combined limits for spin-1 particles.

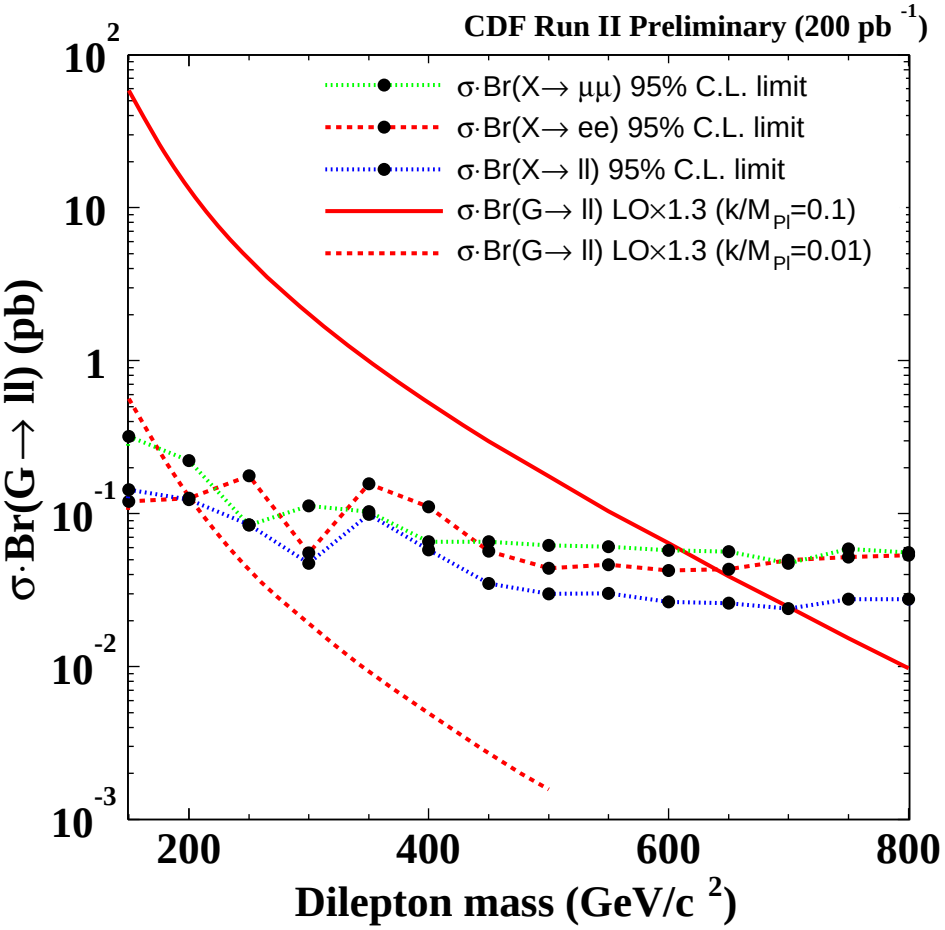

Figure 7.26: 95% C.L. combined limits for spin-2 particles.

Chapter 8

Conclusions

"Somewhere, there is something incredible waiting to be known."

Carl Sagan

We have set preliminary 95% CL $\sigma \cdot BR(\mathrm{X} \to \mu^+\mu^-)$ upper and mass lower limits on various predicted new particles using the dimuon decay channel. The data used compromised of approximately 200 pb^{-1} of $\mathrm{p\bar{p}}$ collision data from CDF II taken at $\sqrt{s}$ = 1.96 TeV between spring 2002 and fall 2003. Above an invariant mass of 500 $\mathrm{GeV/c^2}$, 95% CL upper $\sigma \cdot BR(\mathrm{X} \to \mu^+\mu^-)$ limits are $\gtrsim$ 50 pb, similar for the three different spin categories. Preliminary mass limits are also placed, as listed below.

- Z′ gauge boson: SM-Like Z′ boson limit, $\mathrm{M(Z'_{SM})} > 735\ \mathrm{GeV/c^2}$

- First excited state of RS Graviton: M(G) > 605 GeV/c^2 for k/M_{Pl} of 0.1
- $\not{R}_p$ $\widetilde{\nu}$: M($\widetilde{\nu}$) > 665 GeV/c^2 for λ'^2·BR of 0.01.

We have surpassed the sensitivity and tightened the limits for new physics compared with the Run I high mass dimuon resonance searches. We have used CMX detector for the first time in dimuon resonance searches also presented the first results from Run II. Current limits of the CDF experiment exceed published limits of previous direct searches in the dimuon channel, as well as the ongoing collider direct limits. We have also pioneered search strategies and exploration of some models. Similar results are also presented in the combined dilepton mode. With the sensitivity doubled, the limits are more stringent in the dilepton channel and also exceed previously published direct limit results.

8.1 Future Prospects

CDF has been taking collision physics data since 2002. Both during the time of the analysis presented here and afterward, the understanding of the CDF detector and its data has improved, as well as the analysis and data taking platforms. The analysis performed here can be repeated when a large enough luminosity is achieved to surpass these limits considerably. The significance of the slight excesses observed in the data, as described in earlier chapters, should also be tested with more data. The parts

of the CDF muon system not utilized in this analysis (BMU, CMX miniskirts) may be added in future as well. With larger event samples, an analysis which involve a simultaneous fit to the invariant mass spectrum and the dimuon angular distribution may be performed. A search which uses forward-backward asymmetry of the dimuons may also be performed [1]. High mass dimuons can also be used to search for beyond the SM in models for which the excess is a continuous spectrum. Two examples are the large extra dimensions and compositeness [153]. CDF has preliminary results in dielectrons channel for large ED searches where lower bounds on the Planck scale has been placed [154].

Tevatron Run IIA will continue through 2005, at which point Run IIB will take over after various accelerator and detector upgrades. By the year 2009, the Tevatron baseline goal for integrated luminosity is 4.4 $pb^{-1}$and the design goal is 8.5 pb^{-1}. The prospects of $\sigma \cdot BR(Z' \rightarrow \mu^+\mu^-)$ at the CDF experiment using larger luminosity data samples is given in Figure 8.1, for three different luminosities [2]. The limit reach Tevatron is calculated via simple counting limit method, assuming absence of observation and backgrounds without systematic errors on the acceptance and efficiency. The $\sigma \cdot BR$ limits are inversely proportional to the luminosity. Therefore, at 6 fb^{-1}, the limits of 0.2 $fb^{-1}$are expected to be about 25-30 times better. The

[1]Such an analysis is being planned, using the dielectron channel, which has higher $|\eta|$ coverage as compared to muons [152].

[2]Here, an average of base and design luminosity goals have been taken to represent highest limit prospects for a $\mathcal{L}$ expected to be achieved around 2007.

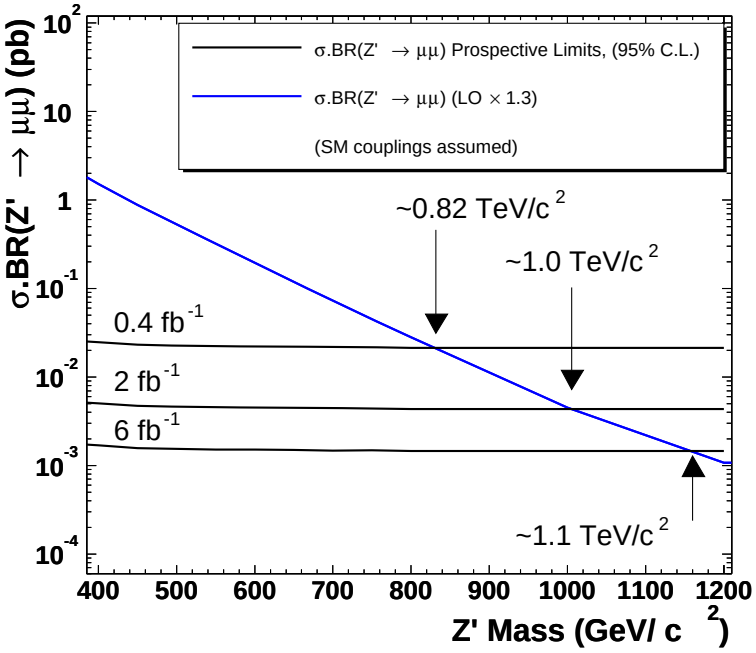

Figure 8.1: Future prospects for Z'_{SM} at the Tevatron.

mass limits are, as described earlier in Chapter 1, have a non-linear (logarithmic) dependence on the luminosity, so the mass reach will be about 1.1 TeV/c^2at 6 fb^{-1}.

Near the end of this decade, the two general purpose experiments (ATLAS and CMS) at the Large Hadron Collider [43] (LHC) will start taking data at $\sqrt{s} = 14$ TeV of proton-proton collisions. This will be the beginning of a new era in high energy physics. What is referred to as "high mass" final states in this analysis, will be considered as "low mass" final states, for the available energies at the LHC. Many models that we have explored in this analysis will be explored at multi-TeV scales.

We illustrate the LHC expectations using the SM-like Z′. Figure 8.2 shows the $\sigma \cdot BR(\mathrm{Z'_{SM}} \to \mu^+\mu^-)$ at $\sqrt{s} = 14$ TeV proton-proton collisions at the LHC. The cross sections are calculated using Pythia and CTEQ5L PDF set, similar to the Tevatron Z′ calculations used in the analysis. For a 500 GeV/c^2 Z′, the production cross sections increase by about an oder of magnitude compared to the Tevatron energies [3]. For a 2 TeV/c^2 Z′, the $\sigma \cdot BR$ is approximately 200 fb. The anticipated integrated luminosity collected for the LHC in the first year of running is about 20 fb^{-1} for L = 2×10^{33} cm^{-2}s^{-1} with a possible start-up in spring 2007 [155]. Assuming a 50% acceptance times detection efficiency for a 2000 GeV/c^2 Z′, about 2000 events are expected to be observed, which is a significant event yield. Therefore, depending on the backgrounds for the signals expected, the LHC experiments will have potential to make exciting discoveries. In case of no signal observation, they will also rule out or tighten the parameter spaces of many proposed models, many of which we have already explored within the context of this analysis.

[3] A similar statement can be made for the production cross section of Z_H within little Higgs model.

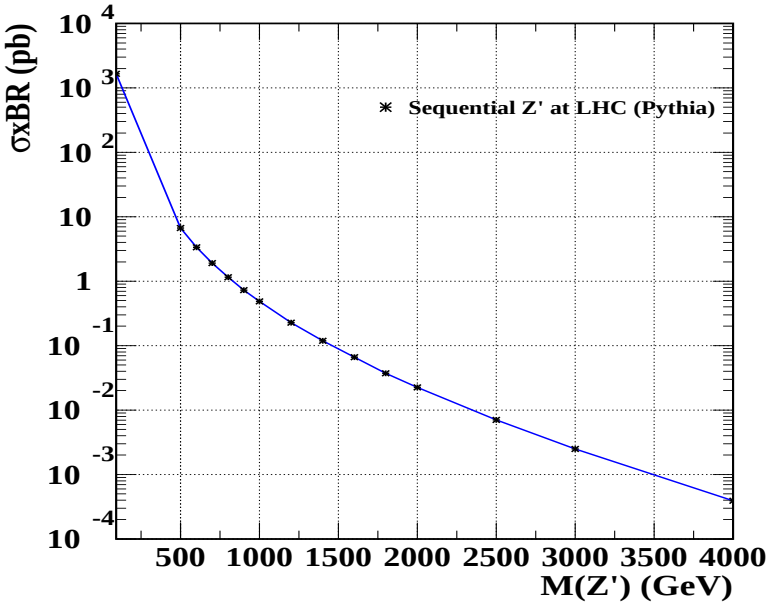

Figure 8.2: $\sigma \cdot BR(\mathrm{Z}' \to \mu^+\mu^-)$ as a function of a $\mathrm{Z}'_{\mathrm{SM}}$ at the LHC.

Bibliography

[1] Q. R. Ahmad *et al.*, SNO Collaboration, Phys. Rev. Lett. **89**, 011301, 2002; K. Eguchi *et al.*, KamLAND Collaboration, Phys. Rev. Lett. **90**, 021802, 2003; Y. Fukuda, Super-Kamiokande Collaboration, Phys. Rev. Lett. **81**, 1562–1567, 1998; A. Aguilar, LSND Collaboration, Phys. Rev. D **64**, 112007, 2001.

[2] D. N. Spergel *et al.*, Astrophys. J. Suppl. **148**, 175, 2003.

[3] L. M. Kraus, *"Dark Matter in the Universe"*, Sci. Am. **255**, 58-68, 1986.

[4] P. J. E. Peebles and B. Ratra, *"The Cosmological Constant and Dark Energy"*, Rev. Mod. Phys. **75**, 559-606, 2003.

[5] A. D. Sakharov, JETP Lett. **5**, 24-27, 1967.

[6] E. W. Kolb and M. S. Turner, *"Grand Unified Theories and the Origin of the Baryon Asymmetry"*, Ann. Rev. Nucl. Part. Sci. **33**, 645–696, 1983; W. Buchmüller and M. Plumacher, Int. J. Mod. Phys. A **15**, 5047–5086, 2000.

[7] K. Ikado, *"Search for New Physics in Dielectrons in $p\bar{p}$ Collisions at $\sqrt{s}$ = 1.96 TeV"*, Ph.D. Dissertation, Waseda University, December 2003.

[8] S. L. Glashow, Nucl. Phys. **22**, 579 (1961); S. Weinberg, Phys. Rev. Lett. **19**, 1264, 1967; A. Salam, in Proceedings of the 8th Nobel Symposium on Elementary Particle Theory, Relativistic Groups and Analyticity, edited by N. Svartholm, p. 367 (Almquist and Wiksells, Stockholm, 1968).

[9] H. Fritzsch, M. Gell–Mann, and H. Leutwyler, *Phys. Lett.* **B47**, 365 (1973); D. Gross, and F. Wilczek, Phys. Rev. Lett. **30**, 1343, 1973; H. D. Politzer, Phys. Rev. Lett. **30**, 1346, 1973.

[10] LEP/SLD Electroweak Working Group, LEPEWWG/2002-01.

[11] W. Hollik, and G.Duckeck, *"Electroweak Precision Tests at LEP"*, Springer Tracks in Modern Physics, Volume 162, Edited by: G. Höhler, 2000.

[12] G. Breit, *"Theory of Resonance Reactions"*, Handbuch der Physik XLI/1 Springer, Berlin, , 1959.

[13] S. D. Drell and T. M. Yan, Phys. Rev. Lett. **25**, 316, 1970, Ann. Phys. (N.Y), 66, 578 (1971).

[14] J. H. Christenson *et al.*, Phys. Rev. Lett. **25**, 1523, 1970.

[15] G. Arnison *et al.*, the UA1 Collaboration, Phys. Lett. B **126**, 398, 1983; P. Bagnaia *et al.*, the UA2 Collaboration, Phys. Lett. B **129**, 130, 1983.

[16] F. del Aguila, M. Quiros and F. Zwirner, Nucl. Phys. B **287**, 457, 1987.

[17] G. Sterman *et al.*, *"Handbook of Perturbative QCD"*, Rev. Mod. Phys. **67**, 157-248, 1995.

[18] V. D. Barger and R. J. N. Phillips, *"Collider Physics"*, Addison-Wesley Publishing Company, Inc., 1997.

[19] F. Gürsey, P. Ramond, and P. Sikivie, *"A Universal gauge theory model based on E_6"*, Phys. Lett. B **60**, 177, 1976; F. Gürsey and M. Serdaroğlu, Lett. Nuovo Cimento **21**, 28 (1978).

[20] S. P. Martin, *"A SUSY Primer"*, hep-ph/9709356, April 7, 1999.

[21] J. Ellis, *"Particle Physics and Cosmology"*, astro-ph/0305038, May 2, 2003; P. Langacker and M. Luo, Phys. Rev. D **44**, 817, 1991.

[22] S. Weinberg, Phys. Rev. D **13**, 974-996, 1976; L. Susskind, Phys. Rev. D **20**, 2619, 1979; Farhi and L. Susskind, Phys. Rev. D **20**, 3404, 1979.

[23] N. Arkani-Hamed, A. G. Cohen, and H. Georgi, Phys. Lett. B **513**, 232, 2001.

[24] N. Arkani-Hamed, S. Dimopoulous and G. .R. Dvali, Phys. Lett. B **429**, 263, 1998, hep-ph/9803315.

[25] I. Antoniadis, N. Arkani-Hamed, S. Dimopoulous and G. .R. Dvali, Phys. Lett. B **436**, 257, 1998, hep-ph/9804398.

[26] L. Randall and R. Sundrum, Phys. Rev. Lett. **83**, 3370, 1999, hep-ph/9905221.

[27] K. Dienes, E. Dudas, and T. Gherghetta, Nucl. Phys. B **537**, 47, 1999; A. Pomarol, and M. Quiros, Phys. Lett. B **438**, 255, 1998.

[28] T. Applequist *et al.*, Phys. Rev. D **64**, 035002, 2001; T. Rizzo, Phys. Rev. D **64**, 095010, 2001.

[29] A. Leike, *"The Phenomenology of Extra Neutral Gauge Bosons"*, Phys.Rept. 317, 143-250 (1999); hep-ph/9805494, May 28, 1998.

[30] G. Altarelli, B. Mele, and M. Ruiz-Altaba, Z. Phys. C45, 109 (1989).

[31] J. Erler and P. Langacker, Phys. Lett. B **456**, 68, 1999; hep-ph/9903476.

[32] F. Abe *et al.*, *"Search for New Gauge Bosons Decaying into Dileptons in* $p\bar{p}$ *Collisions at* $\sqrt{s}$ *= 1.8 TeV"*, the CDF Collaboration, Phys. Rev. Lett. **79**, 2191, 1997.

[33] M. K. Pillai, *"A Search for New Gauge Bosons in* $p\bar{p}$ *Collisions at* $\sqrt{s}$ *= 1.8 TeV"*, Ph.D. Thesis, 1996.

[34] K. Hagiwara *et al.*, *Review of Particle Physics*, Phys. Rev. D **66**, 010001, 2002; S. Eidelman *et al.*, *Review of Particle Physics*, Particle Data Group, Phys. Lett. B **592**, 1, 2004.

[35] N. Arkani-Hamed, A. G. Cohen, E. Katz and A. E. Nelson, *hep-ph/0206021.*

[36] T. Han, H.E. Logan, B. McElrath and L. Wang, Phys. Rev. D **67**, 095004, 2003.

[37] T. Sjöstrand, P. Edén, C. Friberg, L. Lönnblad, G. Miu, S. Mrenna and E. Norrbin, Computer Phys. Commun. 135, 2001.

[38] E. Ros, Talk given at the Int. Europhysics Conference on High Energy Physics (EPS2003), Aachen, Germany, July 17th-23rd 2003.

[39] Heather Logan, Phenomenology Institute, University of Wisconsin, private communication.

[40] J. L. Hewett, F. J. Petriello, and T. G. Rizzo, JHEP **0310**, 062, 2003.

[41] H. Davoudiasl, J. L. Hewett, and T. G. Rizzo, Phys. Rev. Lett. **84**, u080, 2000.

[42] P. Traczyk and G. Wrochna, *"Search for Randall-Sundrum Graviton Excitations in the CMS Experiment"*, hep-ex/0207061, Jul 24, 2002.

[43] See, for example: *http://lhc.web.cern.ch/lhc/general/gen_info.htm"*

[44] J. Kalinowski, R. Rueckl, H. Spiesberger and P. M. Zerwas, Phys. Lett. B **414**, 297-304, 1997, hep-ph/9708272, Aug 7, 1997; V. Barger, G. f. Guidice and T. Han, Phys. Rev. D **40**, 2987, 1989.

[45] B. Allanach *et al.*, hep-ph/9906224, March 24, 2000 and references therein.

[46] J. Abdallah *et al.*, the Delphi Collaboration, Eur. Phys. J C **31**, 421-479, 2004.

[47] K. D. Lane and S. Mrenna, Phys. Rev. D **67**, 115011, 1999; K. D. Lane, hep-ph/9903372.

[48] V. M. Abazov *et al.*, *"Search for Heavy Particles Decaying into e^+e^- Pairs in $p\bar{p}$ Collisions"*, the DØ Collaboration, Phys. Rev. Lett. **87**, 061802, 2001.

[49] *"Run II Handbook"*, *http://www-bd.fnal.gov/runII/* .

[50] F. Abe *et al.*, the CDF Collaboration, Phys. Rev. D **50**, 2966, 1994; F. Abe *et al.*, the CDF Collaboration, Phys. Rev. D **51**, 4623, 1995.

[51] the CDF Collaboration, *"The CDF II Detector Technical Design Report"*, FERMILAB-Pub-96/390-E, 1996.

[52] F. Abe *et al.*, Nucl. Inst. Meth. A **271**, 387, 1988.

[53] T. Affolder *et al.*, *"CDF Central Outer Tracker"*, FERMILAB-PUB-03-355-E, Submitted to Nucl.Inst.Meth., 2003.

[54] K. Burkett, Fermilab, private conversation.

[55] CDF Tracking Group, private conversation; See also *http://www-cdf.fnal.gov/internal/detectors/parameters.html.*

[56] C. Hays, Duke University, private conversation.

[57] F. Bedeschi *et al.*, Nucl. Inst. Meth. A **268**, 50, 1988.

[58] F. Bedeschi *et al.*, *"Report of the B_s Task Force"*, CDF Internal Note **7042**, June 1, 2004. *This is not the most comprehensive documentation, but is the most up-to-date of at the time of the writing.*

[59] L. Balka *et al.*, Nucl. Inst. Meth. A **267**, 272, 1988.

[60] Y. Seiya *et al.*, Nucl. Inst. Meth. A **480**, 524, 2002.

[61] G. Ascoli *et al.*, Nucl. Inst. Meth. A **268**, 33, 1988.

[62] Phil Schlabach, Fermilab, private conversation.

[63] A. Artikov *et al.*, Part. Nucl. Lett. **114**, 25-39 (2002).

[64] D. Acosta *et al.*, *"The performance of the CDF Luminosity Monitor"*, Nucl. Inst. Meth. A **494**, 57, 2002; J. Elias *et al.*, *"Luminosity monitor based on Čerenkov counters for* $p\bar{p}$ *colliders"*, Nucl. Inst. Meth. A **441**, 366, 2000.

[65] S. Klimenko, Proceedings 8th International Conference on Instrumentation for Colliding Beam Physics (INSTR02), Novosibirsk, Russia, February 28-March 6, 2002.

[66] M. Gallinaro, FERMILAB-CONF-02-121-E (2002) 11.

[67] K. Terashi, Rockefeller University, private conversation.

[68] M. Karagöz Ünel and R. J. Tesarek, *"Beam Halo Monitoring at CDF"*, Nucl. Inst. Meth. A **506**, 7-19, 2003.

[69] T.M. Shaw *et al.*, IEEE Trans. Nucl. Sci. **47**, 1506, 2000.

[70] K. Maeshima, *"Specifications for the CDF II Master Clock System"*, CDF Internal Note **4509**, April 21, 2000.

[71] A. Meyer, FERMILAB-CONF-01/242-E. Proceedings Computing in High Energy and Nuclear Physics (CHEP'01), Beijing, China, September 3-7, 2001.

[72] E. J. Thomson *et al.*, *"Online Track Processor for the CDF Upgrade*, IEEE Trans. Nucl. Sci. **49**, 1063, 2002.

[73] N. Eddy *et al.*, *"The XTRP System: An Overview"*, *http://web.hep.uiuc.edu/engin/cdf/XTRP/documentation/xtrp.pdf.*

[74] W. Ashmankas *et al.*, *"The CDF Silicon Vertex Trigger"*, FERMILAB-CONF-03/168-E, 2003.

[75] R. Brun and F. Rademakers, *"ROOT - An Object Oriented Data Analysis Framework"*, Nucl. Inst. & Meth. in Phys. Res. A **389**, 81, 1997; See also *http://root.cern.ch/.*

[76] G. Brandenburg *et al.*, *"The CDF Run I Muon System Upgrade"*, CDF Internal Note **6362**, March 7, 2003.

[77] J. D. Bellinger *et al.*, *"A Guide to Muon Reconstruction and Software for Run II"*, CDF Internal Note **5870**, November 4, 2002.

[78] M. Atac, IEEE Trans. Nucl. Sci. **1**, 99, 1984.

[79] R. J. Yarema *et al.*, *"A Surface Mount Amplifier-shaper-discriminator and Preamplifier for the Fermilab CDF Tracking Chambers"*, IEEE Trans. Nucl. Sci. **33**, 933-936, 1986.

[80] H. Reather, *"Electron Avalanches asn Breakdown in Gases"*, Washington Butterworths Advanced Physics Series, 1964.

[81] P. J. Lukens, *"Bunch Tagging in the Muon Chambers"*, CDF Internal Note **5814**, December 19, 2001.

[82] E. James, Fermilab, private conversation.

[83] C. Hays *et al.*, *"The COT Pattern Recognition Algorithm and Offline Code"*, CDF Internal Note **6992**, April 30, 2004.

[84] R. J. Herber, *"The CDF R2 Database Browser for Beginners"*, CDF Internal Note **5591**, June 9, 2001; Trigger and Dataset Working Group: *http://www-cdf.fnal.gov/internal/upgrades/daq_trig/twg/index.html* .

[85] E. Thomson, *"Description of Data Samples for Top Group for Summer 2003"*, CDF Internal Note **6548**, July 1, 2003.

[86] M. Coca *et al.*, *"A First Look at Run 2 High p_{T} Electrons"*, CDF Internal Note **5803**, December 7, 2001, Revision Februry 2, 2003.

[87] H. Kim, *"MIP Energy Scale Comprisons of CHA/WHA Between Run I and Run II"*, CDF Internal Note **6392**, March 21, 2003.

[88] L. Nodulman, *"A Min-Bias Calorimeter Ntuple"*, CDF Internal Note **6364**, July 14, 2003, Revision December 3, 2003.

[89] H. S. Budd, W. K. Sakumoto, *"Determining Gains of Plug Towers using Plug Laser and Source Data"*, CDF Internal Note **6433**, April 28, 2003.

[90] B. Heinmann, *"Offline Calibration of the Calorimeter"*, CDF Internal Note **6406**, April 29, 2003.

[91] S. Klimenko, J. Konigsberg, and T. Liss, *"Average Cross-section of the Inelastic $p\bar{p}$ Scattering at 1800 TeV"*, CDF Internal Note **6314**, February 10, 2003.

[92] S. M. Wang, University of Florida, private conversation.

[93] D. Acosta *et al.*, *"Estimation of CLC acceptance to Inelastic $p\bar{p}$ Interactions"*, CDF Internal Note **6054**, July 26, 2002; J. Konigsberg *et al.*, *"A first Look at the CLC Luminosity Measurements"*, CDF Internal Note **6052**, August 28, 2002.

[94] Good Run List V4 Page, *http://www-cdf.fnal.gov/internal/dqm/goodrun/v4/goodv4.html.*

[95] L. Nodulman, *"Central Electron Issues for Summer 03"*, CDF Internal Note **6558**, July 11, 2003.

[96] M. Karagoz Ünel *et al.*, *"Searches in High Mass Dimuon Channel in CDF Run II Data - Summer '03 Update"*, CDF Internal Note **6602**, August 12, 2003.

[97] R. P. Kokoulin and A. A. Petrukhin, Sov. J. Part. Nucl. **21**, 332, 1990; W. Sakumoto *et al.*, Phys. Rev. D **45**, 3042, 1992.

[98] P. de Barbaro *et al.*, *"A Search for Z' Decaying to $\mu^+\mu^-$ Using Run 1A Data and a First Look at Run 1B Data"*, CDF Internal Note **2910**, February 15, 1995.

[99] P. S. Auchincloss *et al.*, *"Muon interaction in iron in CCFR detector"*, Nucl. Inst. Meth. A **343**, 463, 1994; A. P. Chikkatur *et al.*, *"Tests of a calorimetric technique for measuring the energy of cosmic ray muons in the TeV energy range"*, Zeitschrift Für Physik C **74**, 279-289, 1997.

[100] CERN Application Software Group, CERN Program Library Long Writeup W5013, GEANT - Detector Description and Simulation Tool.

[101] D. Frei, *"Multiple Scattering of Central Muons"*, CDF Internal Note **1430**, April 1991.

[102] A. Taffard, *"Run II Cosmic Ray Tagger*, CDF Internal Note **6100**, February 11, 2003.

[103] H. K. Gerberich , A. V. Kotwal, and C. Hays, *"Cosmic Ray Tagging using COT Hit Timing"*, CDF Internal Note **6089**, August 19, 2002.

[104] L. Cerrito and V. Martin, *"Muon Cuts and Efficiencies for 4.11.1 Analyses"*, CDF Internal Note **6825**, February 3, 2004.

[105] M. Karagöz Ünel *et al.*, *"Searches for New Particles in High Mass Dimuon Channel in CDF Run II Data"*, CDF Internal Note **6344**, 2/26/03.

[106] E. James, Fermilab, private conversation. See also, *http://www-cdf.fnal.gov/internal/physics/joint_physics/docs/mueff.pdf.*

[107] Wolfram Research, Inc., Mathematica, Version 5.0, Champaign, IL (2003).

[108] M. Karagöz Ünel *et al.*, *"Searches in High Mass Dimuon Channel in CDF Run II Data - winter04 update"*, CDF Internal Note **6879**, February 12, 2004.

[109] W. D. Dagenhart, *"Muon Reconstruction Efficiency for Summer 2003 Conferences"*, CDF Internal Note **6612**, July 30th, 2003.

[110] K. Bloom and W. D. Dagenhart, *"Muon Reconstruction Efficiency for Winer 2003 Conferences"*, CDF Internal Note **6347**, March 3, 2003.

[111] D. Glenzinski *et al.*, *"Determination of the Run II COT Tracking Efficiency using the W-No-Track Sample"*, CDF Internal Note **6866**, February 3, 2004.

[112] W. Sakumoto and A. Hocker, CDF Internal Note **6917**, March 5th, 2004.

[113] W. Badgett and P. Derwent, *"Event z-Vertex Efficiency as a Luminosity Correction for Run IA"*, CDF Internal Note **2703**, July 7, 1994.

[114] S. Lai *et al.*, *"An updated Measurement of the Beam Width at CDF"*, CDF Internal Note **6492**, June 4, 2003.

[115] G. Corcella *et al.*, *"HERWIG 6: An Event Generator for Hadron Emission Reactions With Interfering Gluons"*, JHEP **0101**, 10, 2002, hep-ph/0011363, 2002.

[116] C. Hays and A. Kotwal, *"A Search for Doubly-Charged Particles in the Run II Dimuon Data"*, CDF Internal Note **6457**, 6/10/03.

[117] R. Field, *http://www.phys.ufl.edu/ rfield/cdf/tunes/rdf_tunes.html.*

[118] R. Field, *"The Underlying Event in Run II"*, CDF Internal Note **6403**, April 1, 2003; also available at *http://cepa.fnal.gov/CPD/MCTuning/april/FNAL_UE_4-30-03.pdf.*

[119] G. Manca and Y. Kim, *"$Z \rightarrow e^+e^-$ Cross Section Measurement with Run II Data"*, CDF Internal Note **6202**, December 1, 2002.

[120] R. Bonciani *et al.*, Nucl. Phys. B **259**, 424-450, 1998, hep-ph/9801375, 1998.

[121] J. M. Campbell and R. K. Ellis, *"An update on vector boson pair production at hadron colliders"*, Phys. Rev. D **60**, 113006, 1999, hep-ph/9905386, 1999; S. Cabrera *et al.*, CDF Internal Note **6290**, February 11th, 2003.

[122] S. Jadach, Z. Was, R. Decker, and J. H. Kuhn, *"The Tau Decay Library Tauola: Version 2.4"*, Comput. Phys. Commun.76:361-380,1993.

[123] M. L. Mangano, M. Moretti, F. Piccinini, R. Pittau, and A. Polosa, *"ALPGEN, a Generator for Hard Multiparton Processes in Hadronic Collisions"*, JHEP **0307**, 001, 2003, hep-ph/0206293, 2002.

[124] F. Abe *et al.*, Phys. Rev. D **59**, 052002, 1999.

[125] J. C. Collins and D .E. Soper, Phys. Rev. D **16**, 2219, 1977.

[126] A. D.Martin *et al.*, Phys. Lett. B **531**, 216, 2002, updated by J. Stirling.

[127] D. Acosta *et al.*, *"First Measurements of Inclusive W and Z Cross Sections from Run II of the Tevatron Collider"*, the CDF Collaboration, hep-ex/0406078, Jun 28, 2004, submitted to Phys. Rev. Lett., 2004.

[128] R. Hamilton and P. Schlabach, *"Efficiencies of the CMX Single Muon Triggers in Run IA"*, CDF Internal Note **2186**, April 22, 1994; P. Schlabach, Fermilab, private conversation.

[129] H. L. Lai *et al.*, *"Global QCD Analysis of Parton Structure of the Nucleon: CTEQ5 Parton Distributions"*, the CTEQ Collaboration, hep-ph/9903282, 1999.

[130] H. L. Lai *et al.*, *"Global QCD Analysis and the CTEQ Parton Distributions"*, MSUHEP-41024, 1994.

[131] A. D. Martin *et al.*, *"Parton Distributions: a New Global Analysis"*, Eur. Phys. J C **4**, 463, 1998, hep-ph/9803445, 1998.

[132] S. Tsuno, talk given at CDF Higgs meeting, *http://www-cdf.fnal.gov/internal/physics/exotic/higgs/011031/tsuno.ps*, October 31, 2001.

[133] the DØ Collaboration, *"Search for Large Extra Dimensions in the Dielectron and Diphoton Channels with 200 pb^{-1} of Run II Data"*, DØ Public Note 4336 (2004), *http://www-d0.fnal.gov*.

[134] M. Bengtsson, and T. Sjöstrand, Zeitschrift Für Physik C **37**, 465, 1988.

[135] H. S. Kim, UIUC, Talk given at the CDF VeGY meeting, September 4, 2004.

[136] E. Halkiadakis, Rochester University, private conversation.

[137] K. Ikado, K. Maeshima, T. Nelson, and M. Karagoz Unel, *"Search for New Physics in High Mass Dielectrons"*, CDF Internal Note **6746**, December 1, 2003.

[138] D. Acosta *et al.*, *"Search for Lepton Flavor Violating Decays of a Heavy Neutral Particle in $p\bar{p}$ Collisions at $\sqrt{s}$= 1.8 TeV"*, the CDF Collaboration, Phys. Rev. Lett. **91**, 171602, 2003.

[139] M. Gold and K. Maeshima, *"Comments on Model Dependence of Z' Mass Limits"*, CDF Internal Note **1409**, April 15th, 1991.

[140] K. Ikado, K. Kondo, K. Maeshima, M. Karagoz Unel, *"Search for New Particles in High Mass Dielectrons"*, CDF Internal Note **6343**, March 15, 2003.

[141] T. Pratt *et al.*, *"Resonance Searches in High Mass Dimuons"*, CDF Internal Note **6073**, Sept. 5, 2002.

[142] J. Conway and K. Maeshima, *"Poisson Upper Limits Incorporating Uncertainties in Acceptance and Background"*, CDF Internal Note **4476**, March 18, 1998.

[143] K. Lane, Phys. Rev. D **60**, 075007, 1999; hep-ph/9903369, 1999.

[144] S. Mrenna, Fermilab, private conversation.

[145] M. Karagöz Ünel, *"Limits on New Neutral Bosons in E_6 Model Using CDF Run II Dielectron and Dimuon Data"*, CDF Internal Note **6473**, May 28, 2003.

[146] J. Stirling, Durham University, private conversation, through B. Heinmann.

[147] J. Conway, Rutgers University, private conversation. The code is available at CDF statistic web URL: *http://www-cdf.fnal.gov/physics/statistics/statistics_software.html.*

[148] B. Abbott *et al.*, D0 Collaboration, Phys. Rev. Lett. **86**, 1156, 2001; See for example: J. Carlson and D. Gerdes, CDF Internal Note **5391**, October 26, 2001.

[149] D. Choudhury, S. Majhi and V. Ravindran, Nucl. Phys. B **660**, 343, 2003.

[150] M. Karagöz Ünel, *"Searches for New Physics in High Mass Dileptons at CDFII"*, talk given at Phenomenology Symposium, University of Wisconsin-Madison, April 26–28, 2004, *http://www.pheno.info/symposia/pheno04.*

[151] F. Abe *et al.*, Phys. Rev. D **51**, 951, 1995.

[152] C. Ciobanu and G. Veramendi, University of Illinois, UC, private conversation.

[153] E. Eichten, I. Hinchliffe, K. Lane, and C. Quigg, *"Supercollider Physics"*, Reviews of Modern Physics, Vol. 56, No. 4, 1984.

[154] M. Karagöz Ünel, *"Searches for Extra Dimensions at the Tevatron"*, the CDF and DØ Collaborations, FERMILAB-CONF-04-206-Er, Proceedings of the 15th Topical Conference on Hadron Collider Physics (HCP2004), East Lansing, Michigan, June 14-18, 2004.

[155] N. G. Ünel, UCI and CERN, private conversation.

[156] M. Karagöz Ünel, *"Studies on cosmic ray muons using data taken with cosmic ray trigger"*, CDF Internal Note **6633**, October 10, 2003.

[157] K. Maeshima, Fermilab, private conversation.

[158] Dave Dagenhart, Brandeis University, private conversation.

[159] N. Miladinovic, Talk given in the CDF Muon Offline Meeting, September 2, 2003.

[160] F. Abe *et al.*, *"Measurement of Z^0 and Drell-Yan Production and Decay to Dimuons"*, Phys. Rev. D **59**, 052002, 1999, CDF Internal Note **4092**, 11/3/98.

[161] R. J. Tesarek, Fermilab, private conversation.

[162] M. Cordelli *et al.*, *"Timing Calibration of CDF Hadron Calorimeters"*, CDF Internal Note **5856**, February 14, 2002.

[163] M. Franklin, Harvard University, private conversation.

[164] J. D. Stirling, Durham University, private conversation through W. Sakumoto.

[165] R. Hamberg, W.L. van Neerven and T. Matsuura, Nucl. Phys. B **359**, 343, 1991, Erratum-ibid.B644:403,2002.

[166] W. van Neerven, University of Ledien, private conversation.

[167] L. Dixon, SLAC, private conversation; C. Anastasiou, L. Dixon, K. Melnikov, and F. Petriello, Phys. Rev. D **69**, 094008, 2004.

Appendix A

Cosmic Ray Muons in CDF Detector

Cosmic ray muons constitute an important background source for many CDF analyses using muons. This section summarizes studies performed using the data taken with the cosmic ray triggers of CDF in the absence of $p\bar{p}$ beam [156]. We illustrate some basic distributions for muons and document information about the cosmic ray muons as detected in CDF. Studies on the application of the cosmic ray tagging algorithms on these data are also documented.

In order to study cosmic ray muons, two runs that were proposed by the CDF Operations [157] have been selected. These runs were taken with the requirement of no-beam in the Tevatron and that all relevant subsystems were powered, the

solenoid energized and the subsystems were under online "good-run" conditions (see Section 3.5). Table A.1 lists the runs used with information about the data-taking date, the condition of the detector, the trigger table and the number of L3 accepts and rates. The average L3 output rate for the cosmic runs is about 50Hz. About one million events can be collected in six hours of detector running with usually $< 0.5\%$ deadtime in data-taking.

The runs listed in Table A.1 are taken with the "COSMICS" physics table and they are basically formed with the same trigger paths. The main category of triggers are: XFT track-based, di-CMU stubs with large opening angle and calorimeter-only. Although none of the cosmic triggers contain a CMP or CMX requirement, the XFT track requirements match those in the trigger paths for the inclusive high p_{T} CMUP and CMX muons. Because the cosmic ray data are not typically run through the offline reconstruction, we requested that these data be processed. The data are processed using version 4.8.3 of CDF software. The cosmic data need to be requested to be processed. At the time of the study, the cosmic ray data had no L3 trigger filter applied and were written to a single output stream (fileset) and were not split in the production stage with respect to the trigger paths. Therefore, only a portion of cosmic data in these filesets consisted of reconstructible dimuons, which made obtaining a large size of dimuon cosmic data difficult. In addition, cosmic ray tagger modules are not a part of the production executable. the cosmic ray tagger

152412	2002.10.02
	Silicon included, all powered. L3: A:1,568,494, R:49.6 Hz COSMICS [7,137,318]
153215	2002.10.22
	Silicon included, all powered. L3: A:1,308,047, R:48.7 Hz COSMICS [7,169,318]

Table A.1: Good cosmic run list used in analysis. The list is compiled in early 2003.

information needed to be appended to the dataset.

Data collected in the runs used in this analysis contains about three million events, corresponding to about 18 hours of continuous data taking. For running the cosmic ray tagger module and for applying the selection cuts on the processed data, version 4.9.1hpt3 of the CDF offline code is used in accordance with CDF winter 2003 analyses. No prerequisites are applied on the triggers during the study which allows to use examine the whole set of cosmic ray events. Data described above can be used to study the characteristics of muons that are reconstructed from cosmic rays. In Figures A.1-A.4, we plot some basic distributions from the muon collection without further selection cuts. Included in these plots are muon information for those events in which at least one muon was reconstructed. Using data in these plots, we see that the fraction of reconstructed muons (out of about 3 million events) is one event in a hundred. One reason for this is that only a few of the cosmic rays go through the middle of the tracking volume. Many muons undergo bremsstrahlung

in the calorimeter, fire the jet triggers and form the COSMICS_CALOR dataset, for example. (The details of all the topologies that may exist in cosmic data are not presented here.) The muon z distribution falls off around $\pm$ 2 m, which is about 50 cm larger than the COT length. We find the uncertainty of the z determination at high z values to peak around one cm with the tail reaching about five cm. The larger tails of this distribution are due to the tracks which exit the tracking volume far away from the detector center. These tracks pass smaller number of layers and traverse the detector with small polar angles, thus, extrapolated to larger z values than the physical boundary[1]. Figure A.20 is an example of such event types. The tracks ($z_{1,2}$ = -173, -81 cm) in this event fire the back-to-back CMU stub trigger.

In Figure A.2, the track-stub matching variables (Δx and Δz) and the muon ϕ are plotted. For the Δx distribution, we fit two Gaussians. The narrow Gaussian in Δx distribution mostly represents the high-$p_{\rm T}$, good matched CMU, CMP and CMX muons. The wide Gaussian is driven by the lower-$p_{\rm T}$ and poor-reconstructed muons in the sample. The $p_{\rm T}$ dependence of the Δx variable is shown in Figure A.9. The high $p_{\rm T}$ distribution for good muons are shown in Figure A.5 which is further discussed in the following pages. The low $p_{\rm T}$ muon extrapolation is dominated by multiple scattering (see Section 2.3.3). The requirement for matching is $|\Delta x| < 60$ cm at the reconstruction level for muons. The Δz distribution is also fit to double

[1]Two meters is the default requirement of the muon reconstruction algorithm.

Gaussian[2]. The wide component is due to a portion of CMU muons where some CMU chambers fail accurately determining the muon z position [158]. The wide component can also be seen in Figure A.6. The muon ϕ distribution in Figure A.2 shows, as expected, that cosmic ray muons come from the top of the CDF detector (also supported by a narrow $|\eta|$ distribution in Figure A.1).

In Figure A.3 kinematic distributions are plotted. The minimum ionization (MIP) peaks in the hadronic (HAD) and electromagnetic (EM) energy distributions are visible. For both variables, the mean of the distribution is smaller than those obtained when we apply selection cuts (described below). The calorimeter isolation distribution, shown at the right bottom of Figure A.3, has two slopes (with a shoulder around 2 GeV) and a mean of about 0.7 GeV. This feature diminishes when we select good high p_{T} dimuons, where a good high p_{T} muon is defined to be selected with the ID requirements listed in Table 4.1. We discuss this further below.

Figure A.4 shows the track related quantities of the reconstructed muons. The upper right plot in this figure shows the silicon hit multiplicity for the muon tracks. We see a reconstructed track has, on the average, about three silicon hits associated with it. When tracks without a silicon hit are ignored, the average number of hits becomes seven. In the upper left plot, a wide d_0 distribution is observed with shoulders reaching out to ± 6 cm, which is the default muon reconstruction cut. We do see

[2]Note that the Δz variable is not a muon ID requirement for analyses.

some structures in this distribution: there is a core Gaussian about one cm in width, and there are shoulders around $d_0 = \pm 3$ cm over the wider distribution. The wide distribution is expected from the cosmic ray muons, which need not go near the beamline. Some contributions to this structure from the events which contain XFT triggerable-track(s) in them is anticipated. In fact, we observe that only those tracks that go closer to beamline can fire the XFT triggers. This is because XFT requires the beamspot to anchor one end of the track at the pattern recognition level[3] [72]. Additional contributions to the structure in d_0 distribution are also expected from various track reconstruction algorithms with different constraints.

We now apply further cuts to the data sample. We define two sets: **i)** muons that are reconstructed in the cosmic data set in which at least two muons are found within 60 cm of the detector center in an event (*fiducial* muon pair), and **ii)** good muon pair which passes the selection cuts except any cosmic veto cuts. For selection of dimuons, we follow the criteria as in CDF Note 6602, except for a CMX muon, we use the definition of CDF Note 6344 ([105]). This means, we require a muon pair in which one of the legs should be either a CMUP or CMX muon and a CMX muon is any muon with a CMX stub. After we require two good muons in the event, we end up with a sample of about 600 events (a rate of 33 events per hour). About 10%

[3]For cosmic rays, the XFT tracks can have different properties from collision data, since the timing of the tracks are different. This study has been constrained to the reconstructed muons, without recording the trigger information. A study, which takes into account the contributions from different trigger paths, is an interesting project to pursue.

of the final set is CMX muons ($0.6 < \eta < 1.0$). The shape of the d_0 distribution in Figure A.4 is observed not to change: the ratios of the heights of the narrow and wide distributions remains constant and the shoulders at $\pm$ 3 cm exist.

In Figures A.5 and A.6, we investigate the Δx and Δz distributions for the final selected dimuons. The distributions are plotted separately for each muon subdetector. The figures contain information from a CMU and CMP stub only if they contribute to a CMUP muon. Two Gaussians to CMU and CMP and single Gaussian to CMX Δx distributions are fitted. For the Δx variable, all subdetectors agree with observations in the high p_{T} collision data. For the Δz variable, we observe that neither CMU (two Gaussians fit) nor CMX (single Gaussian fit) agree with the high p_{T} MC expectations. The event sample for CMX muons is not large, therefore, we can draw no conclusions for this quantity. However, the broad distribution can be compared with a σ of order of a few cm in high p_{T} MC studies and about 15 cm from J/ψ data [159]. In any rate, the worsening of $\sigma(\Delta z)$ could be due to a few effects, two of which are: a problem in the drift velocity of CMX chambers or a track-stub matching reconstruction artifact. The CMP does not measure the z position of a stub, so a Δz distribution can not be plotted.

The muon HAD and EM energy depositions are plotted in Figure A.7. For these high p_{T} muons, we obtain these MIP mean values: E_{had} = 1.92 GeV and

E_{em} = 0.33 GeV. We also observe that the E_{had} peaks at zero [4] remains. Next, we consider the isolation variable in Figure A.7. The population around 2 GeV visible in Figure A.3 is reduced by the application of muon p_T and identification cuts. The fraction of muons which have zero isolation energy has gone down to about 13% from 22% (all reconstructed muons) and 16% (two reconstructed muons in ±60 cm). The distribution has a mean of 0.47 GeV.

These data give a sample of pure high p_T muons and one can check the ionization "sliding cuts" (optimized for collision muons using MC simulation) on the cosmic muons. These cuts are used in many high p_T analyses at CDF[5]. Although the sample size is smaller after the application of the selection cuts, Figure A.8 shows the momentum dependence of the calorimeter MIP and isolation quantities for the final set of good muons, but with no requirements on MIP or isolation energies. In E_{had} vs p the E_{em} vs p distributions, we do not observe a trend to increase as a function of the muon momentum, as reflected in the cut choices, shown as straight lines. The isolation variable also stays constant as a function of the muon p_T. We anticipate that one of the reasons for not observing the expected behavior could be that the cosmic ray muons tend to come in random directions into the detector whereas the calorimeter structure and readout is optimized for physics collisions from

[4] In physics data, this peak may also partly associated with low p_T muons produced by hadron decay-in-flights faking high p_T muons. Such muons may poor extrapolation to a calorimeter tower. A muon can also pass through a calorimeter crack [161] without any energy deposition.

[5] The optimization of the sliding cuts is discussed in Section 4.1 and CDF4092 [160].

the center of the detector: cosmic ray muons may not be optimal for studying muons in the calorimeter. Figure A.8 also shows the isolation vs the hadronic energy of the muons. The E_{iso} vs E_{had} plot in Figure A.8 has an occupancy at around 2 GeV where E_{had} obtains zero values. These kind of events correspond to the shoulder in the E_{iso} plot in Figure A.3. These events may occur for low p_T muons (which may multiple scatter in the tracking, calorimetry volumes and steel absorbers) and muons with poor calorimeter extrapolation: the MIP energy is attributed to the isolation since the towers the muon passed through may have been missed. It is not too surprising that requiring high p_T muons with tighter track extrapolation match variables eliminates such events, as seen in Figure A.7. We have also checked the distributions as a function of muon track ϕ, to see if there is an asymmetry between the top and the bottom. One of the processes that may be top-bottom asymmetric is that a high momentum muon, after traversing the tracking volume, may undergo bremsstrahlung in the calorimeter. Although there is a slight excess in the high tails for the muons at the bottom of the detector, we have not seen a significant difference. A complete study of these observed effects can be checked against with physics data and MC simulation, which we do not perform here.

The top plot in Figure A.10 shows the difference between the two muon tracks' z_0 (Δz_0) along the beamline. We fit two Gaussians to the distribution which does not have the fiduciality cut. The Gaussian σ's are 0.8 cm and 2.6 cm for this distribution.

The bottom plot in the same figure shows that the $\delta\phi$ between the two muons get narrower with the application of the p_{T} and ID cuts (35% reduction in RMS of the peaks). The events with very near-by tracks in $\delta\phi$ are worth examining. One can speculate that these are showers or decay products of high energetic cosmic rays. Such an event would be similar to that of in Figure A.20, but would be produced within the silicon material, for example. Otherwise, these can be single tracks that are *split/duplicated*, hence make two separate tracks. We check a subset of such events, all of which also accumulate near small $\delta\eta$ region, and we observe that they fit better the latter description. We have observed event 382475 of run 152412 to be such an event where two tracks at $\phi = 5.5$ radians are formed. This event is interesting, in that, there also exist three separate CMP stubs reconstructed at the same ϕ where the different CMP regions overlap and two of them are associated with tracks. Figure A.11 shows the distribution of the η difference of the two muons as a function of the muon η which demonstrates that the muons are also back-to-back in η space as well. Figure A.12 represents the absolute value of the muon d_0's relative to each other. This kind of plot was used in some Run I analyses to estimate the cosmic ray background in conjunction with the sum of the two impact parameters. A similar approach, using the sum of the squares of the d_0's, is available as one method in the CRT.

The ΔTOF distribution in Figure A.13 is consistent with cosmic ray muons. A

detailed examination of the ΔTOF distribution yields an overall resolution from a Gaussian fit as $\sigma = 0.2$ ns. The TOF reconstruction algorithm at the time of the study allows association of a TOF hit information to a track if it is the sole track pointing to the bar, hence, we should not expect any TOF information from those events which are accumulated near zero in $\delta\phi$ distribution (Figure A.10). Figure A.13 shows that the ΔTDC distribution has an small leakage into the positive values, which is a region expected from physics collisions. This is in part due to the fact that the hadron timing resolution decreases with deposited HAD energy and is difficult to calibrate at low energies [161]. More about the hadron timing can be found in a CDF Note ([162]).

Figure A.14 shows the invariant mass distribution using the final good dimuons in the cosmic data. We fit a double exponential function to the distribution. The tail is not perfectly described by the fit: due also to the worsening of the track momentum resolution. We observe that the high mass region fits to a slower decaying function as compared to the low mass region. Figure A.21 illustrates one event that is included in this sample after passing all the cuts. The event is triggered by XFT and contains one CMX muon. Finally, we should point out that no events are left in the sample once we apply the cosmic ray veto cuts.

Studies on Cosmic Ray Vetoing Algorithms:

To perform tests with the CRT [102] and the dicosmic tagger[6], run 152412 is used. We are especially interested in the results for the dicosmic tagger, nevertheless we report on the CRT as well. We use the default .tcl file for the CRT for 4.9.1hpt3 version of CDF code. The fact that the beamline does not exist in cosmic runs poses no problems to the tracking fits in CRT [56]. CRT tags cosmic rays within various classes (topologies) of cosmic muons, such as $\mu+\mu$, $\mu+$ stub or $\mu+$ nothing,... There are no ID cuts applied to the muons in the CRT, except for a loose MIP requirement on the "stubless" muons. Also, worth of noting is that the CRT is implemented such that "promotions" between the classes are made possible to provide the best CR rejection. For example, a $\mu+$ stub can be promoted to a $\mu+$ track, if a mirror track can be reconstructed on the stub side of the tracking volume.

We start by examining the $\mu+\mu$ and $\mu+$ track categories using the summmary listing of the CRT module at the end of the analysis job. Demanding $\mu+\mu$ or $\mu+$ track in a CR tagged event leaves a small fraction of total events to study: about 6 per thousand events in this sample has such topologies. The ratio of events tagged as cosmic ray to the number of events found in each category gives the efficiency of the cosmic ray tagging. The CRT efficiency for $\mu+$ track is $98.06\pm0.45\%$ and for $\mu+\mu$ is $96.84\pm0.18\%$. We find the dicosmic tagger (also referred to as "not outgoing

[6]We refer to the dicosmic tagger as described in Chapter 4. The tagger is used as implemented in CRT.

pair" in CRT module) to be quite inefficient. The dicosmic tagger efficiencies are 72.04±0.48% and 96.54±0.60% for $\mu+\mu$ and $\mu+$ track, respectively. To compare the CRT and dicosmic tag efficiency, muons tagged as CRT in the event sample are kept using the StripCosmicMod module. Due to computation limitations, about 200k events of run 152412 is used for this part of the study. First, we check the dimuon invariant mass dependence of the dicosmic tag efficiency along with the default CRT efficiency. This is shown in Figure A.15. Let us mention that **no** ID and p_{T} cuts have been applied to the muons at this level to keep the sample size large. The dicosmic tagging inefficiency mostly lies below a dimuon invariant mass of 30 GeV/c. This is good news for high mass analysis purposes, however, it tells us the problem is p_{T} dependent. In Figure A.16, we compare the p_{T} of the muons in those events which are neither tagged by the CRT nor by the dicosmic algorithm, separately. We can see that most of the dicosmic tagger inefficiency and CRT inefficiency, driven by the dicosmic tag, lies sharply below 5 GeV/c: there is a lower p_{T} cut on the muons to be applied the dicosmic fit, which translates into a inefficiency in low dimuon mass region.

Figure A.17 shows the d_0 distribution for muons in events which are not tagged by the CRT and by the dicosmic tagger. Most events seen in both these wide distributions can easily be eliminated by the d_0 cut in a high p_{T} muon analysis. However, both distributions have a non-flat behavior (accumulation at small d_0 values) similar

to what we have seen earlier. We see that the bulk of this accumulation belongs to the good muons with p_{T} below 5 GeV/c. Finally, we compare the number of COT hits associated to the muon track. The CRT distribution is pretty flat. Most dicosmic-untagged muons have large number of COT hits associated with them, most of which belong to the muons that are below the 5 GeV/c p_{T} cut. When we apply the 5 GeV cut, we observe that tracks with smaller number of COT hits remain as untagged by the dicosmic tagger [7]. Figure A.22 shows the highest invariant mass (about 27 GeV/c^2) event not tagged by any of the taggers and with both muons have p_{T} larger than 5 GeV. This event is classified as a "hardware problem" event. This type of events usually is handled properly by the tracking reconstruction code and are rejected. However, this particular event, being at the requirement threshold, was not rejected. Let us remind the reader that the event would be eliminated by an application of muon ID cuts.

Figure A.19 shows a fit to the dicosmic efficiency with a function to describe the turn-on behavior. The function used for the fit is given as:

$$\epsilon(M) = \frac{\epsilon_0}{1 + exp((M - M_0)/\delta)} \quad , \tag{A.1}$$

where ϵ_0 is us the tagging efficiency. We perform this fit to a sample of 645 events with

[7] A few rare cases of dicosmic mistags in the forward region in a MC study is outlined in [96].

Table A.2: Results of the fits to the dicosmic efficiency.

Sample	ϵ_0	M_0 (GeV/c)	δ
Full	0.991±0.001	10.78±0.25	1.61±0.27

Table A.3: Results of the dicosmic efficiency calculations.

$M_{\mu\mu}$ (GeV/c)	N_{total}	N_{tagged}	ϵ_0
10-above	207	205	0.990±0.007
10-40	140	138	0.986±0.010
40-above	68	68	$1.00^{+0.00}_{-0.014}$

no minimum $p_{\rm T}$ requirement on the muon pair. Table A.2 summarizes the results. The efficiency numbers more relevant to physics analyses, in which we require fiducial muons of at least 5 GeV/c $p_{\rm T}$, are listed in Table A.3. Requiring fiducial muons alone reduces the sample to 314 events before the $p_{\rm T}$ cut. Although the sample size for this study is small, we can say that the dicosmic tagger is very efficient in the high invariant mass region. We can also deduce that the tagging power of dicosmic tagger equals that of default CRT at high mass[8].

[8]The minimum $p_{\rm T}$ requirement for the dicosmic fit has been lowered in the CDF offline software after the results of this study [56].

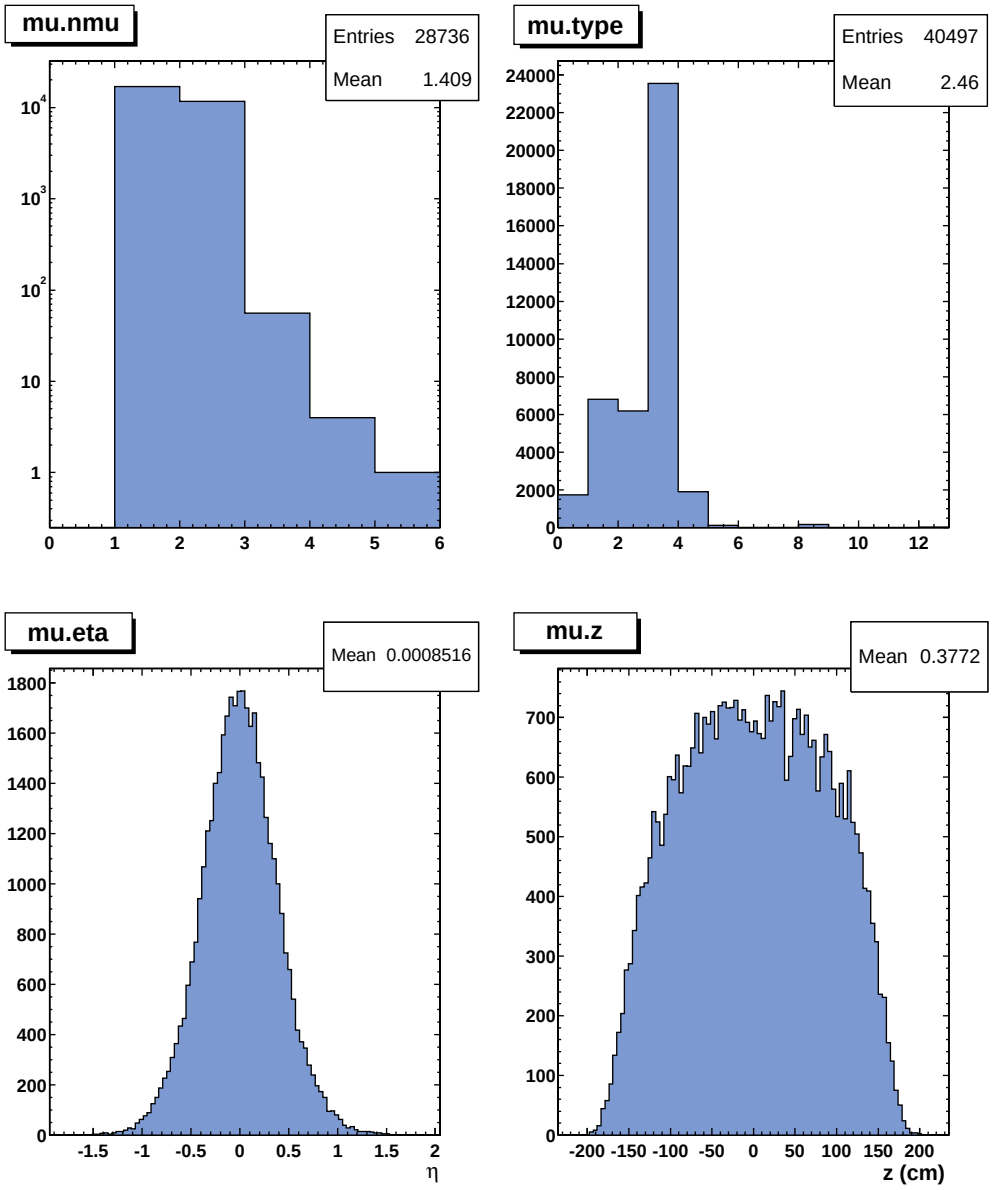

Figure A.1: N_μ, muon type, η and z_0 distributions for the reconstructed muons in the cosmic data. The data is free of any selection cuts.

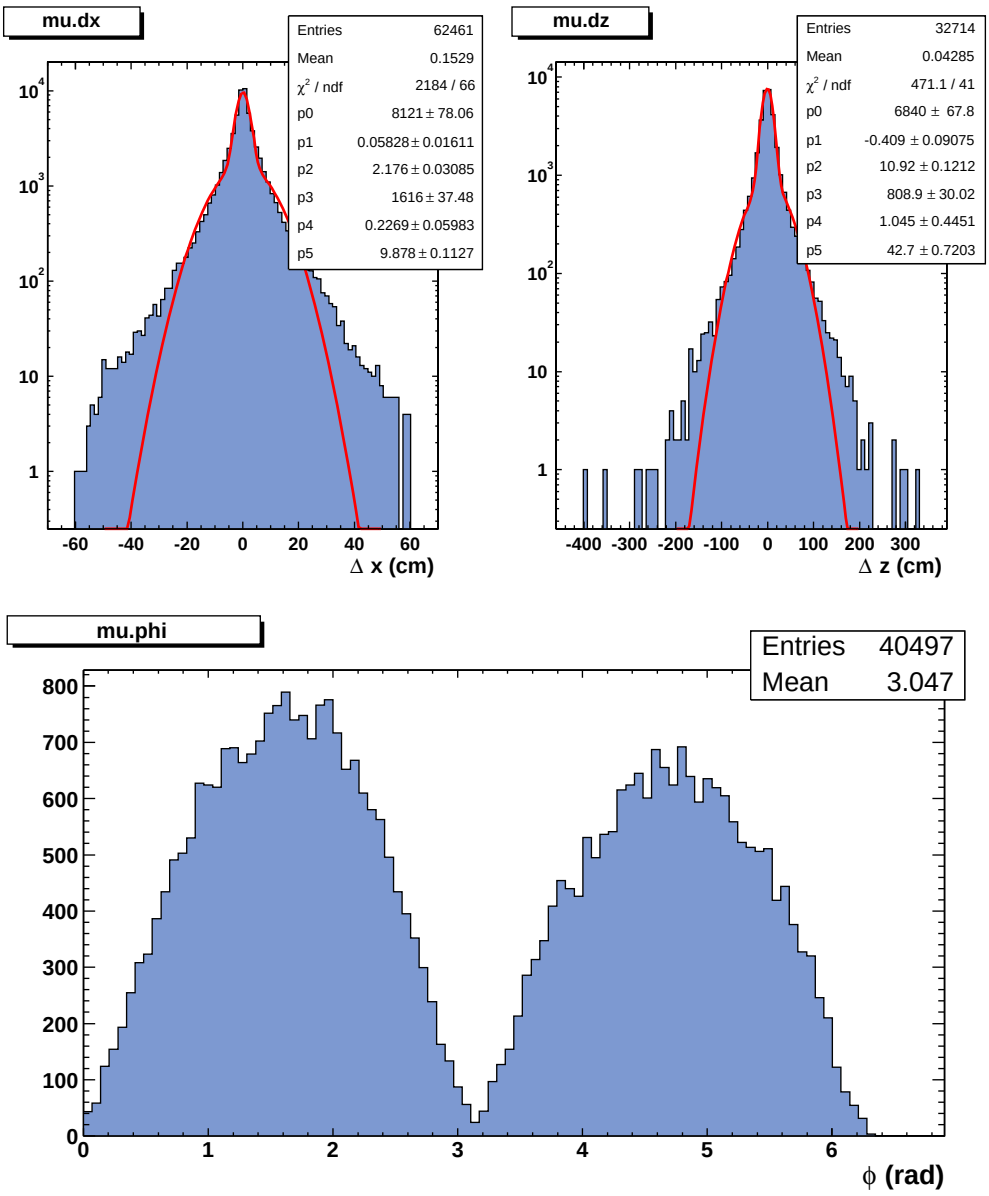

Figure A.2: Track-stub matching and ϕ distribution of the reconstructed muons. The data are free of selection cuts.

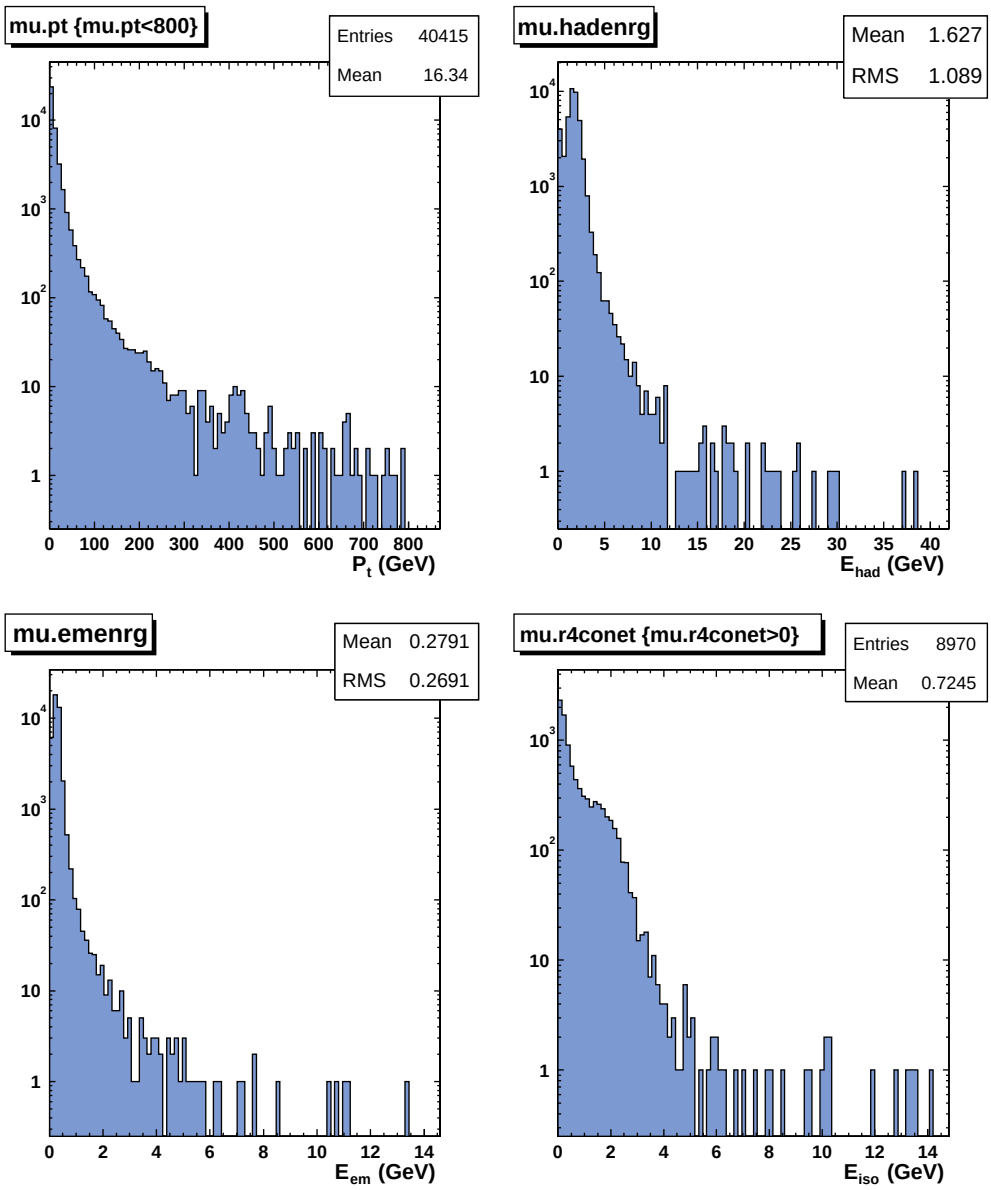

Figure A.3: Kinematic variables for muons. A few overflow events exists in the distributions.

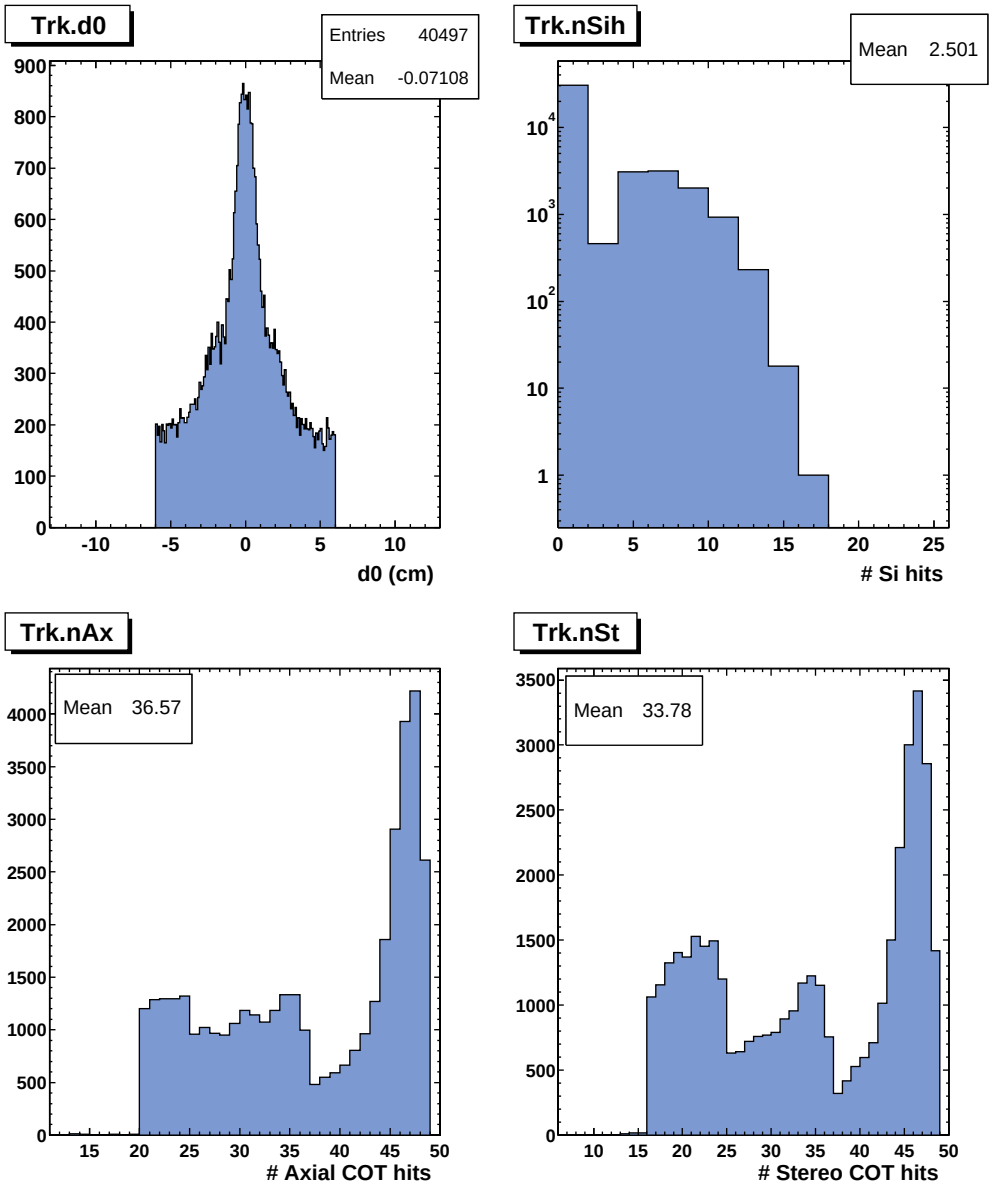

Figure A.4: Muon track parameters (d_0, number of silicon hits per track, number of axial hits and stereo hits attached to a track).

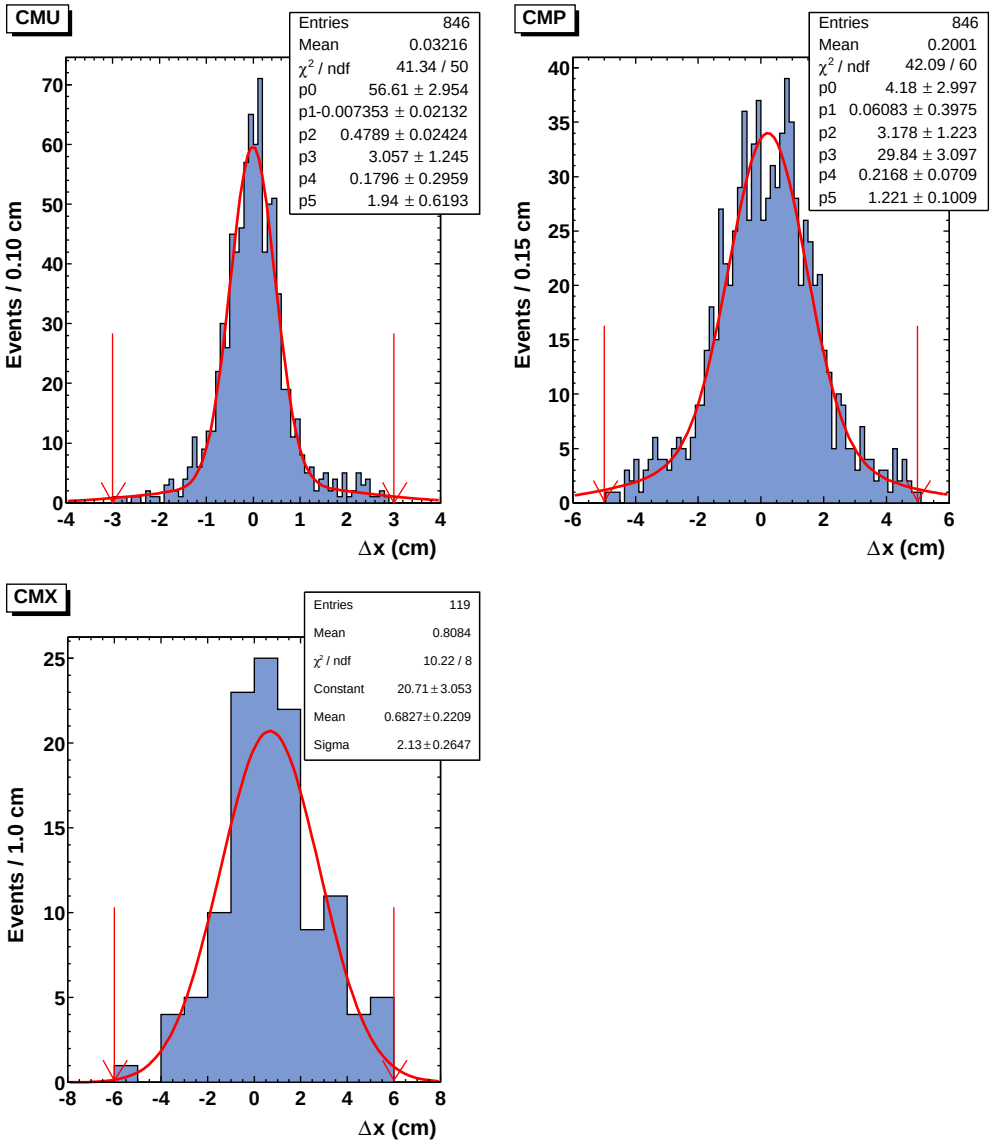

Figure A.5: Track-stub matching parameter, Δx, distributions for CMU, CMP and CMX muons in the final cosmic dimuon sample. Arrows point to the values of the high p_{T} muon requirements for each type.

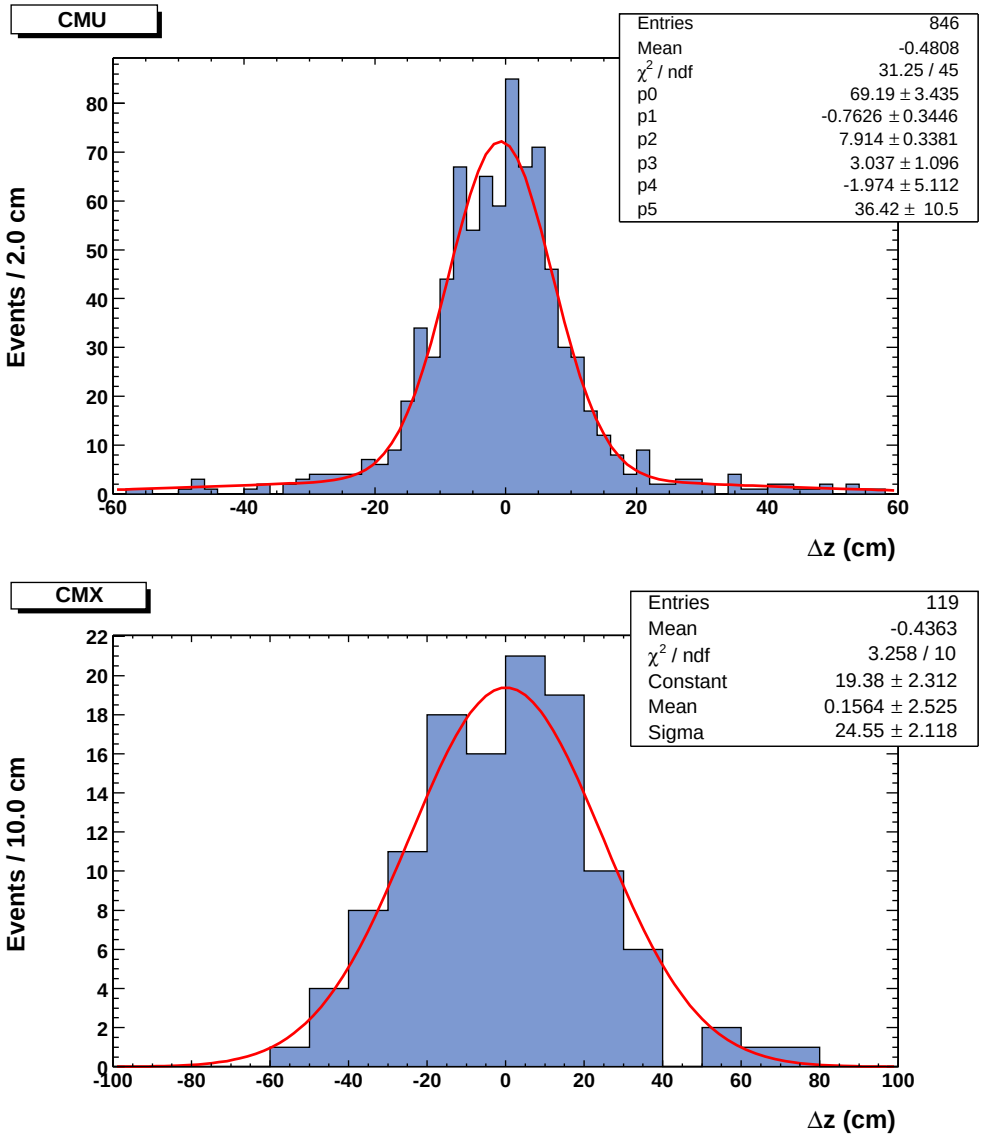

Figure A.6: Track-stub matching parameter, Δz, distribution for CMU, CMP and CMX muons in the final sample of cosmic dimuons.

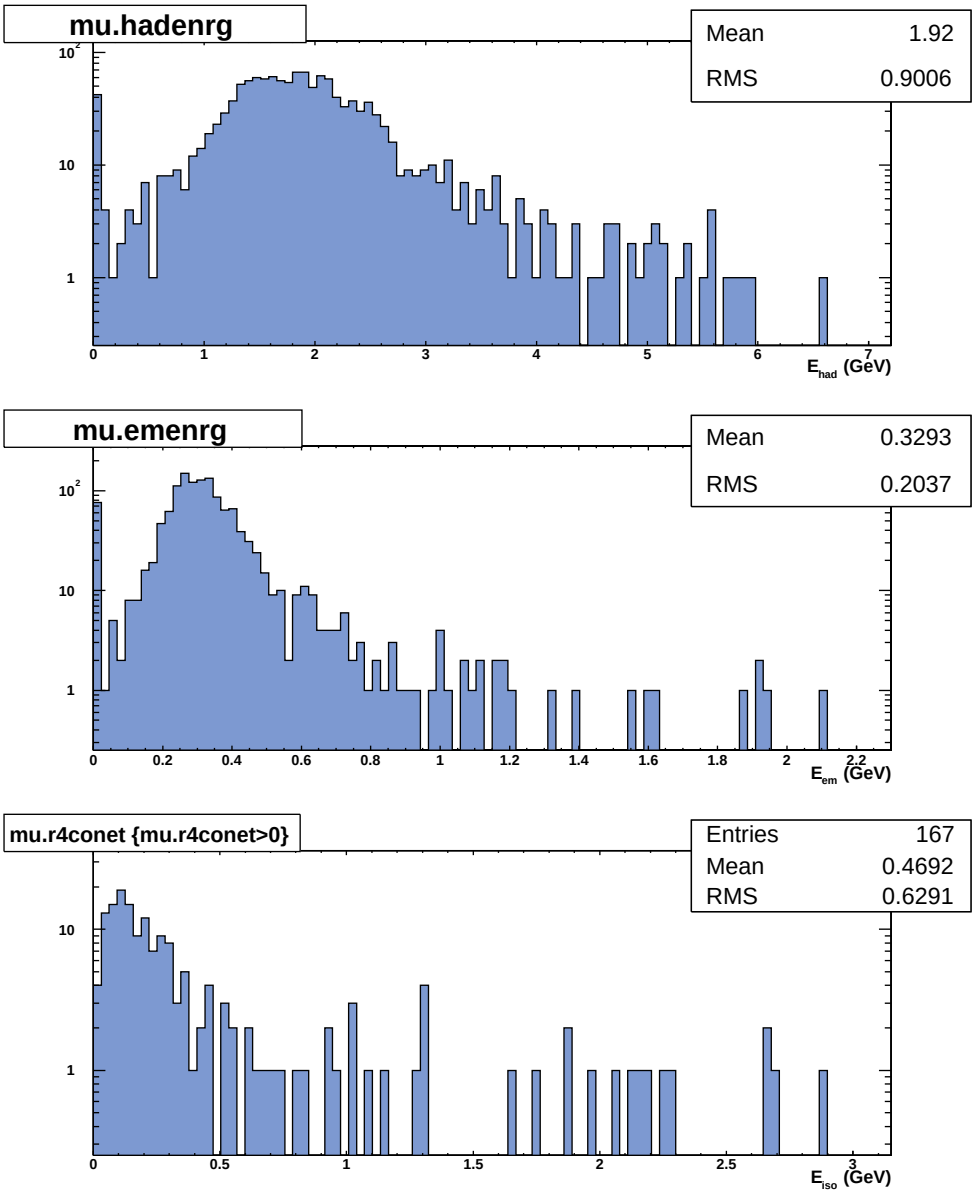

Figure A.7: E_{HAD}, E_{EM} and E_{iso} distributions for the muons in the final cosmic sample.

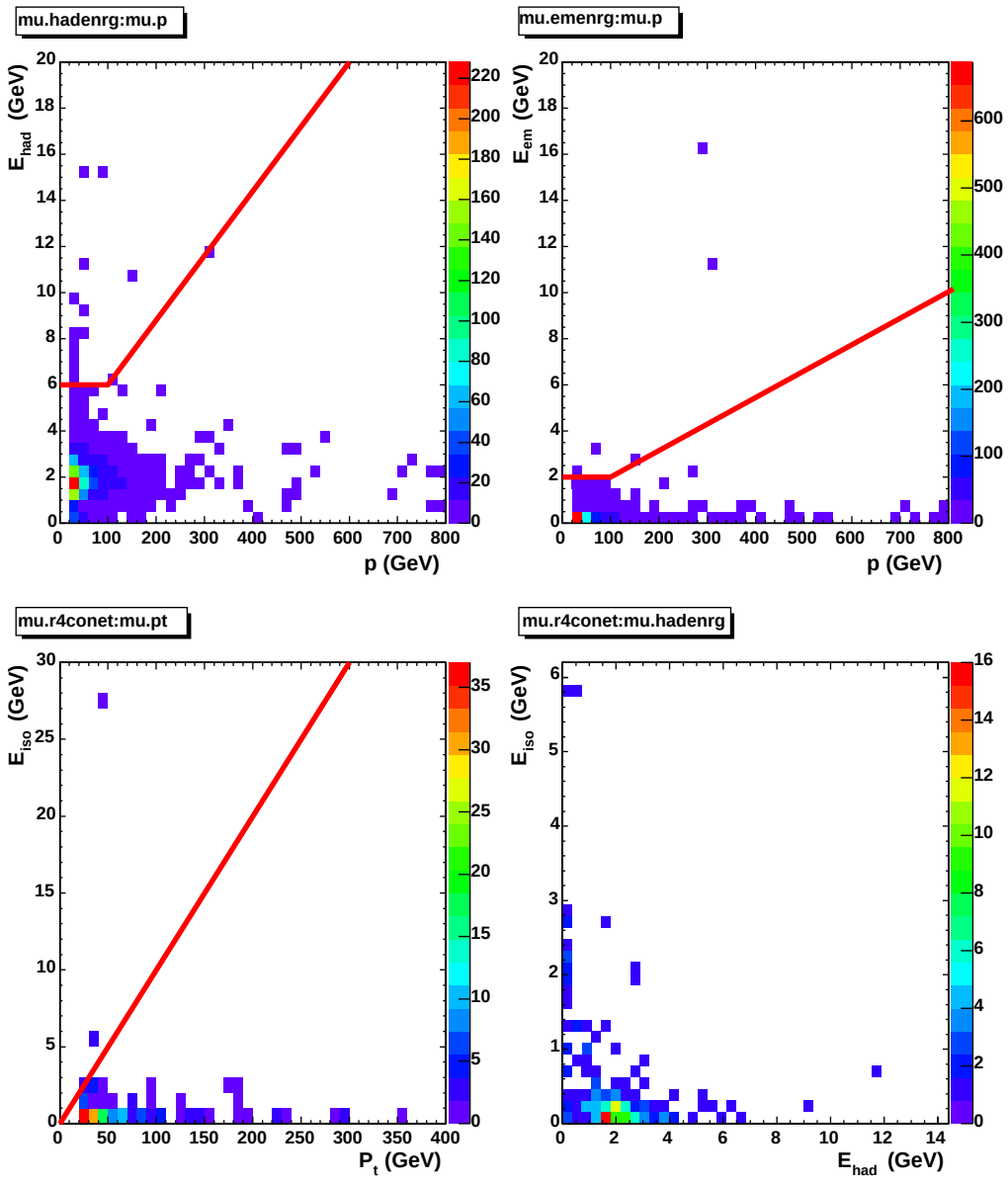

Figure A.8: E_{HAD}, E_{EM} and E_{iso} distributions of muons as a function of muon p_T and p in the final cosmic sample. No MIP or isolation selection requirements have been applied.

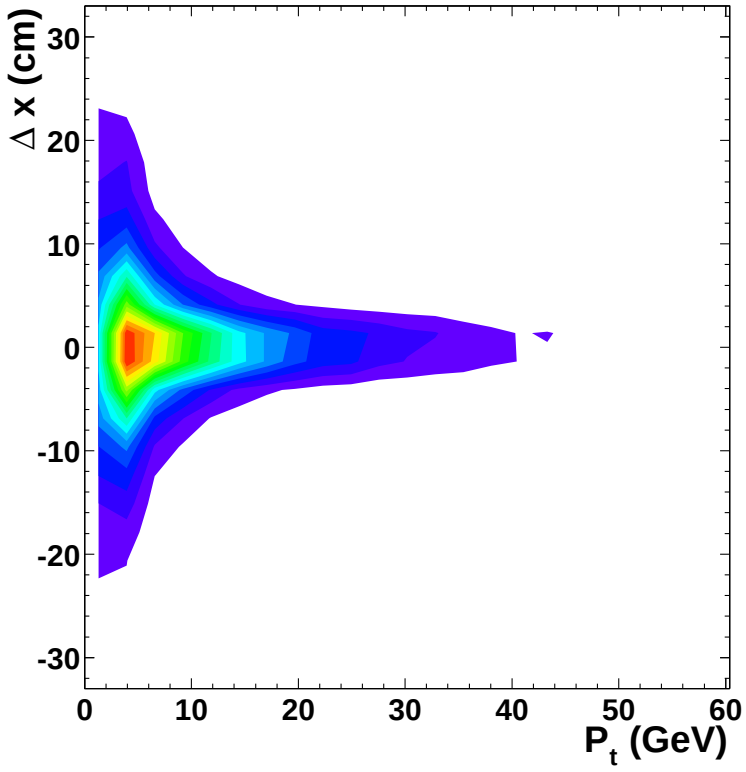

Figure A.9: Δx versus p_{T} of the reconstructed muons in inclusive cosmic ray sample.

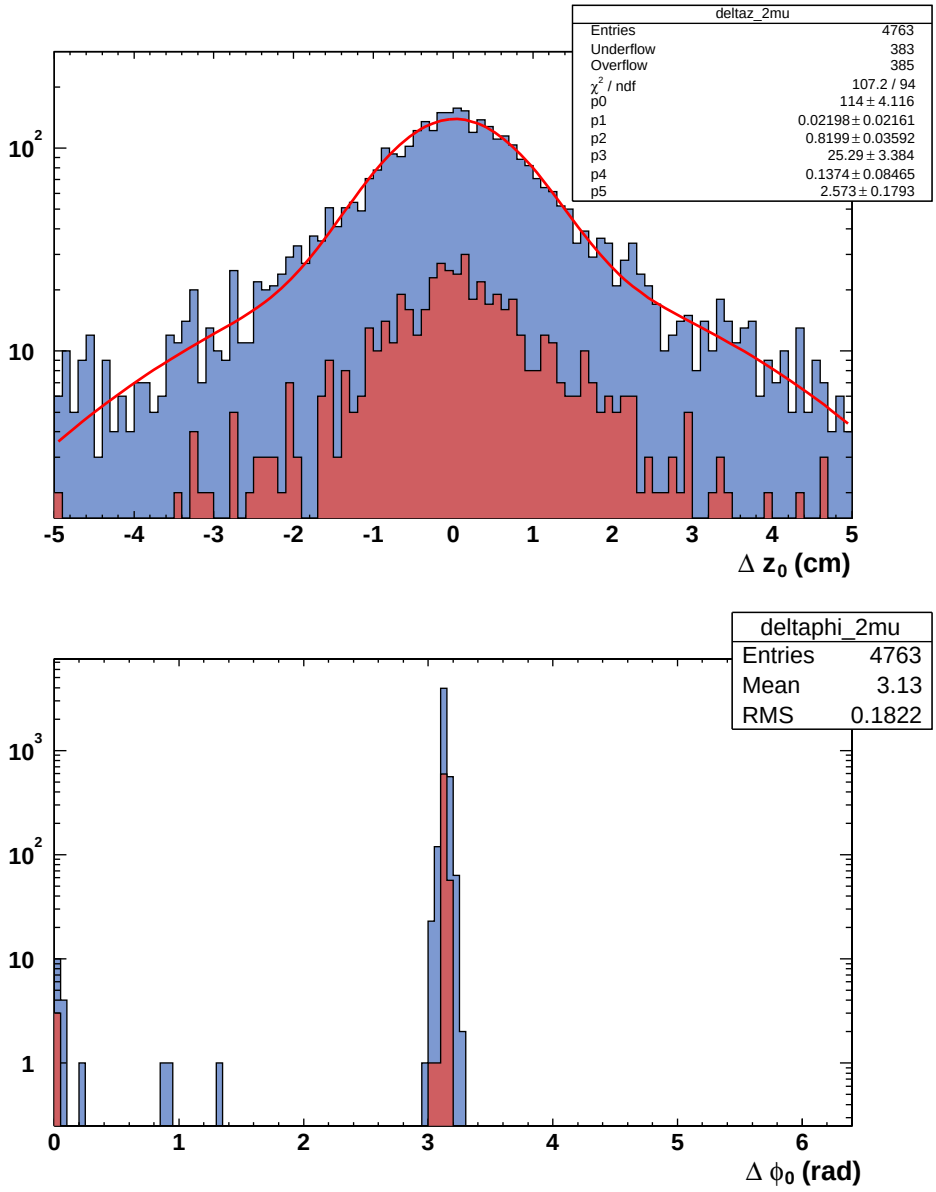

Figure A.10: Δz and $\Delta\phi$ for the muon tracks. Muons passing selection cuts (dark, red) are overlaid on top of the dimuons to which no selection cuts applied (other than detector fiduciality cut) (light, blue). The Δz distribution for the final selection has about 30 overflows (out of 659 total entries).

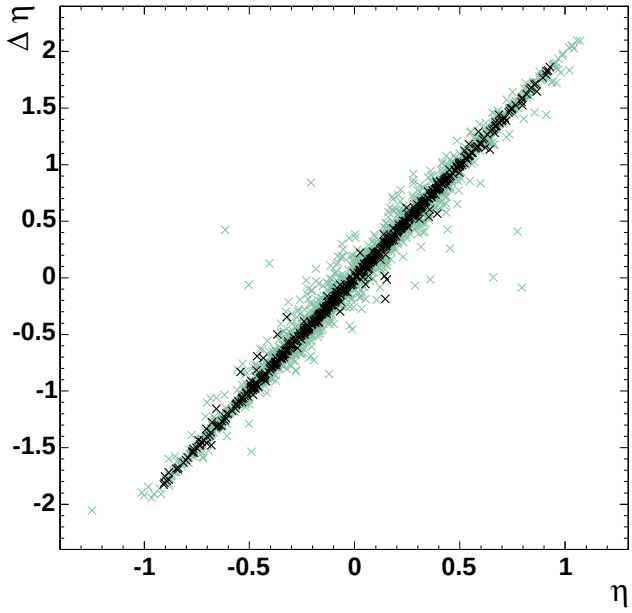

Figure A.11: $\Delta\eta$ vs the first muon η of the good cosmic muon pair (black, dark) overlaid with the fiducial muon pair (green, light).

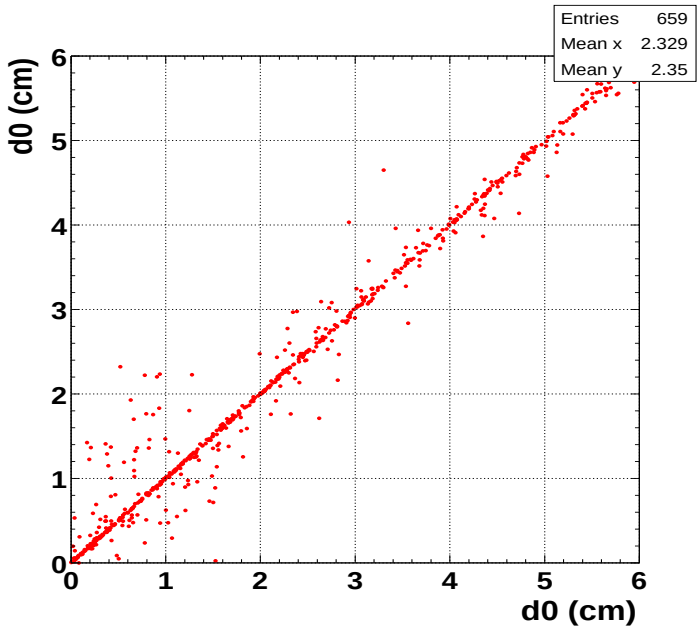

Figure A.12: $|d_{0,1}|$ versus $|d_{0,2}|$ of the final good cosmic muon pair.

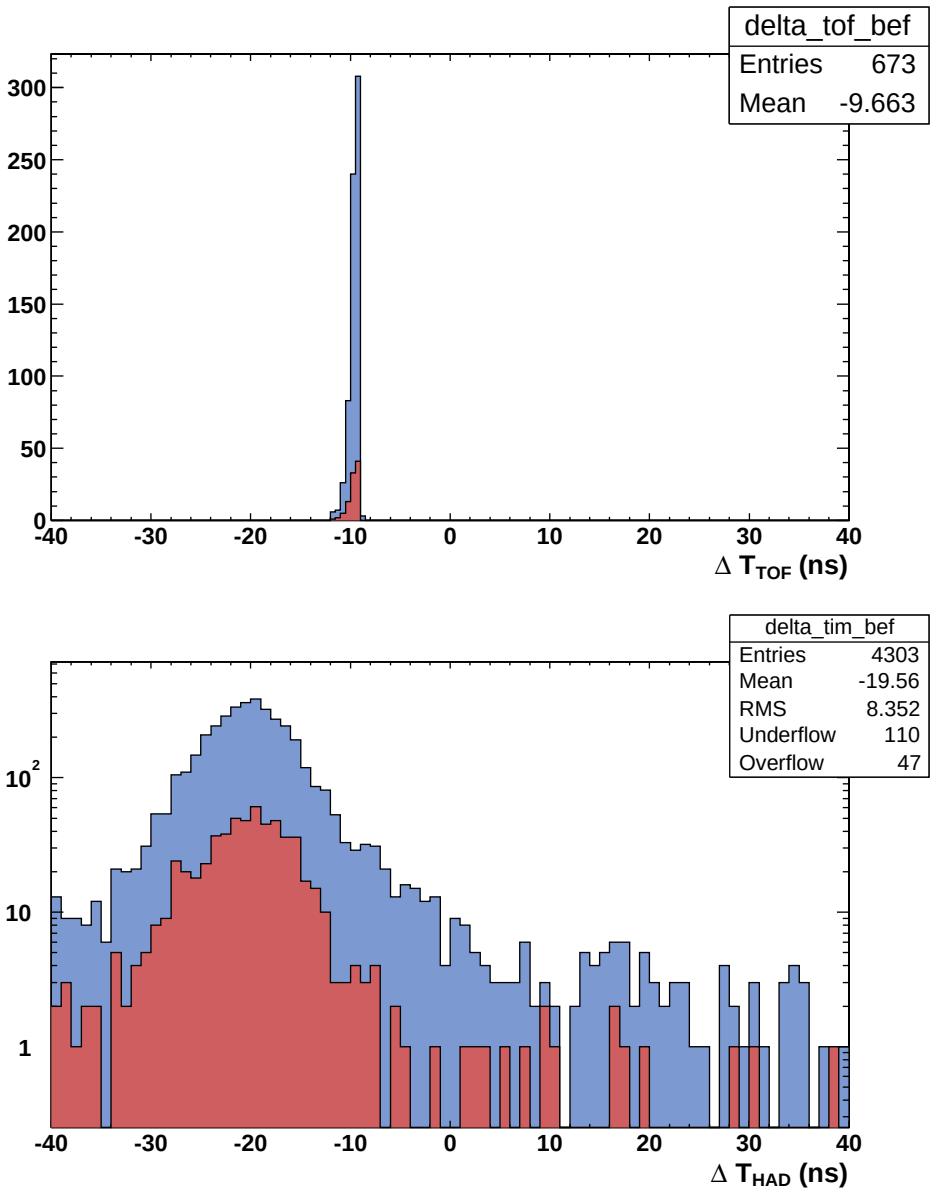

Figure A.13: ΔTOF (top) and ΔTDC (bottom) for the timing variables. Dimuons passing selection cuts (darker, red histogram) are overlaid on top of the dimuons to which only detector fiduciality cut was applied (blue histogram).

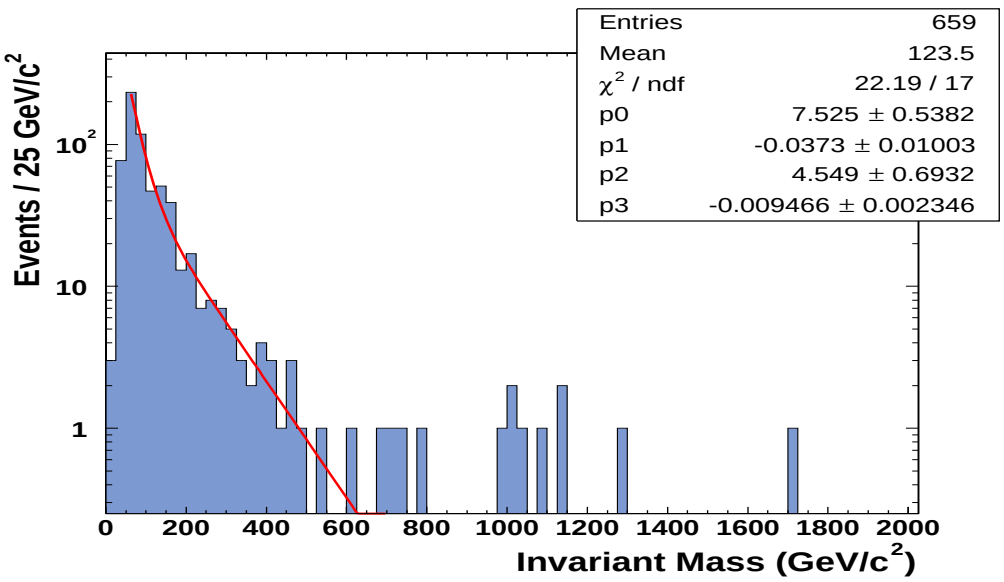

Figure A.14: Invariant mass spectrum of good high p_{T} dimuons in the cosmic ray data fitted to a double exponential.

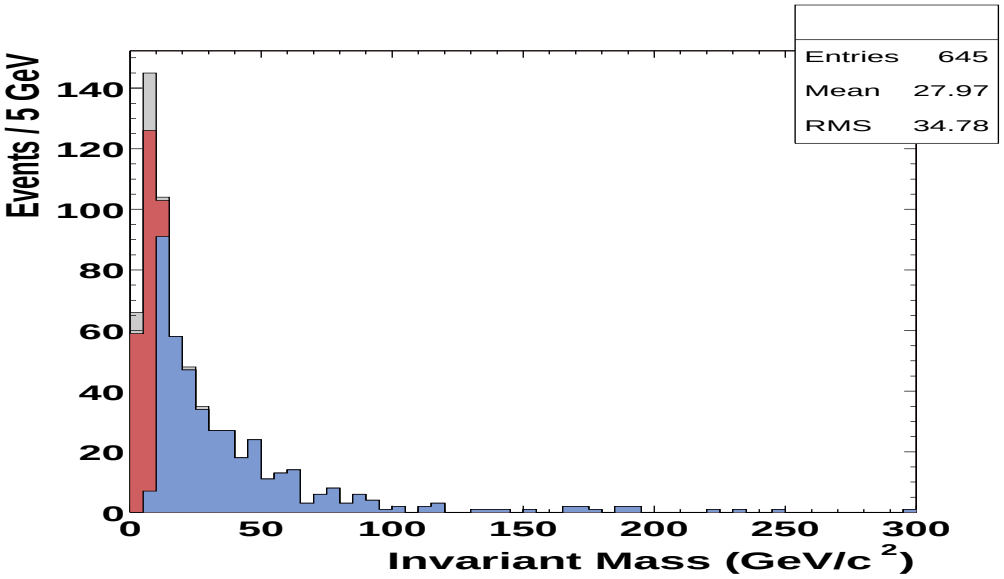

Figure A.15: Invariant mass spectrum of reconstructed dimuons in cosmic data. The blue (lightest) filled histogram represents the total events, red filled (darkest) histogram represents the events which the CRT tagged as cosmic data and blue filled (darker) histogram is the events in which the dicosmic tag is fired.

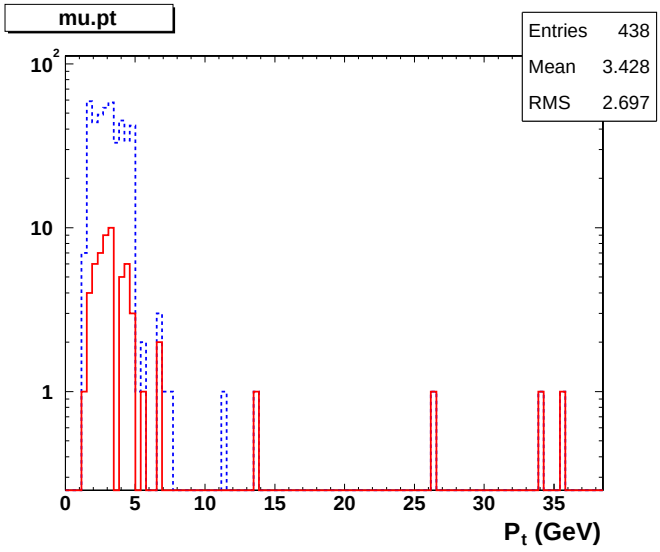

Figure A.16: p_{T} distribution of muons not tagged by the CRT (solid line) and not tagged by the dicosmic tagger (dashed). The plot is not stacked and the high p_{T} region histograms completely overlap.

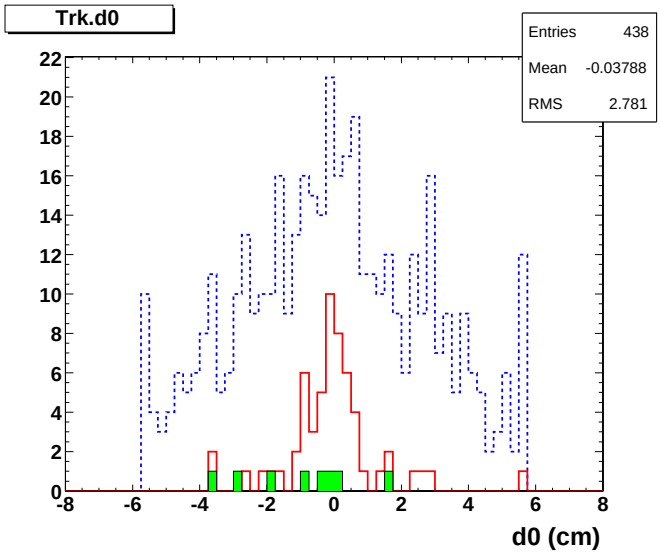

Figure A.17: d_0 distribution of muons not tagged by the CRT (solid line) and not tagged by the dicosmic tagger (dashed). $\mathrm{d_0}$ of muons with $p_{\mathrm{T}} > 5$ GeV/c and failing the dicosmic tagger (filled) is also shown.

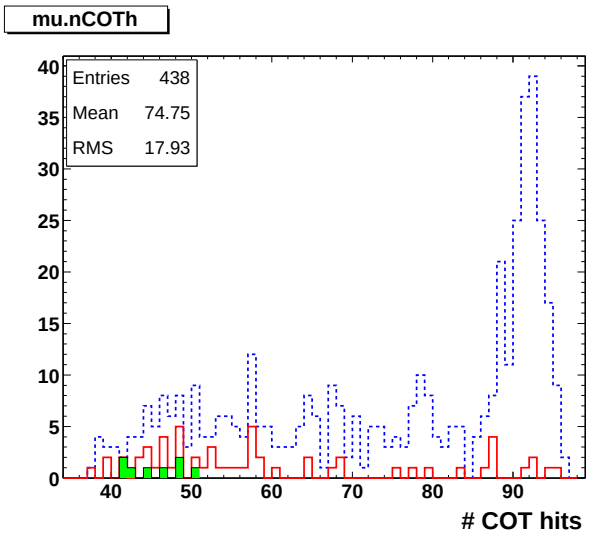

Figure A.18: Number of COT hits for muons not tagged by the CRT (solid line) and not tagged by the dicosmic tagger (dashed). The number of COT hits of the muons with $p_{\mathrm{T}} > 5$ GeV/c failing the dicosmic tagger (filled) is also shown.

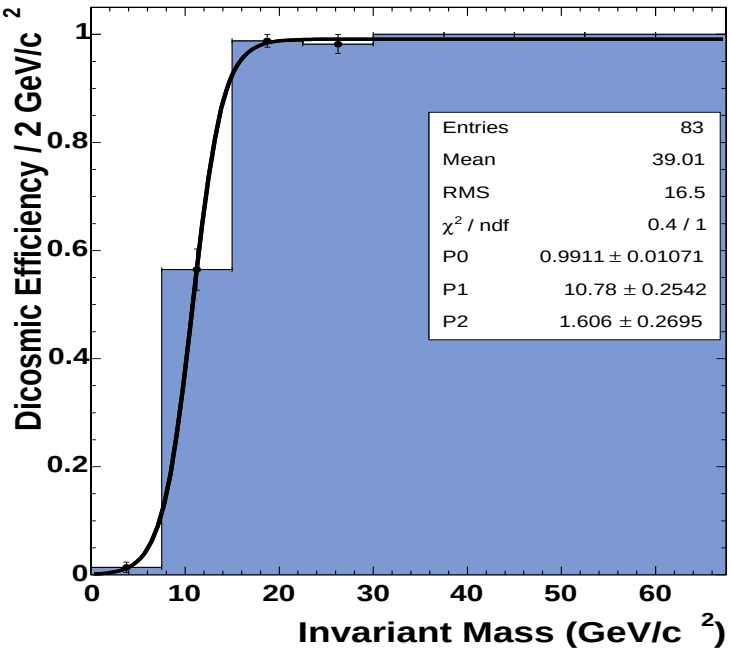

Figure A.19: Efficiency of the dicosmic tagger as a function of $M_{\mu\mu}$.

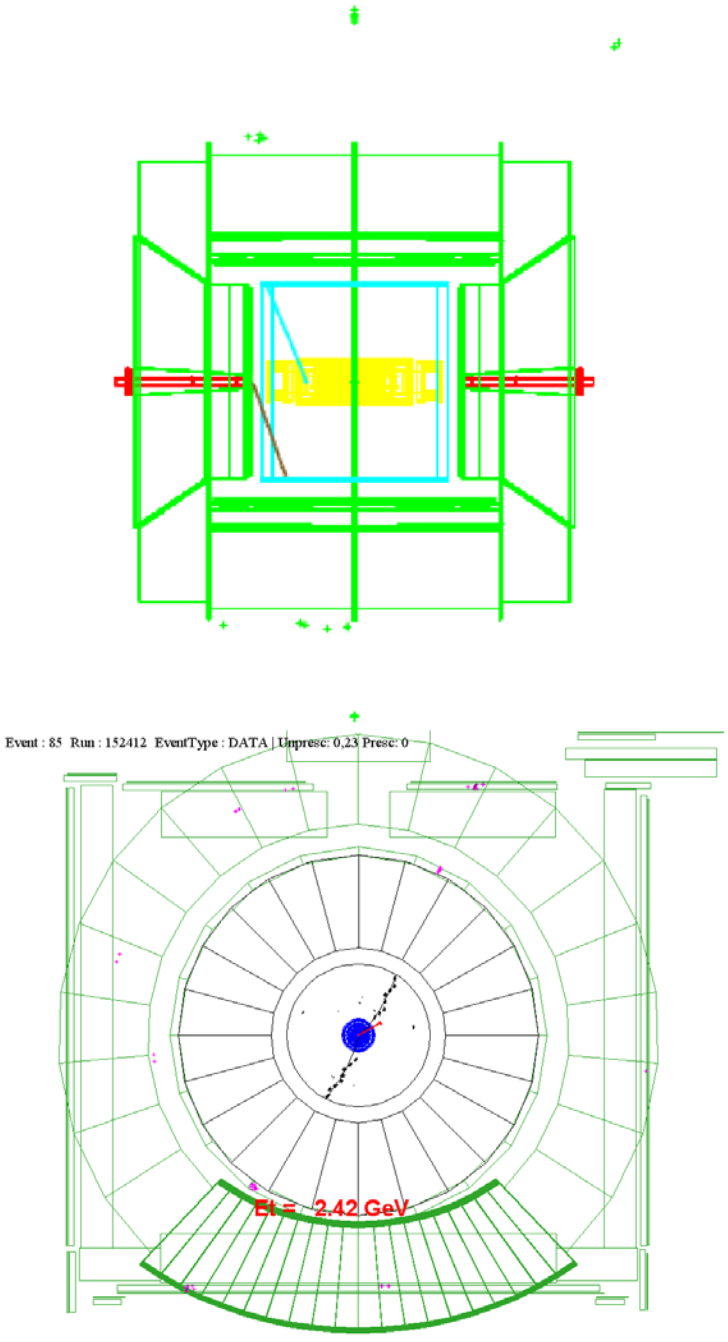

Figure A.20: $r-z$ (top) and $r-\phi$ (bottom) views of event 85 of run 152412 as an example of showering and outside of COT boundary.

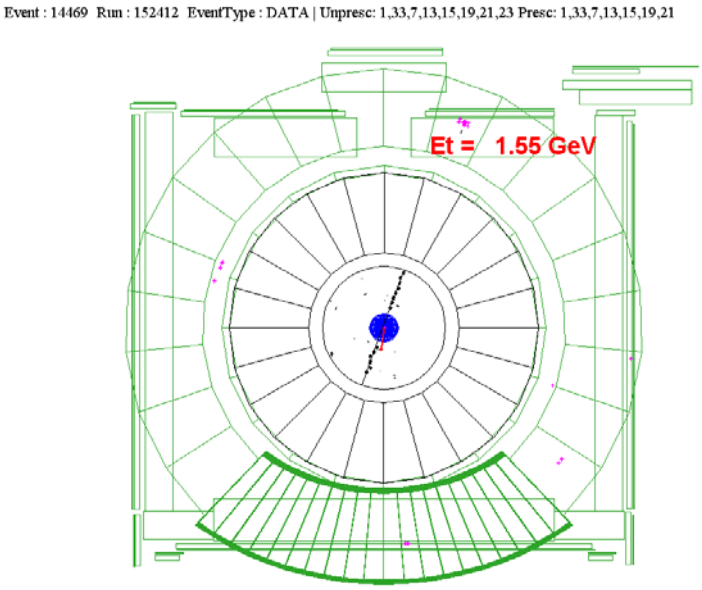

Figure A.21: $r - \phi$ view of event 14469 of run 152412. The event has a CMX muon and a stubless muon with an invariant mass of 140 GeV/c.

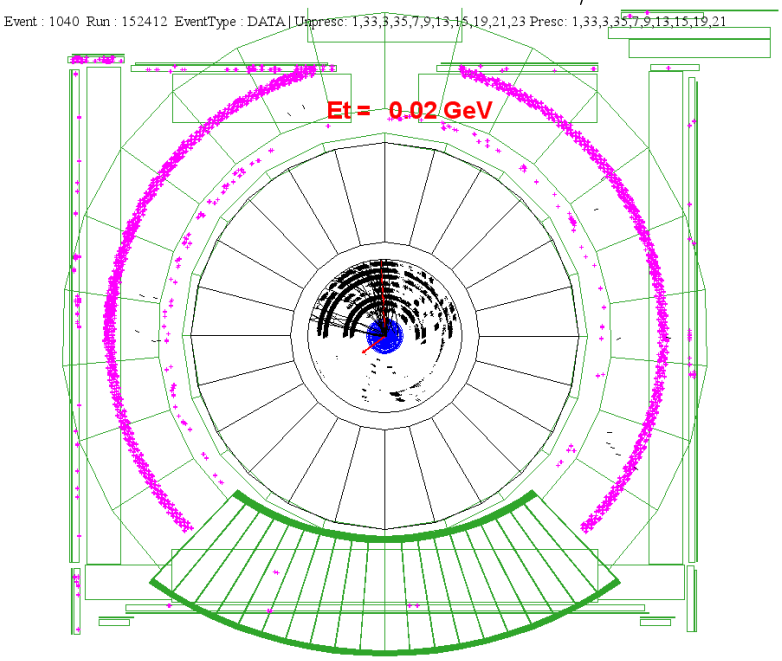

Figure A.22: The $r - \phi$ view of event 1040 of run 152412.

Appendix B

The CDF Collaboration

D. Acosta,[16] J. Adelman,[12] T. Affolder,[9] T. Akimoto,[54] M.G. Albrow,[15] D. Ambrose,[43] S. Amerio,[42] D. Amidei,[33] A. Anastassov,[50] K. Anikeev,[31] A. Annovi,[44] J. Antos,[1] M. Aoki,[54] G. Apollinari,[15] T. Arisawa,[56] J-F. Arguin,[32] A. Artikov,[13] W. Ashmanskas,[15] A. Attal,[7] F. Azfar,[41] P. Azzi-Bacchetta,[42] N. Bacchetta,[42] H. Bachacou,[28] W. Badgett,[15] A. Barbaro-Galtieri,[28] G.J. Barker,[25] V.E. Barnes,[46] B.A. Barnett,[24] S. Baroiant,[6] M. Barone,[17] G. Bauer,[31] F. Bedeschi,[44] S. Behari,[24] S. Belforte,[53] G. Bellettini,[44] J. Bellinger,[58] E. Ben-Haim,[15] D. Benjamin,[14] A. Beretvas,[15] A. Bhatti,[48] M. Binkley,[15] D. Bisello,[42] M. Bishai,[15] R.E. Blair,[2] C. Blocker,[5] K. Bloom,[33] B. Blumenfeld,[24] A. Bocci,[48] A. Bodek,[47] G. Bolla,[46] A. Bolshov,[31] P.S.L. Booth,[29] D. Bortoletto,[46] J. Boudreau,[45]

S. Bourov,[15] C. Bromberg,[34] E. Brubaker,[12] J. Budagov,[13] H.S. Budd,[47] K. Burkett,[15] G. Busetto,[42] P. Bussey,[19] K.L. Byrum,[2] S. Cabrera,[14] P. Calafiura,[28] M. Campanelli,[18] M. Campbell,[33] A. Canepa,[46] M. Casarsa,[53] D. Carlsmith,[58] S. Carron,[14] R. Carosi,[44] M. Cavalli-Sforza,[3] A. Castro,[4] P. Catastini,[44] D. Cauz,[53] A. Cerri,[28] C. Cerri,[44] L. Cerrito,[23] J. Chapman,[33] C. Chen,[43] Y.C. Chen,[1] M. Chertok,[6] G. Chiarelli,[44] G. Chlachidze,[13] F. Chlebana,[15] I. Cho,[27] K. Cho,[27] D. Chokheli,[13] M.L. Chu,[1] S. Chuang,[58] J.Y. Chung,[38] W-H. Chung,[58] Y.S. Chung,[47] C.I. Ciobanu,[23] M.A. Ciocci,[44] A.G. Clark,[18] D. Clark,[5] M. Coca,[47] A. Connolly,[28] M. Convery,[48] J. Conway,[50] B. Cooper,[30] M. Cordelli,[17] G. Cortiana,[42] J. Cranshaw,[52] J. Cuevas,[10] R. Culbertson,[15] C. Currat,[28] D. Cyr,[58] D. Dagenhart,[5] S. Da Ronco,[42] S. D'Auria,[19] P. de Barbaro,[47] S. De Cecco,[49] G. De Lentdecker,[47] S. Dell'Agnello,[17] M. Dell'Orso,[44] S. Demers,[47] L. Demortier,[48] M. Deninno,[4] D. De Pedis,[49] P.F. Derwent,[15] C. Dionisi,[49] J.R. Dittmann,[15] P. Doksus,[23] A. Dominguez,[28] S. Donati,[44] M. Donega,[18] J. Donini,[42] M. D'Onofrio,[18] T. Dorigo,[42] V. Drollinger,[36] K. Ebina,[56] N. Eddy,[23] R. Ely,[28] R. Erbacher,[15] M. Erdmann,[25] D. Errede,[23] S. Errede,[23] R. Eusebi,[47] H-C. Fang,[28] S. Farrington,[29] I. Fedorko,[44] R.G. Feild,[59] M. Feindt,[25] J.P. Fernandez,[46] C. Ferretti,[33] R.D. Field,[16] I. Fiori,[44] G. Flanagan,[34] B. Flaugher,[15] L.R. Flores-Castillo,[45] A. Foland,[20] S. Forrester,[6] G.W. Foster,[15] M. Franklin,[20] J. Freeman,[28] H. Frisch,[12] Y. Fujii,[26] I. Furic,[12] A. Gajjar,[29] A. Gallas,[37] J. Galyardt,[11] M. Gallinaro,[48] M. Garcia-Sciveres,[28] A.F. Garfinkel,[46]

C. Gay,[59] H. Gerberich,[14] D.W. Gerdes,[33] E. Gerchtein,[11] S. Giagu,[49] P. Giannetti,[44] A. Gibson,[28] K. Gibson,[11] C. Ginsburg,[58] K. Giolo,[46] M. Giordani,[53] G. Giurgiu,[11] V. Glagolev,[13] D. Glenzinski,[15] M. Gold,[36] N. Goldschmidt,[33] D. Goldstein,[7] J. Goldstein,[41] G. Gomez,[10] G. Gomez-Ceballos,[31] M. Goncharov,[51] O. González,[46] I. Gorelov,[36] A.T. Goshaw,[14] Y. Gotra,[45] K. Goulianos,[48] A. Gresele,[4] M. Griffiths,[29] C. Grosso-Pilcher,[12] M. Guenther,[46] J. Guimaraes da Costa,[20] C. Haber,[28] K. Hahn,[43] S.R. Hahn,[15] E. Halkiadakis,[47] A. Hamilton,[32] R. Handler,[58] F. Happacher,[17] K. Hara,[54] M. Hare,[55] R.F. Harr,[57] R.M. Harris,[15] F. Hartmann,[25] K. Hatakeyama,[48] J. Hauser,[7] C. Hays,[14] H. Hayward,[29] E. Heider,[55] B. Heinemann,[29] J. Heinrich,[43] M. Hennecke,[25] M. Herndon,[24] C. Hill,[9] D. Hirschbuehl,[25] A. Hocker,[47] K.D. Hoffman,[12] A. Holloway,[20] S. Hou,[1] M.A. Houlden,[29] B.T. Huffman,[41] Y. Huang,[14] R.E. Hughes,[38] J. Huston,[34] K. Ikado,[56] J. Incandela,[9] G. Introzzi,[44] M. Iori,[49] Y. Ishizawa,[54] C. Issever,[9] A. Ivanov,[47] Y. Iwata,[22] B. Iyutin,[31] E. James,[15] D. Jang,[50] J. Jarrell,[36] D. Jeans,[49] H. Jensen,[15] E.J. Jeon,[27] M. Jones,[46] K.K. Joo,[27] S. Jun,[11] T. Junk,[23] T. Kamon,[51] J. Kang,[33] M. Karagoz Unel,[37] P.E. Karchin,[57] S. Kartal,[15] Y. Kato,[40] Y. Kemp,[25] R. Kephart,[15] U. Kerzel,[25] V. Khotilovich,[51] B. Kilminster,[38] D.H. Kim,[27] H.S. Kim,[23] J.E. Kim,[27] M.J. Kim,[11] M.S. Kim,[27] S.B. Kim,[27] S.H. Kim,[54] T.H. Kim,[31] Y.K. Kim,[12] B.T. King,[29] M. Kirby,[14] L. Kirsch,[5] S. Klimenko,[16] B. Knuteson,[31] B.R. Ko,[14] H. Kobayashi,[54] P. Koehn,[38] D.J. Kong,[27] K. Kondo,[56] J. Konigsberg,[16] K. Kordas,[32]

A. Korn,[31] A. Korytov,[16] K. Kotelnikov,[35] A.V. Kotwal,[14] A. Kovalev,[43] J. Kraus,[23] I. Kravchenko,[31] A. Kreymer,[15] J. Kroll,[43] M. Kruse,[14] V. Krutelyov,[51] S.E. Kuhlmann,[2] N. Kuznetsova,[15] A.T. Laasanen,[46] S. Lai,[32] S. Lami,[48] S. Lammel,[15] J. Lancaster,[14] M. Lancaster,[30] R. Lander,[6] K. Lannon,[38] A. Lath,[50] G. Latino,[36] R. Lauhakangas,[21] I. Lazzizzera,[42] Y. Le,[24] C. Lecci,[25] T. LeCompte,[2] J. Lee,[27] J. Lee,[47] S.W. Lee,[51] R. Lefevre,[3] N. Leonardo,[31] S. Leone,[44] J.D. Lewis,[15] K. Li,[59] C. Lin,[59] C.S. Lin,[15] M. Lindgren,[15] T.M. Liss,[23] D.O. Litvintsev,[15] T. Liu,[15] Y. Liu,[18] N.S. Lockyer,[43] A. Loginov,[35] M. Loreti,[42] P. Loverre,[49] R-S. Lu,[1] D. Lucchesi,[42] P. Lujan,[28] P. Lukens,[15] L. Lyons,[41] J. Lys,[28] R. Lysak,[1] D. MacQueen,[32] R. Madrak,[20] K. Maeshima,[15] P. Maksimovic,[24] L. Malferrari,[4] G. Manca,[29] R. Marginean,[38] M. Martin,[24] A. Martin,[59] V. Martin,[37] M. Martínez,[3] T. Maruyama,[54] H. Matsunaga,[54] M. Mattson,[57] P. Mazzanti,[4] K.S. McFarland,[47] D. McGivern,[30] P.M. McIntyre,[51] P. McNamara,[50] R. NcNulty,[29] S. Menzemer,[31] A. Menzione,[44] P. Merkel,[15] C. Mesropian,[48] A. Messina,[49] T. Miao,[15] N. Miladinovic,[5] L. Miller,[20] R. Miller,[34] J.S. Miller,[33] R. Miquel,[28] S. Miscetti,[17] G. Mitselmakher,[16] A. Miyamoto,[26] Y. Miyazaki,[40] N. Moggi,[4] B. Mohr,[7] R. Moore,[15] M. Morello,[44] A. Mukherjee,[15] M. Mulhearn,[31] T. Muller,[25] R. Mumford,[24] A. Munar,[43] P. Murat,[15] J. Nachtman,[15] S. Nahn,[59] I. Nakamura,[43] I. Nakano,[39] A. Napier,[55] R. Napora,[24] D. Naumov,[36] V. Necula,[16] F. Niell,[33] J. Nielsen,[28] C. Nelson,[15] T. Nelson,[15] C. Neu,[43] M.S. Neubauer,[8] C. Newman-Holmes,[15] A-

S. Nicollerat,[18] T. Nigmanov,[45] L. Nodulman,[2] O. Norniella,[3] K. Oesterberg,[21] T. Ogawa,[56] S.H. Oh,[14] Y.D. Oh,[27] T. Ohsugi,[22] T. Okusawa,[40] R. Oldeman,[49] R. Orava,[21] W. Orejudos,[28] C. Pagliarone,[44] F. Palmonari,[44] R. Paoletti,[44] V. Papadimitriou,[15] S. Pashapour,[32] J. Patrick,[15] G. Pauletta,[53] M. Paulini,[11] T. Pauly,[41] C. Paus,[31] D. Pellett,[6] A. Penzo,[53] T.J. Phillips,[14] G. Piacentino,[44] J. Piedra,[10] K.T. Pitts,[23] C. Plager,[7] A. Pompoš,[46] L. Pondrom,[58] G. Pope,[45] O. Poukhov,[13] F. Prakoshyn,[13] T. Pratt,[29] A. Pronko,[16] J. Proudfoot,[2] F. Ptohos,[17] G. Punzi,[44] J. Rademacker,[41] A. Rakitine,[31] S. Rappoccio,[20] F. Ratnikov,[50] H. Ray,[33] A. Reichold,[41] B. Reisert,[15] V. Rekovic,[36] P. Renton,[41] M. Rescigno,[49] F. Rimondi,[4] K. Rinnert,[25] L. Ristori,[44] W.J. Robertson,[14] A. Robson,[41] T. Rodrigo,[10] S. Rolli,[55] L. Rosenson,[31] R. Roser,[15] R. Rossin,[42] C. Rott,[46] J. Russ,[11] A. Ruiz,[10] D. Ryan,[55] H. Saarikko,[21] A. Safonov,[6] R. St. Denis,[19] W.K. Sakumoto,[47] G. Salamanna,[49] D. Saltzberg,[7] C. Sanchez,[3] A. Sansoni,[17] L. Santi,[53] S. Sarkar,[49] K. Sato,[54] P. Savard,[32] A. Savoy-Navarro,[15] P. Schemitz,[25] P. Schlabach,[15] E.E. Schmidt,[15] M.P. Schmidt,[59] M. Schmitt,[37] L. Scodellaro,[42] A. Scribano,[44] F. Scuri,[44] A. Sedov,[46] S. Seidel,[36] Y. Seiya,[40] F. Semeria,[4] L. Sexton-Kennedy,[15] I. Sfiligoi,[17] M.D. Shapiro,[28] T. Shears,[29] P.F. Shepard,[45] M. Shimojima,[54] M. Shochet,[12] Y. Shon,[58] I. Shreyber,[35] A. Sidoti,[44] J. Siegrist,[28] M. Siket,[1] A. Sill,[52] P. Sinervo,[32] A. Sisakyan,[13] A. Skiba,[25] A.J. Slaughter,[15] K. Sliwa,[55] D. Smirnov,[36] J.R. Smith,[6] F.D. Snider,[15] R. Snihur,[32] S.V. Somalwar,[50] J. Spalding,[15] M. Spezziga,[52] L. Spiegel,[15] F. Spinella,[44]

M. Spiropulu,[9] P. Squillacioti,[44] H. Stadie,[25] A. Stefanini,[44] B. Stelzer,[32] O. Stelzer-Chilton,[32] J. Strologas,[36] D. Stuart,[9] A. Sukhanov,[16] K. Sumorok,[31] H. Sun,[55] T. Suzuki,[54] A. Taffard,[23] R. Tafirout,[32] S.F. Takach,[57] H. Takano,[54] R. Takashima,[22] Y. Takeuchi,[54] K. Takikawa,[54] M. Tanaka,[2] R. Tanaka,[39] N. Tanimoto,[39] S. Tapprogge,[21] M. Tecchio,[33] P.K. Teng,[1] K. Terashi,[48] R.J. Tesarek,[15] S. Tether,[31] J. Thom,[15] A.S. Thompson,[19] E. Thomson,[43] P. Tipton,[47] V. Tiwari,[11] S. Tkaczyk,[15] D. Toback,[51] K. Tollefson,[34] T. Tomura,[54] D. Tonelli,[44] M. Tönnesmann,[34] S. Torre,[44] D. Torretta,[15] S. Tourneur,[15] W. Trischuk,[32] J. Tseng,[41] R. Tsuchiya,[56] S. Tsuno,[39] D. Tsybychev,[16] N. Turini,[44] M. Turner,[29] F. Ukegawa,[54] T. Unverhau,[19] S. Uozumi,[54] D. Usynin,[43] L. Vacavant,[28] A. Vaiciulis,[47] A. Varganov,[33] E. Vataga,[44] S. Vejcik III,[15] G. Velev,[15] G. Veramendi,[23] T. Vickey,[23] R. Vidal,[15] I. Vila,[10] R. Vilar,[10] I. Volobouev,[28] M. von der Mey,[7] P. Wagner,[51] R.G. Wagner,[2] R.L. Wagner,[15] W. Wagner,[25] R. Wallny,[7] T. Walter,[25] T. Yamashita,[39] K. Yamamoto,[40] Z. Wan,[50] M.J. Wang,[1] S.M. Wang,[16] A. Warburton,[32] B. Ward,[19] S. Waschke,[19] D. Waters,[30] T. Watts,[50] M. Weber,[28] W.C. Wester III,[15] B. Whitehouse,[55] A.B. Wicklund,[2] E. Wicklund,[15] H.H. Williams,[43] P. Wilson,[15] B.L. Winer,[38] P. Wittich,[43] S. Wolbers,[15] M. Wolter,[55] M. Worcester,[7] S. Worm,[50] T. Wright,[33] X. Wu,[18] F. Würthwein,[8] A. Wyatt,[30] A. Yagil,[15] U.K. Yang,[12] W. Yao,[28] G.P. Yeh,[15] K. Yi,[24] J. Yoh,[15] P. Yoon,[47] K. Yorita,[56] T. Yoshida,[40] I. Yu,[27] S. Yu,[43] Z. Yu,[59] J.C. Yun,[15] L. Zanello,[49] A. Zanetti,[53] I. Zaw,[20] F. Zetti,[44] J. Zhou,[50] A. Zsenei,[18]

and S. Zucchelli,[4]

(CDF Collaboration)

[1] *Institute of Physics, Academia Sinica, Taipei, Taiwan 11529, Republic of China*

[2] *Argonne National Laboratory, Argonne, Illinois 60439*

[3] *Institut de Fisica d'Altes Energies, Universitat Autonoma de Barcelona, E-08193, Bellaterra (Barcelona), Spain*

[4] *Istituto Nazionale di Fisica Nucleare, University of Bologna, I-40127 Bologna, Italy*

[5] *Brandeis University, Waltham, Massachusetts 02254*

[6] *University of California at Davis, Davis, California 95616*

[7] *University of California at Los Angeles, Los Angeles, California 90024*

[8] *University of California at San Diego, La Jolla, California 92093*

[9] *University of California at Santa Barbara, Santa Barbara, California 93106*

[10] *Instituto de Fisica de Cantabria, CSIC-University of Cantabria, 39005 Santander, Spain*

[11] *Carnegie Mellon University, Pittsburgh, PA 15213*

[12] *Enrico Fermi Institute, University of Chicago, Chicago, Illinois 60637*

[13] *Joint Institute for Nuclear Research, RU-141980 Dubna, Russia*

[14] *Duke University, Durham, North Carolina 27708*

[15] *Fermi National Accelerator Laboratory, Batavia, Illinois 60510*

[16] *University of Florida, Gainesville, Florida 32611*

[17] *Laboratori Nazionali di Frascati, Istituto Nazionale di Fisica Nucleare, I-00044 Frascati, Italy*

[18] *University of Geneva, CH-1211 Geneva 4, Switzerland*

[19] *Glasgow University, Glasgow G12 8QQ, United Kingdom*

[20] *Harvard University, Cambridge, Massachusetts 02138*

[21] *The Helsinki Group: Helsinki Institute of Physics; and Division of High Energy Physics, Department of Physical Sciences, University of Helsinki, FIN-00044, Helsinki, Finland*

[22] *Hiroshima University, Higashi-Hiroshima 724, Japan*

[23] *University of Illinois, Urbana, Illinois 61801*

[24] *The Johns Hopkins University, Baltimore, Maryland 21218*

[25] *Institut für Experimentelle Kernphysik, Universität Karlsruhe, 76128 Karlsruhe, Germany*

[26] *High Energy Accelerator Research Organization (KEK), Tsukuba, Ibaraki 305, Japan*

[27] *Center for High Energy Physics: Kyungpook National University, Taegu 702-701; Seoul National University, Seoul 151-742; and SungKyunKwan University, Suwon 440-746; Korea*

[28] *Ernest Orlando Lawrence Berkeley National Laboratory, Berkeley, California 94720*

[29] *University of Liverpool, Liverpool L69 7ZE, United Kingdom*

[30] *University College London, London WC1E 6BT, United Kingdom*

[31] *Massachusetts Institute of Technology, Cambridge, Massachusetts 02139*

[32] *Institute of Particle Physics: McGill University, Montréal, Canada H3A 2T8; and University of Toronto, Toronto, Canada M5S 1A7*

[33] *University of Michigan, Ann Arbor, Michigan 48109*

[34] *Michigan State University, East Lansing, Michigan 48824*

[35] *Institution for Theoretical and Experimental Physics, ITEP, Moscow 117259, Russia*

[36] *University of New Mexico, Albuquerque, New Mexico 87131*

[37] *Northwestern University, Evanston, Illinois 60208*

[38] *The Ohio State University, Columbus, Ohio 43210*

[39] *Okayama University, Okayama 700-8530, Japan*

[40] *Osaka City University, Osaka 588, Japan*

[41] *University of Oxford, Oxford OX1 3RH, United Kingdom*

[42] *University of Padova, Istituto Nazionale di Fisica Nucleare, Sezione di Padova-Trento, I-35131 Padova, Italy*

[43] *University of Pennsylvania, Philadelphia, Pennsylvania 19104*

[44] *Istituto Nazionale di Fisica Nucleare, University and Scuola Normale Superiore of Pisa, I-56100 Pisa, Italy*

[45] *University of Pittsburgh, Pittsburgh, Pennsylvania 15260*

[46] *Purdue University, West Lafayette, Indiana 47907*

[47] *University of Rochester, Rochester, New York 14627*

[48] *The Rockefeller University, New York, New York 10021*

[49] *Istituto Nazionale di Fisica Nucleare, Sezione di Roma 1, University di Roma "La Sapienza," I-00185 Roma, Italy*

[50] *Rutgers University, Piscataway, New Jersey 08855*

[51] *Texas A&M University, College Station, Texas 77843*

[52] *Texas Tech University, Lubbock, Texas 79409*

[53] *Istituto Nazionale di Fisica Nucleare, University of Trieste/ Udine, Italy*

[54] *University of Tsukuba, Tsukuba, Ibaraki 305, Japan*

[55] *Tufts University, Medford, Massachusetts 02155*

[56] *Waseda University, Tokyo 169, Japan*

[57] *Wayne State University, Detroit, Michigan 48201*

[58] *University of Wisconsin, Madison, Wisconsin 53706*

[59] *Yale University, New Haven, Connecticut 06520*

Appendix C

Notations and CDF Acronyms

General:

CAL Calorimeter

CDF Collider Detector at Fermilab (oldly known as Collider Detector Facility)

DAQ Data AcQuisition

EM Electromagnetic

FNAL Fermi National Accelerator Laboratory

HAD Hadronic

HEP High Energy Physics

LINAC LINear ACccelerator

MIP Minimum Ionizing Particle

CDF Detector Specific:

ASD Amplifier-Shaper-Discriminator

BHM Beam Halo Monitor

BMU Barrel (Intermediate) Muon Chamber

BSU Barrel (Intermediate) Muon Scintillator

CCR Central crack gas chamber

CEM Central Electromagnetic Calorimeter

CES Central Electromagnetic strip/wire gas chamber

CHA Central Hadronic Calorimeter

CLC Čerenkov Luminosity Counter

CMP Central Muon Wall Chamber Upgrade

CMU Central Muon Chambers

CMUP CDF Muon which has information from both CMU and CMP Chambers

CMX Central Muon Chamber Extension

COT Central Outer Tracker Chambers

CPR Central Pre-Radiator gas chamber

CSP Central Muon Wall Scintillator Upgrade

CSX Central Muon Scintillator Extension

DIRAC Level 1 calorimeter trigger

DCAS Level 2 calorimeter trigger

IMU Intermediate MUon System

ISL Intermediate Silicon Layer

LØØ Inner-most Silicon Layer

MSX CMX Miniskirt Scintillator

PEM Plug (forward) Electromagnetic Calorimeter

PES Plug Electromagnetic Shower-Max detector

PPR Plug Pre-Radiator scintillators

PHA Plug Hadronic Calorimeter

SVT Secondary Vertex Trigger (for SVX) for the Level 2 trigger

SVX Silicon Vertex barrel Detector

TOF Time-of-Flight (Detector)

TSI Trigger-System-Interface

XFT eXtremely Fast Tracker (for COT) for the Level 1 trigger

XTRP Extrapolation Module from XFT for the Level 1 and Level 2 trigger

WHA Wall Hadronic Calorimeter

Appendix D

Technical View of CDF Detector

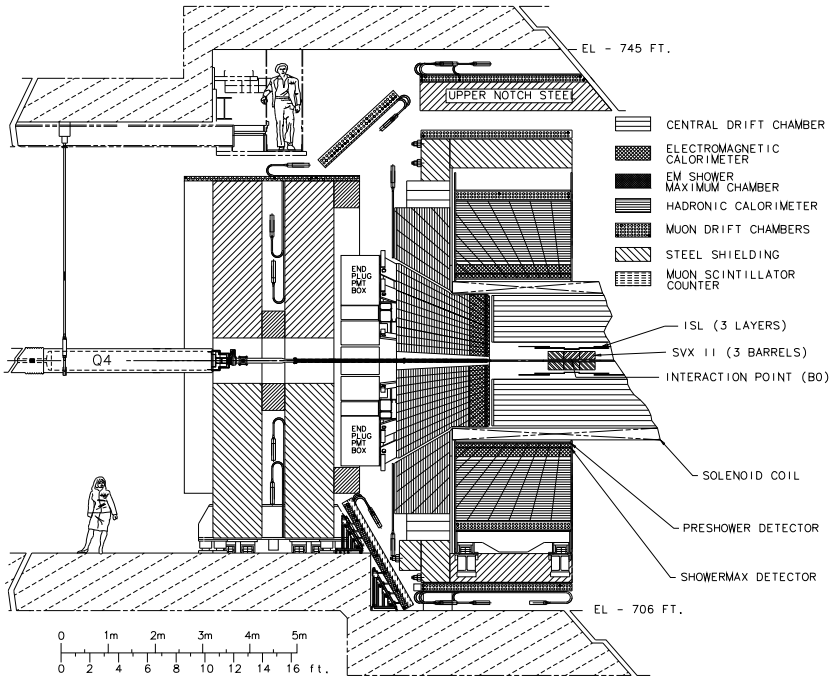

Figure D.1: Elevation view of one half of CDF II Detector.

Appendix E

Beam Related Problems in the CMX Detector

Apart from the increased particle fluence in the CDF muon chambers due to increased energy and luminosity of Run II, the outermost muon chambers have been also exposed to beam losses and halo from the Tevatron and have been observed to be very sensitive to the failures along the beamline which can cause spontaneous beam losses. Since the beginning of Run II numerous isolated and spontaneous breakdown discharges followed by high voltage "trips" have been observed in the muon chambers. A particular case for the CMX detector was in summer 2002, when the chambers started to trip frequently as well as high occupancies were observed in the raw data with high trigger rates. Investigation of currents drawn by the chambers showed

presence of sustained currents.

Figure E.1 shows the anode wire currents for the CMX arches on the west side of the CDF detector for June 30th, 2002. The currents are stored for combination of wedges which follow the HV cabling scheme. Figure E.2 shows the voltage settings for the wedges corresponding to the same data taking period. The nominal chamber operating high voltage for anode is 5.4 kV and stand-by configuration (i.e., no gain configuration) is 2.4 kV. The chambers are usually kept at stand-by when there is no beam in CDF. For this particular date the $p\bar{p}$ collisions started around 9am (Tevatron store 1482) and the CMX HV is set to nominal gain value at the same time. The store ended about 4am July 1, 2002. Initial instantaneous luminosity was moderate at $6.07\times10^{30}cm^{-2}s^{-1}$. The irradiation rate of CMX detector is related to the Tevatron beam intensities and luminosities. Therefore, in most channels the highest current is drawn at the beginning of a store, when the luminosity is highest, then exponentially drops off. This is what is observed in Figure E.1. However, the CMX wedges near the bottom of the arches (below $y = 0$ plane of the CDF coordinate system) showed a behavior of exponential current growth, mostly followed by discharges and trips and stayed in the self-sustained high current mode during "stand-by" configuration until completely unpowered. For example, wedge 21 has increased current drawing into the first two hours of the store at which point it tripped (high voltage and current dropping down to zero). The current self-sustained itself around 30–50 μA when it

was put on standby mode[1]. The long self-sustained currents in the presence of beam for many CMX wedges were associated with symptoms of a glowing mode [163, 62]. Therefore, on August 2, 2002, the alcohol bubbler temperatures were increased to 0° C from 5° C to increase the amount of alcohol vapor as the quenching agent in the gas mixture, in anticipation of curing the problems with these long-sustained currents. It generally takes about a few days for the new concentration of gas+vapor mixture in the chambers to stabilize.

The data in the following weeks had a few isolated cases of growing currents, however, to our best knowledge, a large scale problem as described above was not observed in the following few years of data taking. Also, whenever the quencher composition of the gas mixture changes in the chambers, the drift velocity should be recalibrated. However, the CMX data taken before August 20, 2002 has been declared unusable in any CDF analysis (Section 3.5), so no further action was necessary for this portion of the CMX data. We have further proposed monitoring CSX occupancy for mapping the ϕ dependence of the beam related backgrounds. Similar but less drastic behavior of large current draws in CMX occurred in June 2004 in possible relation with high beam losses. The conditions stabilized before any action on the chamber configurations were taken, except to increase the warning limits to a

[1] At the time of this datataking, the software alarm limits for currents were equal to the hardware limits of the high voltage supplies (200 μA). They were set at a lower value of 25 μA on August 14, 2002.

higher value. The CSX scintillator signals were also started to be set up for monitoring purposes by the CMX/CSX group in collaboration with R.J. Tesarek. To date, no quantitative conclusions were arrived at on why the CMX wedges at the bottom usually show a larger tendency to breakdown.

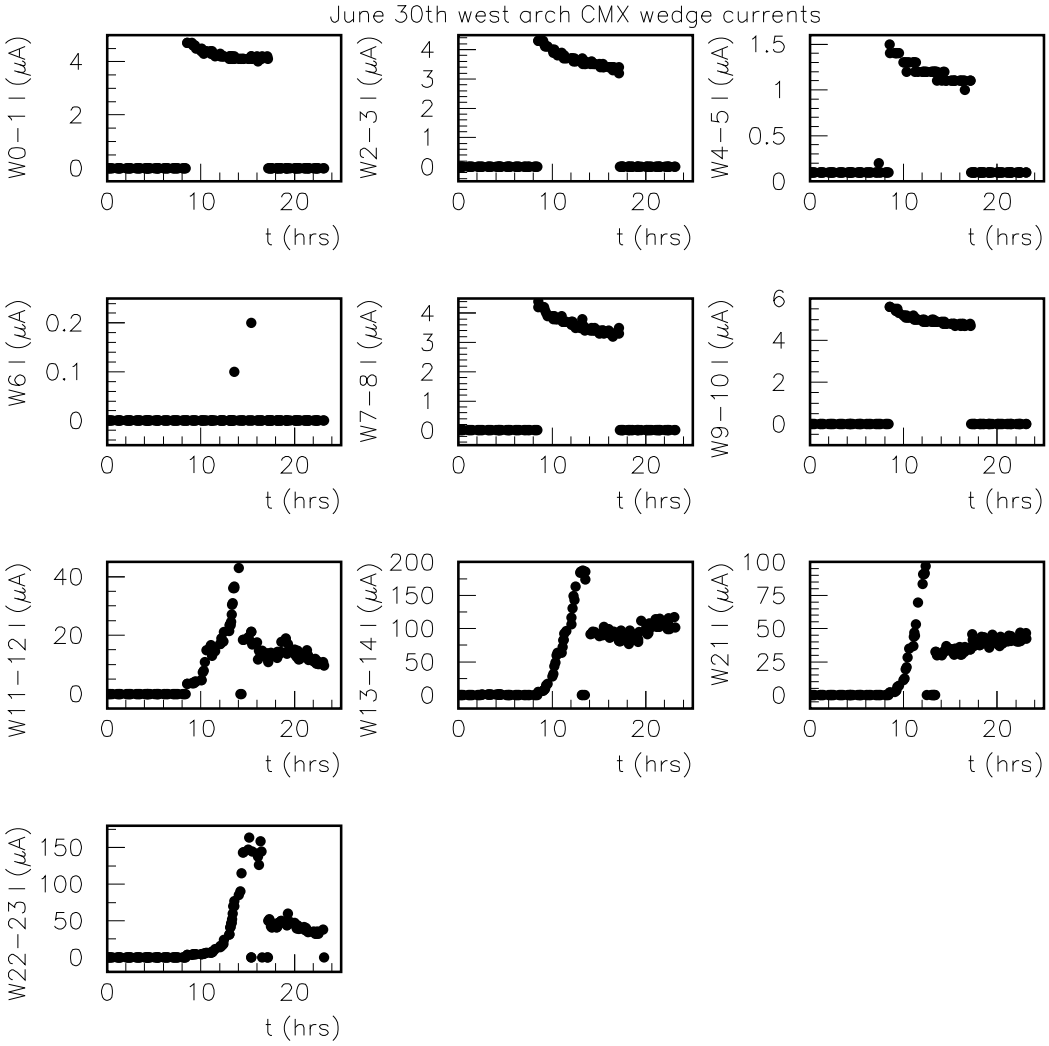

Figure E.1: Anode currents drawn in CMX chambers per wedge for June 30th, 2002. Wedge 6 (W6) is unpowered.

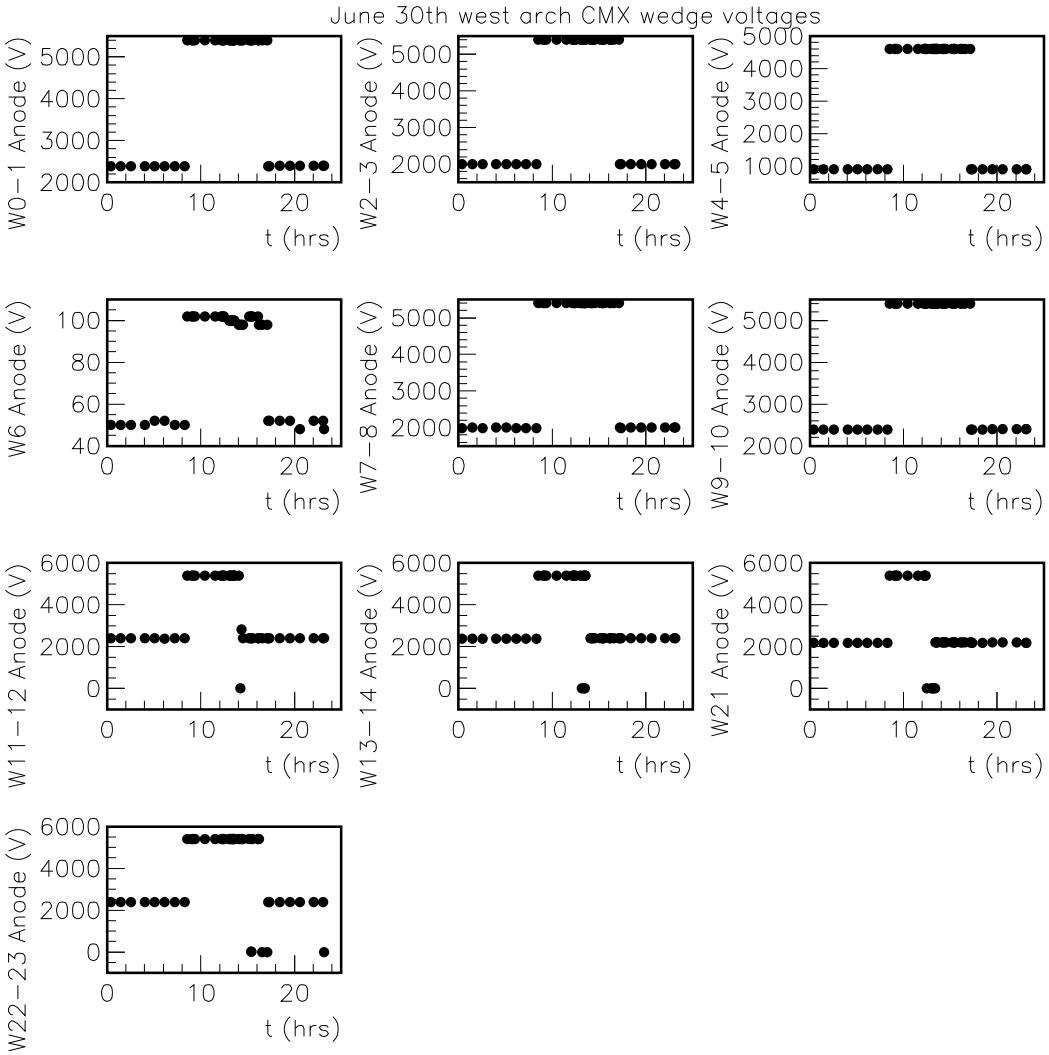

Figure E.2: Voltage settings of CMX wedges for June 30th, 2002. Wedge 6 (W6) is unpowered.

Appendix F

Higher order corrections for Z-like resonances

The QCD (α_s-dependent) higher order corrections are an important part of the cross section estimates in $p\bar{p}$ processes. The cross sections used for extra gauge bosons in this analysis are extracted from Pythia calculated in leading order in α_s . In this section, we compare two estimates of a QCD K-factor for a SM-like heavy Z$'$ boson as a function of the boson mass. One set of cross section numbers for Z$'$ are directly obtained from [146] for which MRST PDF set is used. The cross sections at the Z-boson pole from the same formalism is an updated version [164] of reference [126]. In this context, this set is referred to as "Stirling". The other set of cross sections is calculated by using the program available from W.L. van Neerven. We refer to this

set of cross section values as "HNM".

For the calculations performed using HNM, the Drell-Yan coefficient functions in the $\overline{\rm MS}$ scheme is used. The renormalization (μ), and mass factorization scale (M), have been taken to be the same as the boson mass at each mass the total cross sections are calculated. The cross sections are calculated using a constant value of Fermi coupling constant, G_F (the default selection in the program), instead of using the fine structure constant ($\alpha_{\rm em}$). Therefore, the running of $\alpha_{\rm em}$ as a function of the Z$'$ mass has not been taken into account. For LO calculations GRV98(LO) PDF set and for higher order calculations GRV98(MS) PDF sets are used. $\overline{\rm MS}$ coefficient functions have to be combined with the $\overline{\rm MS}$ parton densities in the same $\alpha_{\rm s}$ order. The pole mass dependence of the K-factor is totally different if this fact is not taken into account. The effects of this is small from NLO to NNLO, but is not negligible from LO to NNLO. The higher order corrections for DY process are very large, mostly due to the considerable size of the renormalization scale, μ, dependent $\alpha_{\rm s}$, which decreases slowly as μ^2 grows. The NLO ($\alpha_{\rm s}^2$) corrected K-factor is insensitive to variations of the factorization scale, M, over 10 GeV$< M <$ 1 TeV [165]. [1] Table F.1 lists the percentage difference for the two calculations. Figure F.1 shows the relative ratio of the NNLO cross sections as a function of mass and the corresponding K-

[1] An updated version of the code is also available which includes improvements such as, the NNLO MRST02 parton densities [166].

	LO	NLO	NLO K-f	NNLO	NNLO K-f
M(Z)=91.12 GeV/c^2	93.4%	99.0%	105.9%	100.3%	107.4%
M(Z)=500 GeV/c^2	92.7%	93.9%	101.3%	97.8%	105.5%
M(Z)=900 GeV/c^2	88.3%	87.5%	99.2%	88.9%	100.7%

Table F.1: Absolute difference in the total Z cross section at $\sqrt{s} =$ 1.96 GeV for two different programs as a function of the mass.

factor. The LO calculations are systematically different regardless of the Z$'$ mass and that the NNLO cross sections agree better for most of the resonance masses. Therefore, most of the discrepancy in the K-factor at lower mass can be attributed to the discrepancy of LO calculations. At this point in time, we do not know the reason for this discrepancy. Some of the differences are also due to the different PDFs used in the two calculations. At high masses, K-factor converges around 1.32, for both calculations. An interesting feature visible in the K-factor (M(Z$'$)) curves in Figure F.1 is the kink around 200 GeV/c^2. The rise of the K-factor up to about this mass value is because the negative quark-gluon contribution diminishes with increasing parton x [146], then the effect of decreasing α_{s} takes over.

It is possible to calculate differential cross sections also as a function of Q^2 and pseudorapidity [166, 167], which have not been performed here.

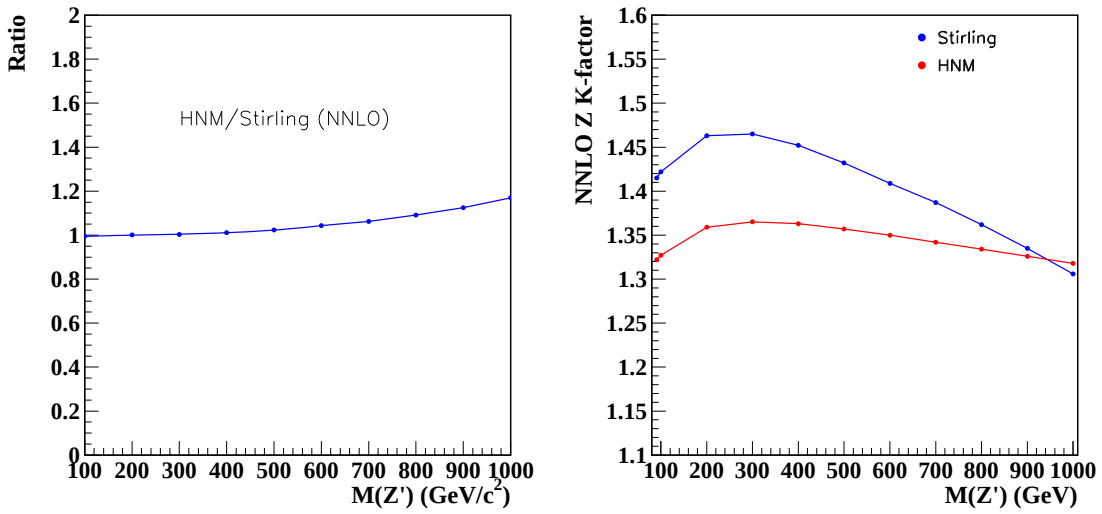

Figure F.1: NNLO cross section ratio (left) and NNLO K-factor curves (right) as a function of mass for two different theory calculations.

Appendix G

Bayesian Counting Limit Setting Method

An earlier version of the high mass dimuon analysis [105] utilized a single experiment counting limit method. A Bayesian approach with a flat prior probability is applied to calculate the 95% CL upper limit on the number of events ($N_{95\%}$) above a certain mass value in the dimuon spectrum. The ingredients necessary to calculate a limit with the method is [147]:

- N_{obs}, events above some apriori chosen invariant mass
- δA, relative signal uncertainty
- N_{bgrnd}, events for the expected background.

- $\delta A \times N_{bgrnd}$, for error on number of background events.

where a Poisson probability of having N_{obs} events given N_{bgrnd} expected events with their respective uncertainties δA and $\delta A \times N_{bgrnd}$. To set the upper limits on $\sigma \cdot \mathrm{BR}(p\bar{p} \to X \to \mu\mu)$, one can use

$$(\sigma \cdot BR)_{95\%}(M) = \frac{N_{95\%}}{\mathcal{L} \times \epsilon \times A(M)} \quad , \tag{G.1}$$

where $\mathcal{L}$ is the luminosity, ϵ is the selection efficiency and $A(M)$ is the signal acceptance.